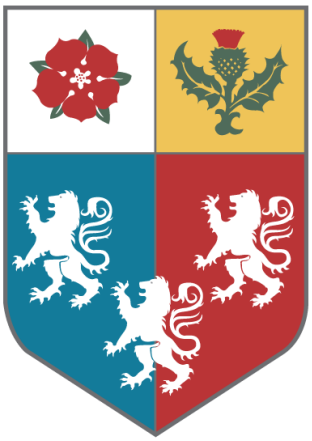
Thermomechanical Behaviours of Unfilled/filled Thermoplastic Polyurethane





Huanming CHEN

Pembroke College

Supervisor: Prof. Clive Siviour

A Thesis submitted for the degree of

Doctor of Philosophy

Trinity Term 2021

Thermomechanical behaviours of unfilled/filled thermoplastic polyurethane

H. CHEN, Pembroke College, University of Oxford

Submitted for the degree of D.Phil., Trinity 2021

ABSTRACT

Thermoplastic polyurethane (TPU) exhibits enormous mechanical performance and extensibility in both engineering, industry and scientific applications. The filled polymer which enclosed rigid particles has mainly improved on mechanical properties. The work focused on three TPUs, carbon-black-filled TPU, supramolecular TPU, and sugar-filled TPU. To characterise their advantages and fundamental properties, thermo-mechanical analysis, mechanical experiments and scattering techniques can be used. However, testing rubber material in high rate responses is difficult. Therefore a principle of time-temperature superposition was employed to associated mechanical behaviour with temperature and loading rates. The principle was as foundation connecting all experiments and modelling procedures to cooperate the thermo-mechanical data with linear viscoelastic theory. Upon this methodology, these behaviours in TPU and its composites can be calibrated, further predicted on high strain rates. The study of the interpretation of the phenomenological model is not only responsible for reproducing strain-stress behaviour from low- to high-strain rates, but also take advantage of time-temperature equivalence on thermo-mechanical behaviour for objectives linking between different conventional experiments. The purpose of the research is to characterise mechanical behaviour on different types of TPU materials, explore their properties especially in high strain rates, at last develop the application of viscoelastic theory in order to describe polymer at large deformation in high rate exepriments.

ACKNOWLEDGEMENTS

Without the support, guidance, and intellectual input of Prof. Clive Siviour, this research would not be possible, and I thank him wholeheartedly. I also would like to thank people who supported my research during my time at the University of Oxford. I would like to thank them in no particular order for their help in enabling me to do the best in research: Igor Dyson, for inducing me into the mechanical testing laboratory and training me on how Instron machine, liquid nitrogen systems, and environmental chamber; Marzena Tkaczyk, for inducing me into the thermomechanical laboratory and training me on how to use the DSC, DMA, and rheometer. Nick Hawkins, for helping me solve many issues I had faced in the laboratory and apparatus set-up; Richard Duffin, for helping the manufacture and component fabrication in the workshop for experimental tests.

I would also like to thank the generous support of the Air Force Office of Scientific Research, and specifically. A further thanks to Pembroke College, who have contributed financially to enable me to attend conferences to make the most of the networking opportunities and present my D.Phil. research to colleagues in the field.

This material and research are based upon the work supported by the Air Force Office of Scientific Research, Air Force Material Command, USAF under Award No. FA9550-15-1-0448.

CONTENT

CHAPTER 1 - INTRODUCTION

1.1 Motivation 1

1.2 Objective 2

1.3 Structure of thesis 2

1.4 Work outline 4

CHAPTER 2 - BACKGROUND & LITERATURE REVIEW

2.1 Thermoplastic elastomers 5

2.1.1 Background and uses 5

2.1.2 Synthesis and morphology 6

2.1.3 T_g and T_m 9

2.1.4 Particulate filled polymers 10

2.1.5 Techniques for structural characterisation 13

2.2 Viscoelastic behaviour and constitutive relations 16

2.2.1 Linear viscoelasticity 17

2.2.2 Generalized Maxwell model and Boltzmann superposition 19

2.2.3 Dynamic properties of elastomers 23

2.2.4 Time-temperature superposition 24

2.2.5 Prony series parametrization 27

2.3 Mechanical experiments from low- to high- rates 30

2.3.1 Low-rate experiments 30

2.3.2 Intermediate-rate experiments 30

2.3.3 High-rate experiments (SHPB, and Piezo-bar) 32

2.4 Reference for Chapter 2 39

CHAPTER 3 - CARBON BLACK-FILLED POLYURETHANE

3.1 Introduction 46

3.2 Paper A: Application of linear viscoelastic continuum damage theory to the low and high strain rate response of thermoplastic polyurethane 47

CHAPTER 4 – SUPRAMOLECULAR SELF-HEALABLE POLYURETHANE

4.1 Introduction 74

4.2 Paper B: Mechanical characterisation and modelling of a thermoreversible supramolecular polyurethane over a wide range of rates 75

CHAPTER 5 – SUGAR-FILLED SUPRAMOLECULAR POLYURETHANE

5.1 Introduction 108

5.2 Paper C: Experimental characterisation and modelling of the strain rate dependent mechanical response of a filled thermo-reversible supramolecular polyurethane 109

CHAPTER 6 – DISCUSSION & LIMITATION

6.1 Introduction 144

6.2 Materials 145

6.3 Time-temperature equivalence 146

6.4 Experimental apparatus considerations 148

6.5 ‘Damage’ models and their capabilities 145

CHAPTER 7 – CONCLUSION

7.1 Conclusion 149

7.2 Future plan 152

APPENDIX

Supplymentary Information for Paper A 155

Supplymentary Information for Paper B 169

Supplymentary Information for Paper C 187

LIST OF TABLE

CHAPTER 1 - INTRODUCTION

Fig. 1-1. The work outline and the methodology for the projects in this thesis 4

CHAPTER 2 - BACKGROUND & LITERATURE REVIEW

Fig. 2-1. Reaction scheme for the synthesis of polyurethanes, by using copolymerization of MDI and ethylene glycol 7

Fig. 2-2. Reaction scheme for the synthesis of polyurethane, by using copolymerization of TDI and polypropylene oxide glycol.....7

Fig. 2-3. The schema of polymeric microstructure in polyurethane, which contains both hard and soft segments to form domain structure. TPU morphology exhibits multi-scale phase separation characterised by heterogeneous morphologies at the micro- and nano- scales. 7

Fig. 2-4. An ideal representation of the modulus of a polymer as a function of temperature, showing the different transitions and the related molecular motions 10

Fig. 2-5. Examples of different thermal processes observed through DSC experiments on a supramolecular PU (SPU), sugar filler, and carbon-black TPU. (a) glass transition in SPU undergoing thermal loops from -70°C to 220 °C, also showing non-reversible transitions; (b) melting sugar above 180 °observed its decomposition process; (c) heat flow in carbon-black TPU, showing a glass transition at 35°C, and a dissociation region at 90 °C 14

Fig. 2-6. (a) Single term for Maxwell model and (b) single term for Kelvin-Voigt model.....18

Fig. 2-7. (a) Standard linear solid (SLS) model I (Kelvin-Voigt representation), (b) Standard linear solid (SLS) model II (Maxwell representation).....19

Fig. 2-8. Generalized Maxwell model 20

Fig. 2-9. The model input (a) and (c) to obtain analytical solution (b) and (d). All elements for stress relaxation and creep are assigned as: E_0=10, E_1=8, E_2=6, E_3=4, E_4=2, E_5=1, η_1=2, η_2=4, η_3=6, η_4=8, η_5=10; input resource for ε=1 or σ=1 was applied to the model, the stress or strain in time-span was obtained, to calculate the relaxation modulus and creep compliance (e). The strain-/stress- input model is introduced in next figure 21

Fig. 2-10. The schema of generalized Maxwell model with 5-Maxwell terms, constructed in Simscape toolbox, MATLAB 22

Fig. 2-11. Implementation of the Boltzman superposition integral for a two term Maxwell model, in which E_0=5, E_1=E_2=10, η_1=5, η_2=10 for monotonic and cyclic loading at 0.1 s^{-1}...23

Fig. 2-12. Production of Master Curve using DMA data for Black rubber. Coloured lines represent isothermal frequency data whilst black line represents the Master Curve.....26

Fig. 2-13. SPU specimen tested in DMA tensile mode (a), and rheometery (b). (c) showed a distinct yielding and plastic deformation for this polymer during the experiment.....27

Fig. 2-14 DMA results (a) on SPU showed necking problem affected the measurement during the experiment. Rheological results (b) showed the data has a good compliance to DMA data around temperature of 0 °C. The limitations of each instrument in performance were discussed in the following Chapter 4 27

Fig. 2-15. Comparisons of Maxwell models with different numbers of terms fit to experimentally master curves. 29

Fig. 2-16. Comparison of generalized Maxwell models fit to (a,b) storage modulus or (c,d) loss modulus. Two methods for determining Prony series from either storage or loss modulus are given.....29

Fig. 2-17. The schema of extensometer for compression and tensile experiments 30

Fig. 2-18. The schema of hydraulic compressor for medium rate 31

Fig. 2-19. The strain rate measurement in hydraulic medium rate experiments, at (a) 1.36 s^{-1}, (b) 11.5 s^{-1}, (c) 40 s^{-1}. The strain-stress data is in (d) 32

Fig. 2-20. The SHPB technique with or without the use of piezoelectric gauges at the bar-specimen interface. The signals from the strain gauge or piezo-gauge were amplified, then recorded and displayed using an oscilloscope 33

Fig. 2-21. SHPB experiment on black rubber at 2020 s^{-1} using magnesium bars, the second test has better incident wave as a proper pulse shaper was used. The pulse shaper removes some oscillations in the incident stress wave and in the resulting specimen response 36

Fig. 2-22. Barrelling and non-constant strain rate observed in high rate experiments for carbon-black rubber at a strain rate of about 2000 s^{-1} (a), up to 0.45 in true strain (b). Using high-speed digital photographs clearly shows the sample deformation, which illustrates the problems associated with SHPB tests on soft materials 37

Fig. 2-23. Piezo-titanium bar test on sugar filled SPU at strain rate of 545 s^{-1} (a). Full inpout-output signals (b) and force equilibrium (c) are given. The advantage of using piezo-electric transducer on output bar, is to minimise the noise and increase accuracy of the transmission wave to obtain more accurate data for material behaviour (d) 38

CHAPTER 3 - CARBON BLACK-FILLED TPU

Fig. 3-1 Generalized Maxwell model 51

Fig. 3-2. Moduli E’ and E’’ as a function of temperature: DMA data obtained from isothermal frequency sweeps at four frequencies: 0.5, 2, 5 and 10 Hz 55

Fig. 3-3. TTS applied to E’ – log f plots from DMA experiments: (a) master curve of E’ – log *f* at 25 °C and (b) E’ – log *f* plots at selected temperatures, as indicated in the figure 55

Fig. 3-4. Shift factor vs. temperature at reference temperatures of 25 °C and -27 °C; WLF equation evaluated at Tg = -27 °C with parameters C1 =7.3 °C, C2 =45 °C 56

Fig. 3-5. (a) Storage modulus E' , (b) Loss modulus *E'' vs.* log *f* showing Prony series fit ...57

Fig. 3-6. (a) Storage modulus E', (b) Loss modulus *E'' vs.* log *f* showing Prony series fit for various reference temperatures 57

Fig. 3-7. Numerical model of DMA experiment using dual cantilever configuration 58

Fig. 3-8. Comparison of analytical and FE model outputs with DMA experiment: (a) Full range of frequencies; (b) 10 Hz; (c) 5 Hz; (d) 2 Hz; (e) 0.5 Hz 59

Fig. 3-9. The process to determine the phenomenological damage factor: (a) stress-strain curves from compression experiments and Boltzmann superposition principle at three strain rates, 22.5 °C; (b) comparison of local stiffnesses from experiments and Boltzmann superposition; (c) the parameters α =0.058, β =0.042 for the phenomenological damage factor (i.e. the ratio of the stiffnesses in (b)) were determined from the average of three strain rates: 0.09 s^{-1}, 0.009 s^{-1} and 0.0009 s^{-1} by fitting equation (11) to the empirical data. The damage model was calibrated at 22.5 °C.....62

Fig. 3-10. Comparison of experimental data to model predictions when varying strain rates (a) or temperatures (b) in compression experiments. The damage parameters from Fig. 9 (α =0.058, β =0.042) were used. The rate and temperature effects were captured using appropriate TTS master curves (Fig. 6) and the Boltzmann superposition integral equation (12).....62

Fig. 3-11. Data obtained in cyclic tensile experiments with constant temperature of 16.8 °C but varying strain rates of 0.08 s^{-1}, 0.008 s^{-1} and 0.0008 s^{-1}. The local stiffnesses from the Boltzmann superposition integral and experiments are plotted, (a), to compare the damage parameters α =0.058, β =0.042 from compression in Fig. 9(c) to the empirical ratio from tensile

experiments, (b). The same parameters are adopted with strain reset at the start of the unloading process, to produce the simulation, (c), at 16.8 °C 64

Fig. 3-12. A multi-cyclic tensile experiment was executed at 16.8 °C and 0.008 s^{-1} strain rate. The existing parameters of α =0.058, β =0.042, (a), were used for the entire model, (b); while the switchable parameters: α_1 =0.058, β_1 =0.042 for the primary loading, and α_2 =0.012, β_2 =0.417 for the remaining, (c), exhibits better results, (d) 65

Fig. 3-13. Experimental configuration for SHPB test.....66

Fig. 3-14. High strain rate compression experiments were executed at 18.7 °C at three strain rates: 765 s^{-1}, 1350 s^{-1} and 2020 s^{-1}. The existing parameters of α =0.058, β =0.042, (a), were used again for the model simulation (b) 67

CHAPTER 4 - SUPRAMOLECULAR THERMOREVERSIBLE TPU

Fig. 4-1. Chemical structure of the supramolecular polyurethane, featuring urea morpholine end groups, used in this study and a schematic illustration of formation and dissociation of the polymer network when an appropriate stimulus, such as heat, is applied 79

Fig. 4-2. ^{1}H NMR spectroscopic data for SPU specimens following different thermal processing regimes, using air-cooling, water-cooling, or controlled cooling rates 81

Fig. 4-3. GPC results for three types of SPU specimens: ‘raw’, ‘single’ and ‘repetitive’, demonstrating that the molecular weights do not change with repeated processing 82

Fig. 4-4. DSC experiments with different cooling rates performed on an initially cast specimen (a) measured heat flow for the different heating and cooling loops (b) detail of heating loops 83

Fig. 4-5. SAXS data obtained at 25 °C for ‘raw’ material, and ‘single’ SPU specimens prepared using different thermal processing regimes. All samples experienced a heating rate of 2 °C min-

[1] to a temperature of 80 °C before being cooled in air, in water or at controlled rates between 1 and 10 °C min^{-1} 84

Fig. 4-6. Stress-strain relationships in (a) air- and (b) water-cooled specimens under compression: 'single' specimens have undergone a single thermal treatment, while 'repetitive' specimen received four thermal treatments. The compression were performed at ambient temperature between 19-21 °C, differences between the curves might be due to temperature variations.....85

Fig. 4-7. Rheological analysis at different (a) heating rates or (b) cooling rates of 1, 2, 5, 10, 20 °C min^{-1}. Mean data for the cooling and heating portions of the loops (at 2 °C min−1) are also shown. The full sets of results from cooling and heating, respectively, are shown in (c) and (d). These data also show that processing at different rates does not affect the subsequent properties. Oscillation frequency 1 Hz and amplitude 0.1% 86

Fig. 4-8. Application of the Arrhenius equation based model to (a) heating and (b) cooling rates of 1, 2, 5, 10, 20 °C min^{-1}. The reference curve was the average of cooling and heating at 2 °C min−1, representing the temperature rate $\dot{T} \to 0$. The experimental temperature profiles and model parameters of r_0=2 s^{-1} and U/k=1312 K were used. Oscillation frequency 1 Hz and amplitude 0.1%. 88

Fig. 4-9. (a) DMA data showing isothermal frequency sweeps at different temperatures. The DMA performs well from -60 to 30 °C but inaccuracies are apparent above 10 °C. (b) Rheometer data are accurate at higher temperatures but not below -10 °C. Here, DMA data at 10, 0 and 10 °C are overlaid to show the consistency between these two techniques.....90

Fig. 4-10. (a) and (b) A continuous master curve of E′ vs. log *f* generated by applying TTS to E′ vs. log *f* curves at different temperatures from the rheometer and DMA. In particular, (a)

shows the consistency between the two sets of data. A Prony series was fitted to the storage modulus profile in (b) using the full range of frequencies.....91

Fig. 4-11. Schematic of the viscoelastic softening model. The model combines springs and dashpots described by the Prony series, an additional dashpot η^* and a recovery spring E^* .92

Fig. 4-12. (a) A series of linear dashpots was first fitted to the experimental data, the logarithms of the fitted viscosities were found to be linear in log(applied stress), described by the function given and extrapolated to high strain rates. (b) The character of the non-linear dashpot was determined by finding the solution to the ODE formed for $\eta*$ against σ; this was then sampled at the points shown to produce a lookup table for the model 93

Fig. 4-13. (a) A series of specimens were compressed to different strains, ε_f, (in experiments lasting a few minutes) and allowed to recover a period of a few hours before being reloaded, whilst the strain, ε_0, was monitored; some of the samples were then reloaded. (b) a value of E^* = 0.85 kPa allowed the model to capture the recovery history of a number of samples, including those loaded cyclically (1-3) or monotonically (4) to different strains. All experiments were executed at a temperature of 25 °C.....94

Fig. 4-14. Model outputs for a sample compressed at 0.01 s^{-1}, 25 °C. The figure shows stress-strain relationships and strain time histories in different components of the model 95

Fig. 4-15. Isolated generalized Maxwell model compared to low and medium rate compression experiments, at a temperature of 25°C but varying strain rates.....96

Fig. 4-16. Viscoelastic softening model with linear dashpot $\eta*$ linear (strain-rate dependent) and nonlinear dashpot $\eta*$ nonlinear (stress-dependent value), compared to low strain rate compression experiments, at a temperature of 25°C but varying strain rates.....97

Fig. 4-17. Viscoelastic softening model with linear dashpot $\eta*$ linear (strain-rate dependent) and nonlinear dashpot η∗nonlinear (stress-dependent value), compared to low strain rate compression experiments, at a temperature of 25°C but varying strain rates.....97

Fig. 4-18. Experimental configuration for SHPB test.....98

Fig. 4-19. The high-strain rate compression experiments, at a temperature of 17 °C. The value of $\eta*$ linear used was 0.47, 0.44, 0.36 for strain rates of 530, 820 and 1220 s^{-1}, obtained from the linear fitting in Fig. 12a. The models using η∗nonlinear used the table derived in in Fig. 12b. The stress-strain curves for the viscoelastic Maxwell model and the full model using the two identified dashpots are shown.....98

Fig. 4-20. The viscoelastic softening model compared to a multi-cyclic compression experiment.....101

Fig. 4-21. The viscoelastic softening model under stress-control (e.g. the zero-stress vs. time as input profile) to simulate the recovery process. The figures display (a) strain profiles of the full model, dashpot and Maxwell elements. (b) The model simulation of first recovery and second recovery compared to the empirical data. The measured strain data are given in Table SI 4.....101

CHAPTER 5 - SUGAR-FILLED SUPRAMOLECULAR TPU

Fig. 5-1: The supramolecular healable polyurethane used in this study, featuring urea morpholine end groups 113

Fig. 5-2: Schematic diagram of the SHPB experiment.....115

Fig. 5-3: (a) Stress-strain data for filled and unfilled SPU tested in monotonic and cyclic compression experiments at a strain rate of 0.01 s^{-1} and 25 °C. The apparent Young's modulus is 7.2 MPa for the unfilled polymer and 15, 55 and 145 MPa for filled polymer specimens G25,

G50 and G75 respectively. The empirical reinforcement factor, Rtest, is calculated as 2 (G25), 7 (G50) and 20 (G75). These ratio values can be optimally fitted by the Guth equation when P=3.9, which gives R_{Guth} as 3.2, 8.5 and 16.8. The predicted Young's modulus from the viscoelastic polymer model at 0.01 s^{-1} is about 7.5 MPa for unfilled polymer, which gives predicted Young's moduli of about 24, 64 and 126 MPa for G25, G50 and G75. Parameters used in other reinforcement equations are: υ_m=0.49 for Kerner equation; E_p=250 MPa for the series and parallel model; x=0.3 for the Hirsch model 118

Fig. 5-4: (a) Comparison of model stress-strain curves with and without particle reinforcement to experimental data for three different filled SPUs; (b) Empirical damage factor compared to those obtained using different values of ε_a in Eq. (5-9); (c) Comparison of stress strain curves produced using three values of εa, in Eq. (5-9), to experimental data.....120

Fig. 5-5: Stress-strain simulation using different value of εa and k in Eq. (5-11). The parameters R_{Guth}, ε_a, k were: G25: 3.2, 0.07, 0.35; G50: 8.5, 0.05, 0.6; G75: 16.8, 0.035, 0.85.....121

Fig. 5-6: Damage curve using damage Eq. (5-12) with different values of ε_a and k. The empirical damage was determined by $E_{secant,test}$ / (E_m × R_{Guth}). E_m is the local secant modulus determined by the viscoelastic polymer model.....122

Fig. 5-7: Strain-stress behaviour modelled using damage Eq. (5-12) with different values of ε_a and k. The ultimate stress was determined *via* $\sigma=E\varepsilon$.....123

Fig. 5-8: Model implementation for specimens of G25, G50 and G75, in which (a) the Guth reinforcement equation was used to reinforce the viscoelastic polymer model, (b) the damage equation with optimal values of εa and k from Eq. (5-12) was used to perform (c) the modelling of the composite behaviour at 0.01 s^{-1} and 25 °C. The parameters, R_{Guth}, ε_a, k were assigned to the three types of composites as follows G25: 3.2, 0.055, 0.4; G50: 8.5, 0.048, 0.68; G75: 16.8, 0.042, 0.99.....124

Fig. 5-9: Model implementation for specimens of G50, C50 and I50, in which (a) the Guth reinforcement equation was used to reinforce the viscoelastic polymer model, (b) the damage equation with optimal value of ε_a and k from Eq. (5-12) was used to perform (c) modelling of the composite behaviour at 0.01 s^{-1} and 25 °C. The parameters R_{Guth}, ε_a, k were assigned as G50: 8.5, 0.048, 0.68; C50: 8.5, 0.054, 0.61; I50: 8.5, 0.06, 0.54 125

Fig. 5-10: (a) and (b) show the linear relations between fitting parameters ε_a , k and filler particle size and volume fraction. These two 2D plots correspond to 3D surfaces (c) and (d). From surface plots (c) and (d), a unique set of damage parameters can be extracted for any particle diameter and volume fraction. For example, the parameters RGuth, ε_a, k were assigned to specimens of I30 and C65 as: I30: 4, 0.065, 0.31; C65: 13, 0.051, 0.78 126

Fig. 5-11: Model implementation for specimens of I30 and C65. (a) Comparison of model with Guth reinforcement equation, but no damage, to the experimental data; (b) comparison of full model with damage to the experimental data. The parameters, R_{Guth}, ε_a, k, were assigned as I30: 4, 0.065, 0.31; C65: 13, 0.051, 0.78, to model the behaviour at 0.01 s^{-1} and 25 °C 127

Fig. 5-12: Model implementation for specimen G50, in which (a) the Guth reinforcement equation was used to reinforce the viscoelastic polymer model, (b) the damage parameters ε_a and k were used to model the composite behaviour (c) from 0.001 to 0.01 s^{-1} and 25 °C. The parameters, R_{Guth}, ε_a, k were assigned as G50: 8.5, 0.048, 0.68 128

Fig. 5-13: Model implementation for specimen G50, in which (a) the Guth reinforcement equation was used to reinforce the viscoelastic polymer model, (b) the damage parameters ε_a and k from the quasi-static experiments were used to model the composite behaviour (c) at high rates and 20 °C. The parameters, R_{Guth}, ε_a, k were assigned as G50: 8.5, 0.048, 0.68 129

Fig. 5-14: Model implementation for specimen G70, in which (a) the Guth reinforcement equation was used to reinforce the viscoelastic polymer model, (b) the damage parameters ε_a

and k were extracted from Fig. 5-10 to model the composite behaviour (c) at high rates and 20 °C. The parameters, R_{Guth}, ε_a, k were assigned as G70: 14.9, 0.043, 0.93 129

Fig. 5-15: Model implementation for specimen G75, in which (a) the Guth reinforcement equation was used to reinforce the viscoelastic polymer model, (b) the damage parameters ε_a and k from the quasi-static experiments were used to model the composite behaviour (c) at high rates and 20 °C. The parameters, R_{Guth}, ε_a, k were assigned as G75: 16.8, 0.042, 0.99 130

Fig. 5-16: The amount of temperature rise predicted at strain intervals of 0.1 in composites of G50, G70 and G75 131

Fig. 5-17: Model implementation for specimen G50: the 'new' viscoelastic polymer model with adiabatic heating effects was compared to previous polymer model (a); the Guth reinforcement equation was used to reinforce the 'new' viscoelastic polymer model (b); the same damage parameters ε_a and k was used (c), to compare the 'new' model outputs with empirical data (d). The modelling of the composite behaviour performed at 0.01 s^{-1} and 20 °C. The parameters, R_{Guth}, ε_a, k were as follows: G50: 8.5, 0.048, 0.68 133

Fig. 5-18: Model implementation for specimen G70: the 'new' viscoelastic polymer model with adiabatic heating effects was compared to previous polymer model (a); the Guth reinforcement equation was used to reinforce the 'new' viscoelastic polymer model (b); the same damage parameters ε_a and k was used (c), to compare the 'new' model outputs with empirical data (d). The modelling of the composite behaviour performed at 0.01 s^{-1} and 20 °C. The parameters, R_{Guth}, ε_a, k were as follows: G70: 14.9, 0.043, 0.93 133

Fig. 5-19: Model implementation for specimen G75: the 'new' viscoelastic polymer model with adiabatic heating effects was compared to previous polymer model (a); the Guth reinforcement equation was used to reinforce the 'new' viscoelastic polymer model (b); the same damage parameters ε_a and k was used (c), to compare the 'new' model outputs with

empirical data (d). The modelling of the composite behaviour performed at 0.01 s^{-1} and 20 °C. The parameters, R_{Guth}, ε_a, k were as follows: G75: 16.8, 0.042, 0.99 134

Fig. 5-20: Strain recovery in specimens (a) SPU, G25, G50, G75 (c) SPU, G50, C50, I50 at 37 °C. The gradient of the logarithmic recovery is plotted against volume fraction (b) and filler size (d).....135

CHAPTER 6 - DISCUSSION & LIMITATION

Fig. 6-1. CB-TPU rate dependence (a). Mastercurves of storage modulus, calculated from DMA experiments compared to characteristic stress (~0.05 ε) from monotonic loading (b). This demonstrates the effect of the glas transition on the high strain rate response.....146

Fig. 6-2. CB-TPU temperature dependence (a). Stress at ~0.05 ε against temperature, showing the transition from rubbery to glassy as the temperature is reduced (b).....147

CHAPTER 1 INTRODUCTION OF THESIS

1.1 Motivation

Polyurethane, a rubbery polymer, has been used in engineering and industrial fields over the last century. It has particular benefits of flexibility and durability for uses in bumpers, automobile parts, seals products, moulded gaskets and ducts, connectors and tapes, as well as load mitigation and vibration damping.

In general, polyurethane is soft and flexible at room temperature; however, it is stiffer, and even brittle at low temperatures. When the temperature returns to ambient, it becomes relative soft and flexible again. These properties and behaviours, which are reversible and known as temperature dependence. Therefore, the mechanical properties in the application are highly dependent on the working temperature. In addition, the polymer has good extensibility and capability of elongation during slow deformation, but becomes stiffer if loading rates are increasing or under impact. These features are known as rate dependence. Therefore, understanding the polymer's behaviour at different temperatures, loading rates, large deformation, etc, is significant to use it safely and effectively. However, testing the soft polymer in high-strain rates and large deformation is difficult. It generally requires more sensitive sensors and is affected by the low speed of sound in the material.

From the theoretical level, using viscoelastic theory might be helpful to predict polymer behaviour at high strain rates, by linking the property transitions between different temperatures and loading rates. For example, the polymer properties at low temperature and normal strain rates are equivalent to the behaviour undergoing normal temperature and high strain rates. However, this equivalence is only validated at very small strains. To address the above difficulties of characterising large deformation and high rate behaviour, it is necessary to develop a model to reproduce, calibrate and predict the behaviour of polyurethane materials.

1.2 Objective

The overall objective of this thesis is to characterize the thermo-mechanical behaviour in three representative polyurethane polymer / polymer-composites, and model their mechanical behaviour from low-to-high strain rates. More specifically, the aim is to develop a viscoelastic-based model which combines experimental data and the time-temperature superposition principle to reproduce the general behaviour of the polyurethane material, and also be capable of predicting large deformation and high strain rate behaviour. The research explores the application of dynamic mechanical results and empirical low-rate experiments to characterise the polymer and its composites at higher rates and different temperatures. Three applicable phenomenological models are proposed, one in each project of the study. The ultimate aim is to provide supplementary data and a practicable modelling method for these polyurethane materials to be used in future industry and scientific research.

1.3 Structure of Thesis

Chapter 2 begins with an overview of the polyurethane polymer, considering its composition, molecularity, conformation and morphology and transition temperatures. Techniques to characterise and quantify these properties are introduced. The principle of viscoelastic theory, associated with empirical thermo-mechanical behaviour and time-temperature superposition is reviewed. Finally, the techniques used to perform mechanical experiments from low-to-high strain rates is reviewed, the limitations of each testing method are discussed.

Chapter 3 introduces the characterisation and modelling work for carbon-black filled polyurethane (CB-TPU) undergoing deformation from low- and high-strain rates. The thermo-mechanical properties were analysed via dynamic mechanical analysis (DMA), to construct a viscoelastic model which performed polymer behaviour in time-temperature dependence. A strain-induced continuous damage model was used, to expand the scope of application of the viscoelastic model from small to large deformation. The model was then applied to reproduce

the strain-stress behaviour in monotonic compression, cyclic tensile and high strain rate compression experiments.

Chapter 4 presents well-rounded investigations in one soft, synthetic, healable supramolecular polyurethane (SPU). The properties in molecular conformation and morphology after different thermal histories were analysed. The Arrhenius equation was employed to reproduce rheological behaviour for the SPU under controlled thermal processes. DMA experiments characterised thermo-mechanical properties within the principle of time-temperature superposition. Based on these empirical data, a viscoelastic-based model was proposed, to calibrate polymer mechanical behaviour from low to moderate strain rates, and further to predict high strain rate behaviour. The strain recovery was also modelled.

Chapter 5 develops the application of the viscoelastic-based model (from Chapter 4) to representative particulate-polymer, in-house fabricated sugar-filled SPU composites. The model incorporated the viscoelastic-based model for the polymer matrix, with a filler reinforcement equation and debonding damage equation. The model is capable of reproducing the mechanical behaviour of different composites at low strain rates. The strain-induced damage mechanism and continuous damage theory were used. Adopting the model parameters from low rates, the model is capable of predicting the mechanical behaviour of the same composite in high strain rate experiments.

The discussions for objective polymer and each project are given at each chapter. In Chapter 6, the principle of time-temperature equivalence, experimental compliance, model frameworks and their limitations are discussed. The key outcomes from the overall study are outlined. Finally, Chapter 7 gives some suggestions for the future work necessary for the continued improvement of the study on TPU.

1.4 Work Outline

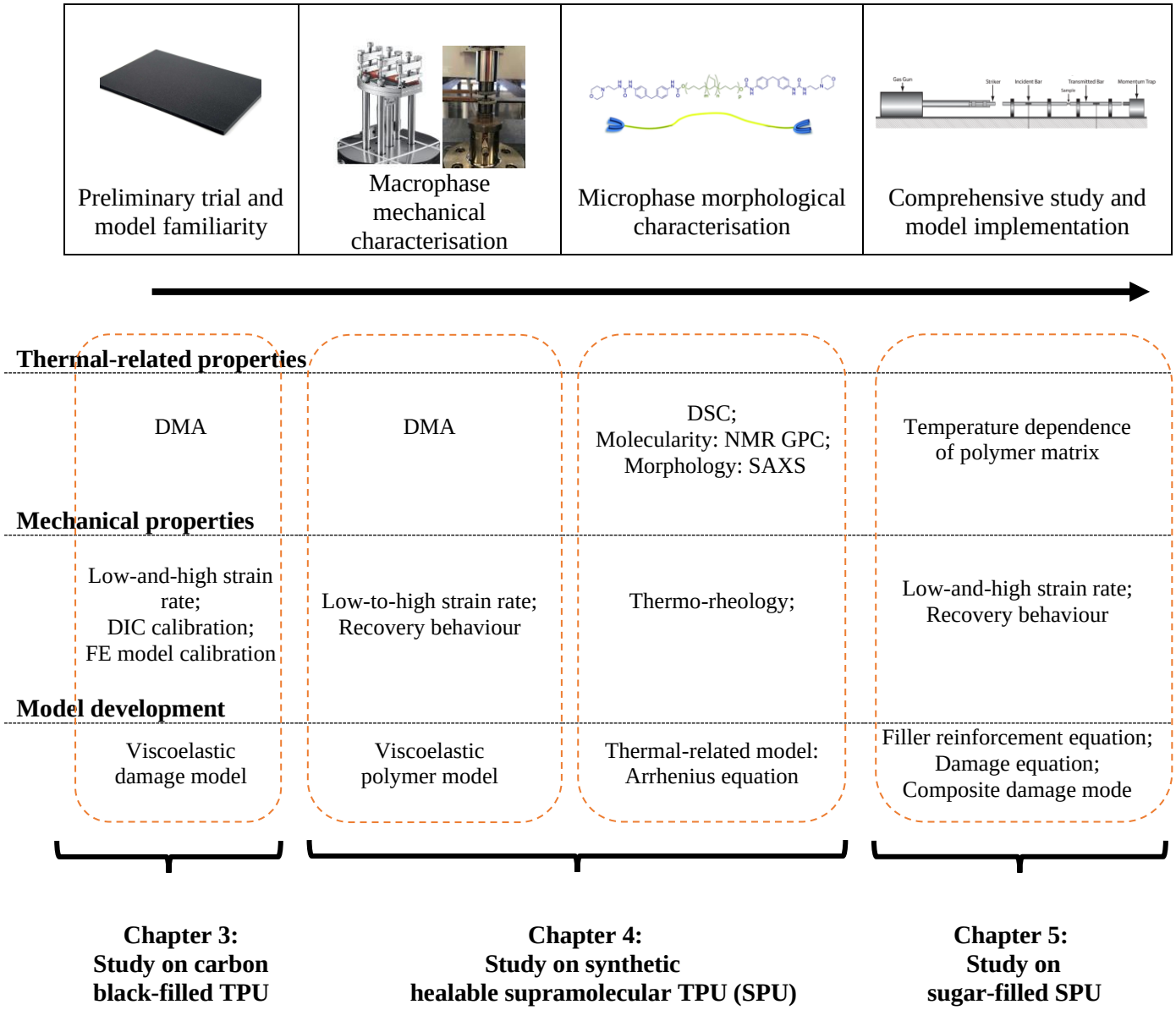


Fig. 1-1. The work outline and the methodology for the projects in this thesis.

CHAPTER 2 BACKGROUND & LITERATURE REVIEW

2.1 Thermoplastic Elastomers

2.1.1 Background and uses

Synethetic elastomers are soft, deformable polymers displaying rubbery elasticity at ambient temperatures. These materials have been developed early in the 20th century, and extensive modification of physical and chemical properties is now possible, allowing use in a range of applications. Polyurethanes are an important class of elastomeric materials presenting excellent properties such as abrasion resistance, chemical and corrosion resistance, temperature-related flexibility, and a wide range of mechanical strength and toughness according to the variety of chemical structure and processing during manufacture[1–4]. The properties can be tailored depending on the end-use, enabling their utilization for a variety of applications including structural foams, coatings (or films), filled composites, and fibre-reinforced structure[5].

Polyurethane polymers can be either thermosetting or thermoplastic, depending on whether they are crosslinked or not. Thermosetting polyurethane has a strong chemically cross-linked molecular structure, e.g. sulphur mediated crosslinker, producing a material with higher tensile strength and better resistance to swelling, abrasion and thermal degradation. In most cases, such cross-links tie together carbon atoms from different chains, which prevents the polymer from melting, producing a good thermal tolerance until the polymer decomposes at a high temperature. This means that recycling requires high energy input and additional chemical agents to dissolve the crosslinks[6].

The non-crosslinked equivalent, thermoplastic polyurethane (TPU) is another versatile elastomer in which polymer chains have a larger degree of mobility. This morphology provides TPU with flexible properties at ambient temperature, and the ability to be molded into desired shapes in elevated temperatures. Although the properties of TPU exhibit temperature sensitivity, it also provides superb impact resistance, corrosion resistance, durability and

flexibility[7,8]. At present, self-healing supramolecular TPUs have been invented[9,10], in which the overall polymer structure is formed by non-covalent interactions between molecules to assemble monomeric units into the polymeric structure. This feature enables these polymers to heal micro-cracks or voids with or without external stimuli (e.g. heat, light, etc.), to restore mechanical properties, improve recyclability and optimize service life[11].

2.1.2 Synthesis and morphology

In terms of synthesis, polyurethane is generally polymerized by reacting isocyanate compounds with polyols. The former contains two or more isocyanate groups per molecule (R-(N=C=O)$_n$), and the latter has on average two or more hydroxyl groups per molecule (R'-(OH)$_n$). The most commonly used isocyanates are the aromatic diisocyanates, such as toluene diisocyanate (TDI) and methylene diphenyl diisocyanate (MDI); the polyol can be either ethylene glycol (EG), butanediol glycol (BDO), diethylene glycol (DEG) or other monomers with hydroxyl groups; the urethane link (-NH-(C=O)-O-) is formed, connecting isocyanates and polyols groups. Chain extenders, the amine-terminated compound with hydroxyl in low molecular weight, are usually attaching with isocyanate components to stiffen the overall morphological structure. The hard segments, formed from the isocyanate and chain extenders in rigid and highly polar, are stiff and immobile; while the low polarity soft segments, i.e. polyols, generally have long molecular chains and high molecular weight, normally present a mobile behaviour and coiled formation[12]. The typical synthetic processes including two or more polyol hydroxyls adhering to each monomer are shown in Figures 2-1 and 2-2; a representative schema about polymeric morphology with hard- and soft- segments content in detailed domain structures is shown in Fig. 2-3.

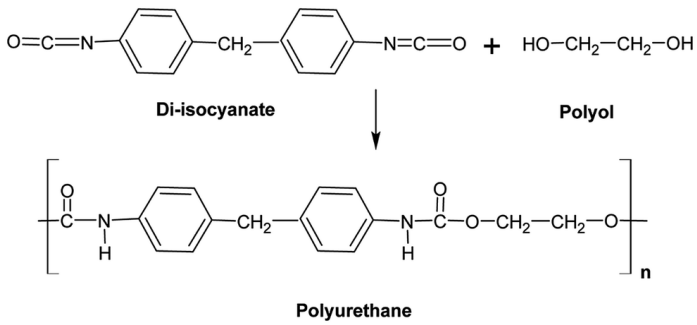


Fig. 2-1. Reaction scheme for the synthesis of polyurethanes, by using copolymerization of MDI and ethylene glycol.

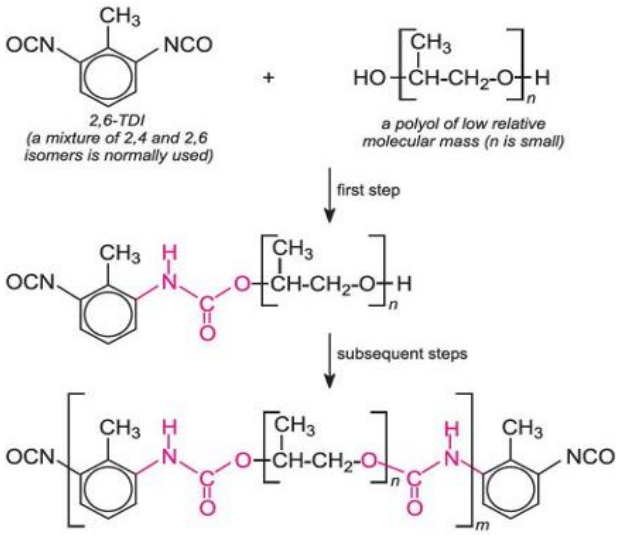


Fig. 2-2. Reaction scheme for the synthesis of polyurethane, by using copolymerization of TDI and polypropylene oxide glycol.

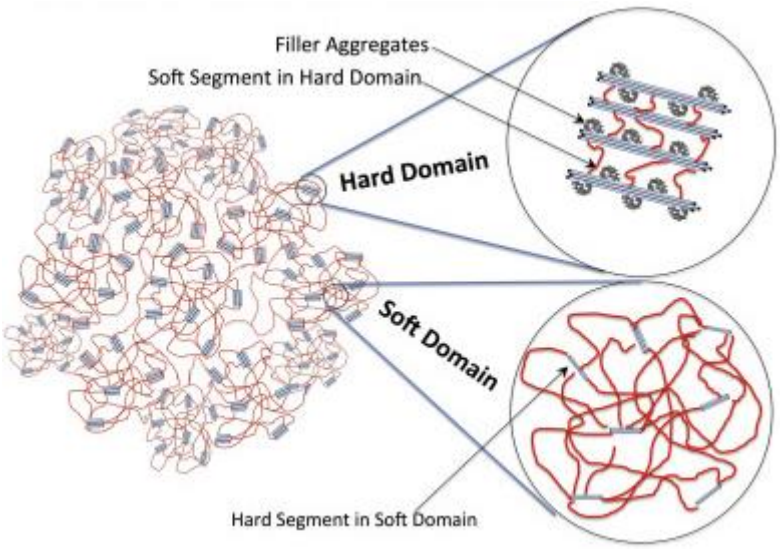


Fig. 2-3. The schema of polymeric microstructure in polyurethane, which contains both hard and soft segments to form domain structure. TPU morphology exhibits multi-scale phase separation characterised by heterogeneous morphologies at the micro- and nano- scales[13].

In TPU, the differences in polarity between hard and soft segments produce phase separation in the molecular structure, giving micro-domains owing to the immiscibility of these hard and soft segments. The significant phase separation is due to their microphase-separated structures resulting from the immiscibility between the soft segment and hard segment. Thus, desirable properties of TPUs can be achieved by controlling types and lengths of the segments, the crystallinity of phase domains (both soft and hard), the intersegment compatibility, as well as the glass transitions and the crystals' melting temperature. The urethane groups link the hard segments and the flexible segments together using both covalent and non-covalent bonds, and are usually arranged at the borderline between domains. The hard domains are constituted by the hard segments interacting with each other; they act as rigid fillers, and are responsible for the rigidity of the TPUs, presenting a relatively high melting temperature. Higher content of hard segment increases the initial modulus but limits extensibility[14,15]. On the other hand, the soft domains are mainly formed by soft segments in free motion and high flexibility, present a relatively low softening temperature. The content of soft segments contributes to material behaviour at large elongations and relative resilience before break or failure. In semi-crystalline TPU, increasing molecular weight in the soft segment contributes to a higher degree of incompatibility between the soft and hard domains, as well as enhanced extensibility and toughness due to the possible appearance of crystallites in the soft domains[16–18]. Additionally, hydroxyl chain extenders or side-branch polymerization can be used to balance the molecular weight of isocyanate groups to reach a desired strength and viscosity in the final TPU products[19–21], and specific composition and phase ordering also enrich the hydrogen bonds and improve the ultimate mechanical properties[22].

The degree of phase separation within a PU material is dependent on many factors in both molecularity and molecular conformations, such as types of prepolymers by diisocyanate and polyol[23,24], type of chain extending compound[14] and segments[24], synthetic method[24,25]. The

hard segment domains are typically dispersed in a soft segment matrix and often form a spherulitic structure where the hard segments have ordered orientation[26,27], either one phase or both phases in crystalline formation. The hard domain crystallizes more easily, but crystalline formation in the soft domain also stiffens the material properties[16,18,28]. The existence of crystals serves as an additional load-bearing component, therefore, increase the polymer strength[29]. Besides in higher degree of crystallinity, other methods to improve the mechanical properties for TPUs, include enhancement of immiscibility[30,31], improvement in intermolecular hydrogen bonding[31], alternations in cross-links entanglements[32], or improvement of the intramolecular interactions between chain-folding features to improve the mechanical properties[22,33,34].

2.1.3 T_g and T_m

As discussed above, TPU is known to be a segmented block copolymer composing of 'hard' and 'soft' segments. The soft segment has a glass transition below the normal operating temperature and is, therefore, rubbery. The hard segment has its glass transition or its melting temperature above the ordinary operating temperature and is, therefore, either glassy and/or crystalline. The degree of crystallinity is directly related to whether a polymer melts like a typical solid or whether it transitions between glassy and rubbery states. Highly crystalline polymers exhibit a more traditional melting point, T_m, while amorphous solids prefer a range of states with less glassy and more rubber-like or vice versa around glass transition temperature, T_g, due to the amorphous regions and uncoiled chains in a free state. In semi-crystalline polymer, the crystalline region remains unaffected when polymer undergoes the glass transition, and melts at a higher temperature[2].

The transition behaviour is described more specifically in terms of molecular motions in Fig. 2-4. At elevated temperature, polymer chains are mobile, which permits slippage in

layers so that the polymer is soft and viscous. On the contrary, lowering the temperature inhibits large-scale molecular motion of the main chain[35], and the polymer moves from the rubbery to glassy state. Further cooling the polymer to the beta transition temperature, T_β, or even lower temperature excited gamma transition, T_γ, the inter-lock of motion (e.g. bending, wiggle, etc.) in side-chains makes polymer much stiffer and more brittle, but TPUs at such transition in super-low-temperature are not the view investigated in this thesis.

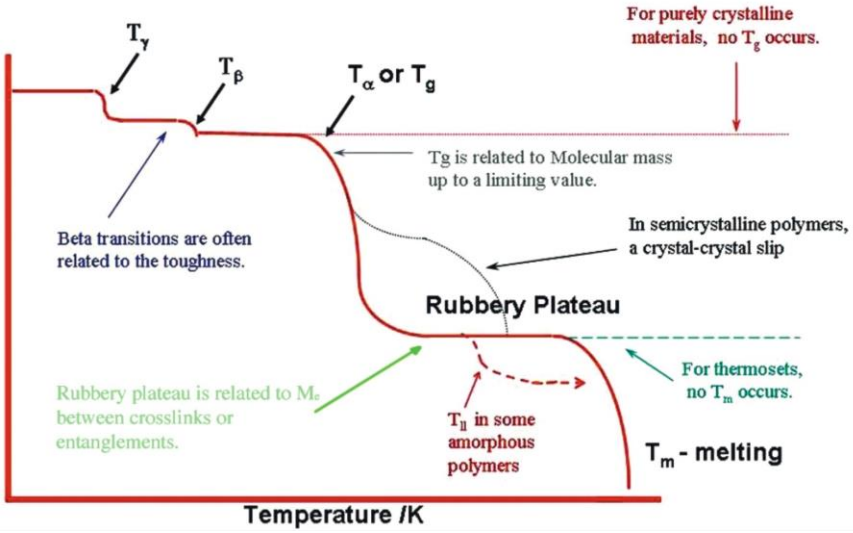


Fig. 2-4. An ideal representation of the modulus of a polymer as a function of temperature, showing the different transitions and the related molecular motions[36].

2.1.4 Particulate filled polymers

To expand the application of polymers in different sectors, rigid fillers are often added to achieve higher performance of mechanical properties. The selection of fillers includes organic fillers, e.g. carbon black[37,38], inorganic fillers, e.g. SiO_2[39–43] or $CaCO_3$[44] powder particles, micro-cellulose[45], rigid nanofibers or laminae[46,47], to modify the physical and mechanical properties without changing the nature of the polymer.

The improvement of mechanical properties in filled polymers strongly depends on the bonding condition that transfers stress into particles from the matrix, the particles themselves being micro- or nano-particles that are much stiffer than the matrix[48]. When carbon black is incorporated, its influence on the properties of the compound depends on its morphological

parameters, such as the particle size and the surface chemistry, as well as the degree of dispersion of the carbon black in the rubber. The mechanical properties, e.g. Young's modulus, increase significantly with filler loading, but are relatively less sensitive to particle size[49,50]; the observed effect on modulus has been observed to increase when the particle size is below a critical dimension (e.g. 30 nm) but the ultimate change was varied on different types of fillers and matrix[50]. Another factor of importance is whether the interface maintains the continuity of stress from the matrix to the filler. If there is strong adhesion, the molecular mobility of the polymer is strictly constrained, which further affects the properties. Additionally, if polymer is vulcanized during mixing, the crosslink density near the filler surfaces may be different to that in the bulk rubber.

The failure behaviour of filled polymer undergoes progressive steps from small to large deformation until rupture (in tension) or fracture (in compression) appear. For very small amplitude oscillatory strains, the Payne effect describes a reduction in dynamic storage modulus and appearance of a peak in loss tangent as the oscillatory strain amplitude is increased[51]. This behaviour is due to the presence of the breakdown of the filler network starting at strains as low as about 0.1%, going along with a significant decrease of storage modulus. As the strain increases, micro-voids, debonding and crazing are likely to occur, causing an irrecoverable reduction in overall strength. At moderate strain, the finite extensibility of the polymer network may cause an increase in stiffness, which might be enhanced by strain-induced crystallization (e.g. in natural rubber) to give extra strength. At very large deformation, the behaviour of strain softening may be produced by mechanisms that include polymer–particle slippage, interface separation, phase fracture, crack growth, and large-scaled vacuole formation, etc, until the material breaks. Another feature of filled polymer is the famous Mullins effect[52]: marked hysteretic responses at large deformation during uniaxial cyclic loading[53]; the reloading stress is less than that on the initial loading for

elongations below the (historical) maximum elongation achieved previously. The observed stiffness reduction was initially assumed to be caused by the rupture of fillers, but this is insufficient to explain a similar phenomenon in unfilled polymers. Another possible mechanism is untangling or breakage of weak crosslinks in unfilled polymer as a secondary mechanism together with the physical separation of filler-polymer interfaces as the primary cause. Other physical interpretations include chain breakage at the interface between the rubber and the fillers, slipping of molecules, rupture of the clusters of fillers, chain disentanglements, and energy dissipation/re-absorption[52].

The mechanism of debonding failure was assumed in our study to characterise, understand and model empirical results obtained from filled TPUs. The rigid filler has much better load-bearing capacity than that of the polymer itself. The great stress concentration occurred around the carbon-black particles in inhomogeneous structures and then transmitted to the whole system, providing numerous improvement in rigidity[54]. Griffith's criterion here can be used to interpret how reinforcement was taken from the strong bonding interactions and prevent the micro-craze in crack tip under the concentration of large stress[55,56]. It is to understand the debonding behaviour in such interface that the net reduction in elastic energy spread to the fracture surface energy in failure, the debonding-induced cracks agreed with empirical observations from literature[57], decreases the overall elastic energy in the entire system. In a modification of debonding model, the mechanically stored energy around a spherical inclusion is generally used for the creation of new crack surfaces as the initiation of debonding[58]. Upon straining, the filler particles become progressively debonded and no longer bear loads. This causes gradual softening of the material. The total volume of specimen might increase due to voids during debonding process, this dilatational deformation has been used in another approach to model debonding *via* overall volume strain[59]. Meddad et al.[60] considered both debonding damage and viscoelastic softening in PP and PA6 filled with up to 50 %vf.

Jerabek et al.[61] found that the debonding stress decreased with decreasing strain rate and increasing temperature. Verified by SEM micrography, the initiation of debonding, and subsequent plastic void growth have been considered to be one of the major softening mechanisms. Localized plastic deformation might emerge in the relatively weak matrix phase, this may relate to the concentration of shear bands or the combination of the shear bands and matrix dilatational bands associated with the interface interaction[62]. In further studies, debonding was observed, and identified as the initiation of micro-voids or micro-cracks propagation that decreased the local strength and stiffness, eventually facilitating a global loss of load bearing capacity in the material[37,63–66].

2.1.5 Techniques for structural characterisation DSC GPC NMR SAXS

In TPUs, the immiscibility of 'hard' and 'soft' segments results in phase separation, which predominates the general mechanical properties, which are either glassy, rubbery or viscous, depending on the operating temperature. All TPUs exhibit a glass transition; some semi-crystalline TPUs in addition exhibit melting of the crystalline structure at elevated temperature. Investigating and correlating between thermal and structural properties give many insights into the characterisations of polymer.

Differential Scanning Calorimetry (DSC) is a thermo-analytical technique to observe heat flow into or out of a material as a function of time or temperature. Quantifying the heat amount during the thermal processing, any change over the temperature ramps is representative of the morphology. For temperature from low/ambient to a high degree, the corresponding enthalpy process and heat flow provided a rapid, direct determination for polymer crystallinity, other fundamental properties like phase segregation, glass transitions, crystallisation[16], melting[67], and intermolecular bonding (e.g.hydrogen bonding[68]) can be determined[69,70]. An example of DSC on specimens of unfilled SPU (Fig. 2-5a), pure sugar (Fig. 2-5b) and carbon-

black TPU (Fig. 2-5c), demonstrates the ability to characterise glass transition, melting-to-decomposition, and hydrogen dissociation, respectively.

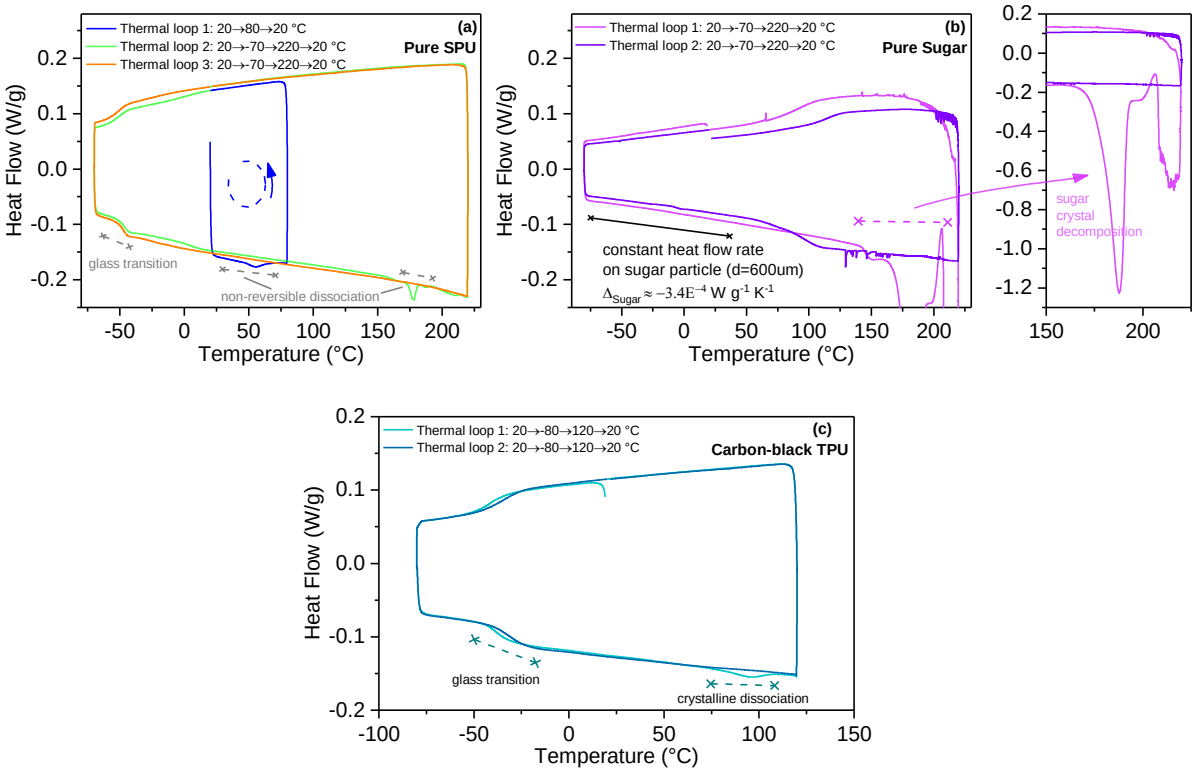


Fig. 2-5. Examples of different thermal processes were observed through DSC experiments on a supramolecular PU (SPU), sugar filler, and carbon-black TPU. (a) glass transition in SPU undergoing thermal loops from -70°C to 220 °C, also showing non-reversible transitions; (b) melting sugar above 180 °observed its decomposition process; (c) heat flow in carbon-black TPU, showing a glass transition at 35°C, and a dissociation region at 90 °C.

Another technique to investigate morphological changes is small-angle X-ray scattering (SAXS), one of the X-ray scattering techniques used to characterise the size, shape, distribution of macromolecules; porosity of internal structures; ordered structure or non-homogeneous morphology; phase-based miscibility and crystallinity in polymer[71,72], in nanoscale resolution. It measures the intensities of X-rays scattered by a sample as a function of the scattering angle, as very small angles, typically in the range of 0.1 ° to 10 °. From Bragg's law it is understood that with decreasing scattering angle, increasingly larger structural features are being probed. The photon energy irradiated through the specimen, the transmitted beam and secondary

scattered waves travel down to the beam stopper, displayed a perceptible scattering pattern with radiation wave on 2D detector. The scattered intensity is collected as a function of scattering angle, of which a distribution of scattering vector from the detector centre is displayed. It provided fluctuations information of electronic densities in the matter with specific scatterer's position therefore reveal the spatial correlations and characterise the morphology (geometry and structure) in the sample. Witzleben et al.[71] used SAXS to investigate the morphological properties in size and shape of crystalline zones in TPUs at different temperatures at the nanoscale. SAXS can be simultaneously performed with DSC to examine annealing-induced changes in morphology and the degree of variance in average inter-domain spacing[33]. SAXS has also been used to characterise the micro-phase separation to present the hydrogen bonding on immiscibility associated with temperature changes[10], and also to quantitatively show morphological changes or strain-induced interdomain evolution[73–75]. The use of SAXS during tensile tests of TPUs constructed a field of scattering maps, to inspect the local structure, neighbour domains, micro-strain evolution during continuous straining experiments[73,76]. A SAXS signal is to observe whenever a material contains structural features on the length scale of nanometers, typically in the range of 1-100 nm. For smaller scale investigation, wide-angle X-ray scattering (WAXS), also known as wide-angle X-ray diffraction (WAXD), probes for structures in the material on the much smaller length scale, that of interatomic distances, e.g. lattice spacing[73].

Nuclear magnetic resonance (NMR) spectroscopy is an important method for materials characterisation and for the study of polymer structure-property relationships. The polymer specimen dissolved into solvents, examined within a magnetic resonance field. The NMR pattern includes the chemical shift (in unit of ppm at frequency) and signal intensity, representing specific chemical environment or functional groups in subject of atomic markers (^{13}C or ^{1}H). Equivalent chemical environments give the same signal in local fields. Splitting

each signal gives information about the functional groups connecting to the carbon backbone. Therefore, the structure of molecularity (chemical make-up), hydrogen bonds and interactions (based on conformation), molecular weights can be measured from atomic-length scale[9,77–80]. The hydrogen atom's environment and ^{1}H monomer distribution were rendered, the approach works well for polymer has distinctly different mobility and high degree of phase separation when polymer being glassy, crystalline or thermal-degradation[81,82]. This is also as the principle in our experiments of ^{1}H NMR to quantify molecular conformation in thermal processes.

Gel-permeation chromatographic **(**GPC**)** is another method to characterise polymer in molecular level by measuring molecular weight and its density distribution[83]. The technique introduced a specimen dissolved in gel solvent and injected through a chromatography column. Since the different components in polymer have own mobile phase in dynamic, the time for them to exit stationary phase can be determined. The separation time for components elute from column is based on their molecular size: large component has better permeation (i.e. less diffusion in gel solvent) and mobility to penetrate, then to be observed firstly. In GPC, the concentration by weight of polymer at each component was monitored continuously with a detector. The resulting chromatogram therefore gives a weight distribution of the polymer as a function of retention volume or time. GPC can characterise the molecular integrity and weight distribution[80] before and after thermal processing, to investigate any changes (or degradation) on molecular level[84,85]. The technique also able to detect the cross-links dissociation, side-chain breaks, molecular extension[86], as well as the depolymerisation at elevated temperature[84].

2.2 Viscoelastic Behaviour and Constitutive Relations

Thermoplastic polymers show a combination of elastic and viscous behaviour depending on the specific working temperature. As the temperature decreases, the stress at a given strain increases , whist the opposite effect is observed with increasing temperature[87,88]. The latter is

equivalent to the behaviour over long-time spans; on the contrary, low-temperature behaviour is equivalent to that observed in very high-rate loadings. Sarva et al.[89] and Yi et al.[90] have explored rate-dependent behaviour of TPUs up to 10^4 s^{-1}, demonstrating the strong dependence of the stress–strain behaviour on the transitions from rubbery to leather to glassy with increasing strain rate; Liao et al.[91] also found that TPUs exhibited a yield-like, leather- or glass-like behaviour in high strain rate tensile tests at 6500 s^{-1}, or at temperature drop down to -40 °C. The dependence on time-span (loading rates) or ambient temperature (thermal effects), with a specific emphasis on large strain high strain rate properties have been reviewed for many other thermoplastic polymers, e.g. PMMA[92,93], PVDF[94].

2.2.1 Linear viscoelasticity

The behaviour of viscoelastic materials is usually discussed by reference to two components: elastic solid and viscous liquid. The former exhibits instantaneous deformation and recovery under applied load. The latter has no defined shape and therefore undergoes irrecoverable deformation under applied stress. Viscoelasticity describes an intermediate phenomenological behaviour between elasticity and fluid-like viscosity, loading-induced deformation with hysteretic recovery and time dependence. Neglecting any potential chemical reaction or molecular degradation, viscoelastic behaviour can be described by using simple physical analogues: Hookean springs and Newtonian dashpots, with constitutive equations

Hooke's law $$\sigma = E\varepsilon \quad (2\text{-}1)$$

Newton's law $$\sigma = \eta \frac{d\varepsilon}{dt} \quad (2\text{-}2)$$

where E is Young's Modulus of the spring, and η is viscosity of the dashpot.

The simplest two models combining these elements are the Maxwell (Fig. 2-6a) and Kelvin-Voigt models (Fig. 2-6b), which combine one elastic spring and one viscous dashpot in series or parallel. The Maxwell model exhibits stress relaxation (Eq. (2-5)) only, while the Kelvin-Voigt model represents creep recovery (Eq. (2-8)). The expression for the relationship

between ε and σ is formulated using Hooke's Law and Newton's Law.

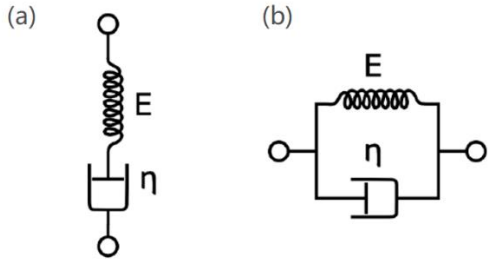


Fig. 2-6. (a) Single term for Maxwell model and (b) single term for Kelvin-Voigt model.

Maxwell model $$\dot{\varepsilon}=\dot{\varepsilon}_s+\dot{\varepsilon}_d,\ \sigma=\sigma_s=\sigma_d, \tag{2-3}$$

Equivalence $$\sigma+\frac{\eta_1}{E_1}\dot{\sigma}=\eta_1\dot{\varepsilon}, \tag{2-4}$$

Stress relaxation $$\sigma(t)=\varepsilon_0 E(t),\ E(t)=E_1 e^{-t/\tau_1},\ \tau_1=\frac{\eta_1}{E_1}, \tag{2-5}$$

where in the stress relaxation, the model is subjected to an initial strain ε_0 at $t=0$.

Kelvin-Voigt model $$\dot{\varepsilon}=\dot{\varepsilon}_s=\dot{\varepsilon}_d,\ \sigma=\sigma_s+\sigma_d, \tag{2-6}$$

Equivalence $$\sigma=E_1\varepsilon+\eta_1\dot{\varepsilon}, \tag{2-7}$$

Creep $$\varepsilon(t)=\sigma_0 J(t),\ J(t)=\frac{1}{E_1}(1-e^{-t/\tau_1}),\ \tau_1=\frac{\eta_1}{E_1}, \tag{2-8}$$

where in the creep behaviour, the model is subjected to an initial stress as zero at $t=0$.

The Three-element model was proposed to describe more realistic material responses, shown in Equations (2-9) and (2-10), can describe both creep-elongation and relaxation. The 'solids' models (Fig. 2-7) react instantaneously as elastic materials, before going on to exhibit time dependent deformation; they recover completely, but not instantly, upon unloading. The stress-strain behaviour can be derived using the deferential equation, solved either using an integral formulation (the Botltzman superposition integral) or Laplace transform[95].

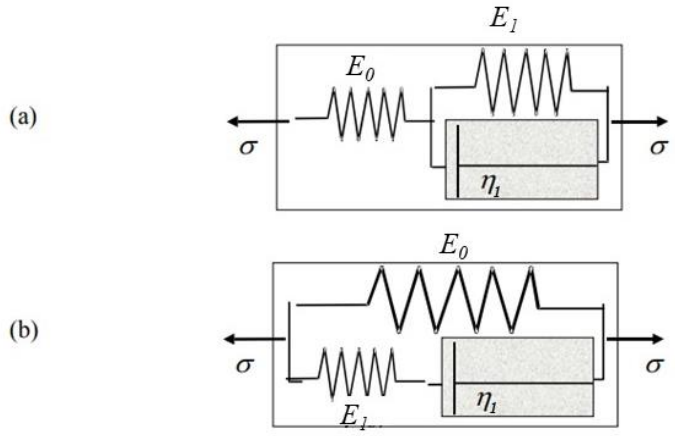


Fig. 2-7. (a) Standard linear solid (SLS) model I (Kelvin-Voigt representation), (b) Standard linear solid (SLS) model II (Maxwell representation).

SLS model I
$$\sigma + \frac{\eta}{E_0 + E_1}\dot{\sigma} = \frac{E_0 E_1}{E_0 + E_1}\varepsilon + \frac{E_1 \eta_1}{E_0 + E_1}\dot{\varepsilon},\ \tau_{c1} = \frac{\eta_1}{E_1}, \tag{2-9}$$

SLS model II
$$\sigma + \frac{\eta}{E_1}\dot{\sigma} = E_0\varepsilon + \frac{(E_0 + E_1)\eta_1}{E_1}\dot{\varepsilon},\ \tau_1 = \frac{\eta_1}{E_1}, \tag{2-10}$$

where τ_1 is relaxation time, τ_{c1} is retardation time, these values are different for different materials. E_0 is from the time-independent element, generally it represents the modulus when time is infinite long or the ultimate relaxed modulus at a very long time from relaxation experiments.

2.2.2 Generalized Maxwell model and Boltzmann superposition

The SLS model with one term is insufficient to describe realistic polymer behaviour, as a real polymer typically has a spectrum of relaxations. The generalized Maxwell model, shown in Fig. 2-8, can be used instead. It contains identified elastic and viscous elements to characterise the overall material properties. The model has a relaxation modulus that combines the simultaneous effect from multiple Maxwell elements in parallel (with strain-stress equivalence shown in Equations (2-11) and (2-12)), producing the time-dependent modulus shown in Equations (2-13) and (2-14). As an example of the response, the analytical solutions of stress relaxation and creep compliance are shown in Fig. 2-9. The outputs were produced using the Simscape model in Fig. 2-10.

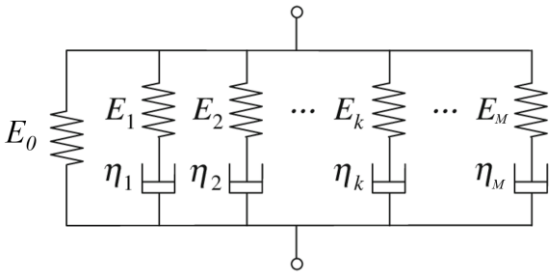


Fig. 2-8. Generalized Maxwell model.

Model equivalence

$$\dot{\varepsilon} = \dot{\varepsilon}_{Spring} = \dot{\varepsilon}_{Maxwell_1} = \dot{\varepsilon}_{Maxwell_2} = \cdots = \dot{\varepsilon}_{Maxwell_N}, \tag{2-11}$$

$$\sigma = \sigma_{Spring} + \sigma_{Maxwell_1} + \sigma_{Maxwell_2} \cdots + \sigma_{Maxwell_N}, \tag{2-12}$$

Stress relaxation

$$E(t) = \frac{\sigma}{\varepsilon_0} = E_0 + E_1 e^{-t/\tau_1} + E_2 e^{-t/\tau_2} + \cdots + E_M e^{-t/\tau_M}, \tag{2-13}$$

$$E(t) = E_0 + \sum_{i=1}^{m} E_i \exp\left(-\frac{t}{\tau_i}\right), \tau_i = \frac{\eta_i}{E_i}. \tag{2-14}$$

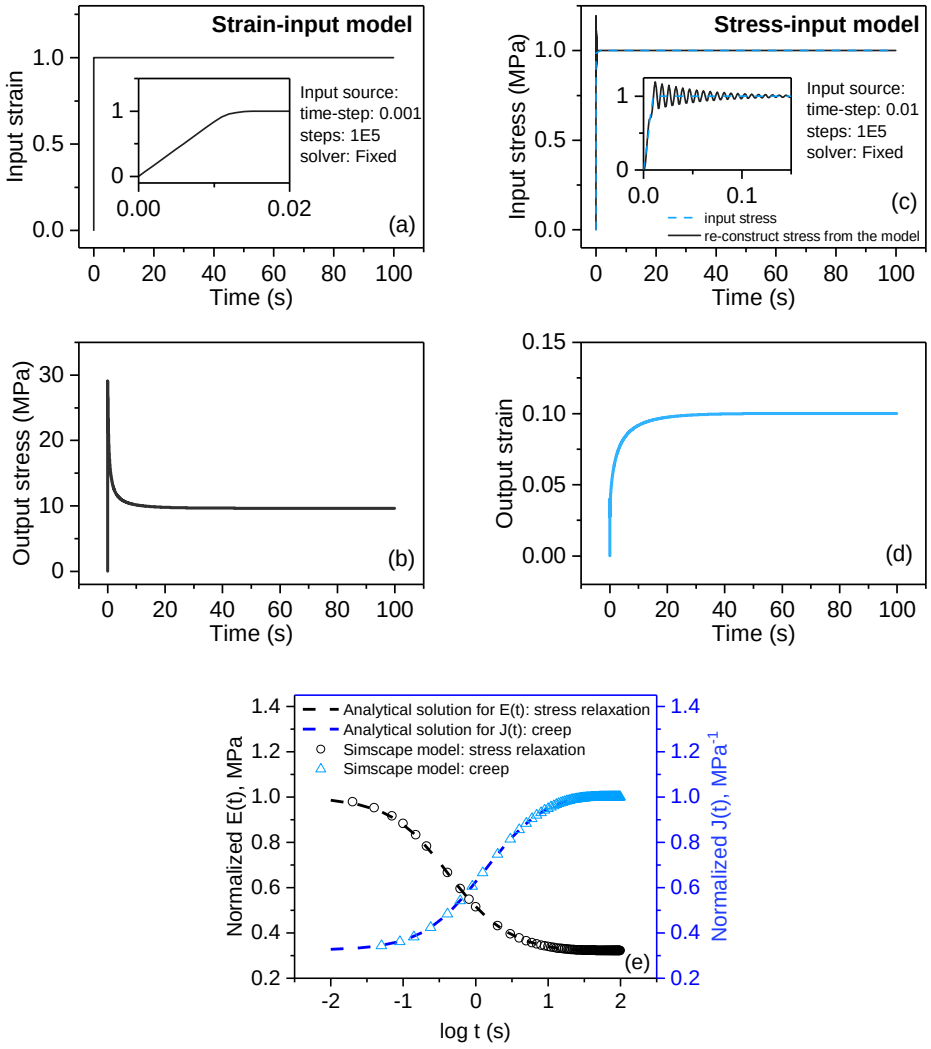


Fig. 2-9. The model input (a) and (c) to obtain analytical solution (b) and (d). All elements for stress relaxation and creep are assigned as: E_0=10, E_1=8, E_2=6, E_3=4, E_4=2, E_5=1, η_1=2, η_2=4, η_3=6, η_4=8, η_5=10; input resource for ε=1 or σ=1 was applied to the model, the stress or strain in time-span was obtained, to calculate the relaxation modulus and creep compliance (e). The strain-/stress- input model is introduced in next figure.

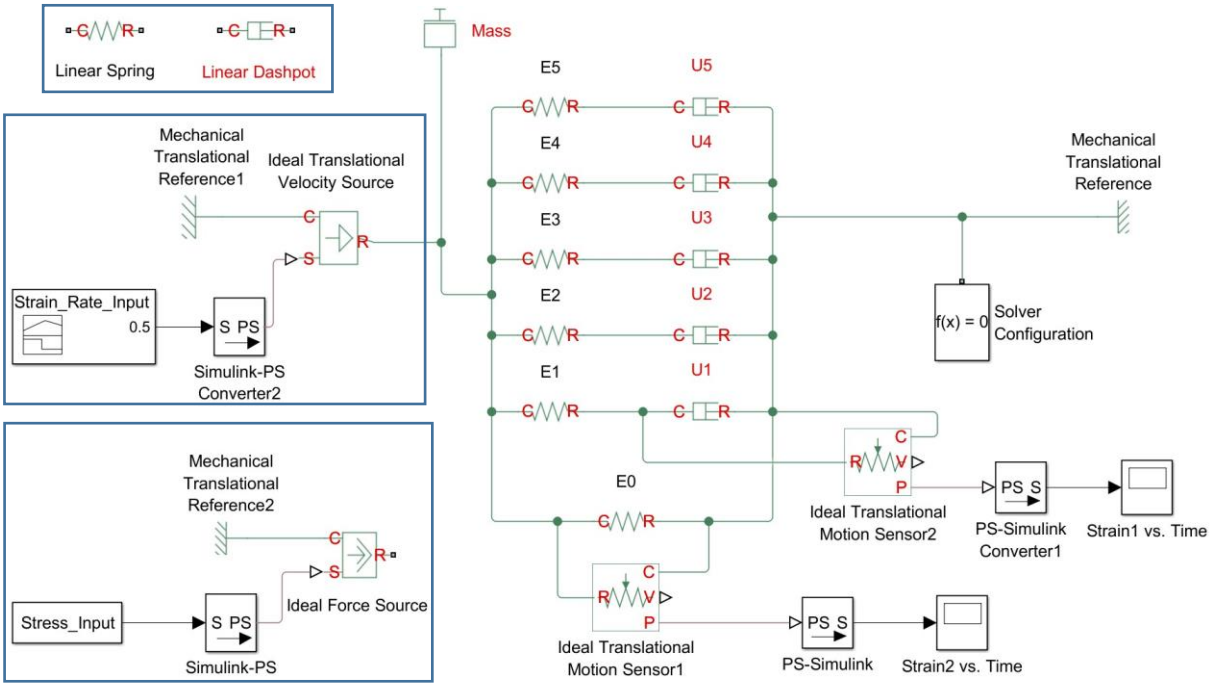


Fig. 2-10. The schema of generalized Maxwell model with 5-Maxwell terms, constructed in Simscape toolbox, MATLAB.

In order to produce a stress-strain curve representing the response to monotonic loading, the response at each 'time step' must be produced by combining previous 'time steps'. This can be done using the Boltzmann superposition principle, shown Equations (2-15) and (2-16). The principle proposed an imagination of a series of infinitesimal strain steps, in a function of the entire past loading history of the system,

$$\varepsilon(t) = \Delta\sigma_1 J(t-\tau_{c1}) + \Delta\sigma_2 J(t-\tau_{c2}) + \Delta\sigma_3 J(t-\tau_{c3}) + \cdots, \qquad (2\text{-}15)$$

where $J(t-\tau_{ci})$ is the creep compliance function. Each loading step makes an independent contribution to the final deformation, and the total deformation can be obtained by the addition of all the contributions. The summation of the all integrals is

$$\varepsilon(t) = \int_0^t J(t-\tau_c)\, d\sigma(t). \qquad (2\text{-}16)$$

From the inspiration of Boltzmann superposition principle on creep accumulation, the stress relaxation behaviour can be represented in an exactly complementary process under same principle framework. Consider a stress relaxation programme in which incremental strains at 'time step', by Equations (2-17) to (2-19),

$$\sigma(t) = \Delta\varepsilon_1 E(t-\tau_1) + \Delta\varepsilon_2 E(t-\tau_2) + \Delta\varepsilon_3 E(t-\tau_3) + \cdots, \quad (2\text{-}17)$$

where $E(t-\tau_i)$ is the effective stress modulus at each time increment. This can then be converted into an integral

$$\sigma(t) = \int_0^t E(t-\tau)\frac{d\varepsilon(\tau)}{d\tau}d\tau. \quad (2\text{-}18)$$

If the stress and strain are zero at $t=0$, $d\varepsilon/ds$ describes the strain rate history for $t>0$, and, for constant strain rate

$$\sigma(t) = \int_0^t E(t-\tau)\dot{\varepsilon}(\tau)\,d\tau, \quad (2\text{-}19)$$

where $\dot{\varepsilon}(\tau)$ is the applied strain rate to the system. Fig. 2-11 shows an example of using the Boltzmann superposition principle to simulate monotonic and cyclic loadings.

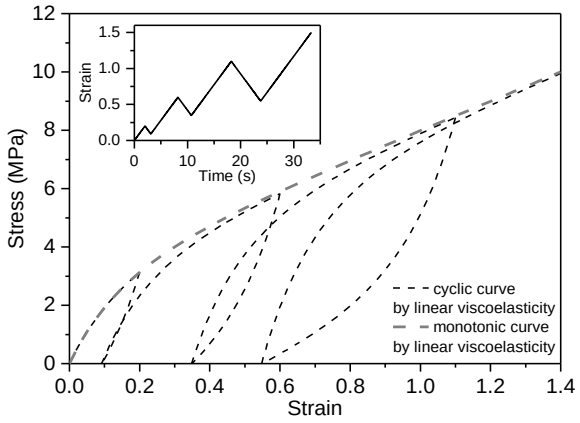


Fig. 2-11. Implementation of the Boltzman superposition integral for a two-term Maxwell model, in which E_0=5, E_1=E_2=10, η_1=5, η_2=10 for monotonic and cyclic loading at 0.1 s^{-1}.

2.2.3 Dynamic properties of elastomers

In practice, the viscoelastic properties of the polymer, for small amplitudes, are often obtained using experimental techniques that provide oscillatory loading, such as the DMA technique described later. Under this loading, purely elastic materials have stress and strain in phase, whilst in purely viscous materials, strain lags stress by 90°. Viscoelastic materials exhibit behaviour somewhere between these. The analytical solution for dynamic stress-strain response of viscoelastic system described by the Generalised Maxwell model and undergoing oscillatory deformation is shown in Equations (2-20) and (2-21), with phase angle in Eq. (2-

22).

Storage modulus E

$$E'(\omega) = E_0 + \sum_{i=1}^{n} E_i \frac{\tau_i^2 \omega^2}{1+\tau_i^2 \omega^2}, \quad (2\text{-}20)$$

Loss modulus E''

$$E''(\omega) = \sum_{i=1}^{n} E_i \frac{\tau_i \omega}{1+\tau_i^2 \omega^2}, \quad (2\text{-}21)$$

Phase shift factor

$$\tan\delta = \frac{E''}{E'}, \quad (2\text{-}22)$$

where ω is the frequency of the applied deformation.

2.2.4 Time-temperature superposition

The equivalence of time and temperature dependence is a significant property in many polymers. The simplest interpretation of equivalence is that mechanical properties at one set of temperature and frequency conditions are approximately equal to those at either a lower temperature or higher frequency, or vice versa. Appropriate experimental data can be obtained using dynamic mechanical analysis (DMA) to analyse the viscoelastic material using either temperature or frequency sweeps. The DMA applies a sinusoidal force to a sample and measures its resulting deformation, or applies the deformation and measures the force. The machine can also apply a constant force/deformation to measure creep/relaxation modulus. The material's response can be characterised as a function of temperature, frequency, time, stress or a combination of these control parameters, depending on the intended use of the data[96–98].

A common approach is to perform DMA experiments using frequency sweeps from, say, 10^{-2} to 10^{2} Hz over a wide range of temperatures. For higher frequency tests, the electrodynamic shaker[99] or resonance technique[100] might be used. Conventional DMA experiments can be performed using several sample geometries, including single/dual-cantilever, three-point bend, tension/compression or shear tests[101]. Although the technique is very sensitive to the effects of polymer transitions, the absolute values of the modulus are known to often show large discrepancies between specimens and different loading clamps with only minor changes in experimental conditions[102].

Single cantilever or dual cantilever modes are usually used for high modulus materials, whose ends will be less affected by clamping deformations and which are difficult to deform in tension or compression configurations because of the high loads required. The three-point bending mode is considered as pure bending, as the sides of the specimens are free to move; however there is a risk of losing contact between the loading anvil and the specimen when testing viscoelastic materials at higher loading frequencies. Data from cantilever configurations must account for the shear in the specimen, and this is done automatically from the machine. In one of the papers presented later, results are shown from FE simulations of DMA experiments in order to validate the data obtained from the machine used.

To illustrate the use of time-temperature equivalence, it is instructive to demonstrate a manual implementation of time-temperature superposition (TTS). Here, Fig. 2-12 shows how modulus data from each isothermal frequency sweep can be shifted in the frequency axis in order to overlap with its neighbour. The process is repeated for all the sweeps until the data form a smooth, continuous curve, the 'master curve'. This allows models, such as the Prony series described below, to be calibrated, and also allows data to be obtained representing a wide range of frequencies from experiments performed over a much narrower range; examples can be reviewed[103,104]. The parameter to shift each isotherm is known as the shift factor, $\log a_{i_i-1}$. The Williams–Landel–Ferry (WLF) equation is often used to describe the temperature dependence of the shift factors between the glassy and rubbery states, which will be discussed further in Chapter 3&4.

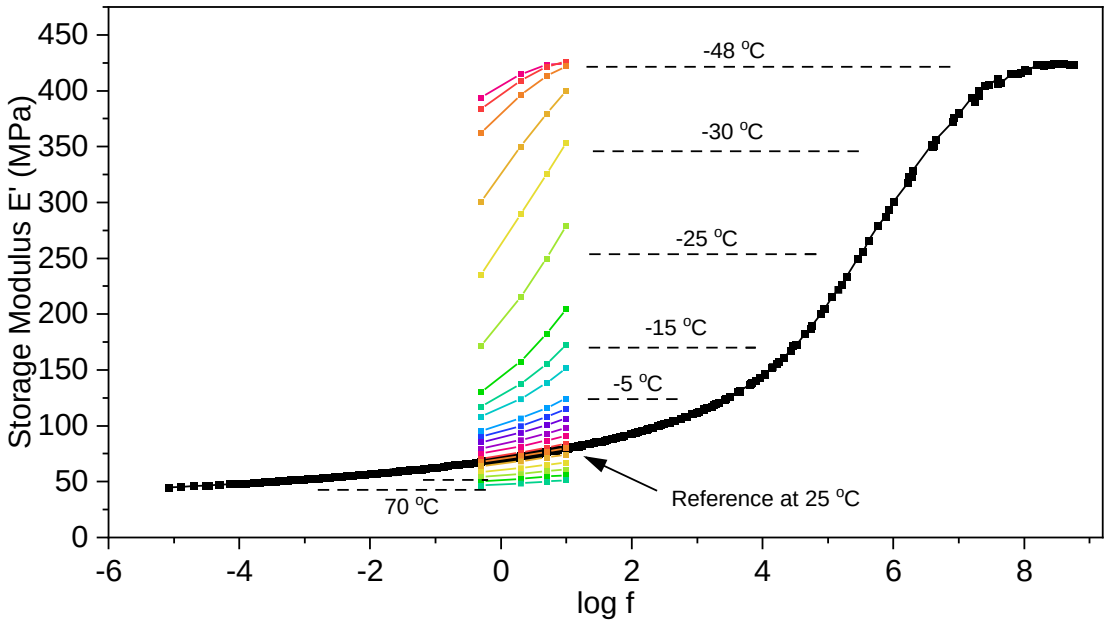


Fig. 2-12. Production of Master Curve using DMA data for Black rubber. Coloured lines represent isothermal frequency data whilst black line represents the Master Curve.

Whilst the DMA is suitable for performing experiments on stiff polymers, the lower modulus polymers that are also examined in this thesis cannot be tested in this way, especially at higher temperatures where the specimens become viscous and soften, tending to collapse under their own weight, shown in Fig. 2-13. In these cases, rheometry was used. Conversely, the rheometer is not able to produce accurate data at low temperatures; instead, data from the rheometer and DMA can be combined to produce a single master curve, taking advantage of the ability to cover the full temperature domain, shown in Fig. 2-14. The capacity of frequency sweep in rheometer can perform over 10^3 Hz but in experiments only performed up to 10^2 Hz[105], to minimize the mismatch error of shear velocity between rheometry and the sample surface.

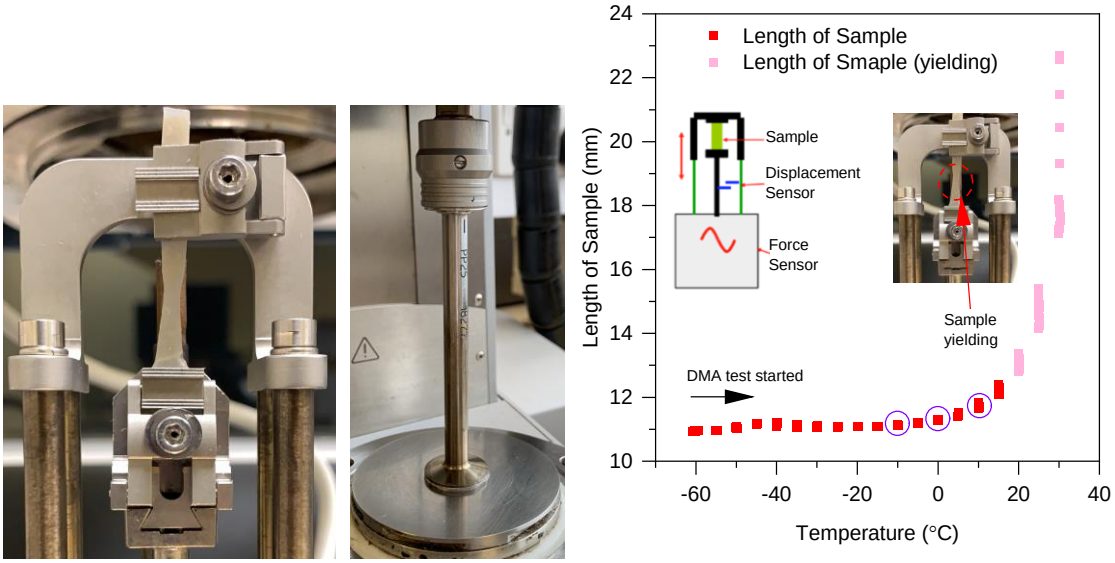


Fig. 2-13. SPU specimen tested in DMA tensile mode (a), and rheometery (b). (c) showed a distinct yielding and plastic deformation for this polymer during the experiment.

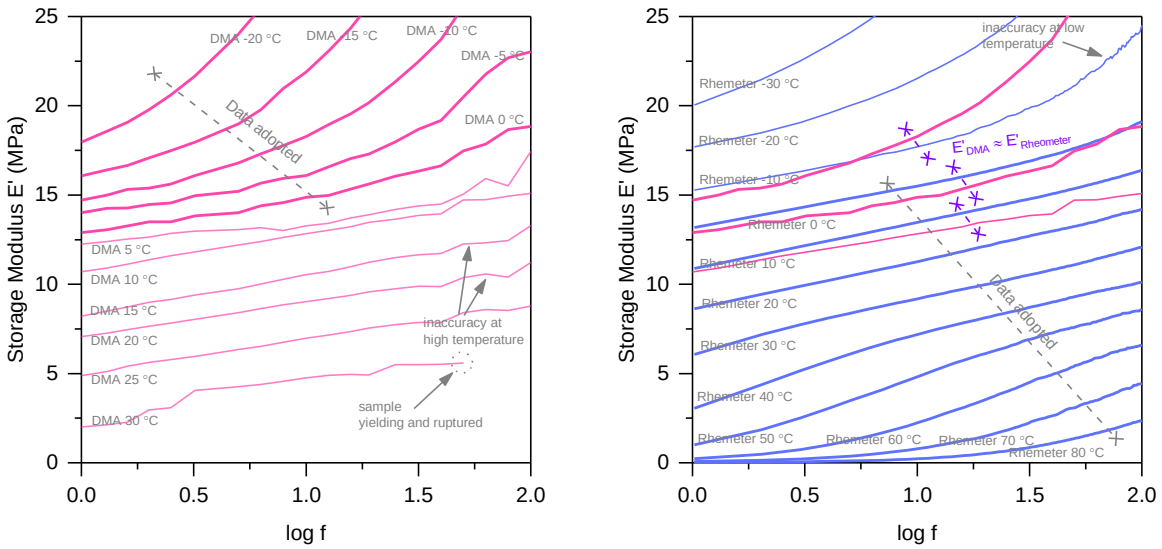


Fig. 2-14. DMA results (a) on SPU showed necking problem affected the measurement during the experiment. Rheological results (b) showed the data has a good compliance to DMA data around temperature of 0 °C. The limitations of each instrument in performance were discussed in the following Chapter 4.

2.2.5 Prony series parametrization

The relaxation and retardation time spectra are used to calculate the stress relaxation, creep and dynamic mechanical behaviour. This is often done using the Alfrey approximation: each Maxwell term in the SLS system can be expressed by Eq. (2-23) where the modulus expression in a single Maxwell unit is replaced by a step function with $H(\tau)$.

$$E(t) = E(t=0) + \int_{-\infty}^{\infty} H(\tau) \exp\left(\frac{-t}{\tau}\right) d(\ln \tau). \quad (2\text{-}23)$$

If we assume that $exp(-t/\tau)=0$ at $t=\tau$; while $exp(-t/\tau)=1$ for $t<\tau$. The equation can be simplified as

$$E(t) = E(t=0) + \int_{\ln \tau}^{\infty} H(\tau) d(\ln \tau). \quad (2\text{-}24)$$

The modulus in relaxation in one single time step at time τ is expressed as

$$H(\tau) = \left[\frac{dE(t)}{d\ln(t)}\right]_{t=\tau}, \quad (2\text{-}25)$$

which is known as the 'Alfrey approximation'.

The relaxation time spectrum can be replaced by the expression of frequency in terms of the real and imaginary parts from complex modulus, the equation now becomes

$$H(\tau) = \left[\frac{dE'(f)}{d\ln(f)}\right]_{1/f=\tau} = \frac{\pi}{2}\left[E''(f)\right]_{1/f=\tau}. \quad (2\text{-}26)$$

In mathematics, the integral of $H(\tau)$ in the variable of frequency diagrammatically represents the integration of real modulus plot *E' vs. f*, or the imaginary modulus plot *E'' vs. f.*

Using this approach, the Prony series can be defined and the stiffness assigned to each term in the generalized Maxwell model. The number of terms must be chosen. In practice, more terms allow a closer match to the Master curve, e.g Fig. 2-15. It is generally infeasible to fit both storage modulus and loss modulus by one single distribution of Maxwell terms. The determination of Prony series in this thesis was performed using the storage modulus, so that it could be related to the stiffness observed in monotonic or cyclic experiments. The unmatching results in the loss modulus, shown in Fig. 2-16, might arise because of the instrument compliance, material geometry, or the inhomogeneous deformation during loading.

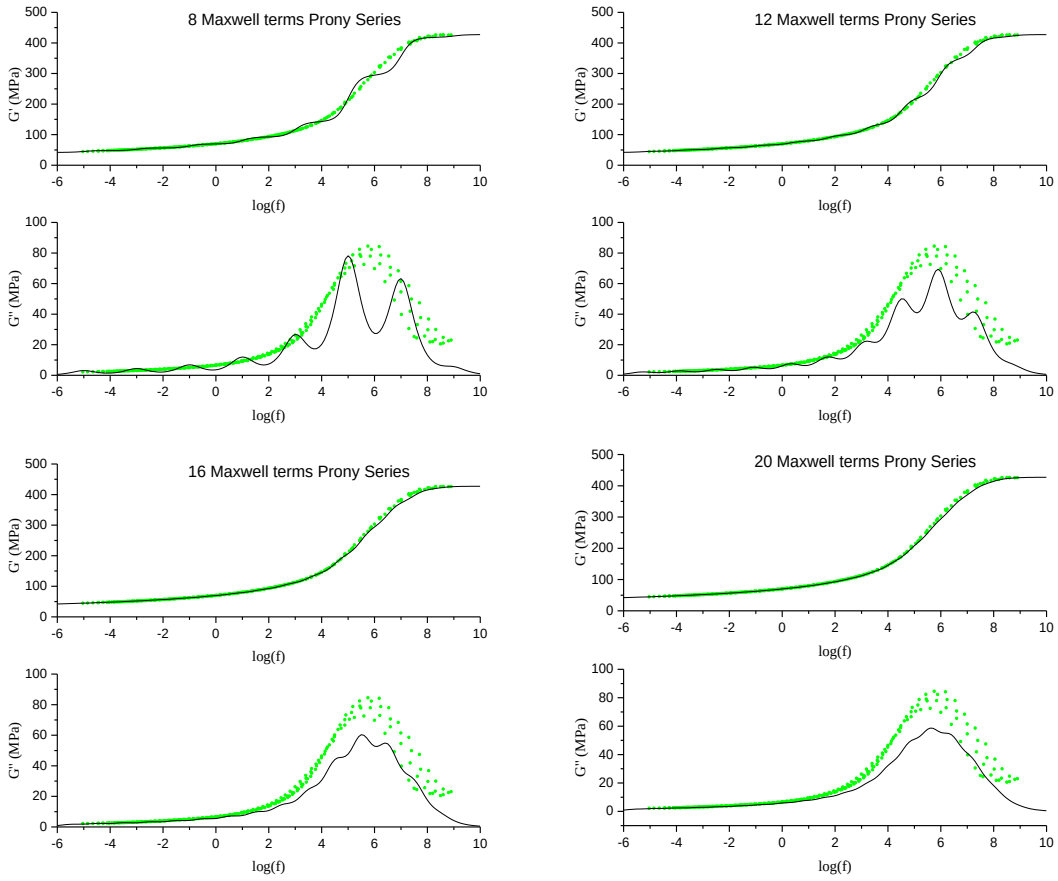


Fig. 2-15. Comparisons of Maxwell models with different numbers of terms fit to experimentally master curves.

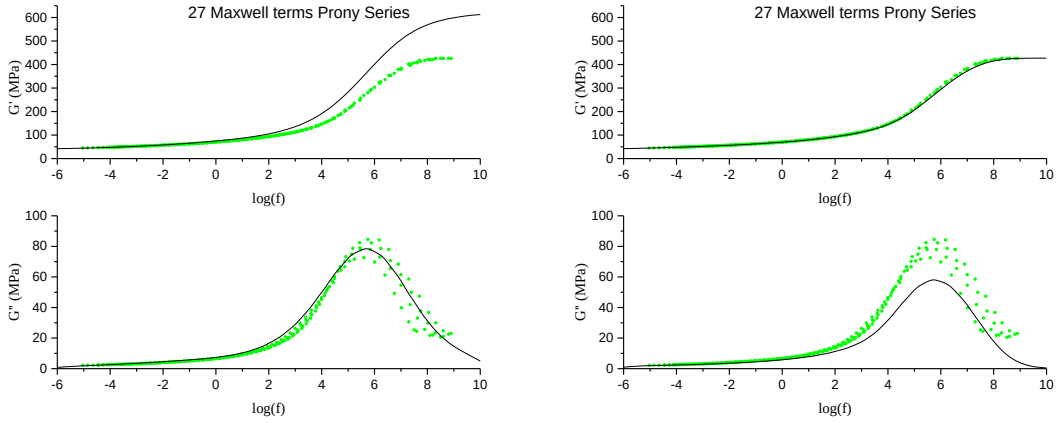


Fig. 2-16. Comparison of generalized Maxwell models fit to (a,b)storage modulus or (c,d) loss modulus. Two methods for determining Prony series from either storage or loss modulus are given.

2.3 Mechanical Experiments from Low-to-high Rates

2.3.1 Low-rate experiments

Low strain rate experiments are conventionally performed in servo-hydraulic or screw-driven machines from 10^{-5} to 1 s^{-1}. In compression, cylindrical specimens are compressed between metal anvils, with grease or Vaseline lubrication on the anvil surface to avoid friction in compression experiments. The crosshead is moved at the required speed to obtain the desired true strain rate, whilst a load-cell attached to the crosshead is used to record the force supported by the specimen. To avoid the effects of machine compliance when measuring strain, two types of clip-on extensometers, shown in Fig. 2-17, were used in compression and tension for both strain calculation and machine control.



Fig. 2-17. The schema of extensometer for compression and tensile experiments.

2.3.2 Intermediate-rate experiments

Intermediate strain rate experiments have developed over the years, depending on the type of materials, and the property to be determined. The existing intermediate strain rate testing machines are divided based on the loading mechanism: high-speed servo-hydraulic testing machines (shown in Fig. 2-18), drop-weight towers[106–109], flywheel machine[110], long Hopkinson bars[111], or hybrid testing apparatus which combining a servo-hydraulic machine with the split Hopkinson bar technique[112,113].

Over the past decade, commercial load frame manufacturers have developed a new family of high-speed servo-hydraulic testing machines specifically designed to cope with the

dynamics of intermediate strain rate testing. However, the apparatus is still very heavy, the sudden engagement of the setup generates a high amplitude stress wave which might cause oscillations at the system's natural frequency[114]. A drop tower apparatus is typically used to study the crushing and collapsing behaviour of the material by dropping a mass on a structural component. The flywheel is another type of testing machine that uses kinetic energy to fracture specimens at different intermediate strain rates[115]. The rotary speed is accelerated until the required flywheel velocity is reached; a jack is triggered which pushes a hammer to impact the specimens[116]. A long Split Hopkinson pressure bar is another design to achieve intermediate loading rates. The apparatus settings are similar to the typical SHPB experiment (described below) but with extension of the striker and incident bar. However, these systems present challenges in wave dispersion and profile distortion due to long travel distances in the bars. This testing apparatus is also too large (too long) to fit in many laboratories.

In this research, an in-house hydraulic machine specifically produced to have small components (reducing inertia and hence oscillation in the obtained data) was used for strain rates between 1 and 50 s^{-1}. Even in this machine, care must be token: only use data obtained at a constant strain rate in the specimen (Fig. 2-19).

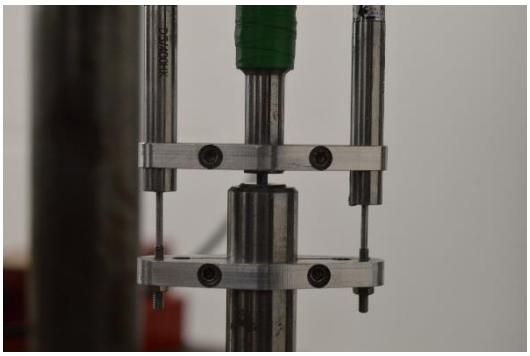


Fig. 2-18. The schema of hydraulic compressor for medium rate.

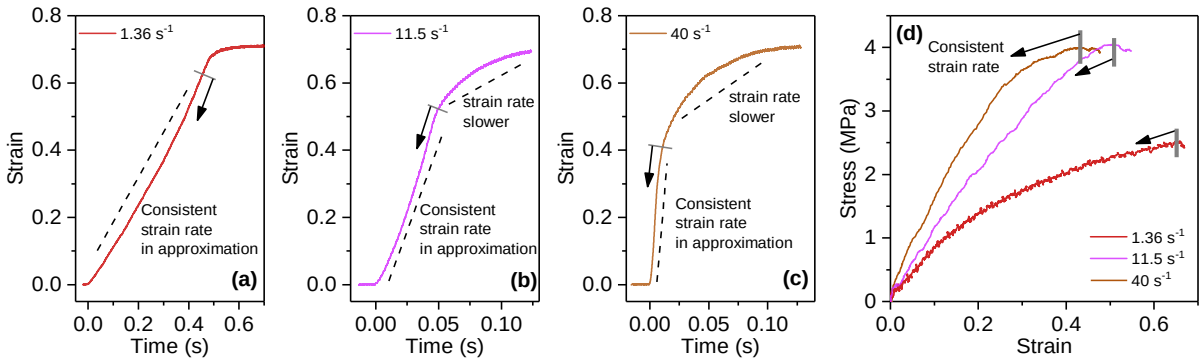


Fig. 2-19. The strain rate measurement in hydraulic medium rate experiments, at (a) 1.36 s^{-1}, (b) 11.5 s^{-1}, (c) 40 s^{-1}. The strain-stress data is in (d).

2.3.3 High-rate experiments (SHPB, and Piezo-bar)

The split Hopkinson pressure bar (SHPB) is widely used to explore high strain rate behaviour of polymers[93,109,117–121] and polymer-based composites[122,123]. Considering the literature on materials relevant to this thesis, Sharma et al.[124] conducted high rate compression tests on polyurethane at strain rate of 1600 s^{-1}. Yi et al.[90] tested three representative polyurethane with different hard segment ratios in high rate up to 10^4 s^{-1}. Sarva et al.[89] performed high rate experiments at rates from 10^{-3} s^{-1} to 10^4 s^{-1} and found polymer become brittle in high rate region.

The conventional SHPB apparatus includes a striker, incident, transmission bar and other supplementary recording devices, e.g. high-speed camera. When the striker is fired, impacting the incident bar and created an ‘incident’ stress wave travelling along the bar towards the specimen. At the bar-specimen interface, the reflected wave and transmitted wave generated and in opposite direction. The wave signals of the incident, reflected and transmitted pulses are measured by strain gauges attached to the incident and transmission bars[125]. For soft polymer measurement, the piezo-electric gauge can be used to record pulse signals more precisely, shown in Fig. 2-20.

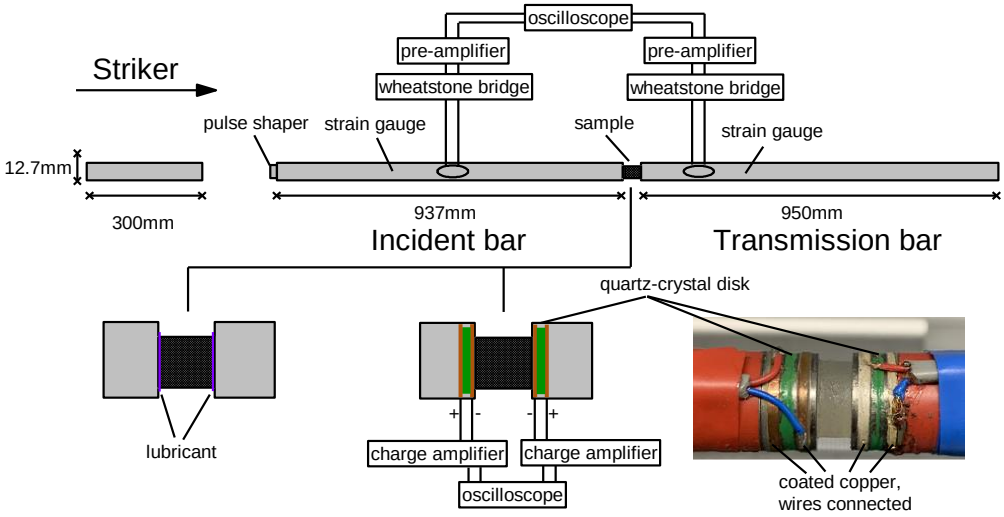


Fig. 2-20. The SHPB technique with or without the use of piezoelectric gauges at the bar-specimen interface. The signals from the strain gauge or piezo-gauge were amplified, then recorded and displayed using an oscilloscope.

The initial cross-sectional area and length of specimen are used to calculate the dynamic stress, strain, and strain rate. One-dimensional wave propagation theory is assumed to perform these calculations based on the recorded strains in the input and output bars. The striker generally has the same material and diameter as the incident bar, and the stress and strain amplitude of the incident pulse is decided by the striker velocity and the stress wave speed in the striker, shown in Equations (2-27) and (2-28).

$$\sigma_i = \frac{1}{2}\rho_B C_B V_{st}\,, \tag{2-27}$$

$$\varepsilon_i = \frac{1}{2}\frac{V_{st}}{C_B}\,. \tag{2-28}$$

In order to ensure that measurements made on the specimen are truly representative of material behaviour, it is important to confirm that the specimen is in static equilibrium. This is done by monitoring the stress at both ends of the specimen using the gauge signals from the input and output bars, effectively checking that

$$\varepsilon_i + \varepsilon_r = \varepsilon_t\,. \tag{2-29}$$

Assuming that the stress waves propagate in both the incident and transmission bars without dispersion, the strain rate and stress in the specimen can be calculated from the incident[125], transmitted and reflected signals by time-shifting these to the bar-specimen interfaces, then the strain rate and strain are is

$$\dot{\varepsilon} = \frac{c}{l_s(t)}\left[\varepsilon_i(t) - \varepsilon_r(t) - \varepsilon_t(t)\right], \tag{2-30}$$

$$\varepsilon = \frac{c}{l_s(t)}\int_0^t \left[\varepsilon_i(t) - \varepsilon_r(t) - \varepsilon_t(t)\right] dt, \tag{2-31}$$

where the ε_i, ε_r and ε_t are the measured strain pulses measured in the bars, l_s is the length of the specimen, and $c = \sqrt{E_{bar} / \rho_{bar}}$ is the longitudinal wave velocity in the bar. The stress can be calculated from

$$\sigma(t) = \frac{A_b}{2A_s} E_{bar}\left[\varepsilon_i(t) + \varepsilon_r(t) + \varepsilon_t(t)\right], \tag{2-32}$$

where A_b / A_s is the ratio of cross-section area between bar and specimen. More usually, however, only the signal from the transmission bar is used as this gives less noise:

$$\sigma(t) = \frac{A_b}{A_s} E_{bar}\left[\varepsilon_t(t)\right]. \tag{2-33}$$

The SHPB technique has developed significantly in the past decades, however, it is still very challenging to identify the properties of a soft material in high rates tests[126], because of several issues:

(1) Weak signal transmission. This is directly related to the transmitted signal ε_t measured on the transmission bar, which may be too weak to be accurately sensed by the strain gauge compared to the background noise level[127]. Direct force measurement methods may instead be used, including piezoelectric sensors or force transducers near the bar-specimen interface. This allows the measurement of the transmitted force history without disturbing the one-dimensional force transmission in the bar, and improves the detective ability to low-amplitude strain signals. Another method is to amplify the signals by enhancing bar surface

strain amplitude, this is done by reducing the transmission bar cross-sectional area[128], or using a bar material with a lower Young's modulus, i.e. aluminum alloy, magnesium or polymeric bar (e.g. polycarbonate)[129,130]. Additionally, in order to deform a specimen to large strains, large stresses may be required in the incident wave. However, if the incident wave is rectangular and has much larger stresses than those required to deform the specimen, then the reflected wave will be almost equal in magnitude and opposite in sign to the incident wave. The signals contain large oscillations, generally observed in the front face (i.e. small times) that make it difficult to identify the real polymer behaviour, since this is calculated from the differences in the waves. It is also noticed that using a softer bar affects the pulse intensity, producing larger strain, but a lower strain rate[125].

(2) Dynamic non-equilibrium. Static stress equilibrium in the specimen is required for the measured behaviour to truly correspond to the material properties. The loading build-up in the specimen is through the multiple reflections of stress waves in the axial direction, hence specimens with higher stress-wave speed achieve uniform loading more quickly. Generally, it is difficult to determine the stress accurately at the front face of the specimen because of oscillations in the incident wave[119,131] (also discussed in previous paragraph). For soft polymers, low wave speeds result in non-equilibrated stresses causing non-uniform deformation, which invalidates the experimental results for material property characterisation. A plastic piece of deformable materials, called a pulse shaper, is often placed at the impact site of the incident bar[129], to smooth the incident pulse by filtering out high-frequency components in the waveform (shown in Fig. 2-21). The desired pulse shaper is such that it can filter high-frequency dispersive pulse signals and facilitate constant strain-rate deformation in the specimen under dynamic stress equilibrium without severe oscillations in the loading history. The strain rate in the specimen thus can be determined by striker pulses, shown in Eq. (2-34). When the specimen is loaded uniformly, the axial stress on the two end faces is the same, which

can be expressed in terms of the measured quantities as force (or stress) being the same at the two ends of the specimen during an experiment, shown in Eq. (2-35). This can also be measured directly using the force transducers mentioned in the above figure.

$$\dot{\varepsilon} = -2\frac{c}{l_s(t)}\varepsilon_r(t), \tag{2-34}$$

$$\sigma(t) = \frac{A_b}{A_s}E_{bar}\varepsilon_t(t). \tag{2-35}$$

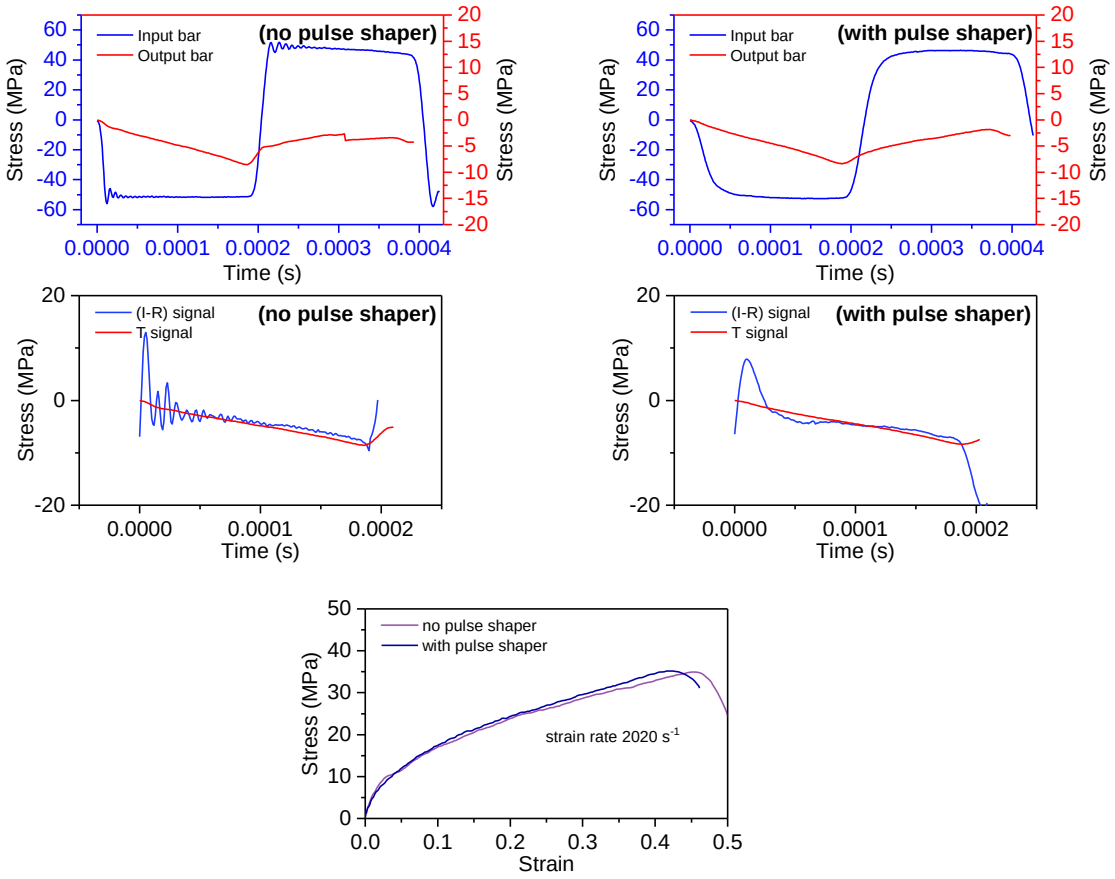


Fig. 2-21. SHPB experiment on black rubber at 2020 s^{-1} using magnesium bars, the second test has better incident wave as a proper pulse shaper was used. The pulse shaper removes some oscillations in the incident stress wave and in the resulting specimen response.

(3) Nonhomogeneous deformation and non-constant strain rate. The non-homogeneous deformation can result in a non-equilibrium stress state. Thin specimens (i.e. specimens with a small axial dimension) are often used to promote stress equilibrium. However, the friction on the interfaces between the specimen and the bars may become a concern. To minimize the

friction effects in this study, the bar ends were lubricated with a thin layer of vaseline[127], however, shear-induced barrelling might still emerge, especially at the large strain region shown in Fig. 2-22.

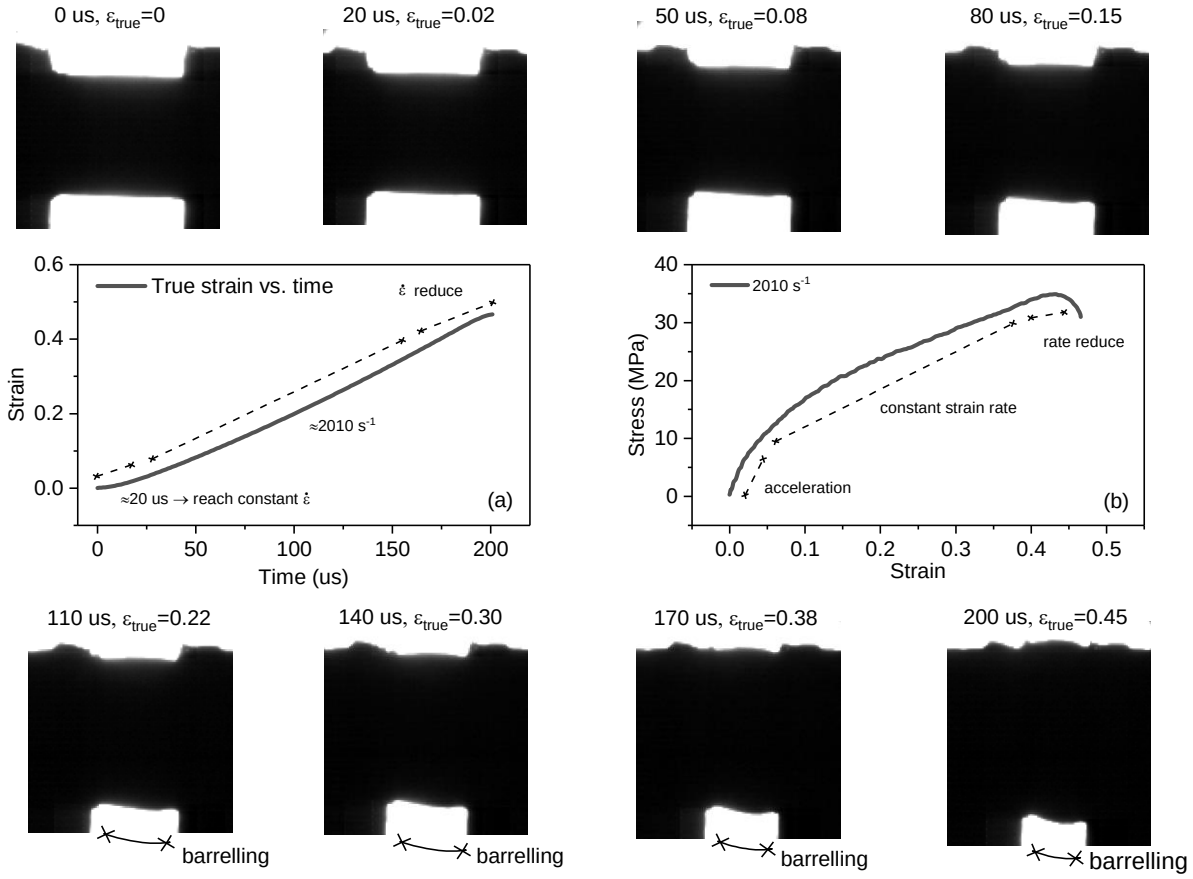


Fig. 2-22. Barrelling and non-constant strain rate observed in high rate experiments for carbon-black rubber at a strain rate of about 2000 s^{-1} (a), up to 0.45 in true strain (b). Using high-speed digital photographs clearly shows the sample deformation, which illustrates the problems associated with SHPB tests on soft materials.

(4) Piezo-bar implementation. For soft material tests, only a small portion of the loading pulse is transmitted through the specimen into the transmission bar, so the transmitted strain signal, ε_t, has a small amplitude[128]. To accurately measure these signals, piezo-electric gauges were used. The piezo-signal can be calibrated with signals from the surface-mounted strain gauge to determine the conversion factor between the measured voltage and the force, thus allowing the determination of the actual force on the piezo-disk, shown in Fig. 2-23. Mounting gauges at both ends of the specimen also helps to clarify stress equilibrium in the specimen.

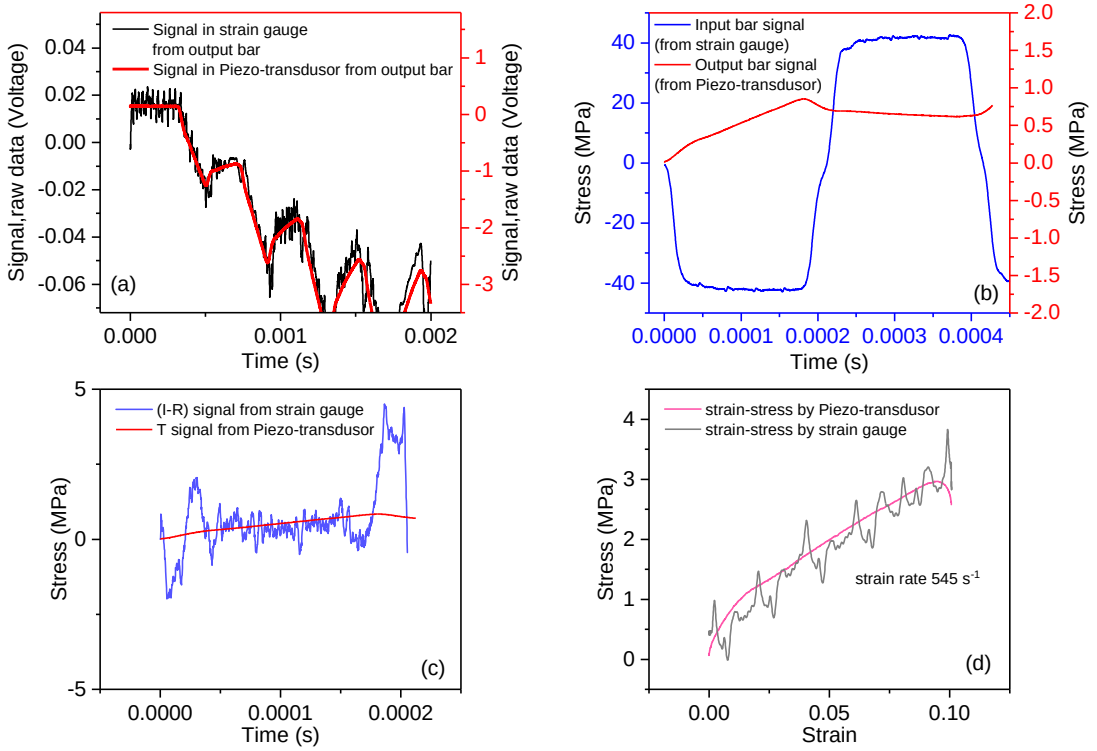


Fig. 2-23. Piezo-titanium bar test on sugar filled SPU at strain rate of 545 s^{-1} (a). Full inpout-output signals (b) and force equilibrium (c) are given. The advantage of using piezo-electric transducer on output bar, is to minimise the noise and increase accuracy of the transmission wave to obtain more accurate data for material behaviour (d).

(5) inertial effects. The inertia effects result from the need to accelerate the specimen, especially in the early stages of the experiment. In particular, these effects must be separated from the intrinsic rate dependence of the specimen material. In quasi-static experiments, inertial forces are negligible because accelerations are only on the order of 0.01 m s^{-2}. However, the rise time of the incident (loading) pulse in the SHPB apparatus is typically around 20 μs. It is therefore necessary to ensure that the specimen is small enough to make these forces negligible compared to the intrinsic material strength. The inertial contribution to the measured stress can be approximated using energy-based analyses to consider the rate of material change[132], given in Equations (2-36) and (2-37).

$$\sigma_{inertia} = \rho\ddot{\varepsilon}\left(\frac{a^2}{8}-\frac{h^2}{6}\right)+\rho\dot{\varepsilon}^2\left(\frac{a^2}{16}+\frac{h^2}{6}\right)-\rho\frac{hv^2}{2}, \tag{2-36}$$

where the $\ddot{\varepsilon}$ is the acceleration of strain rate in short time pulse, a is the radius; v is velocity.

2.4 References

1. Petrović ZS, Ferguson J. Polyurethane elastomers. *Prog Polym Sci*. 1991;16(5):695-836.
2. Prisacariu C. *Polyurethane Elastomers: From Morphology to Mechanical Aspects*. Springer Science & Business Media; 2011.
3. Das A, Mahanwar P. A brief discussion on advances in polyurethane applications. *Adv Ind Eng Polym Res*. 2020.
4. Ulrich H. Polyurethanes. *Encycl Polym Sci Technol*. 2002;4.
5. Khatoon H, Ahmad S. A review on conducting polymer reinforced polyurethane composites. *J Ind Eng Chem*. 2017;53:1-22.
6. Post W, Susa A, Blaauw R, Molenveld K, Knoop RJI. A review on the potential and limitations of recyclable thermosets for structural applications. *Polym Rev*. 2020;60(2):359-388.
7. Atiqah A, T Mastura M, A Ahmed Ali B, Jawaid M, M Sapuan S. A review on polyurethane and its polymer composites. *Curr Org Synth*. 2017;14(2):233-248.
8. Somarathna H, Raman SN, Mohotti D, Mutalib AA, Badri KH. The use of polyurethane for structural and infrastructural engineering applications: A state-of-the-art review. *Constr Build Mater*. 2018;190:995-1014.
9. Feula A, Pethybridge A, Giannakopoulos I, et al. A Thermoreversible Supramolecular Polyurethane with Excellent Healing Ability at 45 °c. *Macromolecules*. 2015;48(17):6132-6141. doi:10.1021/acs.macromol.5b01162
10. Feula A, Tang X, Giannakopoulos I, et al. An adhesive elastomeric supramolecular polyurethane healable at body temperature. *Chem Sci*. 2016;7(7):4291-4300. doi:10.1039/C5SC04864H
11. Hart LR, Harries JL, Greenland BW, Colquhoun HM, Hayes W. Healable supramolecular polymers. *Polym Chem*. 2013;4(18):4860-4870.
12. Akindoyo JO, Beg M, Ghazali S, Islam MR, Jeyaratnam N, Yuvaraj AR. Polyurethane types, synthesis and applications--a review. *Rsc Adv*. 2016;6(115):114453-114482.
13. Pedrazzoli D, Manas-Zloczower I. Understanding phase separation and morphology in thermoplastic polyurethanes nanocomposites. *Polymer (Guildf)*. 2016;90:256-263.
14. Russo R, Thomas EL. Phase separation in linear and cross-linked polyurethanes. *J Macromol Sci Part B Phys*. 1983;22(4):553-575.
15. Sánchez-Adsuar MS. Influence of the composition on the crystallinity and adhesion properties of thermoplastic polyurethane elastomers. *Int J Adhes Adhes*. 2000;20(4):291-298.
16. Korley LSTJ, Pate BD, Thomas EL, Hammond PT. Effect of the degree of soft and hard segment ordering on the morphology and mechanical behavior of semicrystalline segmented polyurethanes. *Polymer (Guildf)*. 2006;47(9):3073-3082. doi:10.1016/j.polymer.2006.02.093
17. Touchet TJ, Cosgriff-Hernandez EM. Hierarchal structure--property relationships of segmented polyurethanes. In: *Advances in Polyurethane Biomaterials*. Elsevier; 2016:3-22.
18. Ma Z, Hong Y, Nelson DM, Pichamuthu JE, Leeson CE, Wagner WR. Biodegradable polyurethane ureas with variable polyester or polycarbonate soft segments: Effects of crystallinity, molecular weight, and composition on mechanical properties. *Biomacromolecules*. 2011;12(9):3265-3274.
19. Heintz AM, Duffy DJ, Hsu SL, Suen W, Chu W, Paul CW. Effects of reaction temperature on the formation of polyurethane prepolymer structures. *Macromolecules*. 2003;36(8):2695-2704.

20. Dusek K, Spirkova M, Havlicek I. Network formation of polyurethanes due to side reactions. *Macromolecules*. 1990;23(6):1774-1781.
21. Lei W, Fang C, Zhou X, Cheng Y, Yang R, Liu D. Morphology and thermal properties of polyurethane elastomer based on representative structural chain extenders. *Thermochim Acta*. 2017;653:116-125.
22. Hermida-Merino D, O'Driscoll B, Hart LR, et al. Enhancement of microphase ordering and mechanical properties of supramolecular hydrogen-bonded polyurethane networks. *Polym Chem*. 2018;9(24):3406-3414.
23. Savelyev Y V, Akhranovich ER, Grekov AP, et al. Influence of chain extenders and chain end groups on properties of segmented polyurethanes. I. Phase morphology. *Polymer (Guildf)*. 1998;39(15):3425-3429.
24. Król P, Pilch-Pitera B. Phase structure and thermal stability of crosslinked polyurethane elastomers based on well-defined prepolymers. *J Appl Polym Sci*. 2007;104(3):1464-1474.
25. Zhang H, Chen Y, Zhang Y, Sun X, Ye H, Li W. Synthesis and characterization of polyurethane elastomers. *J Elastomers Plast*. 2008;40(2):161-177.
26. Aneja A, Wilkes GL. A systematic series of 'model'PTMO based segmented polyurethanes reinvestigated using atomic force microscopy. *Polymer (Guildf)*. 2003;44(23):7221-7228.
27. Fridman ID, Thomas EL. Morphology of crystalline polyurethane hard segment domains and spherulites. *Polymer (Guildf)*. 1980;21(4):388-392.
28. McCrum, N. G., Buckley, C. P. BCB. *Principles of Polymer Engineering*. Oxford University Press; 1997.
29. Waletzko RS, Korley LTJ, Pate BD, Thomas EL, Hammond PT. Role of increased crystallinity in deformation-induced structure of segmented thermoplastic polyurethane elastomers with PEO and PEO- PPO- PEO soft segments and HDI hard segments. *Macromolecules*. 2009;42(6):2041-2053.
30. Gooch A, Murphy NS, Thomson NH, Wilson AJ. Side-chain supramolecular polymers employing conformer independent triple hydrogen bonding arrays. *Macromolecules*. 2013;46(24):9634-9641.
31. Eastwood E, Viswanathan S, O'brien CP, Kumar D, Dadmun MD. Methods to improve the properties of polymer mixtures: optimizing intermolecular interactions and compatibilization. *Polymer (Guildf)*. 2005;46(12):3957-3970.
32. Chattopadhyay DK, Sreedhar B, Raju KVSN. Effect of chain extender on phase mixing and coating properties of polyurethane ureas. *Ind Eng Chem Res*. 2005;44(6):1772-1779.
33. Martin DJ, Meijs GF, Gunatillake PA, McCarthy SJ, Renwick GM. The effect of average soft segment length on morphology and properties of a series of polyurethane elastomers. II. SAXS-DSC annealing study. *J Appl Polym Sci*. 1997;64(4):803-817.
34. Burattini S, Greenland BW, Merino DH, et al. A healable supramolecular polymer blend based on aromatic $π$- $π$ stacking and hydrogen-bonding interactions. *J Am Chem Soc*. 2010;132(34):12051-12058.
35. Xie R, Lee Y, Aplan MP, et al. Glass transition temperature of conjugated polymers by oscillatory shear rheometry. *Macromolecules*. 2017;50(13):5146-5154.
36. Elmer P. Dynamic Mechanical Analysis (DMA) A Beginner's Guide. *PerkinElmer Ltd Waltham, MA, USA*. 2013:1-23.
37. Dong M, Li Q, Liu H, et al. Thermoplastic polyurethane-carbon black nanocomposite coating: fabrication and solid particle erosion resistance. *Polymer (Guildf)*. 2018;158:381-390.
38. Du W, Liu J, Wang Y, Li Y, Li Z. Polyurethane encapsulated carbon black particles

and enhanced properties of water polyurethane composite films. *Prog Org Coatings*. 2016;97:146-152.
39. Zhou S-X, Wu L-M, Sun J, Shen W-D. Effect of nanosilica on the properties of polyester-based polyurethane. *J Appl Polym Sci*. 2003;88(1):189-193.
40. Chen Y, Zhou S, Yang H, Wu L. Structure and properties of polyurethane/nanosilica composites. *J Appl Polym Sci*. 2005;95(5):1032-1039.
41. Petrović ZS, Javni I, Waddon A, Bánhegyi G. Structure and properties of polyurethane--silica nanocomposites. *J Appl Polym Sci*. 2000;76(2):133-151.
42. Lau K, Gu C, Hui D. A critical review on nanotube and nanotube/nanoclay related polymer composite materials. *Compos Part B Eng*. 2006;37(6):425-436.
43. Sumita M, Shizuma T, Miyasaka K, Ishikawa K. Effect of reducible properties of temperature, rate of strain, and filler content on the tensile yield stress of nylon 6 composites filled with ultrafine particles. *J Macromol Sci Part B Phys*. 1983;22(4):601-618.
44. Bartczak Z, Argon AS, Cohen RE, Weinberg M. Toughness mechanism in semi-crystalline polymer blends: II. High-density polyethylene toughened with calcium carbonate filler particles. *Polymer (Guildf)*. 1999;40(9):2347-2365.
45. Wu Q, Henriksson M, Liu X, Berglund LA. A high strength nanocomposite based on microcrystalline cellulose and polyurethane. *Biomacromolecules*. 2007;8(12):3687-3692.
46. Saha MC, Kabir ME, Jeelani S. Enhancement in thermal and mechanical properties of polyurethane foam infused with nanoparticles. *Mater Sci Eng A*. 2008;479(1-2):213-222.
47. Ma Y, Yokozeki T, Ueda M, Sugahara T, Yang Y, Hamada H. Effect of polyurethane dispersion as surface treatment for carbon fabrics on mechanical properties of carbon/nylon composites. *Compos Sci Technol*. 2017;151:268-281.
48. Tjong SC. Structural and mechanical properties of polymer nanocomposites. *Mater Sci Eng R Reports*. 2006;53(3-4):73-197.
49. Lazzeri A, Thio YS, Cohen RE. Volume strain measurements on CaCO3/polypropylene particulate composites: the effect of particle size. *J Appl Polym Sci*. 2004;91(2):925-935.
50. Fu S-Y, Feng X-Q, Lauke B, Mai Y-W. Effects of particle size, particle/matrix interface adhesion and particle loading on mechanical properties of particulate--polymer composites. *Compos Part B Eng*. 2008;39(6):933-961.
51. Xu Z, Song Y, Zheng Q. Payne effect of carbon black filled natural rubber compounds and their carbon black gels. *Polymer (Guildf)*. 2019;185:121953.
52. Diani J, Fayolle B, Gilormini P. A review on the Mullins effect. *Eur Polym J*. 2009;45(3):601-612. doi:10.1016/j.eurpolymj.2008.11.017
53. Qi HJ, Boyce MC. Constitutive model for stretch-induced softening of the stress-stretch behavior of elastomeric materials. *J Mech Phys Solids*. 2004;52(10):2187-2205. doi:10.1016/j.jmps.2004.04.008
54. Fukahori Y. New progress in the theory and model of carbon black reinforcement of elastomers. *J Appl Polym Sci*. 2005;95(1):60-67.
55. Kraus R, Wilke W, Zhuk A, Luzinov I, Minko S, Voronov A. Investigation of debonding processes in particle-filled polymer materials by acoustic emission: Part I Acoustic emission and debonding stress. *J Mater Sci*. 1997;32(16):4397-4403.
56. Kraus R, Wilke W, Zhuk A, Luzinov I, Minko S, Voronov A. Investigation of debonding processes in particle-filled polymer materials by acoustic emission: Part II Acoustic emission amplitude and energy release by debonding. *J Mater Sci*. 1997;32(16):4405-4410.

57. Zhuk A V, Knunyants NN, Oshmyan VG, Topolkaraev VA, Berlin AA. Debonding microprocesses and interfacial strength in particle-filled polymer materials. *J Mater Sci*. 1993;28(17):4595-4606.
58. Bai SL, Chen JK, Huang ZP, Liu ZD. Interface effect on the mechanical behaviour of rigid particle filled polymer. *Polym Int*. 2001;50(2):222-228.
59. Sinien L, Lin Y, Xiaoguang Z, Zongneng Q. Microdamage and interfacial adhesion in glass bead-filled high-density polyethylene. *J Mater Sci*. 1992;27(17):4633-4638.
60. Meddad A, Fisa B. A model for filler—matrix debonding in glass-bead-filled viscoelastic polymers. *J Appl Polym Sci*. 1997;65(10):2013-2024.
61. Jerabek M, Major Z, Renner K, Móczó J, Pukánszky B, Lang RW. Filler/matrix-debonding and micro-mechanisms of deformation in particulate filled polypropylene composites under tension. *Polymer (Guildf)*. 2010;51(9):2040-2048.
62. Tang L-C, Zhang H, Sprenger S, Ye L, Zhang Z. Fracture mechanisms of epoxy-based ternary composites filled with rigid-soft particles. *Compos Sci Technol*. 2012;72(5):558-565.
63. Oldenbo M, Fernberg SP, Berglund LA. Mechanical behaviour of SMC composites with toughening and low density additives. *Compos Part A Appl Sci Manuf*. 2003;34(9):875-885.
64. Le HH, Ilisch S, Radusch H-J. Characterization of the effect of the filler dispersion on the stress relaxation behavior of carbon black filled rubber composites. *Polymer (Guildf)*. 2009;50(10):2294-2303.
65. Wilbrink MWL, Argon AS, Cohen RE, Weinberg M. Toughenability of Nylon-6 with CaCO3 filler particles: new findings and general principles. *Polymer (Guildf)*. 2001;42(26):10155-10180.
66. Zhang H, Chang H, Li J, Li X, Wang H. High-strain-rate mechanical response of HTPE propellant under SHPB impact loading. *AIP Adv*. 2021;11(3):35145.
67. Chen TK, Shieh TS, Chui JY. Studies on the first DSC endotherm of polyurethane hard segment based on 4, 4 ‘-diphenylmethane diisocyanate and 1, 4-butanediol. *Macromolecules*. 1998;31(4):1312-1320.
68. Chen C-P, Dai SA, Chang H-L, Su W-C, Wu T-M, Jeng R-J. Polyurethane elastomers through multi-hydrogen-bonded association of dendritic structures. *Polymer (Guildf)*. 2005;46(25):11849-11857.
69. Leung LM, Koberstein JT. DSC annealing study of microphase separation and multiple endothermic behavior in polyether-based polyurethane block copolymers. *Macromolecules*. 1986;19(3):706-713.
70. Koberstein JT, Galambos AF. Multiple melting in segmented polyurethane block copolymers. *Macromolecules*. 1992;25(21):5618-5624.
71. Witzleben ST, Walbrueck K, Klein SE, Schulze M. Investigation of temperature dependency of morphological properties of thermoplastic polyurethane using WAXS and SAXS monitoring. 2015.
72. Bertini F, Canetti M, Audisio G, Costa G, Falqui L. Characterization and thermal degradation of polypropylene--montmorillonite nanocomposites. *Polym Degrad Stab*. 2006;91(3):600-605.
73. Sui T, Baimpas N, Dolbnya IP, Prisacariu C, Korsunsky AM. Multiple-length-scale deformation analysis in a thermoplastic polyurethane. *Nat Commun*. 2015;6:6583.
74. Blundell DJ, Eeckhaut G, Fuller W, Mahendrasingam A, Martin C. Real time SAXS/stress--strain studies of thermoplastic polyurethanes at large strains. *Polymer (Guildf)*. 2002;43(19):5197-5207.
75. Kojio K, Matsuo K, Motokucho S, Yoshinaga K, Shimodaira Y, Kimura K. Simultaneous small-angle X-ray scattering/wide-angle X-ray diffraction study of the

microdomain structure of polyurethane elastomers during mechanical deformation. *Polym J*. 2011;43(8):692-699.
76. Stribeck A, Pöselt E, Eling B, Jokari-Sheshdeh F, Hoell A. Thermoplastic polyurethanes with varying hard-segment components. Mechanical performance and a filler-crosslink conversion of hard domains as monitored by SAXS. *Eur Polym J*. 2017;94:340-353.
77. Saalwächter K. Applications of NMR in Polymer Characterization--An Introduction. 2019.
78. Maafi EM, Tighzert L, Malek F. Synthesis and characterization of new polyurethanes: influence of monomer composition. *Polym Bull*. 2011;66(3):391-406.
79. Kuwabara K, Kaji H, Horii F, Bassett DC, Olley RH. Solid-State 13C NMR Analyses of the Crystalline- Noncrystalline Structure for Metallocene-Catalyzed Linear Low-Density Polyethylene. *Macromolecules*. 1997;30(24):7516-7521.
80. Tang Q, Gao K. Structure analysis of polyether-based thermoplastic polyurethane elastomers by FTIR, 1H NMR and 13C NMR. *Int J Polym Anal Charact*. 2017;22(7):569-574.
81. Babra TS, Warriner C, Bazin N, Hayes W, Greenland BW. A fluoride degradable crosslinker for debond-on-demand polyurethane based crosslinked adhesives. *Mater Today Commun*. 2021;26:101777.
82. Babra TS, Wood M, Godleman JS, et al. Fluoride-responsive debond on demand adhesives: manipulating polymer crystallinity and hydrogen bonding to optimise adhesion strength at low bonding temperatures. *Eur Polym J*. 2019;119:260-271.
83. Simon J, Barla F, Kelemen-Haller A, Farkas F, Kraxner M. Thermal stability of polyurethanes. *Chromatographia*. 1988;25(2):99-106.
84. Rosu D, Tudorachi N, Rosu L. Investigations on the thermal stability of a MDI based polyurethane elastomer. *J Anal Appl Pyrolysis*. 2010;89(2):152-158.
85. Rek V, Mencer HJ, Bravar M. GPC and structural analysis of polyurethane degradation. *Polym Photochem*. 1986;7(4):273-283.
86. Furukawa M, Komiya M, Yokoyama T. Characterization of polyurethane network elastomers. *Die Angew Makromol Chemie Appl Macromol Chem Phys*. 1996;240(1):205-211.
87. Zhang L, Yao X, Zang S, Han Q. Temperature and strain rate dependent tensile behavior of a transparent polyurethane interlayer. *Mater Des*. 2015;65:1181-1188.
88. Kendall MJ, Siviour CR. Experimentally simulating adiabatic conditions: Approximating high rate polymer behavior using low rate experiments with temperature profiles. *Polym (United Kingdom)*. 2013;54(18):5058-5063. doi:10.1016/j.polymer.2013.06.049
89. Sarva SS, Deschanel S, Boyce MC, Chen W. Stress-strain behavior of a polyurea and a polyurethane from low to high strain rates. *Polymer (Guildf)*. 2007;48(8):2208-2213. doi:10.1016/j.polymer.2007.02.058
90. Yi J, Boyce MC, Lee GF, Balizer E. Large deformation rate-dependent stress-strain behavior of polyurea and polyurethanes. *Polymer (Guildf)*. 2006;47(1):319-329. doi:10.1016/j.polymer.2005.10.107
91. Liao Z, Yao X, Zhang L, Hossain M, Wang J, Zang S. Temperature and strain rate dependent large tensile deformation and tensile failure behavior of transparent polyurethane at intermediate strain rates. *Int J Impact Eng*. 2019;129:152-167.
92. Kendall MJ, Siviour CR. Experimentally simulating high-rate behaviour: rate and temperature effects in polycarbonate and PMMA. *Philos Trans R Soc A Math Phys Eng Sci*. 2014;372(2015):20130202.
93. Mulliken AD, Boyce MC. Mechanics of the rate-dependent elastic-plastic deformation

of glassy polymers from low to high strain rates. *Int J Solids Struct*. 2006;43(5):1331-1356. doi:10.1016/j.ijsolstr.2005.04.016
94. Siviour CR, Walley SM, Proud WG, Field JE. Mechanical behaviour of polymers at high rates of strain. In: *Journal de Physique IV (Proceedings)*. Vol 134. ; 2006:949-955.
95. McCrum NG, Buckley CP, Bucknall CB, Bucknall CB, Bucknall CB. *Principles of Polymer Engineering*. Oxford University Press, USA; 1997.
96. Jindal P, Sain M, Kumar N. Mechanical characterization of PMMA/MWCNT composites under static and dynamic loading conditions. *Mater Today Proc*. 2015;2(4-5):1364-1372.
97. Saber-Sheikh K, Clarke RL, Braden M. Viscoelastic properties of some soft lining materials: I—Effect of temperature. *Biomaterials*. 1999;20(9):817-822.
98. Kitagawa Y, Yoshida K, Takase K, et al. Evaluation of viscoelastic properties, hardness, and glass transition temperature of soft denture liners and tissue conditioner. *Odontology*. 2020;108(3):366-375.
99. Ramorino G, Vetturi D, Cambiaghi D, Pegoretti A, Ricco T. Developments in dynamic testing of rubber compounds: assessment of non-linear effects. *Polym Test*. 2003;22(6):681-687.
100. Esmaeeli R, Aliniagerdroudbari H, Hashemi SR, JBR C, Farhad S. Designing a new dynamic mechanical analysis (DMA) system for testing viscoelastic materials at high frequencies. *Model Simul Eng*. 2019;2019.
101. Henriques IR, Borges LA, Costa MF, Soares BG, Castello DA. Comparisons of complex modulus provided by different DMA. *Polym Test*. 2018;72:394-406.
102. Deng S, Hou M, Ye L. Temperature-dependent elastic moduli of epoxies measured by DMA and their correlations to mechanical testing data. *Polym Test*. 2007;26(6):803-813.
103. Zeltmann SE, Kumar BRB, Doddamani M, Gupta N. Prediction of strain rate sensitivity of high density polyethylene using integral transform of dynamic mechanical analysis data. *Polymer (Guildf)*. 2016;101:1-6.
104. Ward IM, Hadley DW. *An Introduction to the Mechanical Properties of Solid Polymers*.; 1993.
105. Schroyen B, Vlassopoulos D, Van Puyvelde P, Vermant J. Bulk rheometry at high frequencies: a review of experimental approaches. *Rheol Acta*. 2020;59(1):1-22.
106. Roland CM. Mechanical behavior of rubber at high strain rates. *Rubber Chem Technol*. 2006;79(3):429-459.
107. Roland CM, Twigg JN, Vu Y, Mott PH. High strain rate mechanical behavior of polyurea. *Polymer (Guildf)*. 2007;48(2):574-578. doi:10.1016/j.polymer.2006.11.051
108. Balzer JE, Siviour CR, Walley SM, Proud WG, Field JE. Behaviour of ammonium perchlorate--based propellants and a polymer--bonded explosive under impact loading. *Proc R Soc London Ser A Math Phys Eng Sci*. 2004;460(2043):781-806.
109. Rae PJ, Brown EN, Orler EB. The mechanical properties of poly (ether-ether-ketone)(PEEK) with emphasis on the large compressive strain response. *Polymer (Guildf)*. 2007;48(2):598-615.
110. Viot P, Beani F, Lataillade J-L. Polymeric foam behavior under dynamic compressive loading. *J Mater Sci*. 2005;40(22):5829-5837.
111. Song B, Chen WW, Lu W-Y. Mechanical characterization at intermediate strain rates for rate effects on an epoxy syntactic foam. *Int J Mech Sci*. 2007;49(12):1336-1343.
112. Othman R, Guégan P, Challita G, Pasco F, LeBreton D. A modified servo-hydraulic machine for testing at intermediate strain rates. *Int J Impact Eng*. 2009;36(3):460-467.
113. Song B, Sanborn B, Heister J, et al. Development of “dropkinson” Bar for

Intermediate Strain-rate Testing. In: *EPJ Web of Conferences*. Vol 183. ; 2018:2004.
114. Sahraoui S, Lataillade JL. Analysis of load oscillations in instrumented impact testing. *Eng Fract Mech*. 1998;60(4):437-446.
115. Quinlan MF, Hillery MT. High-strain-rate testing of beryllium copper at elevated temperatures. *J Mater Process Technol*. 2004;153:1051-1057.
116. Viot P. Hydrostatic compression on polypropylene foam. *Int J Impact Eng*. 2009;36(7):975-989.
117. Brown EN, Rae PJ, Orler EB. The influence of temperature and strain rate on the constitutive and damage responses of polychlorotrifluoroethylene (PCTFE, Kel-F 81). *Polymer (Guildf)*. 2006;47(21):7506-7518.
118. Bourne NK, Brown EN, Millett JCF, Gray III GT. Shock, release and Taylor impact of the semicrystalline thermoplastic polytetrafluoroethylene. *J Appl Phys*. 2008;103(7):74902.
119. Gray III GT, Blumenthal WR. Split-Hopkinson pressure bar testing of soft materials. *ASM Handb*. 2000;8:488-496.
120. Siviour CR, Walley SM, Proud WG, Field JE. The high strain rate compressive behaviour of polycarbonate and polyvinylidene difluoride. *Polymer (Guildf)*. 2005;46(26):12546-12555.
121. Furmanski J, Trujillo CP, Martinez DT, Gray III GT, Brown EN. Dynamic-Tensile-Extrusion for investigating large strain and high strain rate behavior of polymers. *Polym Test*. 2012;31(8):1031-1037.
122. Fan JT, Weerheijm J, Sluys LJ. Glass interface effect on high-strain-rate tensile response of a soft polyurethane elastomeric polymer material. *Compos Sci Technol*. 2015;118:55-62.
123. Siviour CR, Laity PR, Proud WG, et al. High strain rate properties of a polymer-bonded sugar: their dependence on applied and internal constraints. *Proc R Soc A Math Phys Eng Sci*. 2008;464(2093):1229-1255.
124. Sharma A, Shukla A, Prosser RA. Mechanical characterization of soft materials using high speed photography and split hopkinson pressure bar technique. *J Mater Sci*. 2002;37(5):1005-1017. doi:10.1023/A:1014308216966
125. Chen WW, Song B. *Split Hopkinson (Kolsky) Bar: Design, Testing and Applications*. Springer Science & Business Media; 2010.
126. Chen WW. Experimental methods for characterizing dynamic response of soft materials. *J Dyn Behav Mater*. 2016;2(1):2-14.
127. Chen W, Lu F, Frew DJ, Forrestal MJ. Dynamic Compression Testing of Soft Materials. *J Appl Mech*. 2002;69(3):214. doi:10.1115/1.1464871
128. Chen W, Lu F, Cheng M. Tension and compression tests of two polymers under quasi-static and dynamic loading. *Polym Test*. 2002;21(2):113-121.
129. Chen W, Zhang B, Forrestal MJ. A split Hopkinson bar technique for low-impedance materials. *Exp Mech*. 1999;39(2):81-85.
130. Harrigan JJ, Ahonsi B, Palamidi E, Reid SR. Experimental and numerical investigations on the use of polymer Hopkinson pressure bars. *Philos Trans R Soc A Math Phys Eng Sci*. 2014;372(2023):20130201.
131. Kuhn H, Medlin D. Asm handbook. volume 8: Mechanical testing and evaluation. *ASM Int Member/Customer Serv Center, Mater Park OH 44073-0002, USA, 2000 998*. 2000.
132. Siviour CR, Walley SM. Inertial and frictional effects in dynamic compression testing. In: *The Kolsky-Hopkinson Bar Machine*. Springer; 2018:205-247.

CHAPTER 3 CARBON BLACK-FILLED TPU

3.1 Introduction

The project started with the outline of work using an empirical correlation method combining quasi-static tests and dynamic mechanical analysis to predict the high strain rates responses for carbon black-filled thermoplastic polyurethane. The model parameters considered linear viscoelastic properties and incorporated generalized viscoelastic model with continuum damage theorem and be able to effectively predict the experimental behaviour from low- and high-strain rates. TPU specimens were tested in compression and tension tests at low rates ($10^{-3} – 10^{-1}$ s^{-1}) using a screw-driven standard quasi-static testing machine and high rates (10^{3} s^{-1}) using Split-Hopkinson pressure bar (SHPB). We characterised the temperature and frequency dependence of this commercial polyurethane from -50 °C to 80 °C to explore the mechanical responses linking its mechanical responses in atmospheric temperature and frequency sweeps. A FE model (by Abaqus FEA) and analytical solutions for DMA dual-cantilever model to confirm the reliability and convince of experimental results. A linear viscoelastic continuum damage model based on the Boltzmann superposition integral and a strain-induced damage criterion was reviewed. The model parameters were appropriately assigned, fitting quasi-static compression experiments varying with strain rates and experimental temperature changes. The results of these experiments formed the dataset that was used for the model development and validation in further cyclic experiments and high strain rate tests. The work in contribution collaborated conventional quasi-static experiments, thermal-dynamic analysis and high rate prediction in one framework of linear viscoelasticity and one theorem of continuum damage mechanics.

3.2 Paper A:

Application of linear viscoelastic continuum damage theory to the low and high strain rate response of thermoplastic polyurethane[1]

Abstract

Background: Understanding the mechanical response of elastomers to applied deformation at different strain rates and temperatures is crucial in industrial design and manufacture; however, this response is often difficult to measure, especially at high strain rates (e.g. >100 s^{-1}), and more predictive methods to obtain constitutive relationships are required. Objective: The objective of the research described in this paper is to develop such methods. Method: The paper outlines a novel approach combining quasi-static monotonic tests in tension and compression, quasi-static cyclic tests in tension, and high strain rate tests in compression, with dynamic mechanical analysis and time-temperature superposition. A generalized viscoelastic model incorporating continuum damage is calibrated. Results: The results show that a model calibrated using data from quasi-static compression and dynamic mechanical analysis can be used to adequately predict the compressive high strain rate response: hence, this paper provides an important step in the development of a methodology that avoids the execution of high-rate experiments, which are affected by the potential errors caused by inertia and wave propagation effects, and which cannot be combined with advanced characterisation methods such as X-ray tomography and electron microscopy. In addition, data from FE models of the dynamic mechanical analysis experiments are provided, along with a discussion of data obtained from tensile and cyclic loading. Conclusions: The paper demonstrates the effectiveness of 'indirect' predictive methods to obtain information about high rate behaviour of low modulus materials.

[1] Chen H, Trivedi AR, Siviour CR. Application of Linear Viscoelastic Continuum Damage Theory to the Low and High Strain Rate Response of Thermoplastic Polyurethane. Exp Mech. 2020:1-12. https://doi.org/10.1007/s11340-020-00608-2

Keywords: Polyurethane, Dynamic mechanical analysis, High strain-rates. Viscoelasticity, Viscoelastic damage

1 Introduction

Thermoplastic elastomers are widely used in engineering and industry, e.g. for bumpers, seals, moulded gaskets and ducts, often working as impact and vibration mitigators. They benefit from advantageous properties such as flexibility, durability and property recovery after deformation, but simul taneously have dependence on polymer network morphology, temperature, strain rate and loading history[1–4].

The empirical behaviour of many polymers between the rubbery and glassy states has the well-known time-temperature equivalence[5]. In the glassy state, at a low temperature, or during deformation at high rates, the polymer chains have inhibited displacement, which raises the stored elastic energy and stiffens the polymer. In the rubbery state, at elevated temperature, the molecular chains have greater mobility owing to increased free volume and energy, and are able to respond on the loading timescale. This dynamic mechanism also responds at low loading rates. The mechanical interpretation can be extended using the time-temperature superposition (TTS) principle, which describes the equivalence of time and temperature to characterise mechanical properties. Inherent properties, in particular over a range of temperatures near the glass transition, can be mapped onto a master curve which can then be fitted using equations such as the Williams-Landel-Ferry (WLF) Eq. (3-1) below to build a coordinate system for either temperature or frequency dependence of mechanical behaviour[6]. This is done by producing a shift factor, $\log a_T$ in Eq. (3-1).

$$\log a_T = -\frac{C_1\left(T - T_{ref}\right)}{C_2 + \left(T - T_{ref}\right)}, \tag{3-1}$$

where C_1 and C_2 are constants, and Tref is the reference temperature at which the master curve is produced. In this paper, time-temperature equivalence is explored as a means to predict high-rate (e.g. > 700 s^{-1}) response of elastomers, using a commercial thermoplastic polyurethane as a model material.

Rate dependence in polyurethanes has been studied[7–9] using direct measurements over the range of strain rates from 10^{-3} s^{-1} to 10^{4} s^{-1}. These studies have found that, in common with other polymers, the flow stress magnitude increases with increasing strain rate. Quasi-static experiments may be performed on conventional screw-driven machines, whilst medium and higher strain rates are investigated using hydraulic machines, drop weight instruments, split-Hopkinson bar apparatus (SHPBs), or ultrasonic machines[5,8,10].

The SHPB, which is widely used for high rate characterisation, requires assumptions about experimental conditions of alignment, stress equilibrium, and inertia[8,11–14]. For this reason, it is not always certain that the observed responses really express the intrinsic material properties at high strain rate[14,15]. In addition, conventional high rate techniques only give average specimen properties. In order to obtain full-field measurements, as well as to identify the accuracy of conventional high-rate data, optical techniques using high-speed cameras, combined with, e.g. photoelasticity, speckle or grid techniques, may be used to obtain additional strain measurements[8].

High rates tests on polymers have been employed to characterise fracture, voiding and cracking behaviours[16]; rate dependence due to the glass transition[7]; and strain-crystallization during deformation[17]. Challenges in data interpretation include non-constant strain rate, oscillations in the incident pulse, inhomogeneous stress and strain, non-isothermal deformation, and impedance mismatch between the specimens and loading system[18–21]. From a material point of view[22], issues such as low magnitude transmitted signals, stress non-equilibrium and inertial effects associated with characterisation of soft materials start to appear when the

strength is less than 10 MPa. The difficult measurements for ‘soft’ materials at high strain rate have led to significant effort to obtain precise results. Authors have made developments including direct measurements using high speed photography[9,23], low impedance bar materials and thinner samples to investigate strain rates up to 10^4 s^{-1}.

In this study, we calibrated the small strain temperature and frequency dependence of a commercial polyurethane, and explored large strain quasi-static compression responses, which were used to predict the high strain rate behaviour of the material. Dynamic mechanical analysis (DMA) was first executed to understand the viscoelastic behaviour as a function of temperature and frequency, producing a master curve as a function of frequency through time-temperature superposition. A numerical (FE) simulation of the DMA experiment was performed, using a Prony series fit to test data. Then, a linear viscoelastic continuum damage model based on the Boltzmann superposition integral and a strain based damage criterion was reviewed, and the model parameters were fitted to the data from these experiments. This model was further used to predict the response in cyclic tensile test and high strain rate compression experiments. The study reported in this paper thus provides an applicable methodology to characterise temperature and strain rate dependent mechanical properties of rubbers, including prediction of high rate behaviour from data obtained in low rate tests.

2 Linear viscoelastic continnum damage theory

Many particulate elastomer behaviours under different loading conditions can be described using phenomenological models with continuum damage criteria[24,25]. Empirically, it is observed that with increasing strain, the stiffness of the material decreases through viscoelastic softening and changes in microstructure. Although there are many polymer-relevant physical interpretations, the issue of understanding and modelling this behaviour still exists. In this paper, a model based on viscoelasticity and continuum damage mechanics is used.

3 Essential viscoelastic physical model

The most general models of viscoelasticity are based on physical rheology, without involving any explicit model of chemical composition or molecular variation. The models are based on mechanical analogues consisting of Hookean springs and Newtonian dashpots, and are used to establish the physical phenomenology of the viscoelasticity under investigation. A typical model consisting of multiple Maxwell elements in parallel with a spring is often used, and is shown in Fig. 3-1.

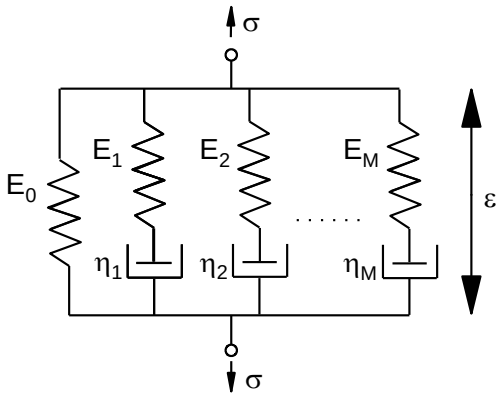


Fig. 3-1 Generalized Maxwell model

The stress relaxation modulus for this model can be written as

$$E(t) = E_0 + \sum_{i=1}^{M} E_i \exp\left(-\frac{t}{\tau_i}\right), \tag{3-2}$$

where E_i denotes the elastic modulus of the spring elements; $\tau_i = \eta_i / E_i$ is the relaxation time of each Maxwell element.

For time varying strains, the Boltzmann superposition principle states that the incremental response of a material to a given deformation is independent of the deformation history. This is only valid in the linear viscoelastic region. Here, stress-strain relations in viscoelastic materials can be represented as the cumulative stress relaxation behaviour resulting from the entire loading history. The Boltzmann superposition allows the stress response over the loading history to be calculated by summing these relaxation results

$$\sigma(t) = E(0)\varepsilon(0_+) + \sum_{i=1}^{M}\int_0^t E_i \exp\left(-\frac{t-s_i}{\tau_i}\right)\frac{d\varepsilon(\Delta s_i)}{ds}ds_i, \tag{3-3}$$

where s is a dummy variable with units of time. Here, as $t \to \infty$, $E(0)$ tends to the long term elastic response, i.e. E_0. If monotonic loading at a single strain rate starts at $\varepsilon = 0$ and $\sigma = 0$, and sufficient time has elapsed since any previous deformation, the stress-strain relation can be calculated from the corresponded strain rate and time accumulation as

$$\sigma(t) = \int_0^t E(t-s)\dot{\varepsilon}(s)ds. \tag{3-4}$$

To apply this model of viscoelastic material properties into finite element simulations, the time domain Prony series is often used[26]. The response is assumed to be isotropic, and the Young's, shear and bulk moduli are time dependent according to

$$E(t) = E(0)\left[1-\sum_{i=1}^{M}\frac{E_i}{E(0)}\left(1-e^{-t/\tau_i}\right)\right], \tag{3-5}$$

$$G(t) = G(0)\left[1-\sum_{i=1}^{M}g_i\left(1-e^{-t/\tau_i}\right)\right], \tag{3-6}$$

$$K(t) = K(0)\left[1-\sum_{i=1}^{M}k_i\left(1-e^{-t/\tau_i}\right)\right], \tag{3-7}$$

where $E(0)$, $G(0)$ and $K(0)$ are the instantaneous elastic moduli in the time domain, and g_i and k_i are moduli ratios for each Maxwell element.

4 Linear viscoelastic continuum damage theory

The viscoelastic model with damage used in this paper was first introduced by Simo[27]. Continuum damage mechanics is employed to develop a simple isotropic damage mechanism, which incorporates softening behaviour under deformation and leads to a progressive degradation in storage modulus in a monotonic test with increasing amplitude. The model is driven from the free energy over any range of deformation which is uncoupled into a volumetric and deviatoric response

$$\Psi(\varepsilon, q) = U^0(tr\varepsilon) + \Psi^0(e) - q:e + \Psi_l(q), \tag{3-8}$$

where $U^0(tr\varepsilon)$ and $\Psi^0(e)$ are the volumetric and deviatoric stored energies, whilst $q:e$ and $\Psi_I(q)$ are the deviatoric and volumetric energies dissipated from the system. In particular, $\Psi_I(q)$ represents the volumetric energy dissipation due to viscous effects, calculated by eliminating viscous deviatoric energy from total viscous energy dissipation.

Material failure during loading is complicated: the range of structural transformations or degradation might include de-bonding, chain breakage, spherule fracture, and lamellae slippage in both micro- and macro-morphologies. In the model, all damage is summarized as an isotropic damage dominated energy dissipation leading to degradation of potential energy. The general stored energy function $\Psi(\varepsilon, D)$ for a material undergoing an isotropic damage process during loading is described as

$$\Psi(\varepsilon, D) = (1-D)\Psi^0(\varepsilon), \tag{3-9}$$

where $(1-D)$ is the damage parameter and ε represents strain.

The continuum damage constitutive equation was developed to give a non-equilibrium viscous stress based on damage dissipation, expressed as

$$S = \bar{g}(\varepsilon_{Max})\frac{\partial\Psi^0(\varepsilon)}{\partial\varepsilon}, \quad \text{where } \varepsilon_{Max} = \underset{S\in(-\infty,t]}{Max}\sqrt{2\Psi^0(\varepsilon(s))}, \tag{3-10}$$

$$\bar{g}(\varepsilon) = \beta + (1-\beta)\left(\frac{1-e^{-\varepsilon/\alpha}}{\varepsilon/\alpha}\right), \tag{3-11}$$

where S is the stress tensor and $\varepsilon(s)$ is the strain tensor, $\bar{g}(\varepsilon)$ represents the integrated damage parameter, empirically formulated by fitting coefficients α ($\alpha \in [0,\infty)$) and β ($\beta \in [0, 1]$) [27]; ε is recognized as the magnitude of true strain in a continuous loading process.

The damage is only considered to affect the global stiffness, as a 'polymer-solid' composite morphology is assumed, rather than changing the viscous properties of the underlying 'polymer'. Hence, integrating viscoelastic behaviour through the Boltzmann superposition principle Eq. (3-4) and isotropic damage process Eq. (3-10) gives a damage

model which is proportional to instantaneous stored strain energy, with empirical softening behaviour emerging from a combination of linear viscoelasticity and material damage affecting the inherent local modulus. In a monotonic test with a constant strain rate, the response can be simplified as

$$\sigma(t) = \int_0^t E(t-s)\,\bar{g}(\varepsilon)\,\dot{\varepsilon}(s)\,ds\,. \tag{3-12}$$

5 Method and Results

The linear viscoelastic properties are first obtained from DMA experiments, which are integrated with quasistatic monotonic tests in compression to determine the phenomenological parameters for the damage model. The aim of this project is to investigate whether the use of linear viscoelastic continuum damage theory in conventional mechanical experiments allows correlation between quasi-static and high strain rate tests. This is done by testing a commercial carbon-black filled TPU elastomer (TPUs-Shore-A90, Bonaprene Products Ltd. UK). Further, the paper explores the prediction of the resultant stress response under tensile and cyclic loading situations.

6 Rheological Model from DMA

Experiments were performed on a DMA machine (TA Q800), in which a beam (sample dimension 60 × 10 × 5 mm) was tested in a dual-cantilever configuration under cyclic deformation. The machine outputs complex modulus (*E'* and *E''*), loss tangent (tan δ), stress, temperature and frequency, the first four of which are calculated from the amplitude and phase of the applied displacement and resultant force. Isothermal frequency sweeps were performed at 2 °C intervals between -48 °C and 80 °C, and frequencies 0.5, 2, 5 and 10 Hz. The displacement amplitude was 30 μm. From the output values of moduli against loading

frequency at each temperature, a master curve of frequency dependence was produced using time-temperature superposition.

Fig. 3-2 shows the dependence of moduli on the temperature at the four different frequencies. For each temperature, it is also possible to plot modulus as a function of frequency, and then to shift these horizontally to produce a master curve of modulus against frequency at a chosen reference temperature (Fig. 3-3).

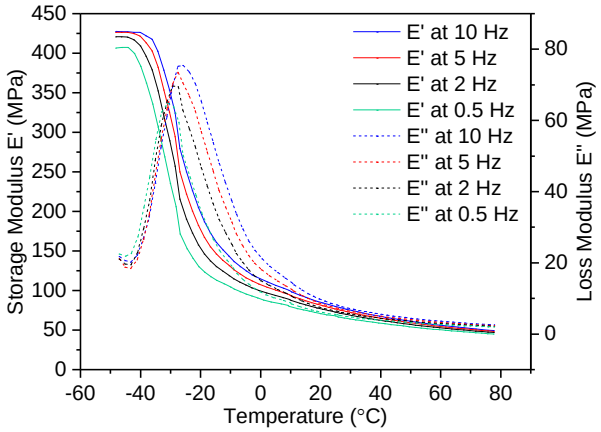


Fig. 3-2. Moduli *E'* and *E''* as a function of temperature: DMA data obtained from isothermal frequency sweeps at four frequencies: 0.5, 2, 5 and 10 Hz.

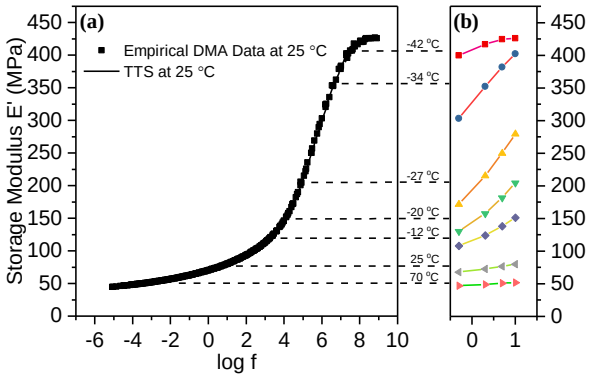


Fig. 3-3. TTS applied to *E'* – log *f* plots from DMA experiments: (a) master curve of *E'* – log *f* at 25 °C and (b) *E'* – log *f* plots at selected temperatures, as indicated in the figure above.

Fig. 3-4 depicts plots of shift factor *vs.* temperature at two reference temperatures. Two approximately tangential lines at high and low temperature can be fitted to the curves; these intersect at the same point on the temperature axis. This intersection point indicates that the

polyurethane has glass temperature, T_g, of about -27 °C. For interest, it is also shown that the WLF formula Eq. (3-1) fitted the empirical data around this point.

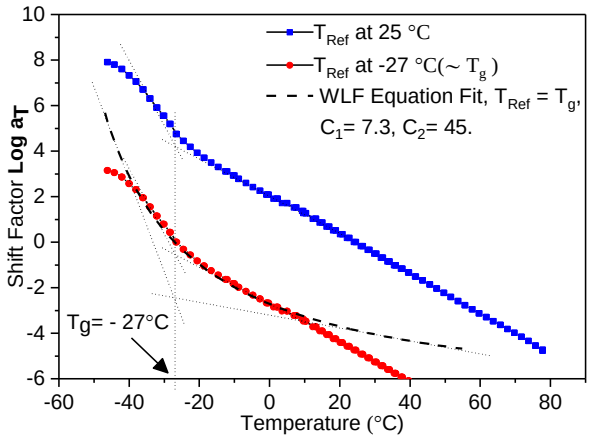


Fig. 3-4. Shift factor vs. temperature at reference temperatures of 25 °C and -27 °C; WLF equation evaluated at T_g = -27 °C with parameters C_1 =7.3 °C, C_2 =45 °C.

The plot of moduli against frequency obtained from TTS can further be described by the Generalized Maxwell Model

$$E'(\omega) = E_0 + \sum_{i=1}^{M} E_i \frac{\tau_i^2 \omega^2}{1+\tau_i^2 \omega^2}, \tag{3-13}$$

$$E''(\omega) = \sum_{i=1}^{M} E_i \frac{\tau_i \omega}{1+\tau_i^2 \omega^2}, \tag{3-14}$$

$$\tan\delta = \frac{E''}{E'}, \tag{3-15}$$

where ω is the angular frequency of the applied deformation, and E_0, E_i and τ_i are the properties of elements from the Generalized Maxwell Model. The storage and loss moduli are defined as the real and imaginary parts of the complex modulus during the dynamic harmonic cyclic loading. The phase shift factor tan δ is the ratio of loss modulus to storage modulus and represents the phase lag between strain and stress responses.

Figures 3-5 and 3-6 show the superposition results for storage, *E'*, and loss, *E''*, moduli, obtained from TTS at a reference temperature 25 °C. The next step is to use the Alfrey Approximation, a method to switch between relaxation measurements and retardation time spectra to parameterise the Prony series for the Generalized Maxwell Model[28]. Further

calculation of Prony series is given in Supplementary Information. It was noted that a single set of Prony series parameters could not fit both the storage and loss moduli accurately, this is likely to be a result of experimental error in the loss values, which are an order of magnitude smaller than the storage. However, it will be seen later that fitting the series to the storage modulus produced a model which agreed well with later compression experiments. The Prony series was then implemented in the model calibration of quasi-static experiments in Eq. (3-12).

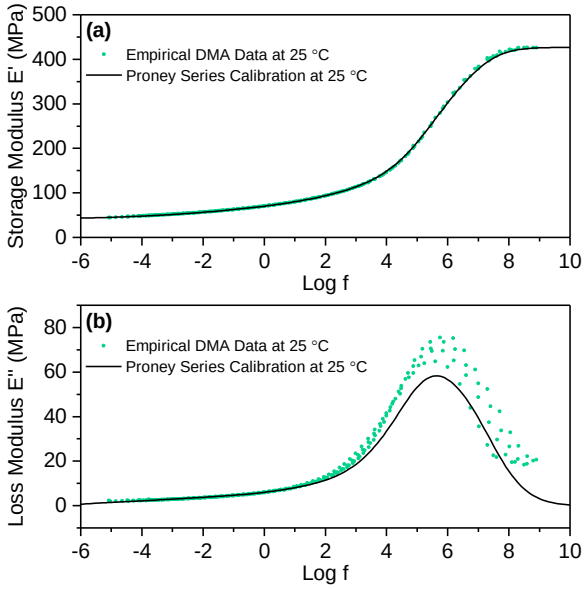


Fig. 3-5. (a) Storage modulus *E'* , (b) Loss modulus *E''* vs. log *f* showing Prony series fit.

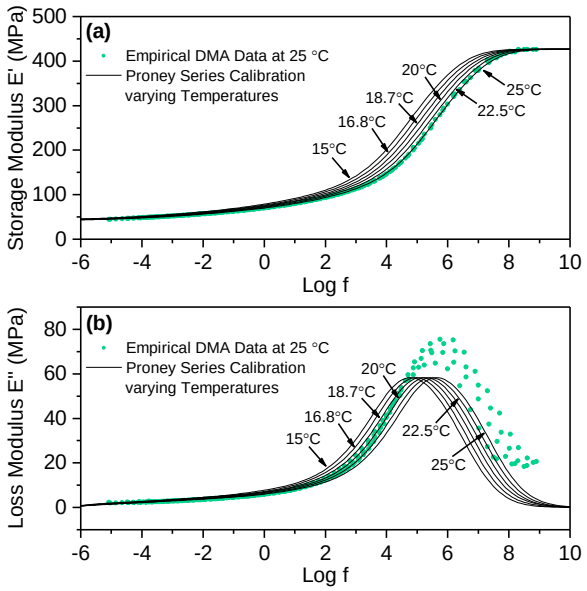


Fig. 3-6. (a) Storage modulus *E'*, (b) Loss modulus *E''* *vs.* log *f* showing Prony series fit for various reference temperatures.

The Prony series was then implemented into FE simulation software (Abaqus FEA) and analytical and FE models of the DMA experiment were performed to confirm the reliability of DMA results; a description of the analytical beam model and the FE material model validation are given in Supplementary Information. The models for the DMA used the same frequencies, specimen dimensions and deflection magnitude as the real experiment. The FE model was meshed using C3D8I elements, with 10 elements through the thickness of the specimen. An oscillating deflection was applied to the surfaces of the beam centre to model the central DMA clamp. The side clamps in the DMA were simulated by using fixed (ENCASTRE) boundary conditions. A picture of the model is shown in Fig. 3-7, whilst the force vs. time results are shown in Fig. 3-8, these show good agreement between the models and the DMA output data, confirming that the tests and derived material properties are consistent.

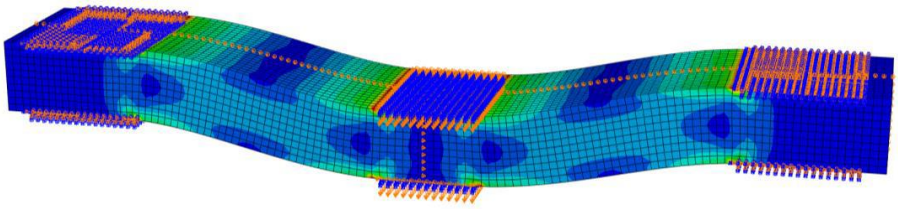


Fig. 3-7. Numerical model of DMA experiment using dual cantilever configuration.

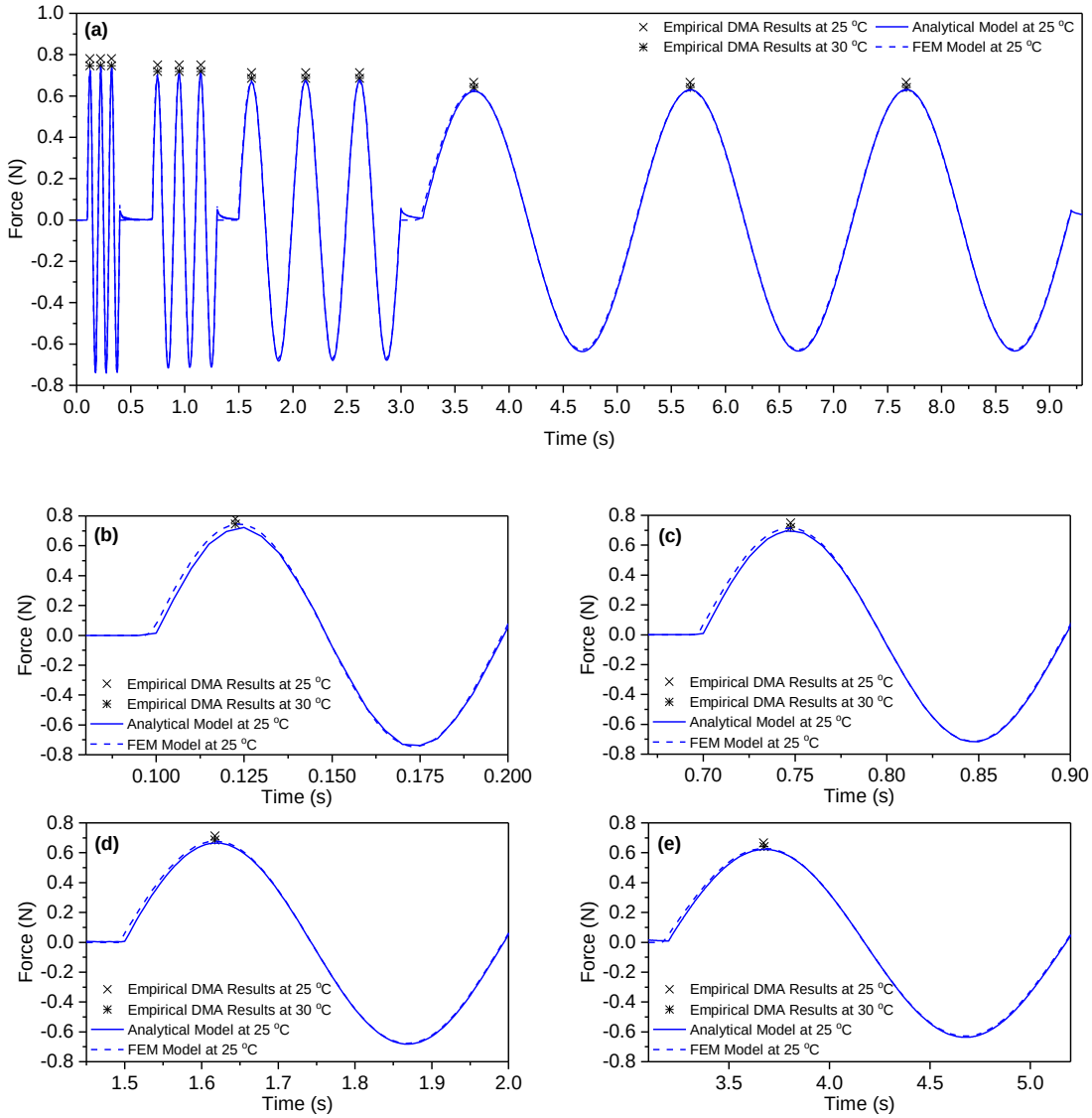


Fig. 3-8. Comparison of analytical and FE model outputs with DMA experiment: (a) Full range of frequencies; (b) 10 Hz; (c) 5 Hz; (d) 2 Hz; (e) 0.5 Hz.

7 Phenomenological damage model from quasi-static compression experiments

Quasi-static experiments were used to calibrate the damage model. Tests with monotonic and cyclic loading were executed in a commercial screw-driven testing machine (Instron 5982). For tensile tests, strips (dimension of 5 × 10 × 200 mm) were used, whilst in compression, cylinders (dimension of 5 mm diameter × 5 mm length) were tested (a full description of the experimental apparatus is given in Supplementary Information). The monotonic tension and compression experiments were performed in true-strain control at target strain rates of 0.1, 0.01 and 0.001 s^{-1}. The resulting force was recorded by a load cell, whilst strain was directly

measured: in tension a travelling extensometer was attached to the specimen; in compression a contacting extensometer was used attached to the loading anvils near to the specimen. The digital image correlation (DIC) technique was also applied to confirm the strains obtained from the extensometers. DIC is a standard technique to obtain full field deformation data by tracking the movement of a random pattern on the specimen surface. Here, a camera (PointGrey Ltd.) was used to capture images of the specimen during tests, and commercial DIC software (DaVis V8) was used to analyse the images. The frame rate was set as 5 fps and an image of an undeformed specimen was set as the reference. The pattern was applied using spray paint. The DIC analysis results showed that the constant true strain rates achieved were 0.08, 0.008, 0.0008 s^{-1} in tension; and 0.09, 0.009 and 0.0009 s^{-1} in compression. The maximum strains used were limited by slipping in the clamp in the tensile experiments.

In general linear viscoelastic continuum damage theory, the damage is mainly dependent on the strain magnitude, independent of the change in loading rate and loading direction[27,28]. Considering experimental evidence to support this modelling approach, Shen et al.[29] conducted *in-situ* SEM tensile experiments on particulate composites and observed that the decrease in effective modulus during deformation attributable to the increasing debonding and void damage. Decohesion and swelling behaviour upon straining were also observed *via* SEM-EDX techniques in carbon black filled EPDM[30]. Besides studies on strain-induced damage by SEM[29–33], other high-resolution microscopic techniques for visualising micro-mechanical and interfacial characterisations include high voltage electron microscopy (HVEM)[34], optical microscopy (OM)[31,35,36], transmission electron microscopy (TEM)[31,34–36], micro-computed tomography (CT)[37,38], strain-terminated atomic force microscopy (AFM)[39] and diffraction contrast tomography (DCT)[40–42] for grain map identification. Coupling in-situ scanning or microscope tests with DIC can allow quantitative investigation of the behaviour of elementary interfaces and interphases of composites, which can provide input into

representative FE models[43]. Deformation-induced softening has been studied by a number of researchers using different models, such as micro-sphere network[44], meso-cell model[45] or Mori-Tanaka micromechanics model[37]. In the paper presented here, a continuum damage process was proposed to govern the constitutive behaviour at large deformations. A comparison between 'inherent' and empirical local stiffness is used to introduce a damage factor $\bar{g}(\varepsilon)$ that represents the magnitude of phenomenological softening. The calibration of material softening was first executed by comparing stress-strain responses generated from DMA data using the Boltzmann superposition principle, to stress-strain data generated in the compression and tension experiments. Initially, compression data were used: Fig. 3-9(a) shows the empirical compression experiments compared to 'inherent' stress-strain curves obtained from the Boltzmann superposition integral. Fig. 3-9(b) compares the local stiffness from the experiments to those from the Boltzmann superposition integral. The damage factor, calibrated by optimising α and β in Eq. (3-11) and Fig. 3-9(c), is successfully fitting the ratio of stiffness in the empirical data. It should be noted that at each strain rate at least three experiments were performed, and the curves shown are chosen from the experiment closest to the mean of the data: the full set of data and model simulation outputs are shown in
Supplementary Information.

The damage model was compared to experiments at different strain rates (Fig. 3-10(a)) and temperatures (Fig. 3-10(b)) separately. These comparisons demonstrate that the model is able to reproduce very accurately the compressive responses with a single set of α and β parameters.

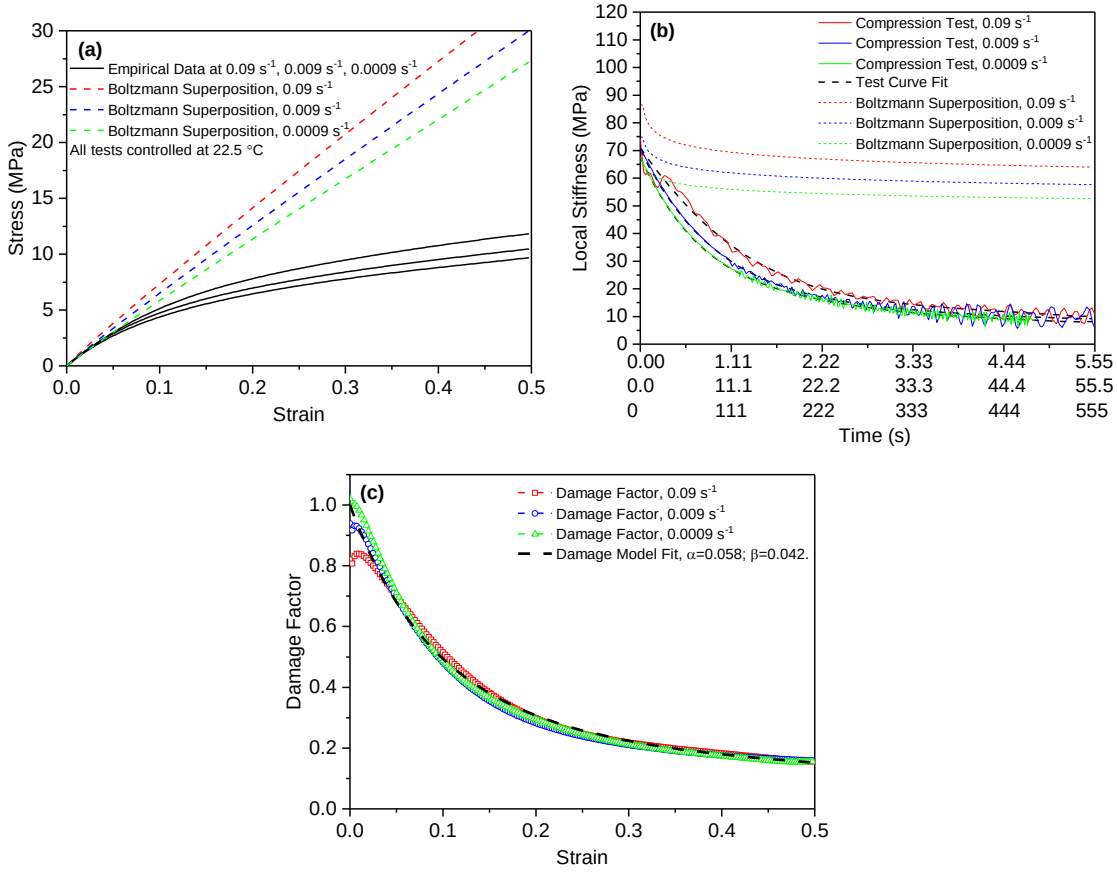


Fig. 3-9. The process to determine the phenomenological damage factor: (a) stress-strain curves from compression experiments and Boltzmann superposition principle at three strain rates, 22.5 °C; (b) comparison of local stiffnesses from experiments and Boltzmann superposition; (c) the parameters α =0.058, β =0.042 for the phenomenological damage factor (i.e. the ratio of the stiffnesses in (b)) were determined from the average of three strain rates: 0.09 s^{-1}, 0.009 s^{-1} and 0.0009 s^{-1} by fitting Eq. (3-11) to the empirical data. The damage model was calibrated at 22.5 °C.

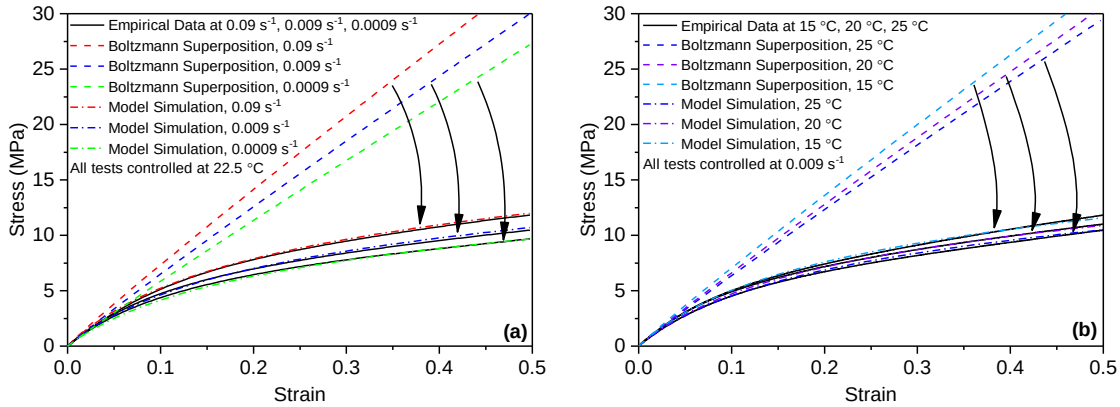


Fig. 3-10. Comparison of experimental data to model predictions when varying strain rates (a) or temperatures (b) in compression experiments. The damage parameters from Fig. 3-9 (α =0.058, β =0.042) were used. The rate and temperature effects were captured using appropriate TTS master curves (Fig. 3-6) and the Boltzmann superposition integral Eq. (3-12).

8 Application in quasi-static tensile cyclic tests

The ambient temperature for the tensile experiments was 16.8 °C, so the Boltzmann superposition integral was recalculated at this temperature for three rates: 0.08, 0.008 and 0.0008 s^{-1}. Cyclic tensile tests with a single loop were executed first: at least three experiments were conducted at each rate, with virgin samples used each time (i.e. nine fresh samples were tested in total). The full set of data is presented in Supplementary Information. Fig. 3-11(a) shows the resulting local stiffnesses from the Boltzmann superposition integrals and one experiment at each rate. These are compared to calculate the damage factors in Fig. 3-11(b).

Here it is noted that the experimentally calculated damage factor exceeds 1. This is probably the result of experimental errors at small strains, in particular measurements of the strains themselves, the calculated damage factor $\bar{g}(\varepsilon)$ cannot exceed 1. It is also noted here that the factors jump on the switch from loading to unloading. Whilst some of the jump in stiffness is accounted for in the viscoelastic response (from the Boltzmann superposition integral) this does not give a full description of the overall material response. As a result, the implementation of the viscoelastic continuum damage was changed so that the damage parameters, α and β, are defined as strain-dependent only but also that the 'strain' is reset at the start of the each cycle, i.e. each time the direction of loading is reversed. The output from this model is then shown in Fig. 3-11(c).

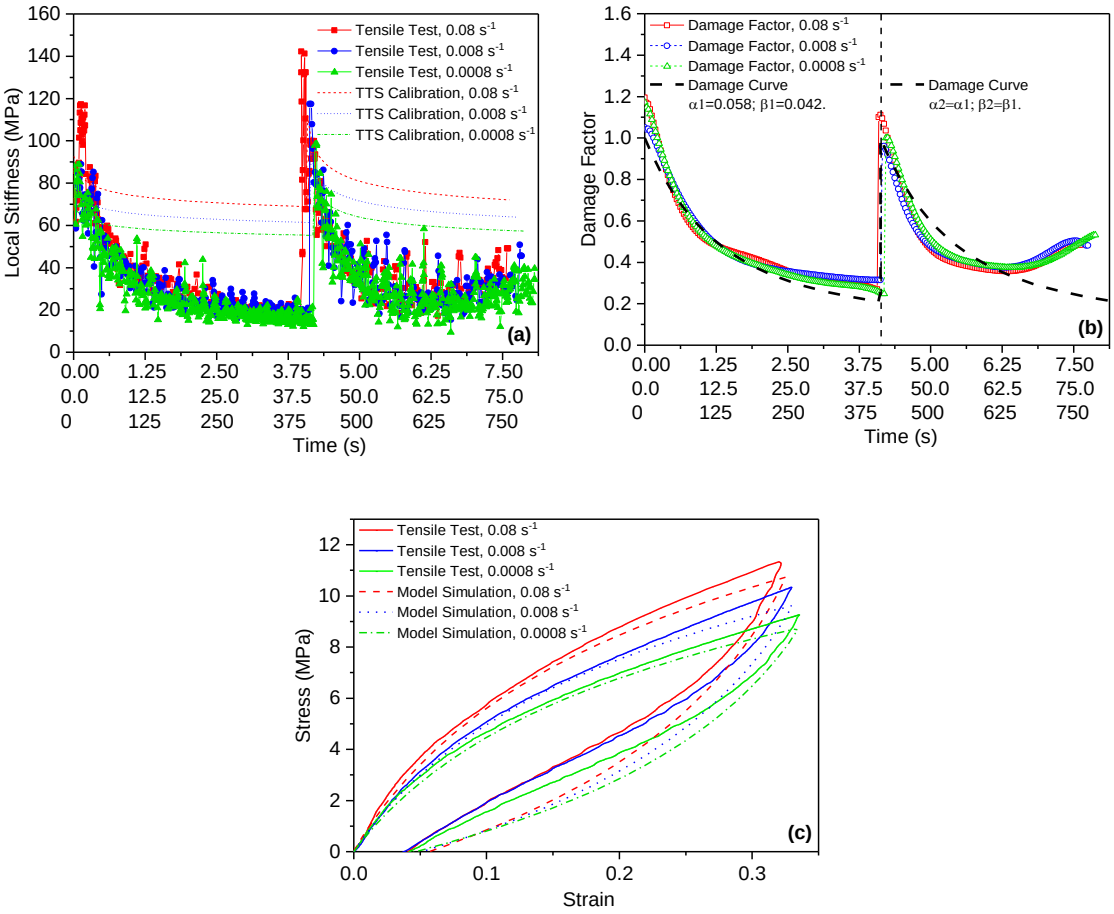


Fig. 3-11. Data obtained in cyclic tensile experiments with constant temperature of 16.8 °C but varying strain rates of 0.08 s^{-1}, 0.008 s^{-1} and 0.0008 s^{-1}. The local stiffnesses from the Boltzmann superposition integral and experiments are plotted, (a), to compare the damage parameters α = 0.058, β = 0.042 from compression in Fig. 3-9(c) to the empirical ratio from tensile experiments, (b). The same parameters are adopted with strain reset at the start of the unloading process, to produce the simulation, (c), at 16.8 °C.

An additional study was performed in which repeated cyclic tests were executed at 0.008 s^{-1} strain rate. Here a single sample was subjected to a large number of cycles in order to assess the damage accumulation. The results (stress-strain curve and damage factor only) are shown in Fig. 3-12, where they are compared to the model used up to this point. A possible improvement to the model is to redefine the parameters during loading. Fig. 3-12 shows that the damage parameters through the entire cyclic loading can be classified into two groups: one for the initial loading process and a second one for the remaining cases. By controlling the second set of parameters, the model was much better able to describe the experiment, consistent

with the so-called 'Mullins effect' and the softening observed during the cyclic loading. In particular, the Mullins effect is the name given to a loss of stiffness that can be correlated to the maximum stress achieved in recent prior loadings, but which recovers over time. This is often observed, in particular, in filled materials. Various physical interpretations have been given[24], including cavities, chain session and disentanglement contributing to damage within the rubber matrix[46–48].

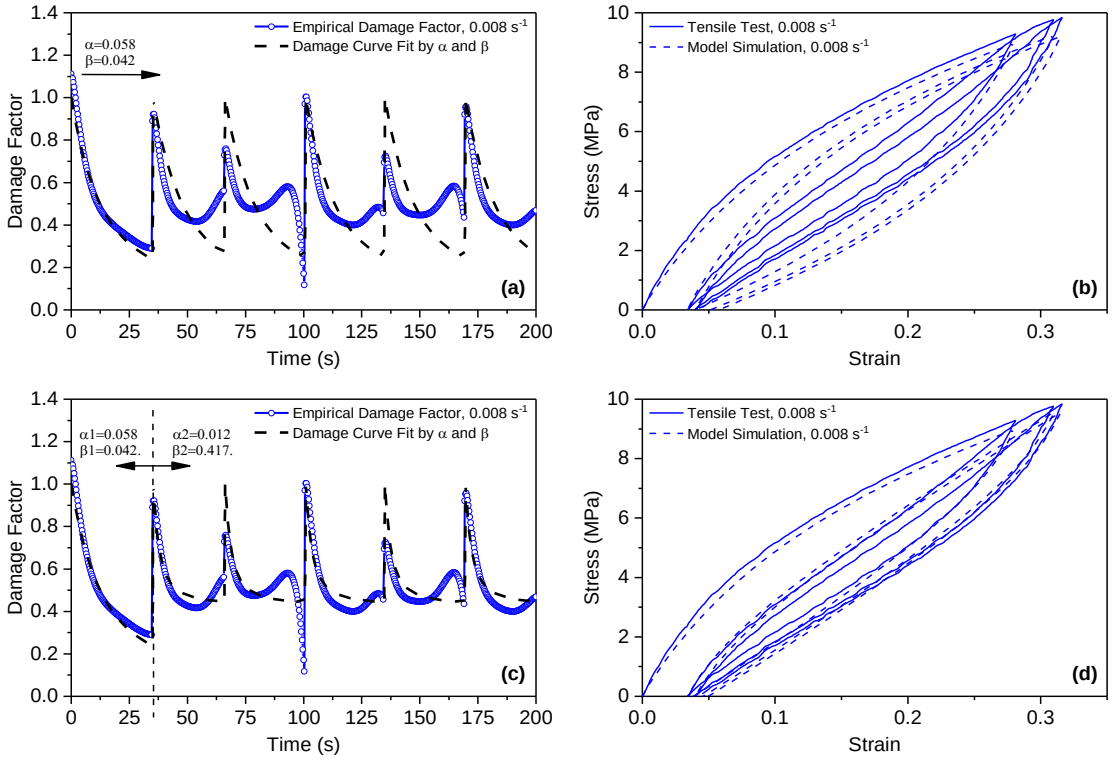


Fig. 3-12. A multi-cyclic tensile experiment was executed at 16.8 °C and 0.008 s^{-1} strain rate. The existing parameters of α =0.058, β =0.042, (a), were used for the entire model, (b); while the switchable parameters: α_1 =0.058, β_1 =0.042 for the primary loading, and α_2 =0.012, β_2 =0.417 for the remaining, (c), exhibits better results, (d).

9 Application to split-Hopkinson bar experiment

The split Hopkinson bar technique is well developed and is now almost a standard method to study the high rate compression of materials[8,49]. In the experiments implemented here, a cylindrical specimen (of 5 × 5 mm) was placed between the ends of two magnesium alloy bars, Fig. 3-13. A smaller 'striker' bar is accelerated towards the incident bar by mean of pressurised gas. This creates a stress wave which travels down to the specimen, the incident wave. At the

bar-specimen interface, a portion of the input wave is reflected and the rest transmitted. The incident, reflected and transmitted waves are measured by strain gauges attached to the bars. These stresses can be used to calculate the deformation rate and force in the specimen, which can be converted to stress and strain.

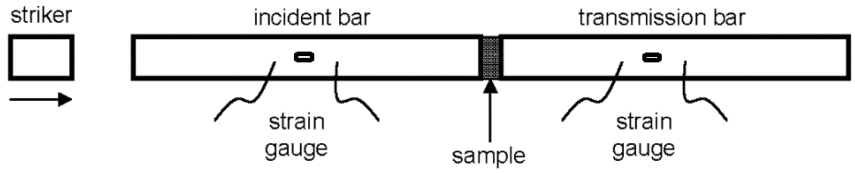


Fig. 3-13. Experimental configuration for SHPB test.

Specifically, the strain rate in the specimen is given by

$$\frac{d\varepsilon}{dt} = \frac{c}{l_s(t)}\left[\varepsilon_i(t) - \varepsilon_r(t) - \varepsilon_t(t)\right], \tag{3-16}$$

where $\varepsilon_i(t)$, $\varepsilon_r(t)$ and $\varepsilon_t(t)$ are the measured strain pulses, $l_s(t)$ is the specimen length and $c = \sqrt{E/\rho}$ is the longitudinal wave-speed in the bar. The stress is given by

$$\sigma(t) = \frac{A_b}{A_s} E\varepsilon_t(t), \tag{3-17}$$

where A_b / A_s is the ratio of cross-sectional area of the transmission bar and the specimen. The key assumption of this analysis is that the specimen is in static equilibrium (i.e. the stress is the same along its length), which in practice means that

$$\varepsilon_i = -\varepsilon_r + \varepsilon_t. \tag{3-18}$$

In order to achieve this, higher strain rates require progressively thinner samples, and indeed this may be difficult or impossible to achieve in specimens manufactured from low wave-speed materials, and must be checked experimentally.

Here, the compression SHPB experiments up to 2000 s^{-1} were executed. The linear viscoelastic continuum damage model was used to predict high strain rate compression data, again using the master curve obtained from DMA experiments. Fig. 3-14 shows comparison of the model and experimental data at 18.7 °C.

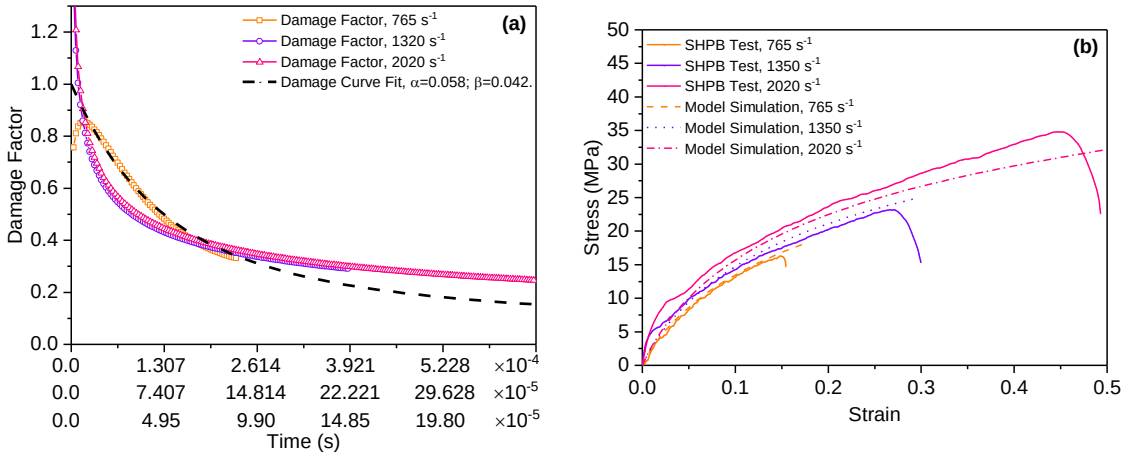


Fig. 3-14. High strain rate compression experiments were executed at 18.7 °C at three strain rates: 765 s^{-1}, 1350 s^{-1} and 2020 s^{-1}. The existing parameters of α =0.058, β =0.042, (a), were used again for the model simulation (b).

Two additional factors must be taken into account when interpreting data from Hopkinson bar experiments. The first is the effect of specimen inertia, owing to the rapid acceleration of the specimen during the experiments. This adds to the stress measured in the system. The specimen is initially at rest, and is accelerated to the peak strain rate 2020 s^{-1}. During this acceleration, inertia-induced stress is encountered in both axial and transverse directions, which add to the inherent material response[50]. The specimen stress measured during a Hopkinson bar experiment may therefore be through of as the sum of stress components[50]:

$$\sigma_T = \sigma_M + \sigma_I + \sigma_F + \sigma_{other}\,, \tag{3-19}$$

where σ_T is the stress measurement, σ_M is the material strength to be measured, σ_I is an enhancement owing to inertia, σ_F is an enhancement owing to friction and σother is the enhancement owing other effects that may be present.

The additional inertia stress can be calculated for an incompressible material as[51]

$$\sigma_I = \rho\ddot{\varepsilon}\left(\frac{a^2}{8}-\frac{h^2}{6}\right)+\rho\dot{\varepsilon}\left(\frac{a^2}{16}+\frac{h^2}{6}\right)-\frac{\rho h\dot{v}}{2}\,, \tag{3-20}$$

where ρ is the material density, $\dot{\varepsilon}$ and $\ddot{\varepsilon}$ are strain rate and strain acceleration, $a \approx 2.5$ mm is the radius, and $h \approx 5$ mm is the height for this specimen, and v represents the speed of the output bar. The magnitude of this inertia stress is only 1700 Pa at a strain rate of 2020 s^{-1}, so that the inertia effect is not significant in these experiments.

The second potential effect is the temperature rise owing to the conversion of mechanical work to heat. The high strain rate experiment is assumed to take place adiabatic conditions. This means that any heat generated during the loading will be retained in the specimen, causing an increase in temperature in Equations (3-21) and (3-22), which can be approximately assuming that all the mechanical work done is converted to heat by[52].

$$\Delta Q \approx \Delta W \rightarrow \int_0^{\varepsilon} \sigma d\varepsilon = \rho C_p \Delta T \,, \tag{3-21}$$

$$\Delta T(\varepsilon) = \frac{\beta}{\rho C_p} \int_0^{\varepsilon} \sigma d\varepsilon \,, \tag{3-22}$$

where W is the work done, Q is the heat generated, σ the true stress, ε the true strain, ρ = 1000 kg m^{-3} the material density, C_p = 1800 J kg^{-1} K^{-1} the specific heat capacity at constant volume and ΔT the rise in temperature. Here, material properties have been obtained from the supplier, Bonaprene Products Ltd., UK.

Using the assumption that all the work is converted to heat, which is a significant overestimate for these materials in which we have shown that quasi-static loading is recoverable, this equation gives a temperature rise of only 0.34 °C at 2020 s^{-1}, which can be ignored.

10 Discussion and Conclusions

A viscoelastic constitutive model with effects of continuum damage has been shown to provide an accurate characterisation of the mechanical behaviour of thermoplastic polyurethane under uniaxial loading from low to high strain rates. A specific viscoelastic damage model for the mechanical behaviour was used and, and when the phenomenological damage criteria were obtained from quasi-static compression experiments, this model was able to predict behaviour in compression at different (quasi-static) rates and temperatures, (quasi-static) tension and high rate compression.

The material used, a commercial thermoplastic polyurethane, showed a strong dependence on both temperature and frequency, which was calibrated using DMA experiments.

The TTS principle was used to produce a master curve from which a Prony series was calibrated to describe the viscoelastic material behaviour. Good results were obtained by using the linear viscoelasticity model thus obtained in numerical and finite element models of the DMA experiments over the full range of frequencies. The observed material softening resulted from material damage was then investigated. The damage was observed to depend on strain magnitude and was characterised by a two-parameter model. By combining this with the Boltzmann superposition integral (for rate and temperature effects), both temperature and rate dependences of the stress-strain response could be simulated. Having calibrated the model using compression data, there is a small difference between this and the tensile results, which may be due to experimental effects, including specimen variability, load application (e.g. frictional boundary in compression) and uneven stress distributions in the deforming specimen. In addition, whilst the model shows good agreement with the cyclic loading data, it was observed that two sets of damage factors improve the fit; this is consistent with damage introduced in the first cycle affecting subsequent results, i.e. with the Mullins effect, although the response under cycles with increased amplitude was not measured in this study. The cyclic loading process was modelled through a combination of the Boltzmann superposition integral combined with the strain-dependent damage factor; when calculating the strain-dependent damage, the strain itself was 'reset' at each reversal of direction. Figures 3-11 & 3-12 for cyclic experiments revealed that the switch of factor parameters on reversal of the direction of loading is effective in simulating the observed response, which indicates loading direction probably does not change the damage criteria in a continuous cyclic process. Finally, the model was shown to predict experimental data in high strain rate experiments. This is significant, as it gives further validation for the use of time-temperature superposition based approaches to predict high rate response. Such indirect methods are increasingly important as we seek to obtain high strain rate data from materials with very low stiffness and sound speeds. Further

work is necessary to fully account for the small differences in damage model between compression and tension, and to explore cyclic loading with different amplitudes. Better understanding and characterisation of filler structure will allow better investigation of the local stiffness degradation and hysteresis behaviours, whilst further validation of the implementation at different strain rates would also give further confidence in this approach.

11 Acknowledgements

This material is based upon work supported by the Air Force Office of Scientific Research, Air Force Material Command, USAF under Award No. FA9550-15-1-0448. We thank Maj M Snyder and Dr. J Foley for their continued support. We also thank Nick Hawkins from the University of Oxford who provided insight and expertise that greatly assisted the polymer research, and Igor Dyson, Richard Duffin and Wolfgang Mix for help with the experimental programme and specimen preparation.

12 Funding

This material is based upon work supported by the Air Force Office of Scientific Research, Air Force Material Command, USAF under Award No. FA9550-15-1-0448.

13 Conflict of interests

The authors declare that they have no conflict of interest.

14 References

1. Prisacariu C. *Polyurethane Elastomers: From Morphology to Mechanical Aspects*. Springer Science & Business Media; 2011.
2. Buckley CP, Prisacariu C, Martin C. Elasticity and inelasticity of thermoplastic polyurethane elastomers: Sensitivity to chemical and physical structure. *Polymer (Guildf)*. 2010;51(14):3213-3224.
3. Kojio K, Furukawa M, Nonaka Y, Nakamura S. Control of mechanical properties of thermoplastic polyurethane elastomers by restriction of crystallization of soft segment. *Materials (Basel)*. 2010;3(12):5097-5110.
4. Jiang L, Wu J, Nedolisa C, Saiani A, Assender HE. Phase Separation and Crystallization in High Hard Block Content Polyurethane Thin Films. *Macromolecules*. 2015;48(15):5358-5366. doi:10.1021/acs.macromol.5b01083

5. Ferry JD. *Viscoelastic Properties of Polymers*. John Wiley & Sons; 1980.
6. Williams ML, Landel RF, Ferry JD. The temperature dependence of relaxation mechanisms in amorphous polymers and other glass-forming liquids. *J Am Chem Soc*. 1955;77(14):3701-3707.
7. Roland CM. Mechanical behavior of rubber at high strain rates. *Rubber Chem Technol*. 2006;79(3):429-459.
8. Field JE, Walley SM, Proud WG, Goldrein HT, Siviour CR. *Review of Experimental Techniques for High Rate Deformation and Shock Studies*. Vol 30.; 2004. doi:10.1016/j.ijimpeng.2004.03.005
9. Siviour CR. High strain rate characterization of polymers. *AIP Conf Proc*. 2017;1793. doi:10.1063/1.4971585
10. Sarva SS, Deschanel S, Boyce MC, Chen W. Stress-strain behavior of a polyurea and a polyurethane from low to high strain rates. *Polymer (Guildf)*. 2007;48(8):2208-2213. doi:10.1016/j.polymer.2007.02.058
11. Gorham DA, Pope PH, Field JE. An improved method for compressive stress-strain measurements at very high strain rates. *Proc R Soc London Ser A Math Phys Sci*. 1992;438(1902):153-170.
12. Chen W, Zhang B, Forrestal MJ. A split Hopkinson bar technique for low-impedance materials. *Exp Mech*. 1999;39(2):81-85.
13. Dioh NN, Leevers PS, Williams JG. Thickness effects in split Hopkinson pressure bar tests. *Polymer (Guildf)*. 1993;34(20):4230-4234.
14. Chen WW, Song B. *Split Hopkinson (Kolsky) Bar: Design, Testing and Applications*. Springer Science & Business Media; 2010.
15. Siviour CR, Jordan JL. High strain rate mechanics of polymers: a review. *J Dyn Behav Mater*. 2016;2(1):15-32.
16. Fan JT, Weerheijm J, Sluys LJ. High-strain-rate tensile mechanical response of a polyurethane elastomeric material. *Polym (United Kingdom)*. 2015;65:72-80. doi:10.1016/j.polymer.2015.03.046
17. Zhao B, Tian N, Liu Y, et al. Strain-induced crystallization of natural rubber with high strain rates. *J Polym Sci Part B Polym Phys*. 2012;50(23):1630-1637. doi:10.1002/polb.23172
18. Chen W, Lu F, Frew DJ, Forrestal MJ. Dynamic Compression Testing of Soft Materials. *J Appl Mech*. 2002;69(3):214. doi:10.1115/1.1464871
19. Song B, Chen W. Dynamic stress equilibration in split Hopkinson pressure bar tests on soft materials. *Exp Mech*. 2004;44(3):300-312. doi:10.1177/0014485104041543
20. Chen W, Lu F, Zhou B. A quartz-crystal-embedded split Hopkinson pressure bar for soft materials. *Exp Mech*. 2000;40(1):1-6.
21. Kendall MJ, Siviour CR. Experimentally simulating adiabatic conditions: Approximating high rate polymer behavior using low rate experiments with temperature profiles. *Polym (United Kingdom)*. 2013;54(18):5058-5063. doi:10.1016/j.polymer.2013.06.049
22. Chen WW. Experimental methods for characterizing dynamic response of soft materials. *J Dyn Behav Mater*. 2016;2(1):2-14.
23. Yoon S-H, Siviour CR. Application of the virtual fields method to rubbers under medium strain rate deformation using both acceleration and traction force data. *J Dyn Behav Mater*. 2017;3(1):12-22.
24. Diani J, Fayolle B, Gilormini P. A review on the Mullins effect. *Eur Polym J*. 2009;45(3):601-612. doi:10.1016/j.eurpolymj.2008.11.017
25. Park SW, Kim YR, Schapery RA. A viscoelastic continuum damage model and its application to uniaxial behavior of asphalt concrete. *Mech Mater*. 1996;24(4):241-255.

doi:10.1016/S0167-6636(96)00042-7
26. Keenan KE, Pal S, Lindsey DP, Besier TF, Beaupre GS. A viscoelastic constitutive model can accurately represent entire creep indentation tests of human patella cartilage. *J Appl Biomech*. 2013;29(3):292-302. doi:10.1016/j.biotechadv.2011.08.021.Secreted
27. Simo JC. On a fully three-dimensional finite-strain viscoelastic damage model: formulation and computational aspects. *Comput Methods Appl Mech Eng*. 1987;60(2):153-173.
28. Ward IM, Hadley DW. *An Introduction to the Mechanical Properties of Solid Polymers*.; 1993.
29. Shen W, Tang CY, Tsui CP, Peng LH. Effects of two damage mechanisms on effective elastic properties of particulate composites. *Compos Sci Technol*. 2002;62(10-11):1397-1406.
30. Candau N, Oguz O, Peuvrel-Disdier E, Bouvard J-L, Pradille C, Billon N. Strain-induced network chains damage in carbon black filled EPDM. *Polymer (Guildf)*. 2019;175:329-338.
31. Lee J, Yee AF. Inorganic particle toughening I: micro-mechanical deformations in the fracture of glass bead filled epoxies. *Polymer (Guildf)*. 2001;42(2):577-588.
32. Tsui CP, Tang CY, Lee TC. Tensile properties and damage behaviors of glass-bead-filled modified polyphenylene oxide under large strain. *Polym Compos*. 2001;22(6):742-751.
33. Cantournet S, Layouni K, Laiarinandrasana L, Piques R. Experimental investigation and modelling of compressibility induced by damage in carbon black-reinforced natural rubber. *Comptes Rendus Mécanique*. 2014;342(5):299-310.
34. Adhikari R, Michler GH, Godehardt R, Ivan'kova EM. Deformation behaviour of styrene/butadiene star block copolymer/hPS blends: influence of morphology. *Polymer (Guildf)*. 2003;44(26):8041-8051.
35. Su J-F, Zhao Y-H, Wang X-Y, Dong H, Wang S-B. Effect of interface debonding on the thermal conductivity of microencapsulated-paraffin filled epoxy matrix composites. *Compos Part A Appl Sci Manuf*. 2012;43(3):325-332.
36. Weon J-I, Gam K-T, Boo W-J, Sue H-J, Chan C-M. Impact-toughening mechanisms of calcium carbonate-reinforced polypropylene nanocomposite. *J Appl Polym Sci*. 2006;99(6):3070-3076.
37. Lim HJ, Choi H, Zhu F-Y, Kerekes TW, Yun GJ. Multiscale damage plasticity modeling and inverse characterization for particulate composites. *Mech Mater*. 2020;149:103564.
38. Liu R, Sancaktar E. Identification of crack progression in filled rubber by micro X-ray CT-scan. *Int J Fatigue*. 2018;111:144-150.
39. Chen Q, Chasiotis I, Chen C, Roy A. Nanoscale and effective mechanical behavior and fracture of silica nanocomposites. *Compos Sci Technol*. 2008;68(15-16):3137-3144.
40. Withers PJ, Preuss M. Fatigue and damage in structural materials studied by X-ray tomography. *Annu Rev Mater Res*. 2012;42:81-103.
41. Wright P, Fu X, Sinclair I, Spearing SM. Ultra high resolution computed tomography of damage in notched carbon fiber—epoxy composites. *J Compos Mater*. 2008;42(19):1993-2002.
42. Maire E, Withers PJ. Quantitative X-ray tomography. *Int Mater Rev*. 2014;59(1):1-43.
43. Pardoen T, Klavzer N, Gayot S, et al. Nanomechanics serving polymer-based composite research. *Comptes Rendus Phys*. 2021;22(S3):1-22.
44. Göktepe S, Miehe C. A micro--macro approach to rubber-like materials. Part III: The micro-sphere model of anisotropic Mullins-type damage. *J Mech Phys Solids*.

2005;53(10):2259-2283.
45. Tsui CP, Tang CY, Fan JP, Xie XL. Prediction for initiation of debonding damage and tensile stress--strain relation of glass-bead-filled modified polyphenylene oxide. *Int J Mech Sci*. 2004;46(11):1659-1674.
46. De Crevoisier J, Besnard G, Merckel Y, et al. Volume changes in a filled elastomer studied via digital image correlation. *Polym Test*. 2012;31(5):663-670.
47. Kraus G, Childers CW, Gruver JT. Properties of random and block copolymers of butadiene and styrene. I. Dynamic properties and glassy transition temperatures. *J Appl Polym Sci*. 1967;11(8):1581-1591.
48. Diaz R, Diani J, Gilormini P. Physical interpretation of the Mullins softening in a carbon-black filled SBR. *Polymer (Guildf)*. 2014;55(19):4942-4947.
49. Gray III GT, Blumenthal WR. Split-Hopkinson pressure bar testing of soft materials. *ASM Handb*. 2000;8:488-496.
50. Siviour CR, Walley SM. Inertial and frictional effects in dynamic compression testing. In: *The Kolsky-Hopkinson Bar Machine*. Springer; 2018:205-247.
51. Gorham DA. Specimen inertia in high strain-rate compression. *J Phys D Appl Phys*. 1989;22(12):1888.
52. Kapoor R, Nemat-Nasser S. Determination of temperature rise during high strain rate deformation. *Mech Mater*. 1998;27(1):1-12.

CHAPTER 4 SUPRAMOLECULAR SELF-HEALABLE TPU

4.1 Introduction

In this chapter the study continues to investigate the material properties from a family of thermoplastic polyurethane, characterise thermo-mechanical properties from experiments, and further explore the constitutive modelling work which can be used employed in both low- and high-rate scenarios. A synthetic, soft, self-healable polyurethane has been targeted, and investigated from three aspects: molecular level, thermos-mechanical dynamics, and rate-dependent behaviour. The effects of thermal history on thermo-reversible properties were characterised using spectroscopy techniques including NMR, GPC, SAXS on molecularity and morphology at a molecular level. Following that, rheometry was employed to understand the variations of rheological behaviour for this polyurethane at different manufacturing thermal history. DMA with tensile configuration was used as supplementary tests to fulfil the low-temperature data, which can be associated with rheometry results at high temperature, from -60°C to 80°C. This wide temperature range allowed linear viscoelasticity to be employed within the principle of time-temperature superposition: a broader frequency regime conformed after proper shifting. and then delivered a modelling perspective of linear viscoelasticity. A form of generalized Maxwell model was implemented, contained user-defined element that was assigned by calibrating experimental behaviour of polymer from low- to moderate-strain rates. Higher strain rates up to 2000 s^{-1} validated this entire model framework with a good compliance to the mechanical properties in rate dependence. By determining the appropriate value of elements in the model, this phenomenological viscoelastic model exhibited a good prediction for self-healable polyurethane undergoing strain-recovery from large deformation at 25 °C, eventually contributed this work to both experimental characterisation and modelling development in the application of viscoelastic theory.

4.2 Paper B:

Mechanical characterisation and modelling of a thermoreversible supramolecular polyurethane over a wide range of rates[1]

Abstract

Understanding the mechanical response of thermo-recoverable elastomers to applied deformation at different strain rates and temperatures is crucial for more effective exploitation of these reusable materials in industrial applications. The research presented in this paper aims to understand the thermal and mechanical responses of a healable, elastomeric supramolecular polyurethane, examining morphology, rheology and mechanical responses from low to high strain rates. The polymer structure for specimens experiencing different thermal histories was characterised using NMR spectroscopy, GPC and SAXS. DSC and rheometry were used to investigate thermomechanical performance during heating and cooling cycles, whilst large strain compression characterisation was performed on a commercial screw-driven test frame, a hydraulic loading system and a split-Hopkinson pressure bar. To describe the mechanical response of the polymer, a viscoelastic softening model was developed and characterised. The model incorporates rheometry and dynamic mechanical analysis (DMA) using the principle of time-temperature superposition (TTS) in a Prony series, combined with a non-linear large strain response, and recovery. The model was able to describe low strain rate behavior under monotonic and cyclic loading, as well as predicting the response to monotonic loading at medium-to-high strain rates from 40 to 1220 s^{-1}. The paper therefore demonstrates the effectiveness of using the viscoelastic theory and its analytical model to calibrate and further predict the mechanical behaviour of polymers at different strain rates: this is particularly useful

[1] Chen H, Hart LR, Hayes W, Siviour CR. Mechanical characterisation and modelling of a thermoreversible superamolecular polyurethane over a wide range of rates. Polymer (Guildf). 2021:123607. https://doi.org/10.1016/j.polymer.2021.123607

for low modulus materials for which high strain rate characterisation is challenging.

Keywords: Viscoelasticity, Polyurethane, DMA, Morphology, High strain-rate

1 Introduction

The development of healable polymers that are capable of repairing damage either on the surface or within the bulk material is an extremely attractive proposition in many industrial applications, with potential to significantly reduce whole life costs and environmental impact[1]. Whilst a number of methodologies to achieve healable materials are known[2], supramolecular materials offer an attractive solution owing to their inherent ability to undergo multiple break/heal cycles without significant loss of performance[3,4]. Recent research has led to the development of specifically designed healable supramolecular polyurethanes (SPU)[5–10] which exhibit thermally-controlled mechanics and recoverable mechanical properties resulting from the use of dynamic and reversible non-covalent interactions such as hydrogen bonds and π-π stacking interactions in the polymer network[1,7,8,11–15]. In previous research, the synthesis of a polyurethane with excellent healing ability at around body temperature has been reported[8], where, following damage, the material's mechanical properties could be recovered efficiently by re-assembly of the supramolecular network. Specifically, the polymer possesses complementary hydrogen bonding motifs which are able to self-assemble, in addition to secondary self-assembly though π-π stacking of the aryl units within the diisocyanate[16,17]. Furthermore, micro phase separation is observed between the apolar polymer backbone and the polar recognition motifs. It has been demonstrated that purification of the SPU is not necessary as the low molecular weight bis-urea by product is able to reinforce the polymer network and impart desirable mechanical properties[18–20]. The nature of these non-covalent interactions permits the material, in common with other supramolecular polyurethanes[21–23], to

be addressable as a result of its inherent thermo-responsive character of the supramolecular interactions, thereby delivering dramatic viscosity changes over well-defined and tuneable temperature ranges, as well as leading to the capability to recover a significant degree of their mechanical strength after damage. As a result of the non-covalent interactions within the network being relatively weak, the recognition motifs within the polymer can assemble or dissociate relatively easily as a consequence of the low thermal activation energy, making it, in common with other supramolecular polyurethanes and polyureas, easy to process at relatively low temperatures[24–26].

In previous research, the material properties of the supramolecular polyurethane have been characterised using dynamic mechanical analysis (DMA) and tensile tests, which revealed a mechanical response that is very sensitive to temperature [8]. However, further understanding of the large-strain mechanical properties is needed for application of the material. In order to use these materials in engineering applications such as polymer-bonded composites[27], it is necessary to characterise and model their mechanical response in different loading regimes, including high strain rate, large strain deformation. However, it can be very challenging to perform high strain rate characterisation of soft materials such as this, owing to issues of weak signal transmission, stress non-equilibrium, and inertial effects being significant compared to material strength[28–31]. Recent studies have shown that it is possible to achieve reliable insights into the high strain rate response of many properties, even at large strains, by a combination of careful experimentation and implementation of time-temperature superposition (TTS) as part of the data interpretation[32–34].

This paper provides an thorough exploration of the mechanical properties of a relatively low molecular weight, supramolecular polyurethane (SPU) which demonstrates healable characteristics[8]. The rheological and morphological properties were characterised along with the large strain compressive response, and a viscoelastic softening model was developed to

describe the mechanical behaviour in monotonic and cyclic compression at low strain rates, monotonic compression from medium to high rates, as well as strain recovery at room temperature. We first characterised the consistency of molecularity and polymer morphology by executing ^{1}H nuclear magnetic resonance (NMR) spectroscopy and gel permeation chromatography (GPC) experiments. Repeatable processability of the SPU was confirmed by both differential scanning calorimetry (DSC) measurements and rheometry. Further rheological analysis under controlled thermal cycles explored the dependence on the rate of change of temperature, which was described using an Arrhenius based model. There was good consistency between data from DSC, small angle X-ray scattering (SAXS) and large strain compression experiments. In order to model the compressive response, fundamental viscoelastic characterisation was first obtained from a dataset assembled from rheological analysis and DMA experiments in which isothermal frequency sweeps were performed over a wide range of temperatures. The time-temperature superposition (TTS) principle was applied to produce a master curve, fitting into a Prony series to produce a generalized viscoelastic model describing small strain behaviour. To capture the large strain response over a wide range of strain rates, an additional characteristic dashpot and spring were combined with the generalized Maxwell model to allow strain softening and recovery to be modelled, respectively. This viscoelastic softening model was implemented in Simscape (MATLAB® & Simulink®), and calibrated using compression experiments at varying strain rates from 10^{-3} to 40 s^{-1}; it was then used to predict the results of high strain rate experiments up to 1220 s^{-1}. The geometric (strain) recovery during low-rate cyclic compression tests at room temperature was also incorporated into the model implementation.

2 Material and background characterisation

2.1 Synthesis of SPU and characterisation methods

Thermoplastic polyurethanes are a class of phase-separated block co-polymer, formed by soft

and hard segments, with varying ratios by mass. The desired material was synthesized as described previously [818]. Firstly, a hydrophobic polyol, namely Krasol™ HLBH-P2000, was reacted with methylene diphenyl diisocyanate (4,4'-MDI) at 80 °C for three hours to afford a prepolymer featuring isocyanate terminals. A hydrogen bonding motif, 4-(2-aminoethyl)morpholine, was then added to the prepolymer to install the end-groups via urea bond formation and afford the desired polyurethane as shown in Fig. 4-1. The polyurethane was designed to permit hydrogen bonding interactions for network self-assembly, consequently achieving a healing capability at readily accessed temperatures around 37 °C[8]. ^{1}H NMR spectroscopy was first used to confirm the synthesis. ^{13}C NMR spectroscopy also corroborated the establishment of urea (156.2 ppm) and urethane (153.8 ppm) linkages in the supramolecular polymer. As an additional conformation of the formation of urethane/urea linkages in the polyurethane, infrared spectroscopy revealed the complete consumption of isocyanates functionalities as observed by the disappearance of the vibration at 2270 cm^{-1}. Furthermore, new absorbances at 1642 cm^{-1} and 1706 cm^{-1} were attributed to the carbonyl stretches in the newly formed urea and urethane bonds, respectively. GPC analysis was conducted to confirm the extent of chain extension in the polyurethane, with an average of 2 hydrogenated poly(butadiene) residues per supramolecular polymer (M_n = 9100 g mol^{-1}).

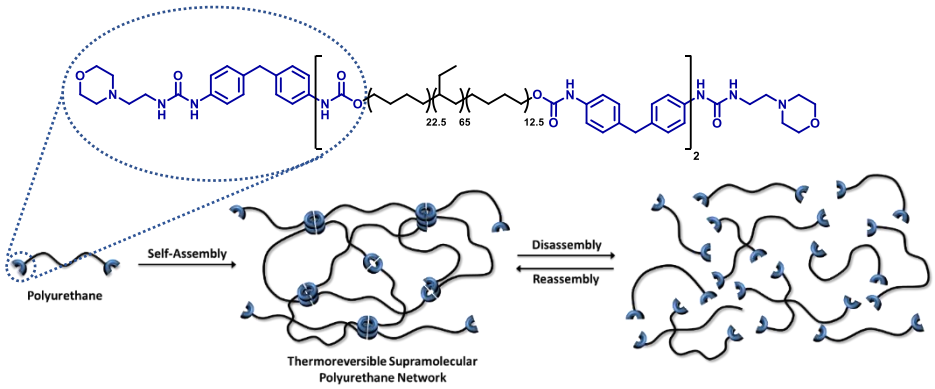


Fig. 4-1. Chemical structure of the supramolecular polyurethane, featuring urea morpholine end groups, used in this study and a schematic illustration of formation and dissociation of the polymer network when an appropriate stimulus, such as heat, is applied

In order to perform the experimental program reported herein, samples of polymer were repeatedly re-melted and re-cast. This gave the requirement and opportunity to assess their stability. 'Raw' samples were produced first, by solution casting from THF into PTFE moulds. The samples were dried at room temperature overnight before drying at 80 °C under vacuum. To produce heat-treated specimens, this material was heated to 80 °C at 2 °C min^{-1} in an oven, and then cooled in air, in water, or under temperature-controlled cooling rates of 2 °C min^{-1} and 10 °C min^{-1}. Temperature profiles were measured using thermocouples embedded into one of the samples within the mould. Typical cooling curves for the air and water-cooled specimens are shown in Supplementary Information (SI), Fig. SI 1. Samples that had each undergone four thermal treatments ('repetitive' specimens) were compared to 'raw' specimens and specimens that had undergone a single thermal treatment ('single' specimens). Spectroscopic and thermal analysis were carried out in order to identify whether any degradation had taken place via modification of the polymer backbone[35], or cross-linking[36,37] of the urethane or urea linkages. This allowed for the determination of whether disruption to the supramolecular network and polymer backbone had occurred over time. Finally, DSC, rheometry and SAXS experiments were performed in order to confirm that the order and assembly of the SPU network had not altered.

2.2 Molecular characterisation

^{1}H NMR spectroscopy was conducted to examine the stability of the SPU under different processing conditions (Fig. 4-2). Samples that had undergone thermal treatment were compared to the raw material and revealed no significant difference in chemical shifts or integration of key resonances. The successful synthesis of the SPU was first confirmed by which revealed a resonance at 4.16 ppm, characteristic of methylene residues adjacent to newly formed urethanes in the polymer backbone. Furthermore, the decoration of the pre-polymer with the hydrogen bonding motif was confirmed by the triplet at 3.33 ppm. This triplet was

assigned to the methylene residue adjacent to the newly formed urea motif within the hydrogen bonding end-groups. The resonance at 4.16 ppm and 3.33 ppm corresponding to the methylene residue adjacent to urethanes and urea moieties, respectively, were unchanged after thermal processing, indicating that the polymer backbone remained intact. Importantly, the integration ratio between end-group resonances and the polymer backbone remained constant after thermal processing when compared to the raw material, demonstrating no alteration to the composition of the polymer network. Furthermore, no additional, new signals were observed in the ^{1}H NMR spectra for any samples after treatment, again demonstrating that the polymers were stable to the thermal processing conditions.

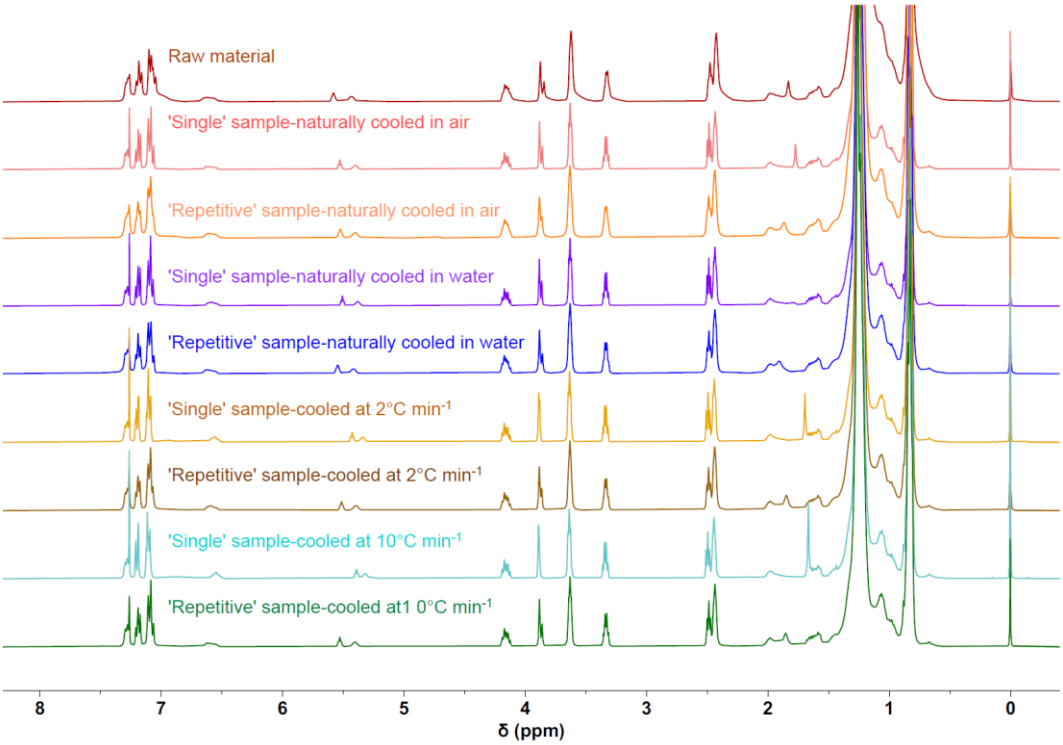


Fig. 4-2. ^{1}H NMR spectroscopic data for SPU specimens following different thermal processing regimes, using air-cooling, water-cooling, or controlled cooling rates.

To further monitor the stability of the SPU under the thermal processing conditions described above, GPC experiments were undertaken to explore any changes in molecular weight (Fig. 4-3*)*. In good agreement with the data collected by ^{1}H NMR spectroscopy, GPC analysis demonstrated no significant difference in the molecular weight of the materials after

processing (M_n between 8650 g mol^{-1} and 8800 g mol^{-1}) compared to the raw material (8750 g mol^{-1}) as revealed by the multi-modal signals at retention times between 13 and 16.5 minutes. Furthermore, the polydispersity of all samples before and after processing was relatively narrow (Đ = 1.45), further revealing that no trans-urethanation had occurred[35].

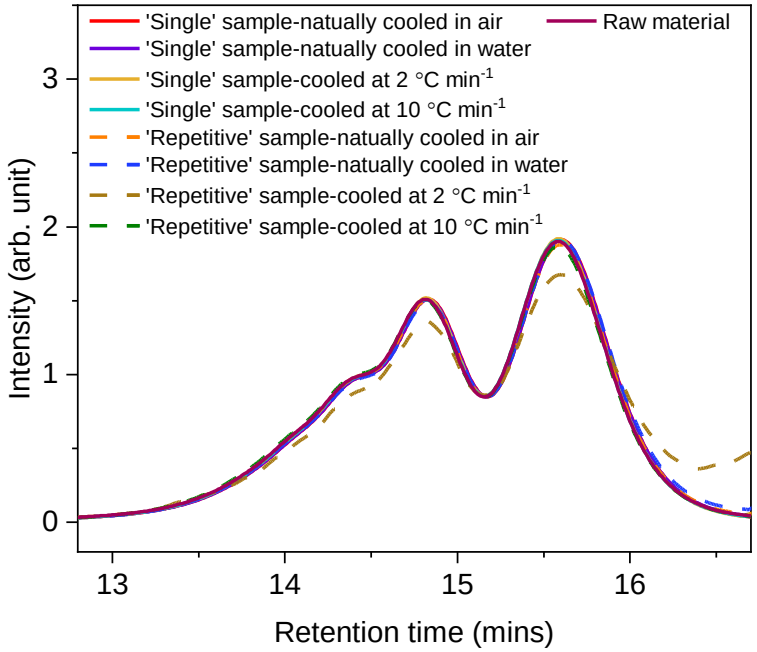


Fig. 4-3. GPC results for three types of SPU specimens: 'raw', 'single' and 'repetitive', demonstrating that the molecular weights do not change with repeated processing.

2.3 Thermal characterisation

DSC was used to examine the thermal properties of the material, focusing on the effect of different cooling rates, Fig. 4-4. A single 'raw' specimen was taken and first cooled to -80 °C at 1 °C min^{-1}; after a 5-minute hold at -80 °C, a constant heating rate of 5 °C min^{-1} was applied until the temperature reached 90 °C, at which temperature the specimen was again held for 5 minutes. The specimen was subjected four cycles of cooling treatments from 90 to -20 °C, at different rates, each followed by heating at 5 °C min^{-1}. Full experimental data from three specimens can be viewed in the SI, Fig. SI 2-4; Fig. SI 5 shows the consistency between heat flow data in the different cooling loops.

The DSC experiments revealed a glass transition at approximately -45 °C, which is the

T_g of the soft domain within the micro-phase separated polymer. A second endothermic transition at around 20 °C was also observed, which may be associated with dissociation of the thermo-reversible supramolecular structure: this is repeated in all of the cycles. In the first heating, an additional broad endothermic dip was observed starting at 40 °C. This was not observed in subsequent cycles, and may be associated with phase separation within the cast material which has insufficient time to reform equilibrium in subsequent loops given the cooling and heating rates imposed[24]; evidence of an additional structure in the 'raw' specimens is shown in the SAXS data below.

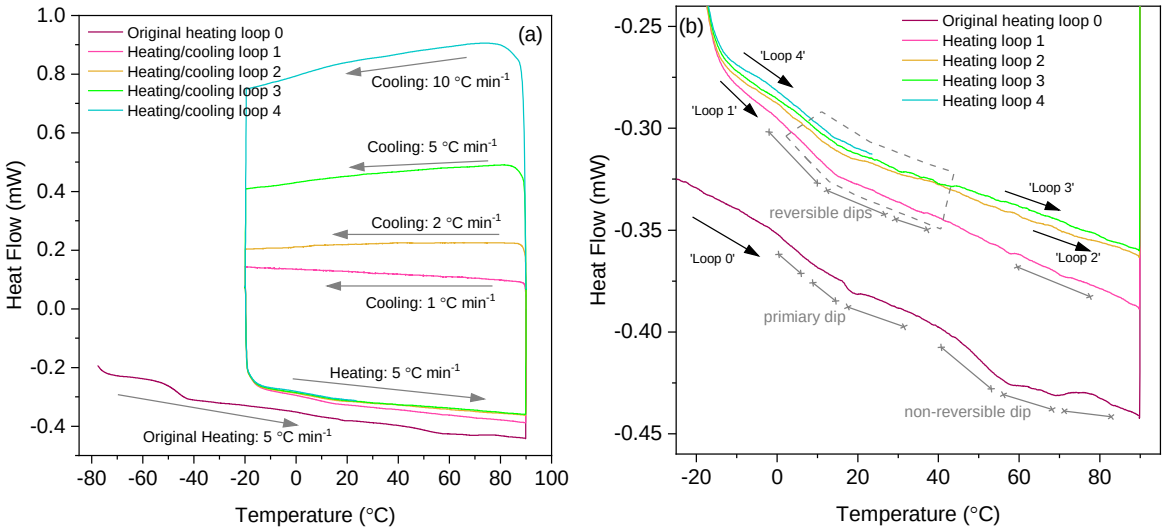


Fig. 4-4. DSC experiments with different cooling rates performed on an initially cast specimen (a) measured heat flow for the different heating and cooling loops (b) detail of heating loops.

2.4 Structural characterisation

Small-angle X-ray scattering (SAXS), was performed to examine the nanoscale structure resulting from different cooling rates. SAXS was executed on both 'raw' and 'single' specimens, results are shown in Fig. 4-5. All SPUs exhibited a typical micro-phase separated morphology as confirmed by the Bragg peak centered at 0.016 $Å^{-1}$, which arises from immiscibility of the polar hard (self-assembling) and apolar soft (polymer backbone) domains[8]. Additionally, the raw material exhibited a slight shallower SAXS profile compared to the processed polymers at high q values (0.011-0.014 $Å^{-1}$) as a result of a potentially modified

micro-phase separation. This may further corroborate the existence of kinetically trapped phase separation, as observed by DSC measurements. Furthermore, the SAXS profiles also possess a reflection centered at 0.061 $Å^{-1}$. This second order SAXS peak ($q\sqrt{3}$) corresponded to hexagonal packing of cylinders within the micro-domains as a result of association of the urethane-urea motifs which allowed to form without disruption. Again, no significant differences were observed in SAXS profiles of the materials post treatment demonstrating that the polymer was stable over the different cooling regimes reported.

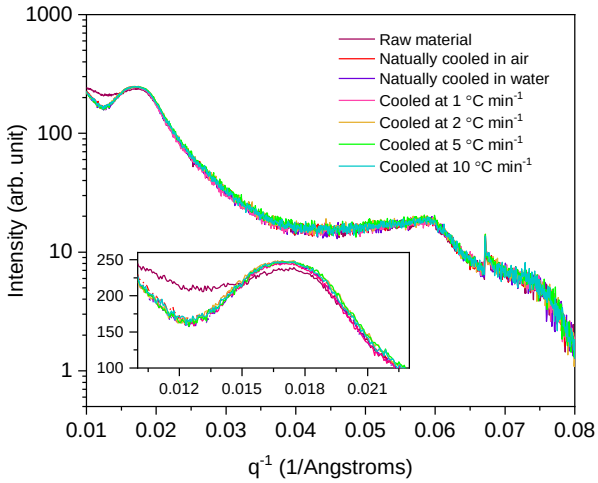


Fig. 4-5. SAXS data obtained at 25 °C for 'raw' material, and 'single' SPU specimens prepared using different thermal processing regimes. All samples experienced a heating rate of 2 °C min^{-1} to a temperature of 80 °C before being cooled in air, in water or at controlled rates between 1 and 10 °C min^{-1}.

2.5 Effect of cooling on mechanical response

In addition, compression experiments were performed on water and air cooled specimens; temperature profiles can be viewed in Fig. SI 1. The compression data, Fig. 4-6, reveal that the material can be re-processed multiple times without degradation of initial stiffnesses, although small differences in behaviour were observed at large strains. This is consistent with the data presented above, in which the results were not affected by processing thermal cycles.

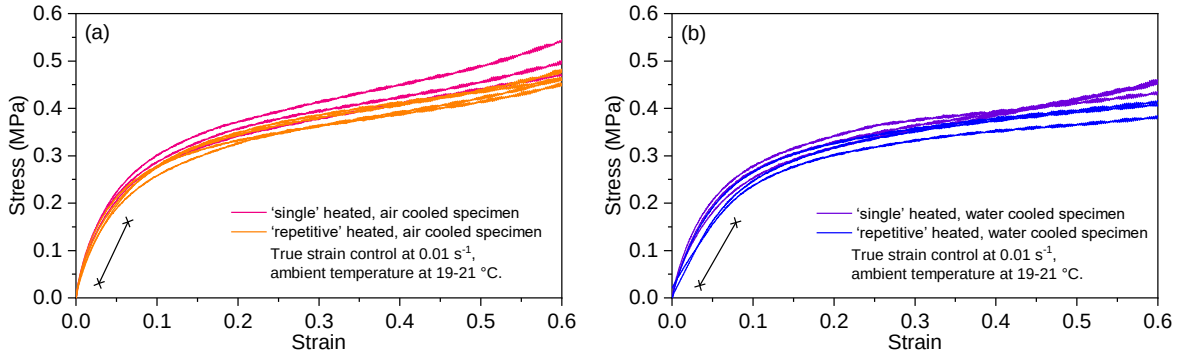


Fig. 4-6. Stress-strain relationships in (a) air- and (b) water-cooled specimens under compression: 'single' specimens have undergone a single thermal treatment, while 'repetitive' specimen received four thermal treatments. The compression were performed at ambient temperature between 19-21 °C, differences between the curves might be due to temperature variations.

2.6 Rheological characterisation

Rheological analysis was conducted to probe the mechanical properties of the materials, and their dependence on temperature and heating rate; data from this analysis were also used to populate later models of this behaviour. Test specimens were made by first melting the pristine solution cast (raw) material, and then casting a disk specimen of 20 mm diameter and 1.5 mm thickness using a PTFE mould (similar to the one in Fig. SI 21); the density was measured as 950 kg m^{-3} and Poisson's ratio is 0.49. Rheometry experiments were performed under a constant oscillatory deformation at 1 Hz, with a 0.1 % shear strain amplitude. Before starting each experiment, the specimen was heated to 80 °C in order to ensure good contact between the specimen and plate. Two series of experiments were initially performed to investigate the effect of heating rate and cooling rate on the mechanical performance of the supramolecular polyurethane: in the first series, the specimens were heated from 20 to 90 °C at five different heating rates, before cooling at a constant 2 °C min^{-1}; in the second, the heating rate was fixed at 2 °C min^{-1} but different cooling rates were employed. In both cases, output data, including moduli and contact force were recorded.

Analysis of rheology data, Fig. 4-7, showed that the higher heating rates gave rise to a higher modulus on heating, but that there was no effect on the properties measured during the

subsequent cooling regimes; similarly, higher cooling rates gave a lower modulus on cooling, but have no effect on the properties during subsequent heating. This is consistent with the DSC data, and SAXS analysis. Further rheological experiments were performed to confirm repeatability of the data from different cycles, and to confirm that the results obtained were not affected by previous cycles (Fig. SI 6). Overall, the data demonstrate the reversibility of material properties, and support the reusability of the material. They also indicate that there is a time dependence in the evolution of the polymer structure, and hence the mechanical response, but that the time taken for the reversal of the temperature ramp at room temperature is sufficient for the subsequent ramp to be unaffected.

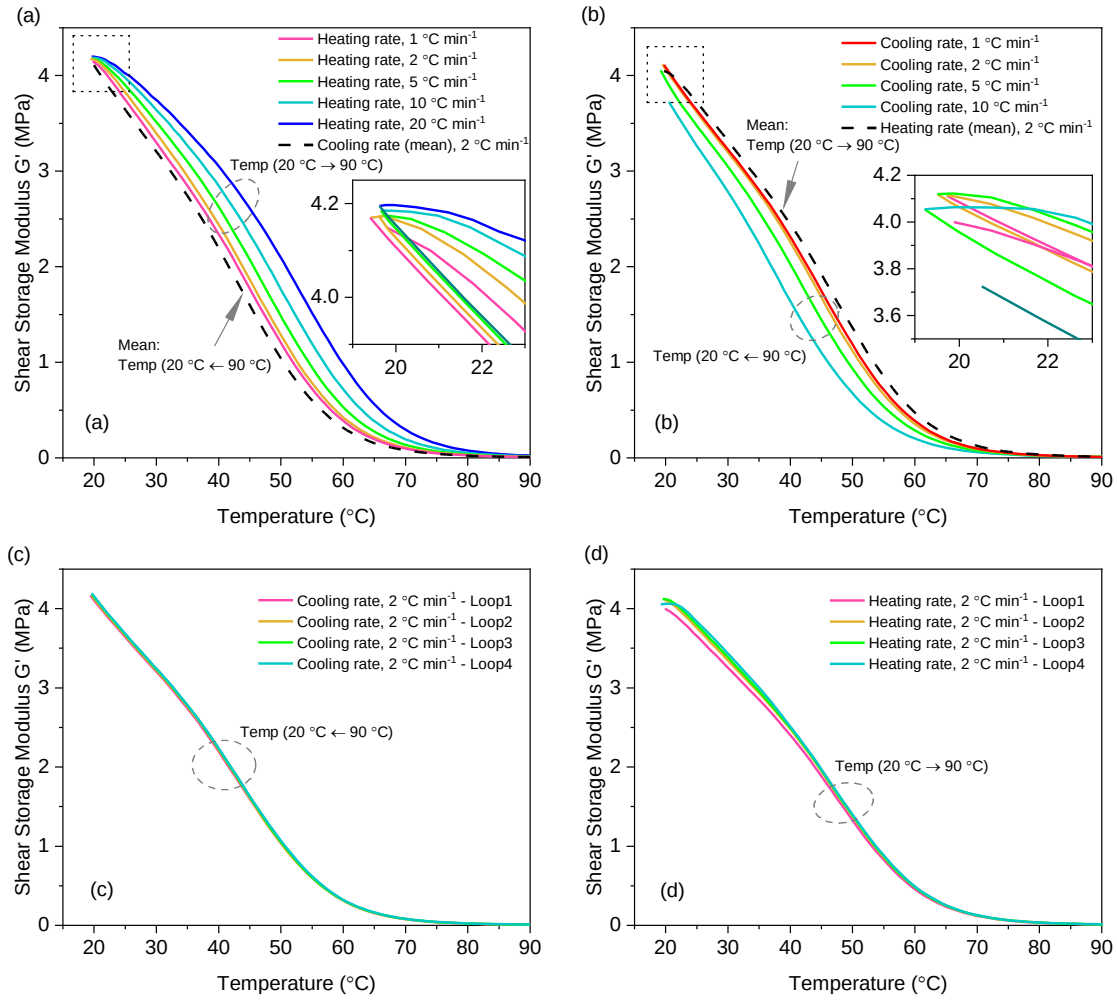


Fig. 4-7. Rheological analysis at different (a) heating rates or (b) cooling rates of 1, 2, 5, 10, 20 °C min^{-1}. Mean data for the cooling and heating portions of the loops (at 2 °C min^{-1}) are also shown. The full sets of results from cooling and heating, respectively, are shown in (c) and (d). These data also show that processing at different rates does not affect the subsequent properties. Oscillation frequency 1 Hz and amplitude 0.1%.

2.7 Models for rheological characterisation

Two simplified models were used to characterise the effects of heating or cooling on observed material properties. The first model, the 'shift method', was based on the observation that data from different heating and cooling rates had a similar shape through the experiment, but were simply offset from one another. This led to the concept that any modulus-temperature profile at a certain heating or cooling rate might be predicted using data obtained from a reference rate. The analytical formulation of this model is introduced in the SI, with implementation shown in Fig. SI 7-8. The second model used a differential equation based on an Arrhenius formation including both time and temperature variables, to calculate the unit moduli on each unit temperature rate. These methods were chosen as they are both commonly used to describe time-temperature equivalence in polymers. The appropriate parameters were found by fitting to the experimental data. Here, the Arrhenius model is described briefly, more detail about both models may be found in the SI.

The second model explicitly captures the evolution of modulus with time and temperature using an Arrhenius equation to model the temperature effect on the rate at which the polymer structure evolves. This relationship is often applied to the physical interpretation of kinetic transformations induced by thermal process[38,39]. The model describes the rate of change of modulus with respect to temperature according to

$$\frac{dG}{dt} = r_0[G - G_{ref}(T)]e^{-\frac{U}{kT}}, \tag{4-1}$$

where G is the current modulus output by the rheometer; $G_{ref}(T)$ is a temperature-dependent reference 'long term' modulus to which the current modulus evolves; r_0 and U are parameters to be calibrated using the empirical data; T is the absolute temperature; and k is the Boltzmann constant, equal to 1.3806×10^{-23} J K^{-1}. In practice, G_{ref} was assumed to be the modulus-temperature profile produced by averaging the cooling and heating curves at 2 °C min^{-1}. Fig. 4-8, shows modulus curves on heating and cooling, as produced by the model, using parameters

of r_0 = 2 s^{-1} and U/k = 1312 K. It is noted that here the measured time-temperature profiles (Fig. SI 10) were used, allowing the model to account for the changes in heating and cooling rate through the experiment, thus representing an advantage of this approach.

Further validation of the model, via comparison to other experiments to verify its capacity and applicability is provided in the Supplementary Information, Fig. SI 12-16.

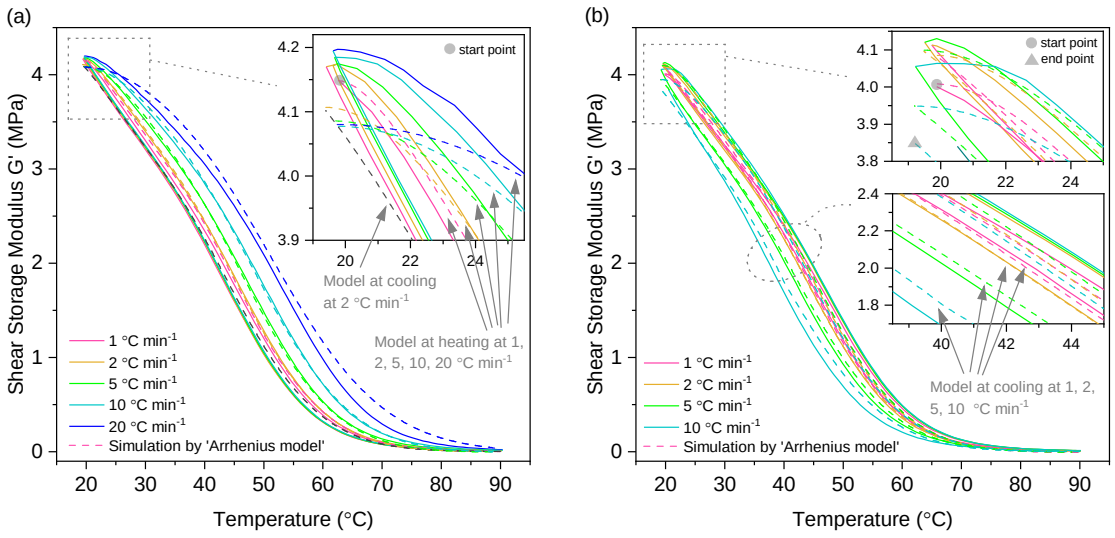


Fig. 4-8. Application of the Arrhenius equation based model to (a) heating and (b) cooling rates of 1, 2, 5, 10, 20 °C min^{-1}. The reference curve was the average of cooling and heating at 2 °C min^{-1}, representing the temperature rate $\dot{T} \to 0$. The experimental temperature profiles and model parameters of r_0=2 s^{-1} and U/k=1312 K were used. Oscillation frequency 1 Hz and amplitude 0.1%.

3 Dynamic mechanical analysis and production of master curves

In order to understand and model the data obtained from monotonic compression testing reported in later sections, thermo-mechanical analysis of the specimens was performed using Rheometry, as described above, and DMA. Each of these systems is able to characterise a different regime of material behaviour: rheometry for elevated temperatures where the material has low modulus, and DMA for low temperatures, for which the stiffness is higher. The empirical behaviour of thermoplastic elastomers between the rubbery and glassy states has the well-known time-temperature equivalence [40]. Making use of this, master curves of the behaviour as a function of frequency at different temperatures were produced from the

experimental data in a manner consistent with the later modelling strategy. The rheometer sample was first prepared by melting at 80 °C, and air cooling in a PTFE mould to produce specimens of diameter 20 mm and thickness 1.5 mm. Once inserted in the rheometer, the specimen was again heated to 80 °C and cooled back to room temperature (at 2 °C min^{-1} for heating and cooling) to ensure full contact with the measurement plates and removal of potential residual stress. Isothermal frequency sweeps (1-100 Hz with 100 measurement points) were then performed at 10 °C temperature intervals from -20 to 80 °C at 0.1 % shear strain.

For the DMA experiments, rectangular samples (5 × 20 mm, thickness 1.2 mm) made in the same manner were tested in a DMA machine (Q800, TA Instruments) in the tensile mode. Isothermal frequency sweeps were again performed, but at 5 °C temperature intervals from -60 to 30 °C, at 0.05 % strain and with 20 frequencies between 1 and 100 Hz. In these DMA experiments, however, the specimen was observed to start exhibiting significant permanent elongation, ether yielding or creep, when the temperature was above 15 °C. Conversely, the rheometer is not able to produce accurate data at low temperatures, below -10 °C this is shown in Fig. 4-9 and Fig. SI 17. Therefore, the experimental data from DMA and rheological analysis were combined together to produce a single master curve, taking advantage of the ability to produce overlapping data, in Fig. 4-10; the shift factors and a Master Curve for *E'',* are given in Fig. SI 18. The shift factors can themselves be fitted by the well-known Williams-Landel-Ferry (WLF) equation[41],

$$\log a_T = -\frac{C_1(T - T_{ref})}{C_2 + (T - T_{ref})}, \tag{4-2}$$

where T_{ref} is a reference temperature, and C_1 and C_2 are constants fitted to the data. Further, the master curve can be fitted by a Prony series

$$E(t) = E(0)\left[1 - \sum_{i=1}^{M} \frac{E_i}{E(0)}\left(1 - e^{-t/\tau_i}\right)\right], \tag{4-3}$$

where *E(0)* is the instantaneous elastic modulus in the time domain, and the values of E_i and $\tau_i = \eta_i / E_i$ are fit to the experimental data. These parameters can also be used to express the

storage and loss moduli as functions of frequency using

$$E'(\omega) = E_0 + \sum_{i=1}^{M} E_i \frac{\tau_i^2 \omega^2}{1+\tau_i^2 \omega^2}, \tag{4-4}$$

$$E''(\omega) = \sum_{i=1}^{M} E_i \frac{\tau_i \omega}{1+\tau_i^2 \omega^2}, \tag{4-5}$$

where ω is the applied frequency. Here, E' and E'' are defined as the real and imaginary parts of the complex moduli during cyclic loading. In this case, the Alfrey Approximation[42] was used to parameterize the Prony series, which was then applied in the model described in the next section; the parameters obtained are given in Tables SI 1-3 at different temperatures, the Prony series at different temperatures are also shown in Fig. SI 19.

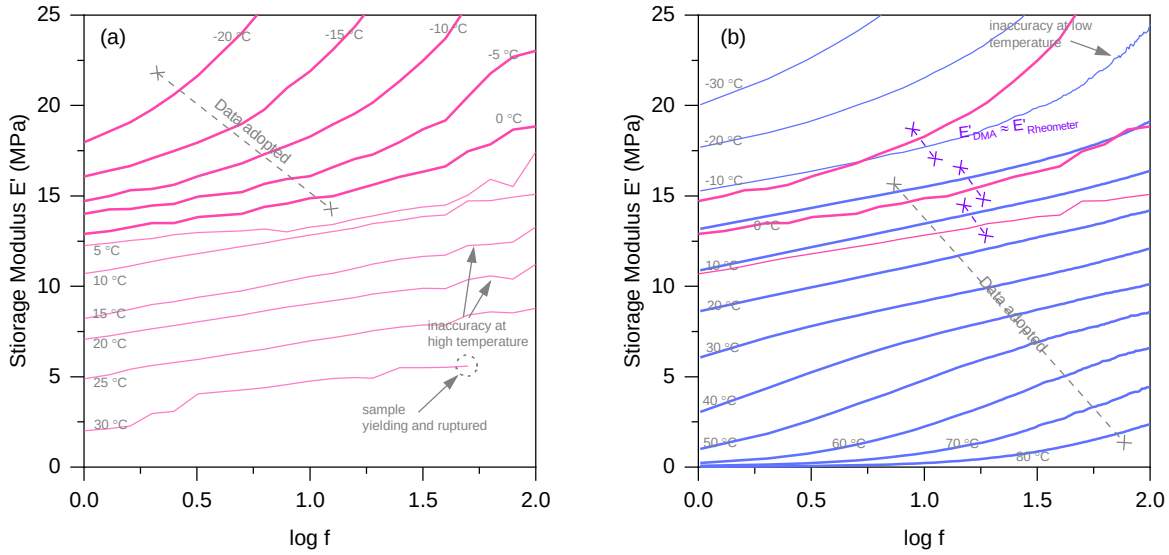


Fig. 4-9. (a) DMA data showing isothermal frequency sweeps at different temperatures. The DMA performs well from -60 to 30 °C but inaccuracies are apparent above 10 °C. (b) Rheometer data are accurate at higher temperatures but not below -10 °C. Here, DMA data at -10, 0 and 10 °C are overlaid to show the consistency between these two techniques.

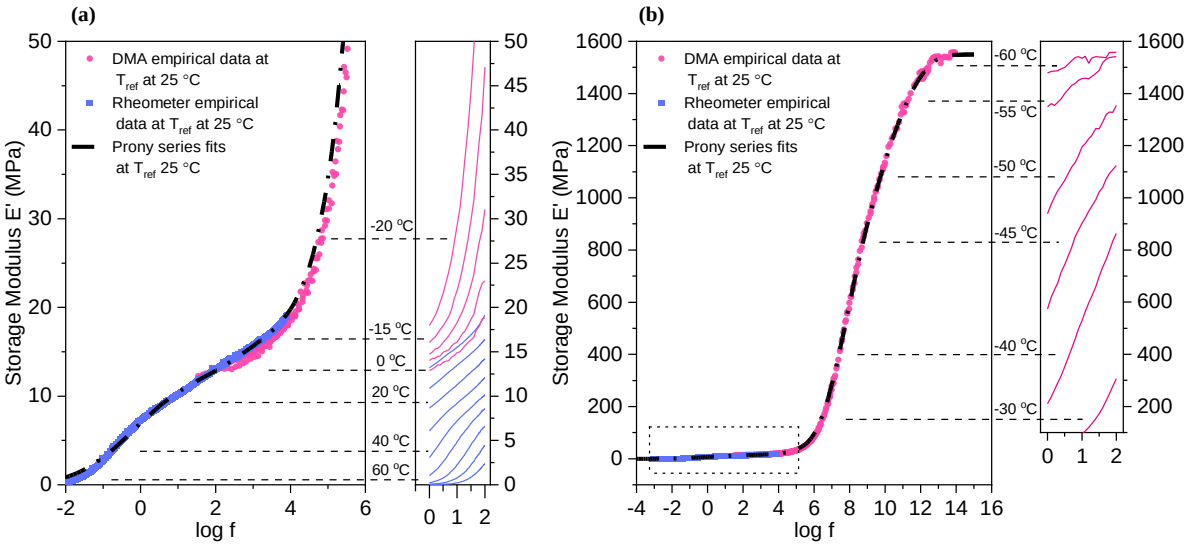


Fig. 4-10. (a) and (b) A continuous master curve of E' vs. log f generated by applying TTS to E′ vs. log f curves at different temperatures from the rheometer and DMA. In particular, (a) shows the consistency between the two sets of data. A Prony series was fitted to the storage modulus profile in (b) using the full range of frequencies.

4 Viscoelastics softening model

Phenomenological models of polymers are commonly used to describe viscoelastic, viscoplastic, and softening behaviour[43–46]. These models often use combinations of Hookean springs and Newtonian dashpots to describe the empirical behaviour[46–50]. A simple model, Fig. 4-11, is proposed here and calibrated using thermo-mechanical data as well as compression tests. Here, the generalized Maxwell model is used to express the fundamental viscoelasticity, calibrated by using the Prony series fit to the rheometer and DMA data as described above; there is an additional dashpot (η^*) added to allow softening at larger strains, observed in the compressive data; finally, an external spring (E^*) captures strain recovery observed upon removal of load. In order to aid the fitting to the experimental data, two forms of the dashpot were used: η^*_{linear}, in which the viscosity was independent of stress level, and $\eta^*_{\textit{non}\text{linear}}$, in which there was stress dependence. The entire model was constructed in Simscape (Simulink, Matlab), shown schematically in Fig. SI 20. In order to calibrate the model, quasi-static compression experiments were performed; the model was later tested against data obtained at higher strain rates. The quasi-static experiments were executed in a commercial screw-driven

testing machine (Instron 5982). Test samples of diameter 6.3 mm and height 7.3 mm were cast in a PTFE mould (see Fig. SI 21) at 80 °C, using the same approach introduced in the rheometry section, and air-cooled to room temperature. Experiments were conducted at strain rates of 0.001, 0.005, 0.01, 0.05, 0.1 and 0.5 s^{-1}; force was recorded using a load cell and strain calculated from local measurements of the axial displacement using an extensometer attached to the loading platens: the experiments were performed at constant true strain rate. After the test, the zero-stress strain recovery was recorded against time.

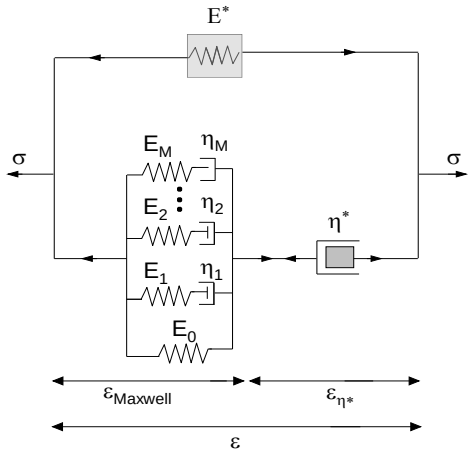


Fig. 4-11. Schematic of the viscoelastic softening model. The model combines springs and dashpots described by the Prony series, an additional dashpot η^* and a recovery spring E^*.

The characterisation of the dashpot (η^*) and spring (E^*) is provided in Fig. 4-12. The strain rate-controlled model was implemented to compute stress-strain responses at different strain rates. The values of η^*_{linear} were defined at each strain rate by optimizing the model to the experimental data. From the outputs, it was observed the model stress-strain response started to flatten around strain 0.6, showing that the dashpot is fully activated. By inputting the initial linear value of η^*_{linear} to match the empirical strain-stress curves (shown later in *Section 5*), the value of stress was determined when $\varepsilon = 0.6$. These values of η^*_{linear} and stress enabled construction of a linear relationship of log η^* against log σ. This implied a relationship of the form

$$\frac{d\sigma}{d\dot{\varepsilon}} = 10^{\beta} \cdot \sigma^{\alpha}, \tag{4-6}$$

where α and β are fitting parameters for the linear relationship. Applying the boundary condition: $\sigma(t=0) = 0$, allows a relationship to be derived between stress and strain rate by in order to characterise the dashpot:

$$\sigma = (\chi\dot{\varepsilon})^{\delta}, \tag{4-7}$$

where χ and δ are determined by solving the differential equation (ODE) in Eq. 4-7.

In the Simulink model, η^*_{linear} can be simply represented by a standard linear dashpot; while for $\eta^*_{nonlinear}$, the behaviour was described using a 'Lookup Table'. This was implemented by fitting well-selected dispersed values along the plot given by the ODE solution. In practice, larger numbers of sampling points were taken at low strain rates, with more dispersed points up to 40 s^{-1}. It is noted that the strain rates experienced in this dashpot are small even when the overall strain rate is high. Now, both η^*_{linear} and $\eta^*_{nonlinear}$ can be inserted into the Simscape model allowing simulation of experiments over the full range of strain rates, as demonstrated in later sections.

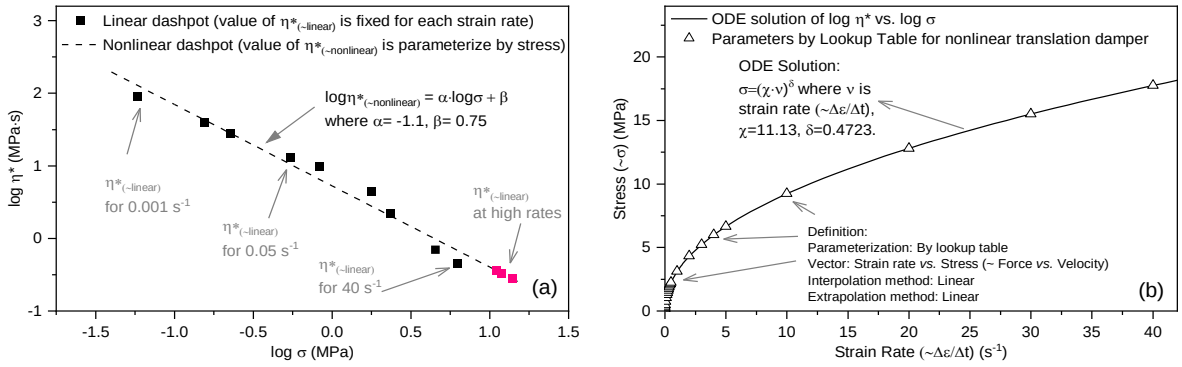


Fig. 4-12. (a) A series of linear dashpots was first fitted to the experimental data, the logarithms of the fitted viscosities were found to be linear in log(applied stress), described by the function given and extrapolated to high strain rates. (b) The character of the non-linear dashpot was determined by finding the solution to the ODE formed for $\eta*$ against σ; this was then sampled at the points shown to produce a lookup table for the model.

The value of the spring, E^*, was then determined. Having derived the stress-strain relationship for loading, the stress history was re-inputted back to the Simscape model using stress-control (Fig. 4-11). To simulate the recovery after compression, a zero-stress period was

added after the loading history to form a full representation of the specimen history, including loading, unloading and recovery. This was done to avoid complications when switching between strain rate and stress control. An appropriate value of E^* (= 0.85 kPa) was fit by comparing the model output to empirical strain recovery data, shown in Fig. 4-13b. All recovery experiments and simulations were performed at 25 °C and recovery data can be reviewed in Fig. SI 22 and Table SI 4.

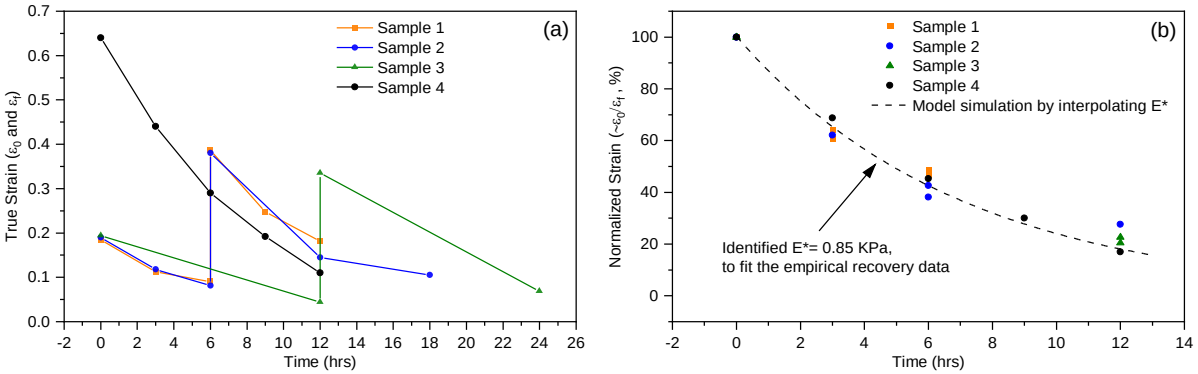


Fig. 4-13. (a) A series of specimens were compressed to different strains, ε_f, (in experiments lasting a few minutes) and allowed to recover a period of a few hours before being reloaded, whilst the strain, ε_0, was monitored; some of the samples were then reloaded. (b) a value of E^* = 0.85 kPa allowed the model to capture the recovery history of a number of samples, including those loaded cyclically (1-3) or monotonically (4) to different strains. All experiments were executed at a temperature of 25 °C.

An example of a full set of model outputs for a monotonic loading is shown in Fig. 4-14. The figure shows the stress-strain behaviour in the Maxwell components, identified spring E^* and the entire model, as well as the strain behaviour of the Maxwell model, identified dashpot $\eta^*_{nonlinear}$ and the whole model, on both short and long timescales.

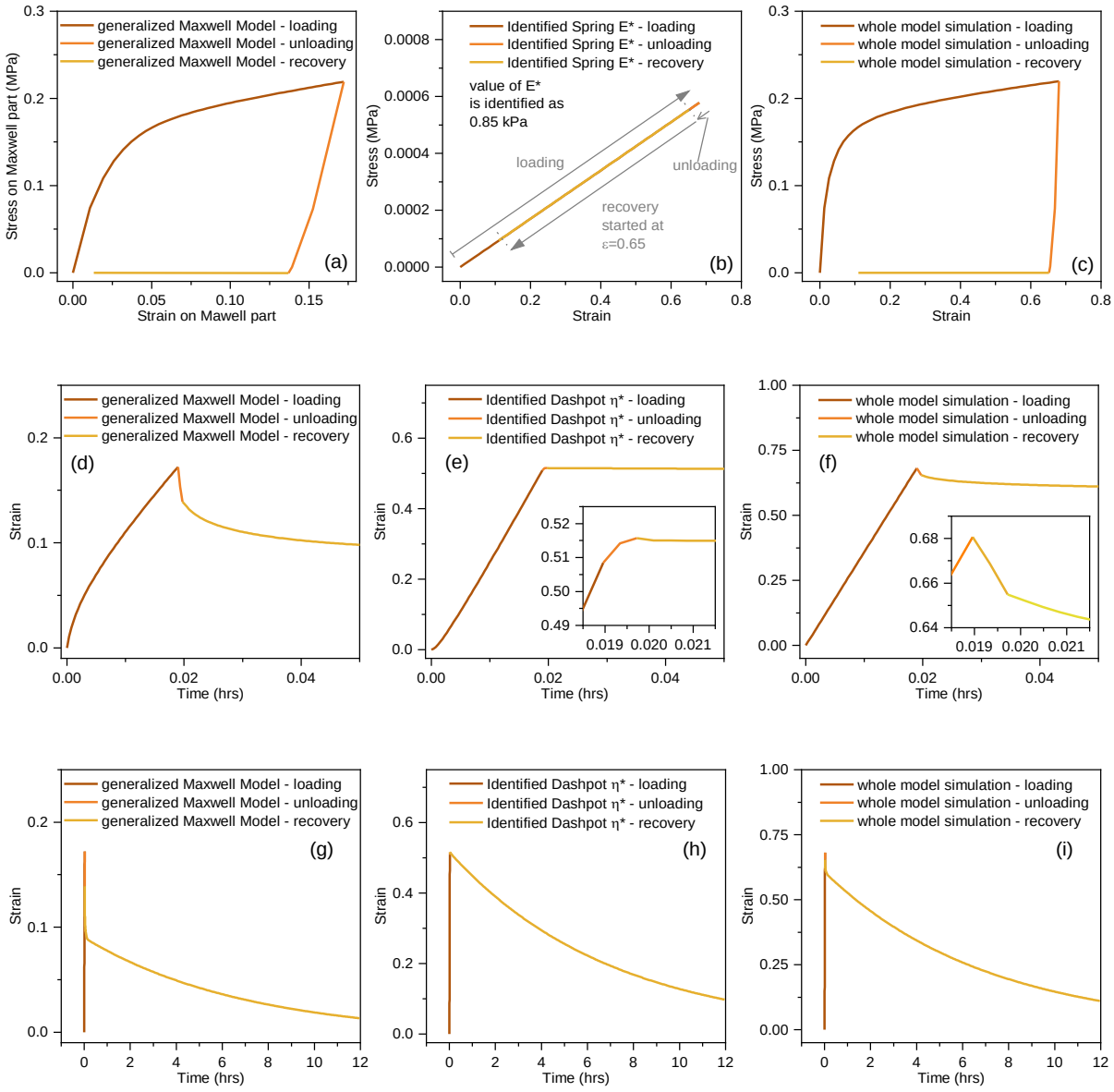


Fig. 4-14. Model outputs for a sample compressed at 0.01 s^{-1}, 25 °C. The figure shows stress-strain relationships and strain time histories in different components of the model.

5 Application of viscoelastic softening model

5.1 Model application at low-to-medium strain rates

Experiments were performed at a constant temperature of 25 °C but various strain rates: true strain rates of 0.001, 0.005, 0.01, 0.05, 0.1 and 0.5 s^{-1} using a commercial screw-driven testing machine (Instron), and true strain rates of 1.36, 11.5 and 40 s^{-1} using an in-house hydraulic

system[2]. The samples had diameter 6.3 mm and thickness 7.3 mm. At least three samples were tested at each rate, the representative data was selected to show in this section. Full data can be viewed in Fig. SI 23-24. The development of the model for loading and (for the lower strain rates) unloading is shown in Fig. 4-15 to 4-17. The isolated generalized Maxwell model is shown in Fig. 4-15, this model over-predicts the specimen response. Then the viscoelastic softening model was applied, Fig. 4-16 and 4-17 which show a comparison of implementations using $\eta*_{linear}$ and $\eta*_{nonlinear}$: firstly the linear implementation, in which a constant viscosity value is fit to each experiment and then the nonlinear implementation, in which a global, stress-dependent $\eta^*_{nonlinear}$ is used. Both models are shown to well describe the experimental data. In particular, at strains below 0.08 the generalized Maxwell model has good agreement, showing that the Prony series derived from DMA and rheometry master curves are sufficient to capture this behaviour. At larger strains, the addition of the extra dashpot and spring allowed the model to describe both the softening (relative to the Maxwell model) and subsequent unloading. An example of the behaviour of the model components can be viewed in Fig. SI 26. A discussion of recovery and cyclic loading will follow in Section 6.

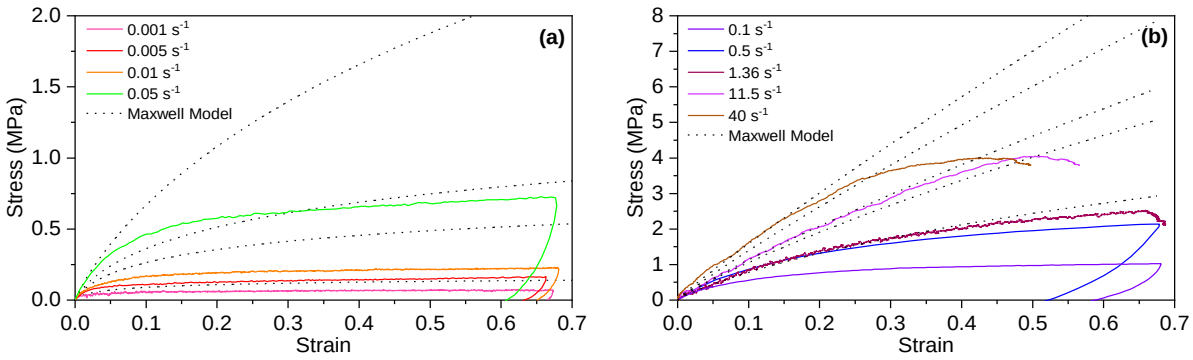


Fig. 4-15. Isolated generalized Maxwell model compared to low and medium rate compression experiments, at a temperature of 25°C but varying strain rates.

[2] These strain rate may be related to the material relaxation frequencies in Fig. 4-10 by assuming that the relevant frequency and strain rate are approximately equal. Whilst this is a simplification, it allows an understanding of the material regime of relevance in these experiments.

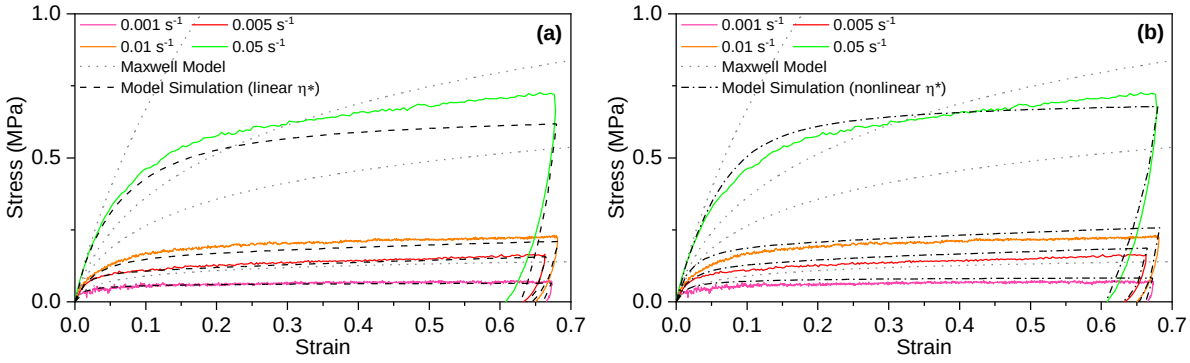


Fig. 4-16. Viscoelastic softening model with linear dashpot η^*_{linear} (strain-rate dependent) and nonlinear dashpot $\eta^*_{nonlinear}$ (stress-dependent value), compared to low strain rate compression experiments, at a temperature of 25°C but varying strain rates.

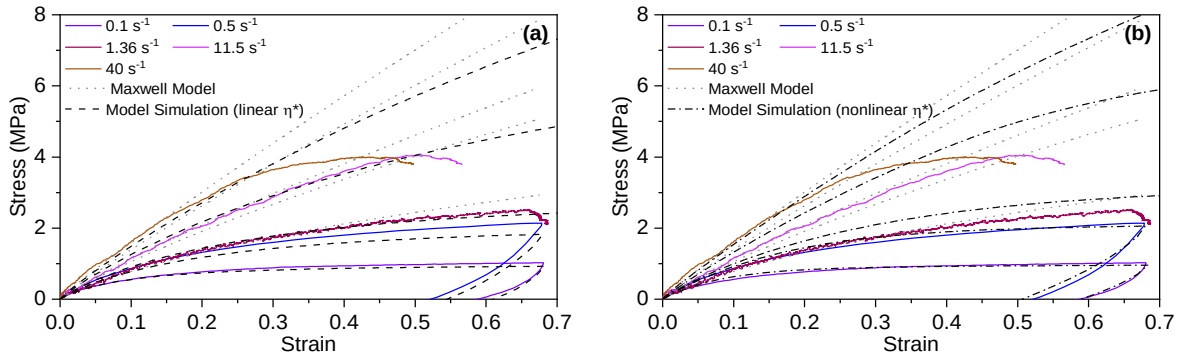


Fig. 4-17. Viscoelastic softening model with linear dashpot η^*_{linear} (strain-rate dependent) and nonlinear dashpot $\eta^*_{nonlinear}$ (stress-dependent value), compared to low strain rate compression experiments, at a temperature of 25°C but varying strain rates.

5.2 Model application at high strain rates

The split Hopkinson bar (SHPB) technique is a standard methodology to study the high rate compression of polymers, as well as other materials[29]. In the experiments in this study, a cylindrical specimen was placed between the ends of two titanium alloy bars, Fig. 4-18. A third striker bar is accelerated using pressurized gas into the incident bar. The subsequent impact creates an 'incident' stress wave which travels along the bar to the specimen. At the bar-specimen interface, some of the waves are reflected and some transmitted. The incident, reflected and transmitted waves were measured by strain gauges attached to the incident and transmission bars. These strain waves were used to calculate the deformation rate and force at the specimen interfaces, from which the corresponding true stress and true strain in the specimen were obtained. Since the stresses supported by this material are very low, a pair of

bars instrumented with an additional pair of sensitive piezo-electric stress gauges, mounted at the specimen bar interfaces, was used for the specimen stress measurements[51].

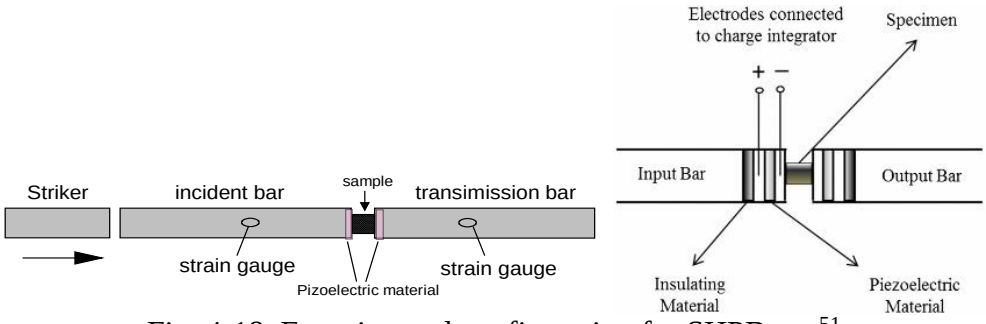


Fig. 4-18. Experimental configuration for SHPB test[51]

Compression SHPB experiments up to 1220 s^{-1} were executed. Full experimental data can be reviewed in Fig. SI 25. For these experiments, the environmental temperature was measured as 17 °C, so a new Prony series was generated by shifting the original master curve from 25 °C (shown in Fig. SI 19 and Table SI 3). The new master curve and new Prony series were then applied to the generalized viscoelastic Maxwell model to form the basic component of the softening model. The value of the additive dashpot and spring were consistent with those used in the previous section: the dashpot η^*_{linear} *and* $\eta^*_{nonlinear}$ were identified from the previous extrapolation in Fig. 4-12. A comparison of the model outputs and experimental data are shown in Fig. 4-19. It is noted that the empirical temperature must be recorded accurately due to the temperature sensitivity of the material, see Fig. SI 28.

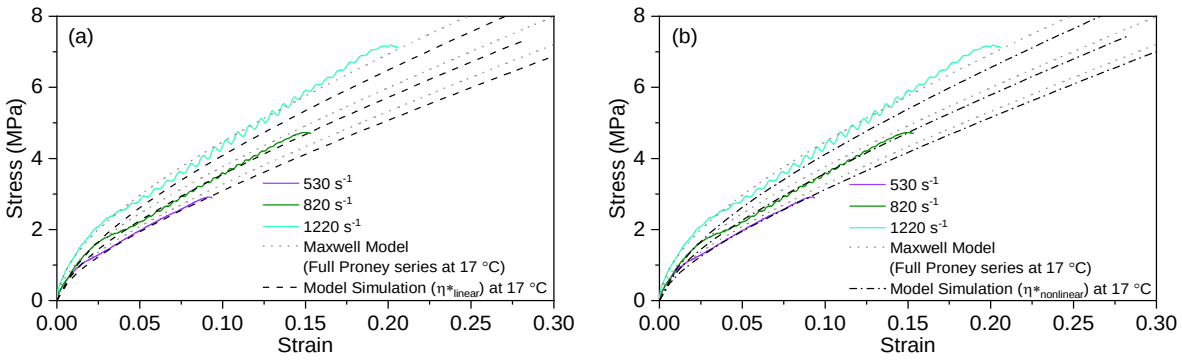


Fig. 4-19. The high-strain rate compression experiments, at a temperature of 17 °C. The value of η^*_{linear} used was 0.47, 0.44, 0.36 for strain rates of 530, 820 and 1220 s^{-1}, obtained from the linear fitting in Fig. 4-12a. The models using $\eta^*_{nonlinear}$ used the table derived in in Fig. 4-12b. The stress-strain curves for the viscoelastic Maxwell model and the full model using the two identified dashpots are shown.

For these experiments, it was observed that the viscoelastic Maxwell model already provides good agreement with the empirical curves, whilst the addition of the viscoelastic softening improves this further (e.g. at 530 and 830 s^{-1}). At these strain rates the resistance of the dashpot to deformation is high, so it does not contribute significant additional strain. Further figures illustrating the stress and strain rate in the dashpot, and other model elements, are given in the Fig. SI 27. Therefore, the softening model is a fully predictive methodology, which enables predict high rate behaviour from the master curve and low rate response.

The effect of specimen inertia must be taken into account when interpreting data from Hopkinson bar experiments. The rapid acceleration of the specimen produces extra stress measured in the system. In this case, the specimen is accelerated to the peak strain rate 1220 s^{-1} from rest. The specimen stress measured during a Hopkinson bar experiment through of the sum of stress components[52]:

$$\sigma_T = \sigma_M + \sigma_I + \sigma_F + \sigma_{other}\,, \tag{4-8}$$

where σ_T is the stress measurement, σ_M is the material strength to be measured, σ_I is an enhancement owing to inertia, σ_F is an enhancement owing to friction and σ_{other} is the enhancement owing other effects that may be present.

The inertia-induced stress is calculated by [52–54]

$$\sigma_I = \rho\ddot{\varepsilon}\left(\frac{a^2}{8}-\frac{h^2}{6}\right)-\rho\dot{\varepsilon}^2\left(\frac{a^2}{16}+\frac{h^2}{6}\right)-\frac{\rho h\dot{v}}{2}\,, \tag{4-9}$$

where ρ is the material density, $\dot{\varepsilon}$ and $\ddot{\varepsilon}$ are strain rate and strain acceleration, a = 4.9 mm is the radius, and h = 7.3 mm is the height, of this specimen, and v represents the speed of the output bar. The magnitude of this inertia stress is only 0.08 MPa at a strain rate of 1220 s^{-1}: the inertia effect is not significant in these experiments.

Another possible effect was the temperature rise owing to the conversion of mechanical work to heat. The high strain rate experiment is assumed to take place in adiabatic conditions as the duration is very short. Therefore any heat generated during the loading will be retained

in the specimen, causing an increase in temperature which can be approximated, assuming that all the mechanical work done is converted to heat, by[55]

$$\Delta Q \approx \Delta W \rightarrow \int_0^{\varepsilon} \sigma d\varepsilon = \rho C_p \Delta T \,, \tag{4-10}$$

$$\Delta T(\varepsilon) = \frac{\beta}{\rho C_p} \int_0^{\varepsilon} \sigma d\varepsilon \,, \tag{4-11}$$

where ΔW is the work done, ΔQ is the heat generated, σ the true stress, ε the true strain, ρ = 950 kg m^{-3} the material density, C_p = 1850 J kg^{-1} K^{-1} the specific heat capacity at constant volume and ΔT the rise in temperature. Here, the heat capacity C_p is obtained from the DSC experiments. Using the assumption that $\beta \rightarrow 1$ for all the work is converted to heat, which is a significant over-estimate for these materials in which we have shown the that quasi-static loading is recoverable, this equation gives a temperature rise of only 0.4 °C at 0.2 strain in strain rate of 1220 s^{-1}, which only causes slight changes in the simulation results, shown in Fig. SI 29.

6 Model application to strain recovery and cyclic loading

As described above, the spring E^* was calibrated to match the recovery of the specimens after leading. Once calibrated, this model was used to simulate cyclic experiments in which the specimen was loaded, unloaded, allowed to rest for 6 hours and then reloaded; an example is given in Fig. 4-20. More information about the strain recovery in the different elements of the model is presented in Fig. 4-21. The most important point to note here is that the same value of E^* successfully describes the behaviour of specimens loaded to different final strains.

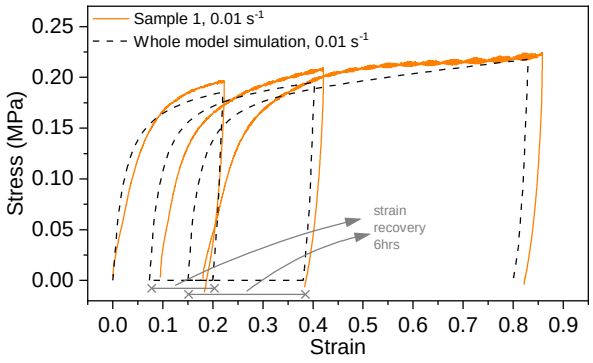


Fig. 4-20. The viscoelastic softening model compared to a multi-cyclic compression experiment.

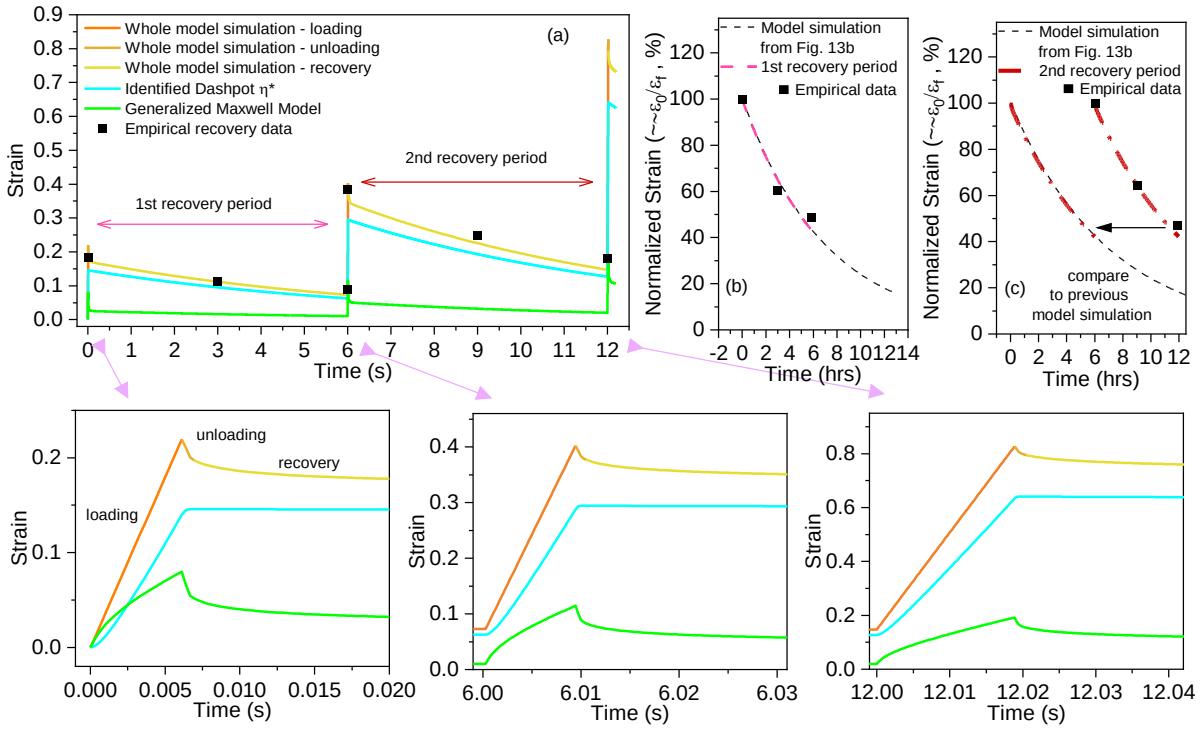


Fig. 4-21. The viscoelastic softening model under stress-control (e.g. the zero-stress vs. time as input profile) to simulate the recovery process. The figures display (a) strain profiles of the full model, dashpot and Maxwell elements. (b) The model simulation of first recovery and second recovery compared to the empirical data. The measured strain data are given in Table SI 4.

7 Conclusions

This paper presents data on the thermo-mechanical response of a supra-molecular polyurethane, and a simple model to capture this response. Structural characterisation has been performed, which, combined with compression data on recycled specimens, show the reusability of the material over multiple cycles. Further, a simple model of the response during rheological characterisation is presented, along with a model for the large strain behaviour which, in particular, is able to predict the high strain rate response

^{1}H NMR spectroscopy, GPC and DSC analysis have shown that the molecular architecture, molecular weight and intermolecular hydrogen bonding of the polymer were not affected by the cooling rate, showed little dependence on cooling rate during processing, and that there was no observable degradation when subjected to multiple heating and cooling cycles. DSC and SAXS analysis also demonstrate that, apart from an initial structure obtained during solution casting, the structure is thermo-reversible; this is also supported by cyclic rheological experiments. Considering the mechanical data, there is a small difference in the response of the material as a result of different cooling rates, as reflected in both the rheometry results and large strain compression data. Further work would be required to understand these changes. The variation in mechanical behaviour in the rheometer experiments was calibrated by two models: the 'shift method' and an Arrhenius based differential equation, in which it is important to consider the exact experimental temperature profile. The time-dependence of the mechanical properties are noted; however, it is also observed that the differences quickly disappear, and the differences observed during cooling do not affect the subsequent heating cycles.

In order to build the large strain mechanical model, characterisation of time and temperature dependence was performed using both DMA and rheometry experiments. These data sets were combined to derive a master curve, which was described using a generalized

Maxwell model and Prony series. Comparison of this model to large strain compression data indicated that it was not able to capture the softening of the material, hence a modified viscoelastic model was developed using an additional dashpot to capture large strain response, and a spring for strain recovery. The model was first fit using linear dashpots with different values according to the loading rate; these were then replaced with a non-linear dashpot. The data demonstrated that a model calibrated using data from experiments performed at low and intermediate strain rates, but was able to predict the response in high strain rate loading up to 1220 s^{-1}. The model was also able to capture strain recovery after compression, and cyclic loading. As well as being applicable to the practical use of this material, the model shows the value of using predictive approaches to measure the high strain rate response, which can be difficult to measure directly. Further research is ongoing to implement this into a model for composites based on this material.

8 Credit authorship contribution statement

Huanming CHEN: Conceptualization, Methodology, Validation, Formal analysis, Investigation, Software, Writing - original draft. **Lewis R. Hart**: Investigation, Visualization, Software, Formal analysis, Writing - review & edit. **Wayne Hayes**: Resources, Visualization, Formal analysis, Writing - review & edit. **Clive R. Siviour**: Resources, Conceptualization, Project administration, Supervision, Writing - review & edit.

9 Declaration of competing interest

The authors declare that they have no known competing financial interests or personal relationships that could have appeared to influence the work reported in this paper

10 Acknowledgements

This material is based upon work supported by the Air Force Office of Scientific Research, Air

Force Material Command, USAF under Award No. FA9550-15-1-0448. The funders had no involvement in study design, collection, analysis and interpretation of data, writing of the report or the decision to submit the article for publication. We are also grateful to the University of Reading for and access to the analytical instrumentation within the Chemical Analysis Facility, we also thank EPSRC (EP/N024818/1) for post-doctoral research fellowship in support of LRH. We thank Prof. Paul Buckley, at Oxford University, for insight and expertise in polymer research. We also would like to thank Igor Dyson for technical support at Oxford University and, in particular, Nick Hawkins for invaluable support with the experiments on the rheometer and DMA.

11 References

1. Chino K, Ashiura M. Themoreversible cross-linking rubber using supramolecular hydrogen-bonding networks. *Macromolecules*. 2001;34(26):9201-9204.
2. Burattini S, Greenland BW, Chappell D, Colquhoun HM, Hayes W. Healable polymeric materials: a tutorial review. *Chem Soc Rev*. 2010;39(6):1973-1985.
3. de Espinosa LM, Fiore GL, Weder C, Foster EJ, Simon YC. Healable supramolecular polymer solids. *Prog Polym Sci*. 2015;49:60-78.
4. Hart LR, Harries JL, Greenland BW, Colquhoun HM, Hayes W. Healable supramolecular polymers. *Polym Chem*. 2013;4(18):4860-4870.
5. Huang WM, Yang B, Zhao Y, Ding Z. Thermo-moisture responsive polyurethane shape-memory polymer and composites: a review. *J Mater Chem*. 2010;20(17):3367-3381.
6. Rivero G, Nguyen L-TT, Hillewaere XKD, Du Prez FE. One-pot thermo-remendable shape memory polyurethanes. *Macromolecules*. 2014;47(6):2010-2018.
7. Feula A, Pethybridge A, Giannakopoulos I, et al. A Thermoreversible Supramolecular Polyurethane with Excellent Healing Ability at 45 °c. *Macromolecules*. 2015;48(17):6132-6141. doi:10.1021/acs.macromol.5b01162
8. Feula A, Tang X, Giannakopoulos I, et al. An adhesive elastomeric supramolecular polyurethane healable at body temperature. *Chem Sci*. 2016;7(7):4291-4300. doi:10.1039/C5SC04864H
9. Petrović ZS, Ferguson J. Polyurethane elastomers. *Prog Polym Sci*. 1991;16(5):695-836.
10. Koberstein JT, Galambos AF, Leung LM. Compression-molded polyurethane block copolymers. 1. Microdomain morphology and thermomechanical properties. *Macromolecules*. 1992;25(23):6195-6204.

11. Stadler R, de Lucca Freitas L. Thermoplastic elastomers by hydrogen bonding 1. Rheological properties of modified polybutadiene. *Colloid Polym Sci*. 1986;264(9):773-778.

12. Lange RFM, Van Gurp M, Meijer EW. Hydrogen-bonded supramolecular polymer networks. *J Polym Sci Part A Polym Chem*. 1999;37(19):3657-3670.

13. Du P, Wu M, Liu X, et al. Diels--Alder-based crosslinked self-healing polyurethane/urea from polymeric methylene diphenyl diisocyanate. *J Appl Polym Sci*. 2014;131(9).

14. Elkins CL, Park T, McKee MG, Long TE. Synthesis and characterization of poly (2-ethylhexyl methacrylate) copolymers containing pendant, self-complementary multiple-hydrogen-bonding sites. *J Polym Sci Part A Polym Chem*. 2005;43(19):4618-4631.

15. Tang X, Feula A, Baker BC, et al. A dynamic supramolecular polyurethane network whose mechanical properties are kinetically controlled. *Polymer (Guildf)*. 2017;133:143-150.

16. Woodward PJ, Hermida Merino D, Greenland BW, et al. Hydrogen bonded supramolecular elastomers: correlating hydrogen bonding strength with morphology and rheology. *Macromolecules*. 2010;43(5):2512-2517.

17. Courtois J, Baroudi I, Nouvel N, et al. Supramolecular soft adhesive materials. *Adv Funct Mater*. 2010;20(11):1803-1811.

18. Salimi S, Hart LR, Feula A, et al. Property enhancement of healable supramolecular polyurethanes. *Eur Polym J*. 2019;118:88-96.

19. Hermida-Merino D, O'Driscoll B, Hart LR, et al. Enhancement of microphase ordering and mechanical properties of supramolecular hydrogen-bonded polyurethane networks. *Polym Chem*. 2018;9(24):3406-3414.

20. Simic V, Bouteiller L, Jalabert M. Highly cooperative formation of bis-urea based supramolecular polymers. *J Am Chem Soc*. 2003;125(43):13148-13154.

21. Merino DH, Slark AT, Colquhoun HM, Hayes W, Hamley IW. Thermo-responsive microphase separated supramolecular polyurethanes. *Polym Chem*. 2010;1(8):1263-1271.

22. Houton KA, Burslem GM, Wilson AJ. Development of solvent-free synthesis of hydrogen-bonded supramolecular polyurethanes. *Chem Sci*. 2015;6(4):2382-2388.

23. Das S, Cox DF, Wilkes GL, et al. Effect of symmetry and H-bond strength of hard segments on the structure-property relationships of segmented, nonchain extended polyurethanes and polyureas. *J Macromol Sci Part B Phys*. 2007;46(5):853-875.

24. Tang X, Siviour CR, Buckley CP, Feula A, Hayes W. Effect of temperature and strain rate on the compressive behaviour of supramolecular polyurethane. In: *EPJ Web of Conferences*. Vol 94. ; 2015:1046.

25. Knoben W, Besseling NAM, Cohen Stuart MA. Rheology of a reversible supramolecular polymer studied by comparison of the effects of temperature and chain stoppers. *J Chem Phys*. 2007;126(2):24907.

26. Gooch A, Nedolisa C, Houton KA, Lindsay CI, Saiani A, Wilson AJ. Tunable self-assembled elastomers using triply hydrogen-bonded arrays. *Macromolecules*. 2012;45(11):4723-4729.

27. Siviour CR, Laity PR, Proud WG, et al. High strain rate properties of a polymer-bonded sugar: their dependence on applied and internal constraints. *Proc R Soc A Math Phys Eng Sci*. 2008;464(2093):1229-1255.

28. Chen WW. Experimental methods for characterizing dynamic response of soft materials. *J Dyn Behav Mater*. 2016;2(1):2-14.

29. Siviour CR, Jordan JL. High strain rate mechanics of polymers: a review. *J Dyn Behav Mater*. 2016;2(1):15-32.

30. Siviour CR. High strain rate characterization of polymers. *AIP Conf Proc*. 2017;1793. doi:10.1063/1.4971585

31. Gray III GT, Blumenthal WR. Split-Hopkinson pressure bar testing of soft materials. *ASM Handb*. 2000;8:488-496.

32. Kendall MJ, Siviour CR. Rate dependence of poly (vinyl chloride), the effects of plasticizer and time--temperature superposition. *Proc R Soc A Math Phys Eng Sci*. 2014;470(2167):20140012.

33. Kendall MJ, Siviour CR. Experimentally simulating adiabatic conditions: Approximating high rate polymer behavior using low rate experiments with temperature profiles. *Polym (United Kingdom)*. 2013;54(18):5058-5063. doi:10.1016/j.polymer.2013.06.049

34. Chen H, Trivedi AR, Siviour CR. Application of Linear Viscoelastic Continuum Damage Theory to the Low and High Strain Rate Response of Thermoplastic Polyurethane. *Exp Mech*. 2020:1-12.

35. Blain M, Cornille A, Boutevin B, et al. Hydrogen bonds prevent obtaining high molar mass PHU s. *J Appl Polym Sci*. 2017;134(45):44958.

36. Chattopadhyay DK, Raju K. Structural engineering of polyurethane coatings for high performance applications. *Prog Polym Sci*. 2007;32(3):352-418.

37. Krol P. Synthesis methods, chemical structures and phase structures of linear polyurethanes. Properties and applications of linear polyurethanes in polyurethane elastomers, copolymers and ionomers. *Prog Mater Sci*. 2007;52(6):915-1015.

38. Menzinger M, Wolfgang R. The meaning and use of the Arrhenius activation energy. *Angew Chemie Int Ed English*. 1969;8(6):438-444.

39. Peleg M, Normand MD, Corradini MG. The Arrhenius equation revisited. *Crit Rev Food Sci Nutr*. 2012;52(9):830-851.

40. Ferry JD. *Viscoelastic Properties of Polymers*. John Wiley & Sons; 1980.

41. Williams ML, Landel RF, Ferry JD. The temperature dependence of relaxation mechanisms in amorphous polymers and other glass-forming liquids. *J Am Chem Soc*. 1955;77(14):3701-3707.

42. Ward IM, Hadley DW. *An Introduction to the Mechanical Properties of Solid Polymers*.; 1993.

43. Colak OU. Modeling deformation behavior of polymers with viscoplasticity theory based on overstress. *Int J Plast*. 2005;21(1):145-160.

44. Colak OU, Dusunceli N. Modeling viscoelastic and viscoplastic behavior of high density polyethylene (HDPE). *J Eng Mater Technol*. 2006;128(4):572-578.

45. Qi HJ, Boyce MC. Constitutive model for stretch-induced softening of the stress-stretch behavior of elastomeric materials. *J Mech Phys Solids*. 2004;52(10):2187-2205.

doi:10.1016/j.jmps.2004.04.008

46. Zhang W, Cai Y. Theory of visco-elasto-plastic damage mechanics. In: *Continuum Damage Mechanics and Numerical Applications*. Springer; 2010:589-721.
47. Khan A, Zhang H. Finite deformation of a polymer: experiments and modeling. *Int J Plast*. 2001;17(9):1167-1188.
48. Khan AS, Lopez-Pamies O, Kazmi R. Thermo-mechanical large deformation response and constitutive modeling of viscoelastic polymers over a wide range of strain rates and temperatures. *Int J Plast*. 2006;22(4):581-601.
49. Sobhanie M, Isayev AI, Fan Y. Viscoelastic plastic rheological model for particle filled polymer melts. *Rheol acta*. 1997;36(1):66-81.
50. Saramito P. A new constitutive equation for elastoviscoplastic fluid flows. *J Nonnewton Fluid Mech*. 2007;145(1):1-14.
51. Kendall MJ, Drodge DR, Froud RF, Siviour CR. Stress gage system for measuring very soft materials under high rates of deformation. *Meas Sci Technol*. 2014;25(7):75603.
52. Gorham DA. Specimen inertia in high strain-rate compression. *J Phys D Appl Phys*. 1989;22(12):1888.
53. Siviour CR, Walley SM. Inertial and frictional effects in dynamic compression testing. In: *The Kolsky-Hopkinson Bar Machine*. Springer; 2018:205-247.
54. Hockly M, Siviour CR. Specimen Inertia in high strain rate tensile testing. In: *EPJ Web of Conferences*. Vol 94. ; 2015:1050.
55. Kapoor R, Nemat-Nasser S. Determination of temperature rise during high strain rate deformation. *Mech Mater*. 1998;27(1):1-12.

CHAPTER 5 SUGAR-FILLED SUPRAMOLECULAR POLYURETHANE

5.1 Introduction

Chapter 4 has introduced a predictive viscoelastic model for supramolecular polyurethane behaving from low to high strain rates, which leads our continuous works on polymer-particulate composites made by this material in this chapter as one of the objectives here is to further investigate their mechanical behaviour. The model results from the previous viscoelastic model of unfilled polyurethane were employed to the modelling work of polymer-particulate system. It is aimed to develop a predictive method with progressive procedures that links the mechanical behaviour between unfilled and filled polymer, characterising mechanical behaviour of filled polymer from the constitutive data of polymer matrix. The modelling procedure performed in three steps: the estimation on mechanical behaviour of polyurethane matrix using identified viscoelastic model; the effectiveness of mechanical properties reinforced from unfilled polymer to filled polymer; the employment of using appropriate damage criteria to eventually reproduce empirical behaviour of polymer composites. Different composites mixed with one of three types of rigid sugar and polyurethane were prepared. The quasi-static experiments performed on these specimens, determined all necessary parameters describing reinforcement and strain-induced damage mechanism, validated the practicability and feasibility of the model applications. In the case of high strain rates, the model correlated parameters with filler dimension and composite compositions, cooperated with mechanical behaviour from polyurethane matrix in the dependence of temperature and loading rates, successfully reproduced the strain-stress for composites at large deformation and high strain rates up to 1800 s^{-1}. The model was calibrated using quasi-static experimental results, able to effectively predict the experimental behaviour of the composite under high strain rates, based on the predictive behaviour from polyurethane matrix and composite compositions.

5.2 Paper C:

Experimental characterisation and modelling of the strain rate dependent mechanical response of a filled thermo-reversible supramolecular polyurethane[1]

Abstract

Composites consisting of a polymer binder filled with various particles are widely used in industrial applications, and good engineering design requires the ability to produce mechanical models of these materials. One weakness of many composites is the use of cross-linked elastomers as matrix materials, which reduces re-usability and recyclability. In this research a recently developed reusable and low temperature processable supramolecular polyurethane was mixed with sugar particles to produce a model composite material with different particle sizes and volume fractions, which was then characterised and modelled. Large strain mechanical properties of the material were characterised in compression at strain rates up to approximately 1800 s^{-1}, supported by measurements of the small strain viscoelastic response at different temperatures and frequencies. A model was developed that combined viscoelastic theory, filler-reinforcement and strain-induced damage. The viscoelastic response was taken from previously published data, whilst the filler reinforcement and damage were calibrated against quasi-static experiments. The model also provided a good prediction of the high strain rate behaviour, for which the effect of adiabatic heating in the sample was also considered. The model parameters were related back to the filler particle size and volume fraction. Finally, a preliminary study of geometry and strength recovery was performed.

Keywords: Supramolecular Polyurethanes, Viscoelasticity, Filler Reinforcement, Debonding, High-strain rates

[1] Chen H, Hart LR, Hayes W, Siviour CR. Experimental characterisation and modelling of the strain rate dependent mechanical response of a filled thermo-reversible supramolecular polyurethane. Submitted to Composites Science and Technology: 05/08/2021

1 Introduction

Recent research has led to the development of synthetic, healable 'supramolecular' polyurethanes (SPUs), able, at relatively low temperatures, to recover their topology and mechanical properties when damaged[1–6]. These polymers have advantages of low-temperature processability, low density, biocompatibility and ductility; however, their low moduli at ambient temperature present challenges for use in load-bearing structures and biomedical applications[7]. Over the last few decades, particulate-filled polymers, made by embedding rigid particles into polymer substrates have attracted great scientific interest and enabled specific applications by improving properties such as stiffness and toughness compared to the polymer binder alone[8]; for example, appropriate fillers have allowed development of composites for bio-applications[79]. Furthermore, fillers can be used to introduce desired functionalities such as thermal conductivity[10,11], electrical conductivity[12], or magnetic performance[13], etc. Common mechanical modifiers include clay[14], carbon-black[15], fumed silica[16] or two-dimensional fillers such as nano-tubes, flakes and fibers[17]. The overall mechanical properties of the composite can depend on the filler size[18,19], filler shape[20,21], filler distribution, alignment[22–24], geometric orientation, and interfacial adhesion between filler and matrix[25–29]. Another purpose of mixing particulates in a soft polymer is to take advantage of the polymer's functionality; for example in polymer bonded explosives or composite propellants[30–32], where the role of the polymer binder is to make the explosive system more resilient and less sensitive during processing and transportation[33–35].

Mechanical experiments in tension, compression or bending are conventionally used to characterise basic composite properties; more complex investigations such as microscopy, spectroscopy and scattering[36] are used to investigate structural evolution[37–40] but these observations must then be linked to the overall mechanical response, which can be challenging. Internal mechanical responses, such as interfacial failure[41,42] and fracture[43,44], can depend on the nature of the filler itself[45,46], the composition[47] and the loading situation (e.g. impact[33,48,49],

ballistic[50,51], fracture testing[52,53]). The development of simple models that link the structure of the composite to its mechanical responses are of importance for effectively utilizing these materials in industry and science. This is the subject of the current paper.

Another purpose of the study reported in this paper is to determine the mechanical properties at high strain rates, and predict this behaviour with a simple model calibrated form low rate data. The conventional method for high strain rate mechanical characterisation of materials is the split-Hopkinson pressure bar[54], which has previously been employed to understand mechanical behaviour of similar filled polymers[33,55,56]. However, there are physical limitations for testing low modulus materials at high strain rates[57,58]. The natural frequency of oscillation of the specimen and the effects of specimen inertia both lead to additional forces that mask the underlying specimen response. Further, for materials that deform at small stresses, it is difficult to accurately measure the forces supported by the specimen using a metallic transmission bar due to weak transmitted signals, compared to the background noise[59]. To ensure that the properties of the specimen are truly representative of the material response, the specimen needs to be loaded uniformly (i.e. in static stress equilibrium). However, the characteristic low wave speeds in low modulus specimens can result in non-equilibrated stresses causing non-uniform deformation in the specimen (i.e. specimen yielding before dynamic stress equilibrium), which invalidates the results obtained[60]. Finally, whilst high-speed imaging can be used to monitor deformation and composite failure[61–64], it is not technically possible to observe microstructural evolution in high strain rate experiments. Hence, there is a requirement for approaches that combine experiments and modelling in order to link low and high strain rate data, with the ultimate aim of better understanding the behavior under high-rate conditions.

In this paper, we characterise and model a particulate composite combining an SPU binder with sugar fillers. As well as being inert and non-toxic, the use of sugar has the

advantage that it is possible to produce specimens with various, but relatively well controlled, particle sizes and filler loadings. We propose a combined modelling method based on a predictive model for the SPU behaviour published in a previous paper[65]. This is combined with models for the modulus enhancement owing to the filler, and the subsequent strength reduction during loading as the filler debonds from the polymer matrix[33,66]. The modelling procedure starts with a viscoelastic polymer model (VPM) for the SPU, characterising the behaviour up to large strains and over a range of strain rates[65]. This model has the advantage of all the parameters being derived from standard rheological and low-rate experiments. The modulus of the composite is then derived using Guth's reinforcement equation. The damage equation is described using a typical phenomenological model for debonding, with parameters that fit to compression stress-strain data, and which can be related to filler volume fraction and particle size. The model was applied to composites with different compositions, deformed over a range of strain rates up to 1800 s^{-1}. For modelling high rate behaviour, the adiabatic heating effect was also incorporated. The model implementations and experimental results in this paper therefore provide an applicable methodology for interpreting the mechanical behaviour of particulate-filled polymers. Since a previous study on this polymer matrix has shown that the polymer has ability to recover mechanical properties[1,33], recovery in these composites was also investigated.

2 Material and Experimental Method

2.1 Synthesis of SPU

The polymer binder, Fig. 5-1, was a healable SPU which has been previously described[1]. The SPU was synthesized using co-polymer polymerization under the reaction of hydrophobic diol, Krasol™ HLBH-P2000 with methylene diphenyl diisocyanate (MDI) at 80 °C for three hours to feature isocyanate end-groups. 4-(2-Aminoethyl)morpholine was then added to install the receptor end-groups *via* urea bond formation, thus the desired SPU with urea morpholine end groups can be formed[1]. The polymer has been designed to permit phase separation, and to allow formation of a self-assembled network *via* non-covalent hydrogen bonding and aromatic π-π stacking. The resulting polymer exhibits low temperature processability, excellent adhesion, healability at body temperature and biocompatibility. The polymer has recently undergone extensive thermo-mechanical characterisation, demonstrating its reusability[65]. Further, a model for rheological behaviour was presented and a constitutive viscoelastic polymer model was proposed for its compression loading behaviour at strain rates up to 1200 s^{-1}.

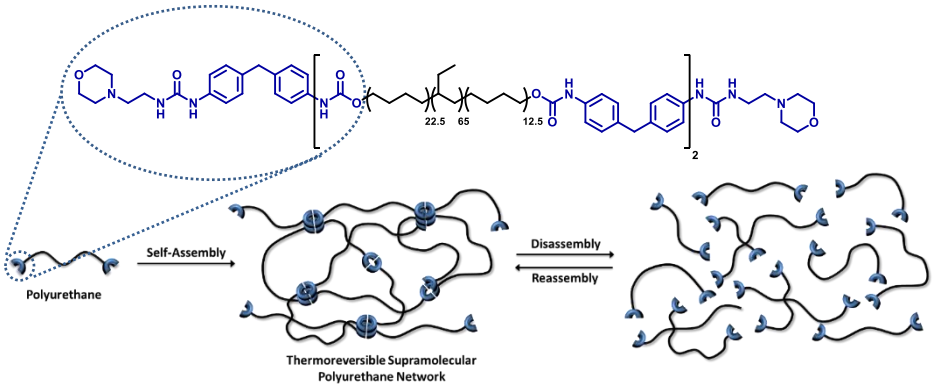


Fig. 5-1: The supramolecular healable polyurethane used in this study, featuring urea morpholine end groups[1]

2.2 Particulate composite: Sugar-filled SPU

The sugar-filled polymer specimens for compression experiments were moulded individually. Three types of sugar particles (Tate & Lyle Ltd, UK) were used: granulated (530-670 μm), caster (270-340 μm) and icing (20-25 μm) sugars; micrographs of the sugar fillers for these three categories are shown in Fig. SI-1; the product specification[67] for particle sizes is also given in Table SI-1. The density of sugar, ρ_f , is 1600 kg m^{-3}.[68] To produce the composite, the appropriate amount of sugar was immersed into molten polymer at 80 °C; stirring, mixing and extruding the compound was performed gently and slowly, to avoid grinding or crushing the sugar particle, and preventing air voids becoming trapped inside the specimens. The mixture was gently injected into a PTFE mould (Fig. SI-2). Cylindrical specimens were prepared, of diameter 6.35±0.1 mm and length 7.4±0.1 mm. Various filler loading densities were used; for granulated sugar, these were 25, 50 70 and 75% (G25, G50, G70 and G75) by volume; for caster sugar 50 and 65% (C50 and C65) and for icing sugar 30 and 50% (I30 and I50). In order to confirm that the specimens were made to the correct composition, their densities were calculated and compared to the theoretical density before experiments; see Table SI-2 for an example.

2.3 Low- and high-rate compression experiments

Low-rate compression experiments were performed in a commercial screw-driven load frame (Instron 5980) using an environmental chamber to maintain a constant temperature of 25 °C. The specimen was centered between two loading anvils and compressed under true strain rate control at 0.01 s^{-1}. The load cell has measurement capacity of 1kN. Force and deformation records from the crosshead were used to calculate the true stress-strain response, assuming that the deformation took place at constant volume. Specimens of composites G25, G50, G75, C50, C65, I30, I50 were tested at a true strain rate of 0.01 s^{-1}, composite G50 was also tested at 0.001 and 0.1 s^{-1}. After the compression experiments, some specimens were held at a constant

temperature of 37 °C, in order to observe their shape recovery.

In order to characterise the response to high strain rate deformation, up to 1800 s^{-1}, high rate experiments were performed using a Split-Hopkinson pressure bar (SHPB)[54,57,69,70]. In this experiment, a cylindrical specimen is placed between the ends of two titanium alloy bars, shown in Fig. 5-2. A third bar, known as a striker, is accelerated in a gas gun until it impacts the incident bar. The impact creates an 'incident' stress wave that travels along the bar to the specimen. At the bar-specimen interface, the wave is partially reflected back along the incident bar and partially transmitted through specimen. The incident, reflected and transmitted waves are measured by strain gauges attached to the incident and transmission bars. These measurements are used to calculate the stress equilibrium, deformation rate and surface force at the bar-specimen interfaces, from which the corresponding true strain-stress behaviour in the specimen can be determined[54,59]. The SHPB experiments were performed at a room temperature of 20 °C.

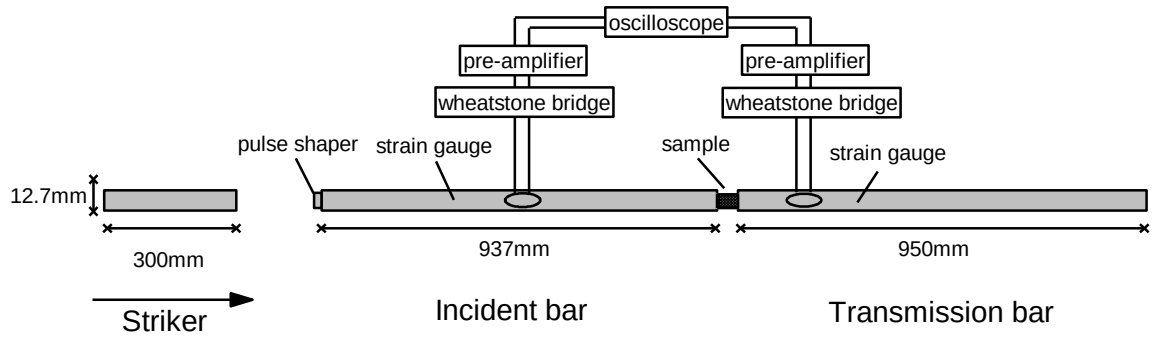


Fig. 5-2: Schematic diagram of the SHPB experiment

3 Modelling and Experimental Results

3.1 Polymer model – viscoelastic theory

The SPU polymer matrix was modelled using a viscoelastic method introduced in previous work[65]. The model was assembled from an empirical Maxwell model combined with an additional dashpot: the former was parameterized by a Prony series that used empirical thermal-mechanical data from rheometry and DMA experiments in the principle of time-temperature superposition; the latter was defined to allow the whole model to fit the empirical rate-

dependence. The overall model enables the large strain response to be described in compression up to ~1200 s^{-1}. The model construction and simulations were executed in Simscape® (Simulink, Matlab®). In this paper, the model was again used for the mechanical behaviour of the unfilled SPU over a range of strain rates, and was combined with a particle reinforcement equation and a damage equation to describe the composite behaviour. The polymer model will be referred to as the viscoelastic polymer model, or VPM.

3.2 Filled polymer – moduli reinforcement

There has been significant research on the mechanical response of particle-filled polymers[71–77]. One of the earliest theories for a composite system with rigid spherical inclusions was based on Einstein's equation[72], which describes the shear modulus of the composite, $G_{c,0}$, in terms of the modulus of the polymer, $G_{m,0}$, and the volume fraction of filler V_f as

$$G_{c,0} = G_{m,0}(1+2.5V_f)\,. \tag{5-1}$$

This equation is most accurate for low filler concentrations in which the stress field around a particular particle is not affected by the others. The Kerner equation[74] considers the effect of the particle-matrix interaction on viscosity constraints. The system has more reinforcing action between fillers at high filler loadings, which significantly increases the internal stress. The stiffness is calculated from

$$G_{c,0} = G_{m,0}\left(1+\frac{V_f}{V_m}\frac{15(1-\nu_m)}{(8-10\nu_m)}\right), \tag{5-2}$$

where the model includes Poisson's ratio of spherical particles, υ_m, and matrix volume fraction, V_m.

The series and parallel model[75] gives upper and lower bounds of the modulus, which depend on the particle distribution as

$$\begin{cases} E_{c,0,-upper} = E_f V_f + E_m V_m \\ E_{c,0,-lower} = \dfrac{E_{f,0}E_{m,0}}{E_{f,0}V_m + E_{m,0}V_f}\,. \end{cases} \tag{5-3}$$

Here, the Poisson's ratio of the filler and matrix are the same, and the model is expressed in modulus, $E_{c,0}$.

The Hirsch model[76], is a summation of series and parallel models in which a parameter, *x*, allows arbitrary contributions between the upper and lower bound solutions:

$$E_{c,0} = x(E_{f,0}V_f + E_{m,0}V_m) + (1-x)\left(\frac{E_{f,0}E_{m,0}}{E_{f,0}V_m + E_{m,0}V_f}\right). \quad (5\text{-}4)$$

The model used in this paper is Guth's reinforcement equation (RE)[73]; here the composite stiffness is calculated as

$$E_{c,0} = E_{m,0}(1 + 0.67PV_f + 1.62P^2V_f^2), \quad (5\text{-}5)$$

where *P* is nominally the aspect ratio for non-spherical particles, but here is treated as a fitting parameter to obtain the correct reinforcement for different volume fractions. In this paper, we define the ratio, $R_{Guth} = E_{c,0} / E_{m,0}$, as a reinforcement factor that increases the modulus of the polymer matrix to that of the composite at the same strain rate and temperature conditions.

To characterise *P*, empirical data from specimens of unfilled SPU, G25, G50 and G75, tested in compression at a strain rate of 0.01 s^{-1}, were used, shown in Fig. 5-3a. The apparent Young's moduli (i.e. initial compression moduli) were extracted and fitted to all the above formulations with appropriate values of $E_{m,0}$ (from the unfilled material), $E_{c,0}$, V_f and using υ_m = 0.49. Fig. 5-3b shows a comparison of the models with the experimental data, indicating that the Guth equation with P = 3.9 gives the best fit.

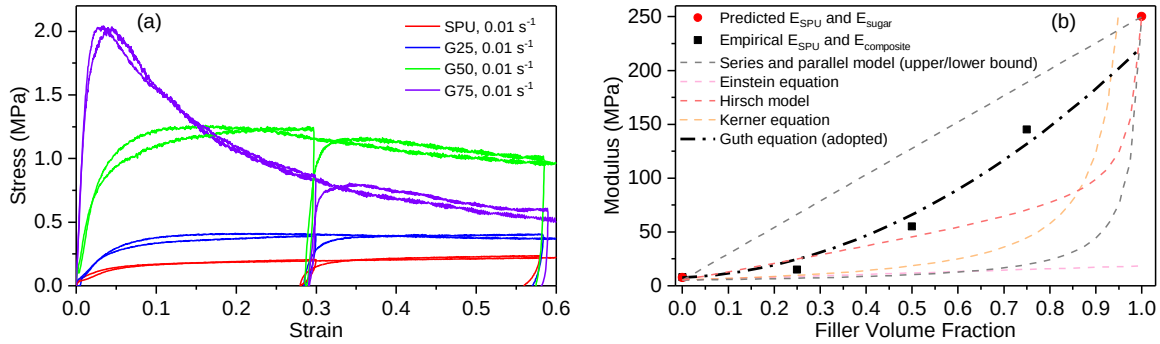


Fig. 5-3: (a) Stress-strain data for filled and unfilled SPU tested in monotonic and cyclic compression experiments at a strain rate of 0.01 s^{-1} and 25 °C. The apparent Young's modulus is 7.2 MPa for the unfilled polymer and 15, 55 and 145 MPa for filled polymer specimens G25, G50 and G75 respectively. The empirical reinforcement factor, R_{test}, is calculated as 2 (G25), 7 (G50) and 20 (G75). These ratio values can be optimally fitted by the Guth equation when P=3.9, which gives R_{Guth} as 3.2, 8.5 and 16.8. The predicted Young's modulus from the viscoelastic polymer model at 0.01 s^{-1} is about 7.5 MPa for unfilled polymer, which gives predicted Young's moduli of about 24, 64 and 126 MPa for G25, G50 and G75. Parameters used in other reinforcement equations are: υ_m=0.49 for Kerner equation; E_p=250 MPa for the series and parallel model; x=0.3 for the Hirsch model.

3.3 Composite model – continuous damage model

The strength of the filled polymer is dominated by the structural integrity of the filler-matrix interface. The debonding surrounds individual crystals at small strains, and forms micro-cracks as the strain increases, resulted in strain softening in the constitutive response[56,78]. This is consistent with the observed behavior of crystals debonding from the binder by Siviour[33]. Li *et al.*[79] observed interface debonding of matrix and particles as the main form of damage at small stress, while at higher stresses micro-cracks along the boundary of crystals and transgranular fracture through crystals developed. Ravindran *et al.*[48] observed localized shear in polymer rich areas and in crystals that experience fracture, indicating another phenomenon of failure evolution. Computational simulations have also been employed[80–84], to verify the initiation of failure in interfacial debonding.

Building on previous research[33], the overall damage is modelled here by degrading the modulus using a function similar in form to the Weibull distribution[8586]. In this previous research, an activation strain, ε_a, was used to parameterize the debonding according to

$$E=E_{c,0}\left[1-\exp\left(-\left(\frac{\varepsilon_a}{\varepsilon}\right)^2\right)\right] \quad (5\text{-}6)$$

$$E_{c,0}=R_{Guth}\times E_{m,0} \quad (5\text{-}7)$$

$$\sigma=E\cdot\varepsilon \quad (5\text{-}8)$$

where $E_{c,0}$ is the Young's modulus of the intact composite predicted using the Guth equation combined with the Young's modulus of the polymer, $E_{m,0}$, from the viscoelastic polymer model. R_{Guth} is the ratio value, calculated from the Guth factors above, Fig. 5-3. The value of ε_a was fit to the experimental data to determine the stress. The model outputs are given in Supplementary Information (Figures SI-3 and SI-4). The limitation of using this constitutive model is that it over-estimates the post-yield softening behaviour.

The first modification to this model was to replace the Young's modulus, $E_{c,0}$, with the full local stiffness from the viscoelastic polymer model; now E_c was defined as the local secant modulus of the composite. This gives

$$E=E_c\left[1-\exp\left(-\left(\frac{\varepsilon_a}{\varepsilon}\right)^2\right)\right], \quad (5\text{-}9)$$

$$E_c=R_{Guth}\times E_m, \quad (5\text{-}10)$$

where R_{Guth} takes the same value as above. Here, E_m is the local secant modulus of the polymer, determined from the viscoelastic polymer model. The activation strain, ε_a, is used again to fit a range of experiments; the modelling process is shown in Fig. 5-4. First, a representative 'undamaged' stress-strain curve was predicted by using R_{Guth} to reinforce the intrinsic polymer strength, shown in Fig. 5-4a. Then, the ratio of the empirical stress-strain curve to this undamaged curve was calculated as a function of strain. Plotting these ratios produces a damage curve with appropriate value of ε_a for each composite, which can be compared to the curves produced by the model in Eq. (5-9) with different values of ε_a, Fig. 5-4b. Finally, the best value of ε_a was used to produce the stress-strain curves in Fig 5-4c. To put this into context, the stress-strain curves produced for different damage factors are shown in Fig. SI-5. There are two weaknesses of this model: the damage starts too late; meanwhile the degraded strength

eventually drops to zero, which is not the case in the experiment.

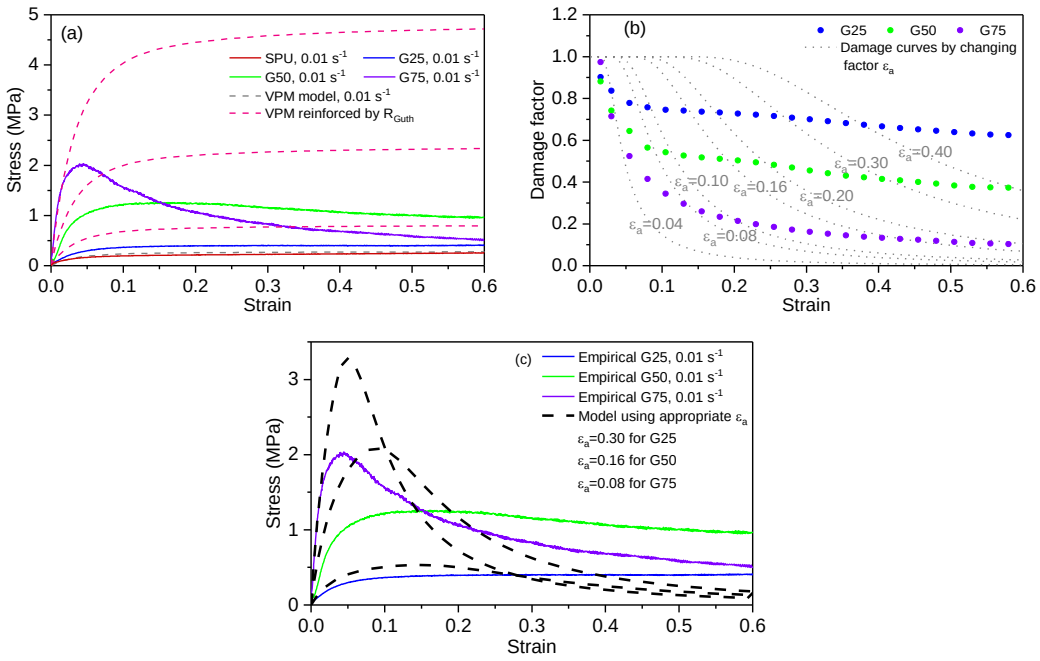


Fig. 5-4: (a) Comparison of model stress-strain curves with and without particle reinforcement to experimental data for three different filled SPUs; (b) Empirical damage factor compared to those obtained using different values of ε_a in Eq. (5-9); (c) Comparison of stress strain curves produced using three values of ε_a, in Eq. (5-9), to experimental data.

To correct the second problem, an additional parameter, *k*, was added to the equation as a mathematical solution to adjust the strength at higher strains, giving

$$E = E_c\left[1 - k\exp\left(-\left(\frac{\varepsilon_a}{\varepsilon}\right)^2\right)\right], \tag{5-11}$$

where *k* represents the residual strength remaining in the filler-matrix system. The two parameters was again fitted to the experimental data, this is explored for different values of ε_a and *k* in Figures SI-6 and SI-7, and the final fits are presented in Fig. 5-5. The addition of parameter, *k*, allows activation energies to be used that the better replicate initial degradation of the modulus, whilst maintaining the material strength at larger strains.

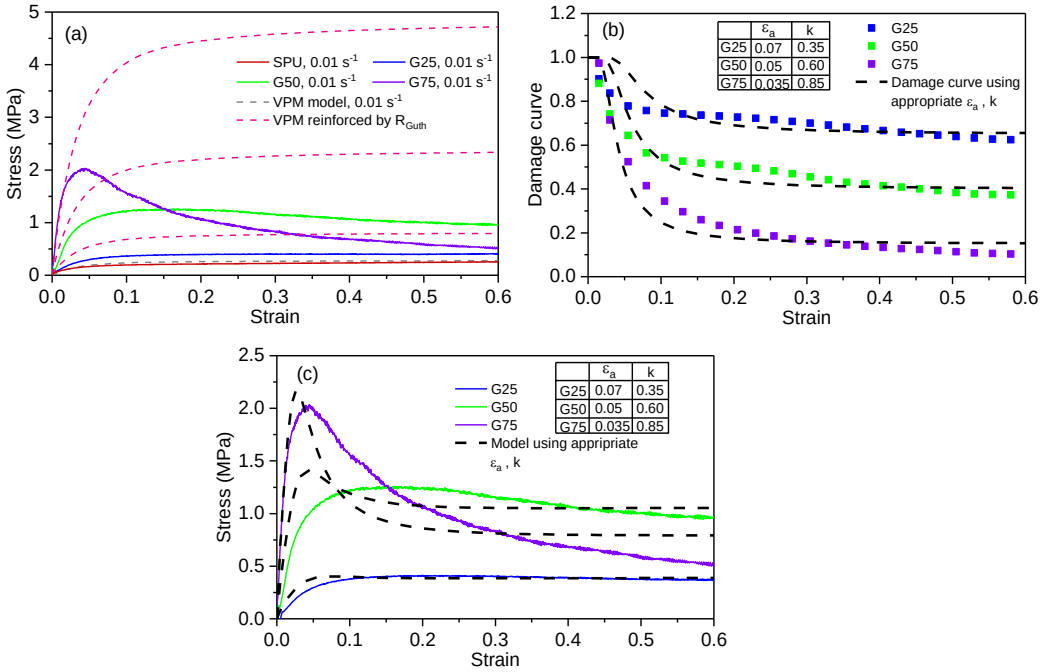


Fig. 5-5: Stress-strain simulation using different value of ε_a and k in Eq. (5-11). The parameters R_{Guth}, ε_a, k were: G25: 3.2, 0.07, 0.35; G50: 8.5, 0.05, 0.6; G75: 16.8, 0.035, 0.85.

Following this modification, it was found that the strength of the material derived from the model remains too *high* at large strains. This was found to be a particular problem for modelling data at high strain rates, for which the matrix material itself maintains increasing stress as strain increases, but the strength of the composite was observed to reach a plateau, see Figures SI-8 and SI-9. The damage model, with the same parameters as had been fit to the low-rate experiments, gives a damage curve with a plateau at strains above 0.15 (Figures SI-8b and SI-9b). This inhibition in decrease of modulus resulted in insufficient damage to replicate the strain softening at large deformation.

The final expression, used in the rest of this paper, modified the dependence of the damage factor on the strain ratio:

$$E = E_c\left[1 - k\exp\left(-\frac{\varepsilon_a}{\varepsilon}\right)\right]. \qquad (5\text{-}12)$$

The effect on both the damage ratio and the resulting stress-strain curves is given in Figures 5-6 and 5-7; for this model, the effect of the two parameters is presented in more detail. Here, the activation strain, ε_a, dominates the initial modulus and position of the peak stress, whilst k

adjusts the behaviour at larger strains. This modelling process: a viscoelastic polymer model for the polymer matrix, Guth equation for the filler reinforcement and this damage equation were chosen to simulate all the experimental data in this study. The ultimate fits to the quasi-static data are shown in Fig. 5-8.

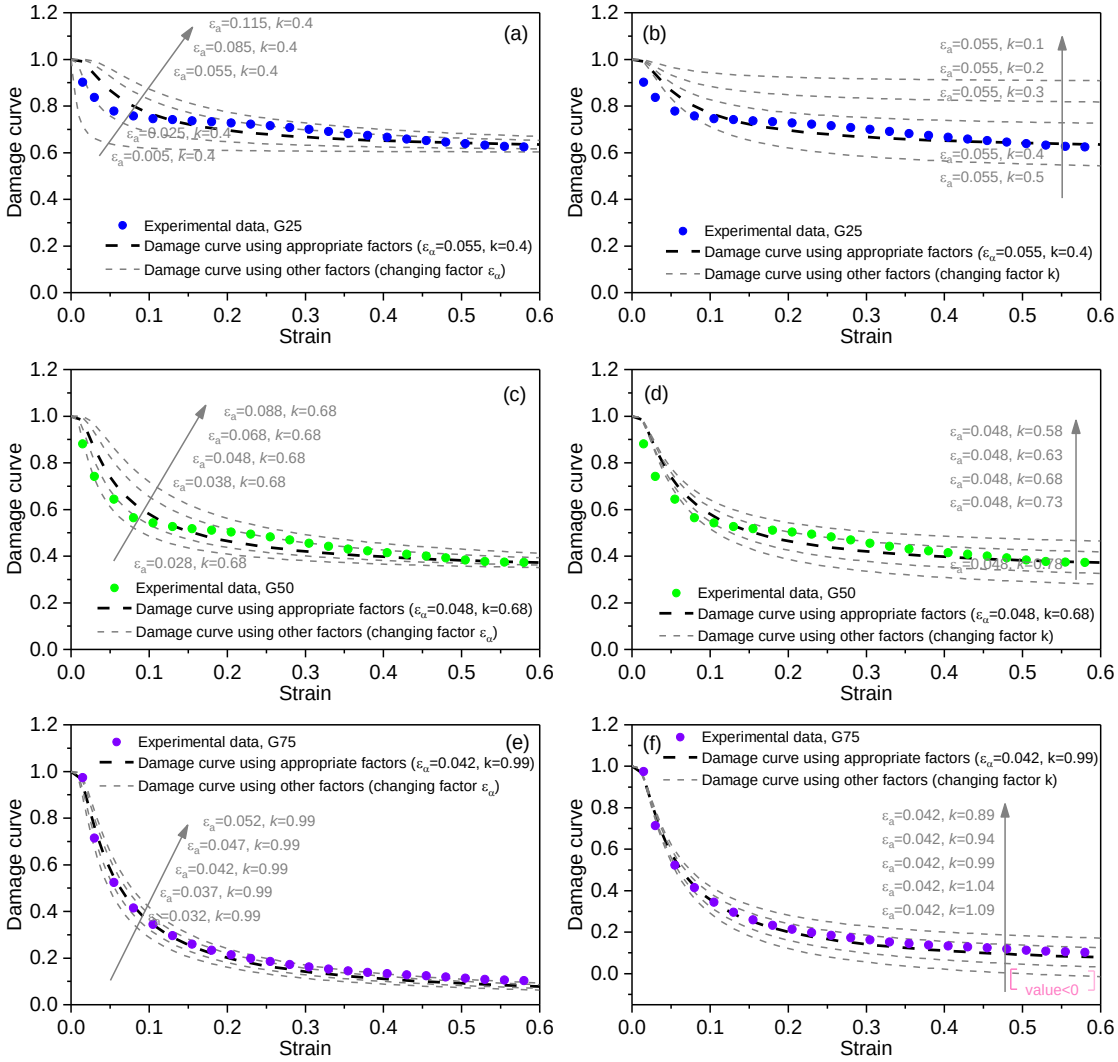


Fig. 5-6: Damage curve using damage Eq. (5-12) with different values of ε_a and k. The empirical damage was determined by $E_{\text{secant,test}} / (E_{\text{m}} \times R_{Guth})$. E_m is the local secant modulus determined by the viscoelastic polymer model.

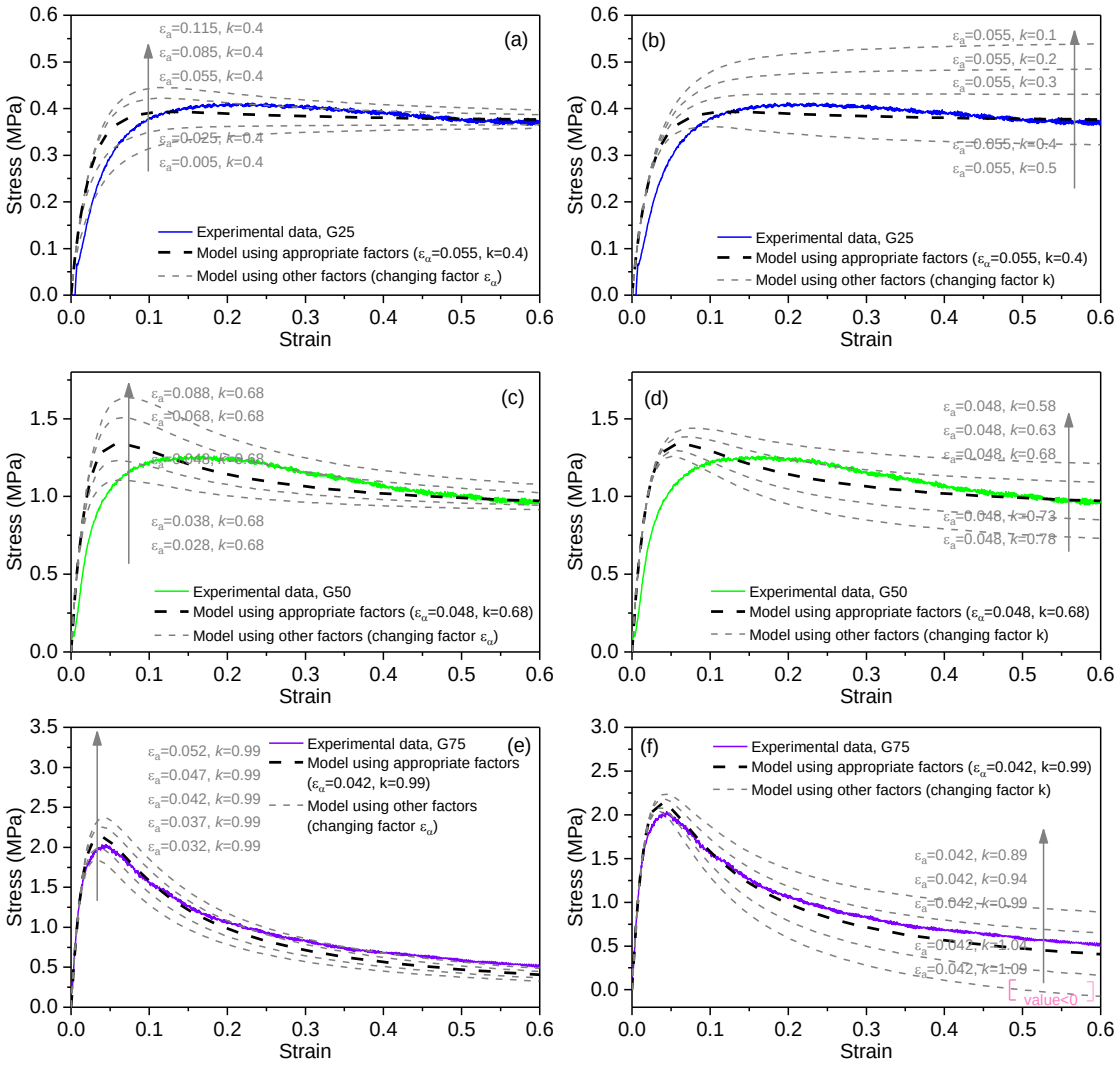


Fig. 5-7: Strain-stress behaviour modelled using damage Eq. (5-12) with different values of ε_a and k. The ultimate stress was determined *via* $\sigma = E \cdot \varepsilon$.

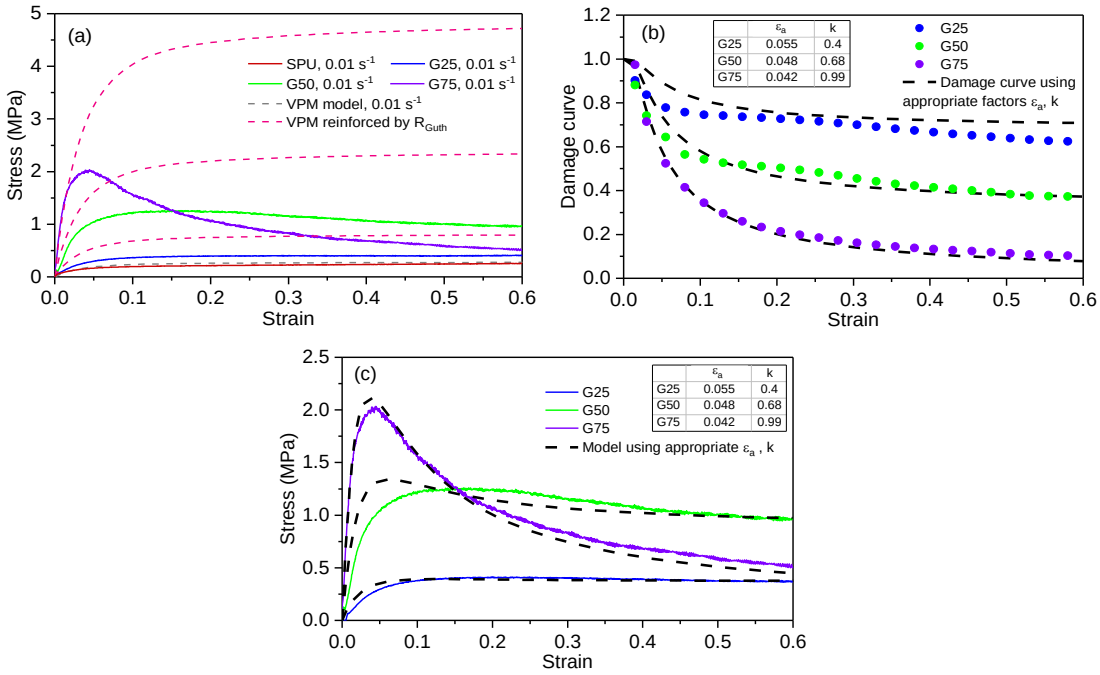


Fig. 5-8: Model implementation for specimens of G25, G50 and G75, in which (a) the Guth reinforcement equation was used to reinforce the viscoelastic polymer model, (b) the damage equation with optimal values of ε_a and k from Eq. (5-12) was used to perform (c) the modelling of the composite behaviour at 0.01 s^{-1} and 25 °C. The parameters, R_{Guth}, ε_a, k were assigned to the three types of composites as follows G25: 3.2, 0.055, 0.4; G50: 8.5, 0.048, 0.68; G75: 16.8, 0.042, 0.99.

3.4 Further model parametrization

The model was fitted to a series of experiments with different particle sizes. In all cases, the viscoelastic polymer model was first used to predict the behaviour of the matrix at each strain rate; then the stress-strain curve was modified using the appropriate reinforcement factor according to the specific filler loadings. Finally, the stress-strain curve thus produced was compared to the empirical data for the same material, to produce a damage factor as a function of strain. Again, parameters ε_a and k were fitted. Results from the granulated sugar specimens with different volume fractions (G25, G50, G75) have been presented above; Fig. 5-9 shows equivalent data from specimens with a fixed volume fraction but different particle sizes: G50, C50 and I50.

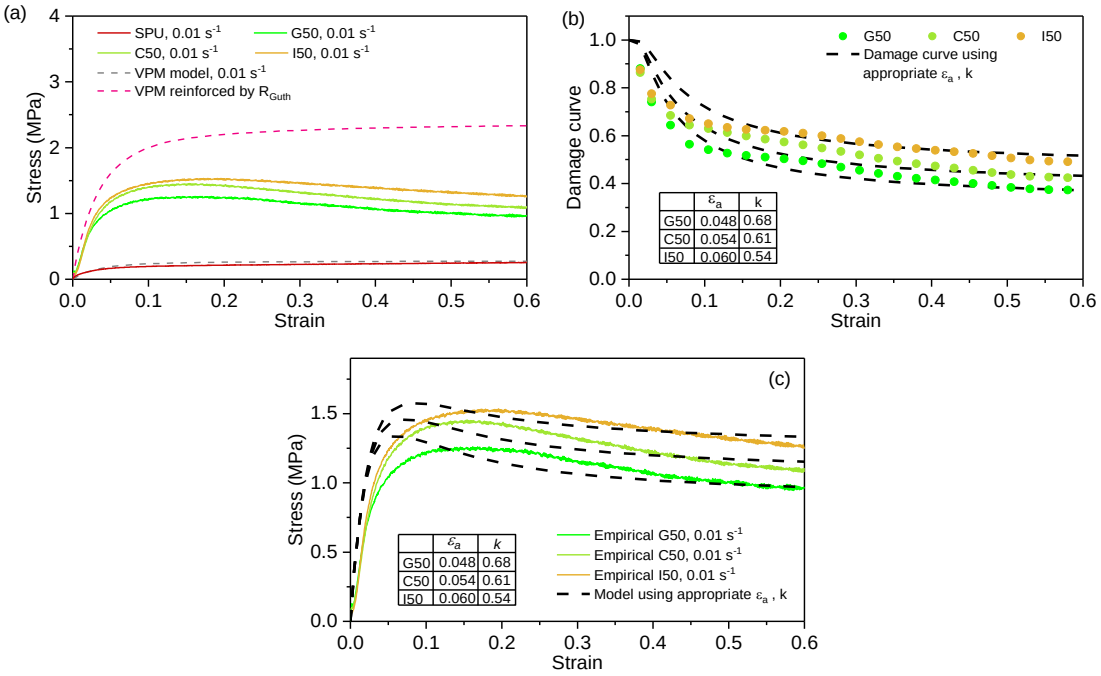


Fig. 5-9: Model implementation for specimens of G50, C50 and I50, in which (a) the Guth reinforcement equation was used to reinforce the viscoelastic polymer model, (b) the damage equation with optimal value of ε_a and k from Eq. (5-12) was used to perform (c) modelling of the composite behaviour at 0.01 s^{-1} and 25 °C. The parameters R_{Guth}, ε_a, k were assigned as G50: 8.5, 0.048, 0.68; C50: 8.5, 0.054, 0.61; I50: 8.5, 0.06, 0.54.

The values of ε_a and k obtained so far were then plotted against the microstructural parameters of filler diameter, d, and filler loading, V_f, Fig. 5-10. In both cases, the relation was observed to be linear, allowing a 3D plane surface to be plotted for each of the two model parameters. From this surface, values of ε_a and k can now can be estimated for a specific composite composition.

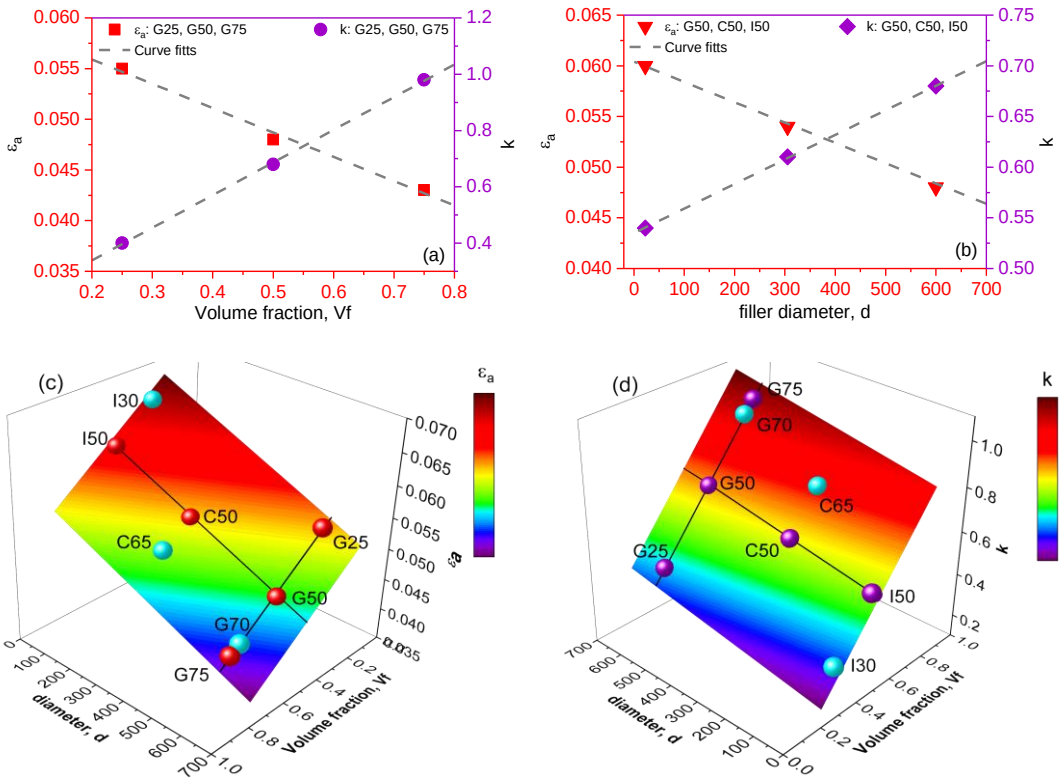


Fig. 5-10: (a) and (b) show the linear relations between fitting parameters ε_a , k and filler particle size and volume fraction. These two 2D plots correspond to 3D surfaces (c) and (d). From surface plots (c) and (d), a unique set of damage parameters can be extracted for any particle diameter and volume fraction. For example, the parameters R_{Guth}, ε_a, k were assigned to specimens of I30 and C65 as: I30: 4, 0.065, 0.31; C65: 13, 0.051, 0.78.

To verify the parametrization, additional compression experiments were performed on materials with different compositions: Icing Sugar with volume fraction 30% (I30) and Caster Sugar with volume fraction 65% (C65), again at 25 °C and 0.01 s^{-1}. The required parameters, ε_a and k, were extracted from the 3D surface plots in Fig. 5-10. Full empirical data for specimens I30 and C65 can be seen in Fig. SI-10. A comparison of the models to experimental data is presented in Fig. 5-11.

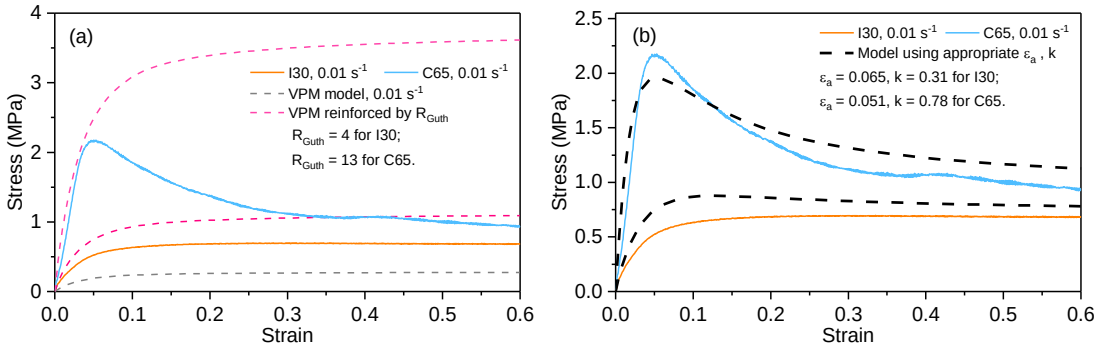


Fig. 5-11: Model implementation for specimens of I30 and C65. (a) Comparison of model with Guth reinforcement equation, but no damage, to the experimental data; (b) comparison of full model with damage to the experimental data. The parameters, R_{Guth}, ε_a, k, were assigned as I30: 4, 0.065, 0.31; C65: 13, 0.051, 0.78, to model the behaviour at 0.01 s^{-1} and 25 °C.

3.5 Model application for low- to high-rate behaviour

Data from further experiments on G50, G70 and G75, and the corresponding models, are shown in Figures 5-12 to 5-15 to validate the model application to both low and high strain rate behavior. To capture the experiments with different loading rates, the viscoelastic polymer model at the same ambient temperatures and strain rates was assigned. To respond to temperature changes, the principle of time-temperature superposition was employed: a master curve of modulus was produced at a new shifted reference temperature, and this curve was used to build a new set of Prony series parameters[65]. This allowed the predicted constitutive behaviour for unfilled SPU at the specific reference temperature to be determined, whilst the values of R_{Guth}, ε_a and k determined above were employed. For compositions that were yet untested, the relevant parameters were assigned by extracting values from 2D/3D mapping plots in Fig. 5-10.

Results from quasi-static experiments and the equivalent models for specimen G50 at 0.001, 0.01 and 0.1 s^{-1} are shown in Fig. 5-12 (the full set of experimental data is shown in Fig. SI-11). The model is able to accurately reproduce the observed behaviour. For higher rate data up to 1800 s^{-1}, Fig. 5-13, the model captures well the initial stiffness and subsequent behaviour at small strains (full data in Figures SI-12 to SI-14); however, the stress was overestimated at large strains compared to the empirical data. Similar observations were made for specimens of

G70 and G75, Figures 5-14 and 5-15. Although it is possible to optimally fit the experimental data and thus improve the model fittings by using an alternative set of parameters (see Fig. SI-15), this reduces the predictive capability of the viscoelastic polymer model and the utilization of parameters from quasi-static experiments; it also removes the correspondence to composite composition. A second approach to achieve better fitting at high strain rates, introduced in the next section, is to consider the effect of adiabatic heating to reduce the stress at large deformation in these experiments.

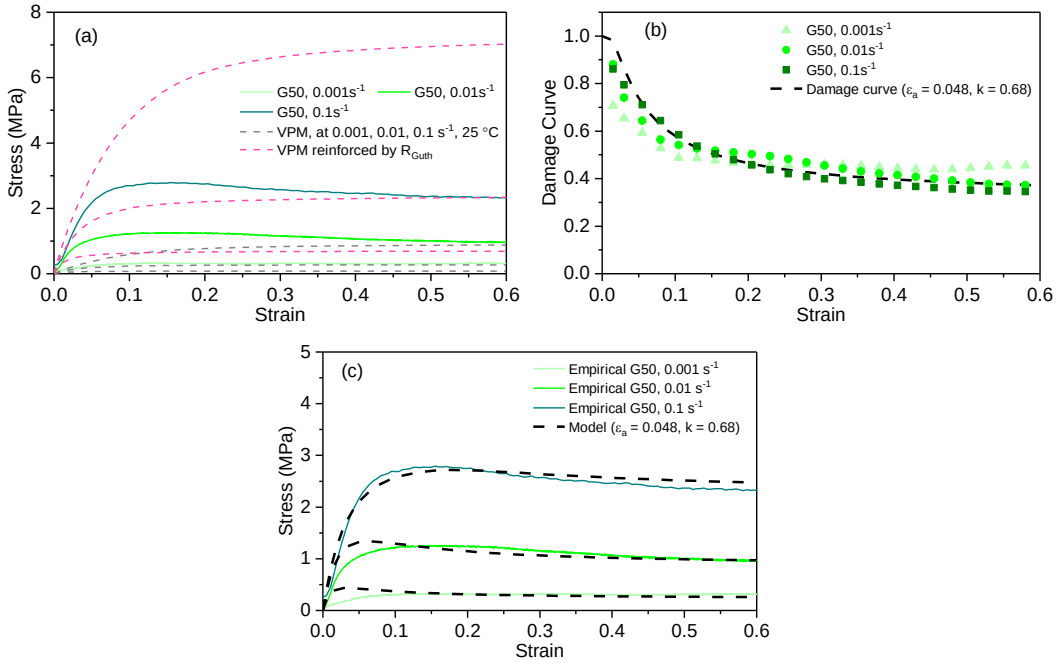


Fig. 5-12: Model implementation for specimen G50, in which (a) the Guth reinforcement equation was used to reinforce the viscoelastic polymer model, (b) the damage parameters ε_a and k were used to model the composite behaviour (c) from 0.001 to 0.01 s^{-1} and 25 °C. The parameters, R_{Guth}, ε_a, k were assigned as G50: 8.5, 0.048, 0.68.

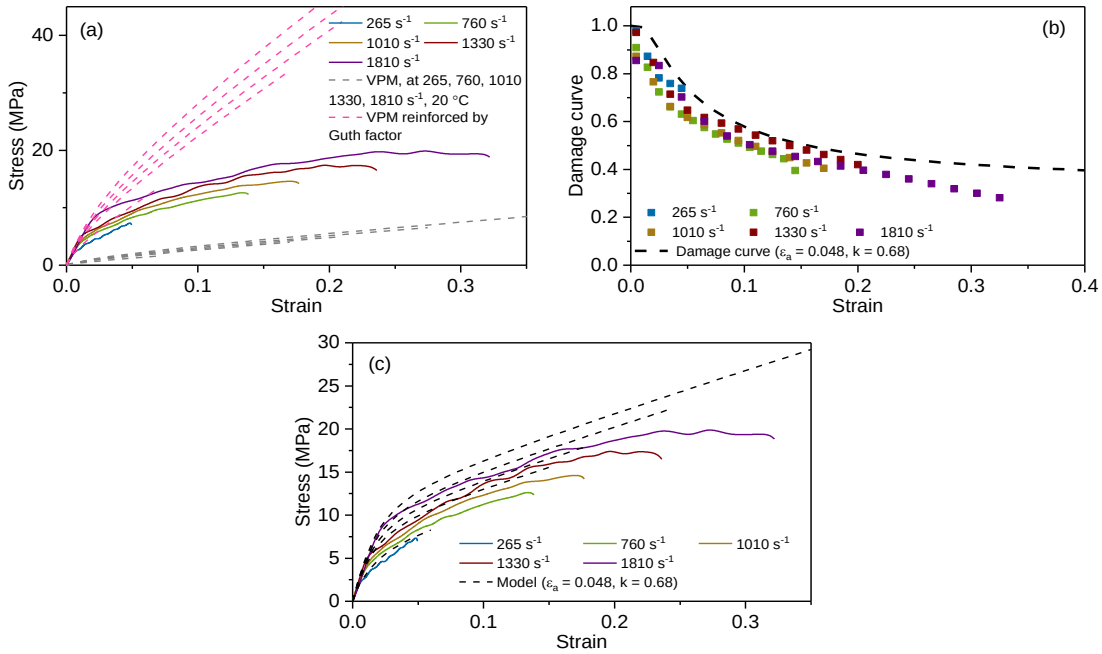


Fig. 5-13: Model implementation for specimen G50, in which (a) the Guth reinforcement equation was used to reinforce the viscoelastic polymer model, (b) the damage parameters ε_a and k from the quasi-static experiments were used to model the composite behaviour (c) at high rates and 20 °C. The parameters, R_{Guth}, ε_a, k were assigned as G50: 8.5, 0.048, 0.68.

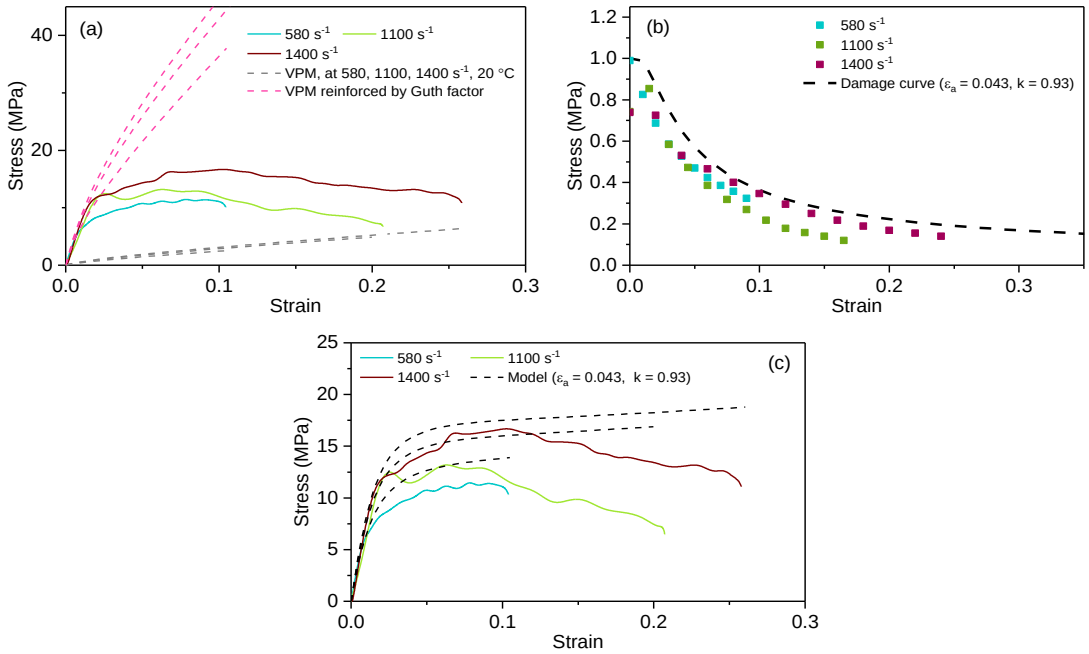


Fig. 5-14: Model implementation for specimen G70, in which (a) the Guth reinforcement equation was used to reinforce the viscoelastic polymer model, (b) the damage parameters ε_a and k were extracted from Fig. 5-10 to model the composite behaviour (c) at high rates and 20 °C. The parameters, R_{Guth}, ε_a, k were assigned as G70: 14.9, 0.043, 0.93.

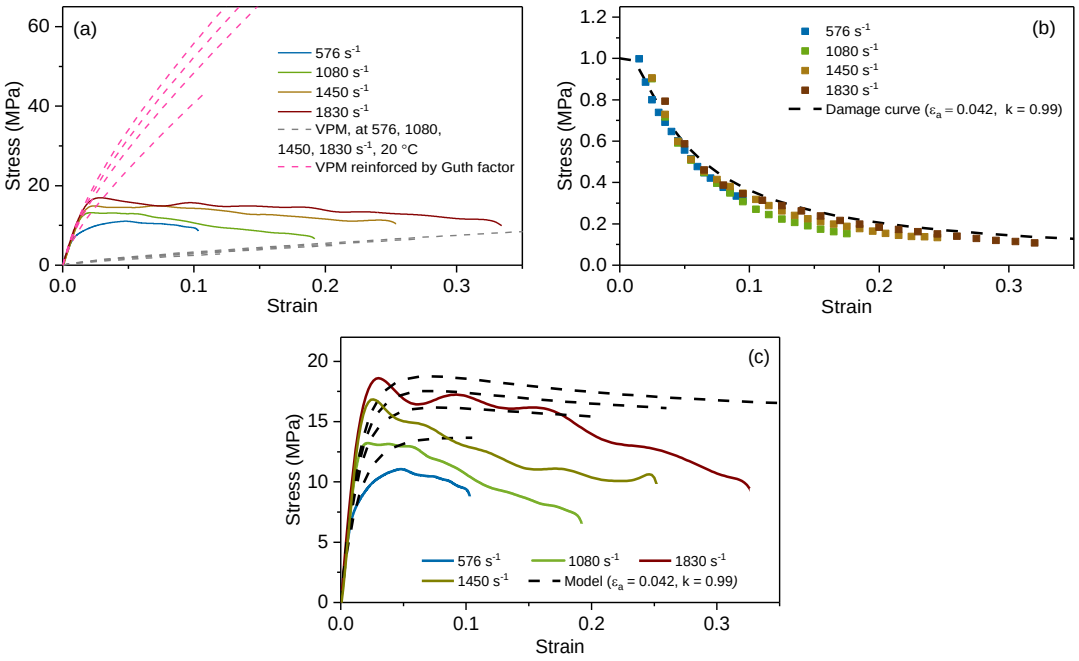


Fig. 5-15: Model implementation for specimen G75, in which (a) the Guth reinforcement equation was used to reinforce the viscoelastic polymer model, (b) the damage parameters ε_a and k from the quasi-static experiments were used to model the composite behaviour (c) at high rates and 20 °C. The parameters, R_{Guth}, ε_a, k were assigned as G75: 16.8, 0.042, 0.99.

3.6 Modelling of adiabatic heating effects

To achieve better prediction of the high rate data, this section introduces an approach to consider the effect of adiabatic heating. Viscoelastic or plastic deformation of the specimen converts work into heat and stored energy. In high strain rate experiments, this causes a temperature rise in the specimen, as there is insufficient time for this heat to conduct into the loading bars: the experiment takes place in adiabatic thermal conditions. This temperature rise may affect the subsequent deformation of the polymer, and hence affect the stress-strain behaviour, especially at large deformation. Fig. SI-16 demonstrates the effect of temperature rises on the behaviour of the polymer, this is somewhat amplified when considering the composite. In terms of adiabatic heating, the temperature rise as a function of strain can be approximately calculated as

$$\Delta T(\varepsilon) = \frac{\beta}{\rho C_p}\int_0^{\varepsilon} \sigma d\varepsilon \,, \tag{5-13}$$

where σ is the true stress, ε the true strain, $\rho = 950$ kg m^{-3} the material density, $C_p = 1850$ J kg^{-1} K^{-1} the specific heat capacity of the polymer, measured from a DSC

experiment, and ΔT represents the rise in temperature; β represents the fraction of work converted to heat during the deformation[87].

In order to verify the degree of impact of adiabatic heating on the composite stress at large deformations, an extreme case was considered at large deformation and high rates. First, the maximum conversion rate, β=1, was used to represent the work done being fully transferred into heat. Secondly, all the deformation was assumed to be adopted within the polymer matrix (see Fig. SI-17), for instance in the G50 specimen the strain rate in the SPU matrix twice the overall (applied) rate. This increase of strain rate in the matrix would be larger (i.e. likely three to four times higher) in specimens of G70 and G75. Using this latter assumption gives the polymer stress-strain curves in Fig. SI-18. Thirdly, the overall strain was divided into several regular intervals, at the end of which the heat generation was calculated. This approach was adopted so that the TTS master-curve only had to be recalculated a limited number of times. Here a strain interval of 0.1 was used in most cases: at each interval step a new stress-strain curve was calculated towards the new raised temperature; the determination of temperature rise at each step can be reviewed in Tables SI-3 to SI-5, Fig. SI. 19. A summary of temperature rises for the steps is shown in Fig. 5-16.

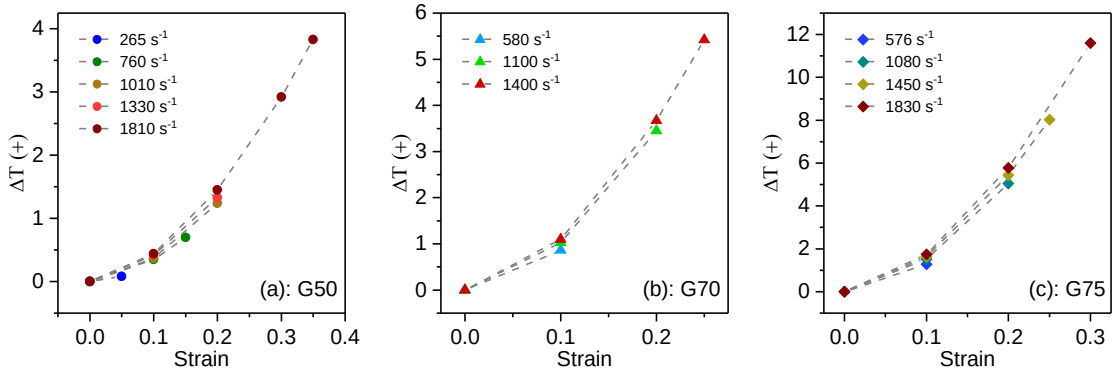


Fig. 5-16: The amount of temperature rise predicted at strain intervals of 0.1 in composites of G50, G70 and G75.

Using these assumptions, the predicted rises in temperature for specimens of G50, G70 and G75 were about 4 to 11 °C. This heating is assumed to cause a change in the mechanical response of the polymer, but not in R_{Guth}, ε_a and k or the sugar response. It is noted that, in fact

ε_a, is likely to change, as the interaction and adhesion between the matrix and filler changes when polymer matrix becomes more viscous, but we assume that this is not significant in this work.

Plots of the viscoelastic polymer model output at each calculated temperature are given in Figures SI-20 to SI-22. These were then used to derive the viscoelastic behaviour during a continuous heating process, shown in Fig. 5-17a, 18a and 19a for specimens of G50, G70, G75 respectively. New strain-stress plots under the assumption of continuous adiabatic heating, after reinforcement by the Guth equation, are given in Figures 5-17b, 5-18b and 5-19b. The ultimate stress-strain behaviour of composites with adiabatic heating effects is illustrated in the rest of Figures 5-17 to 5-19. These data show that including the adiabatic heating effect leads to a small improvement in the model, but does not fully remove the discrepancy between model and experiment.

It is interesting to investigate the effect of incorporating these increased strain rates into the overall mechanical model of the polymer. This is demonstrated in Figures SI-23-27, where it is shown that this change does not give appropriate model outputs. The additional modelling procedure assigned a new value to *R*, but kept, ε_a and *k* the same. Whilst this worked for low-rate experiments the stress behaviour was over-estimated at high rates. This discrepancy is because the modulus in the VPM increases more quickly as the polymer approaches the glassy state. Therefore the factors obtained from the model in the low rate regime are inappropriate to be used to model composite behaviour at high rate regime.

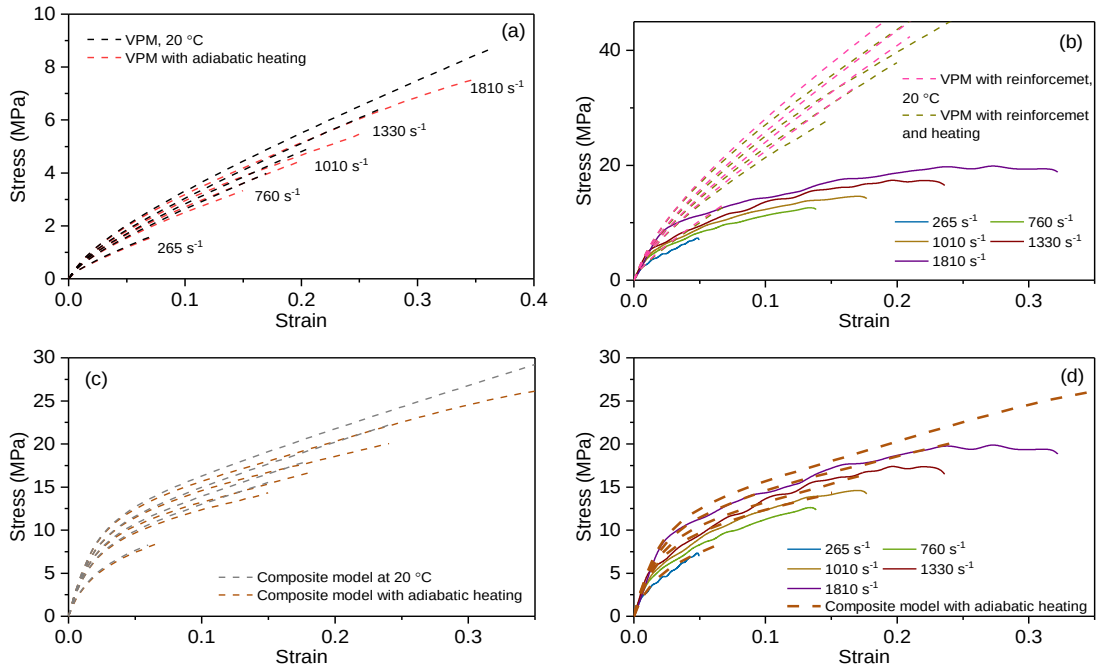


Fig. 5-17: Model implementation for specimen G50: the 'new' viscoelastic polymer model with adiabatic heating effects was compared to previous polymer model (a); the Guth reinforcement equation was used to reinforce the 'new' viscoelastic polymer model (b); the same damage parameters ε_a and k was used (c), to compare the 'new' model outputs with empirical data (d). The modelling of the composite behaviour performed at 0.01 s^{-1} and 20 °C. The parameters, R_{Guth}, ε_a, k were as follows: G50: 8.5, 0.048, 0.68.

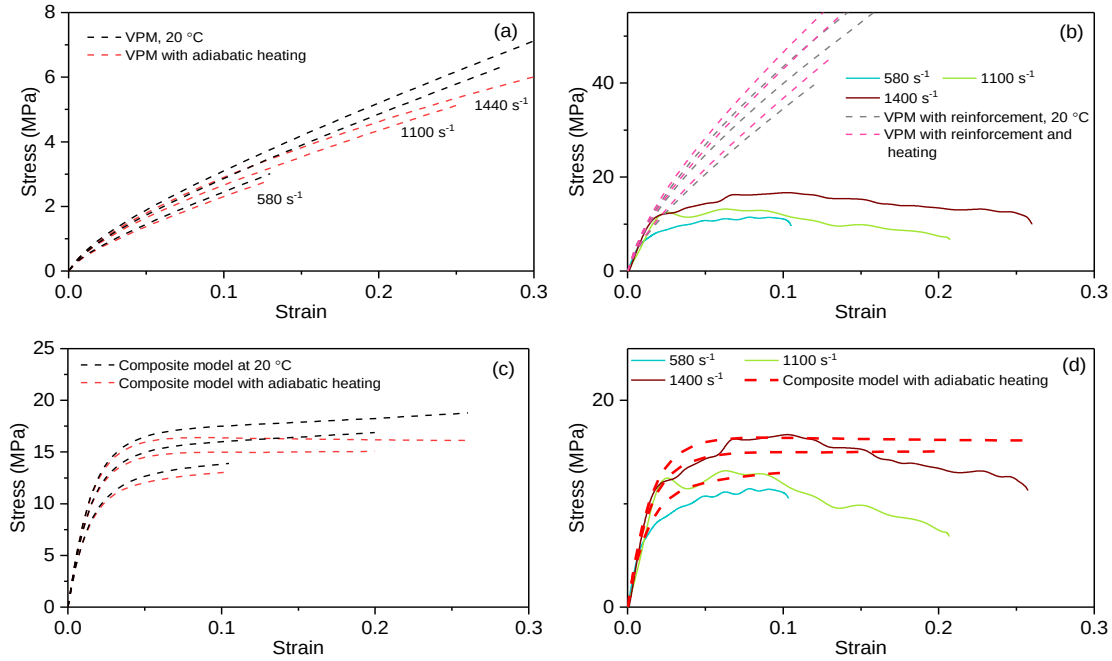


Fig. 5-18: Model implementation for specimen G70: the 'new' viscoelastic polymer model with adiabatic heating effects was compared to previous polymer model (a); the Guth reinforcement equation was used to reinforce the 'new' viscoelastic polymer model (b); the same damage parameters ε_a and k was used (c), to compare the 'new' model outputs with empirical data (d). The modelling of the composite behaviour performed at 0.01 s^{-1} and 20 °C. The parameters, R_{Guth}, ε_a, k were as follows: G70: 14.9, 0.043, 0.93.

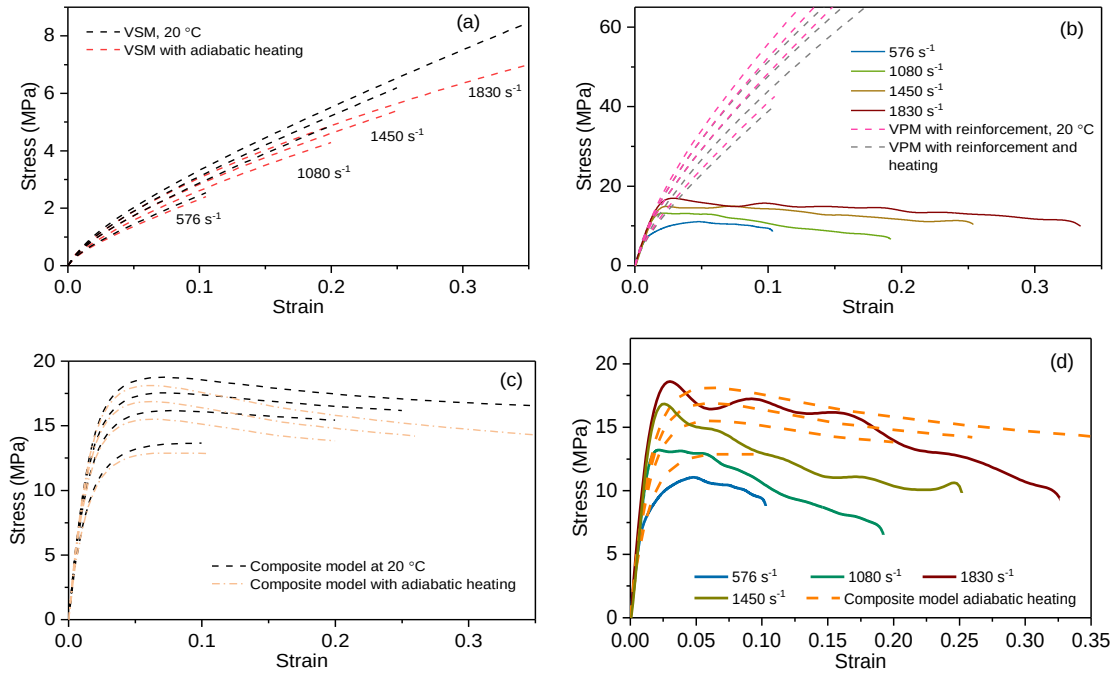


Fig. 5-19: Model implementation for specimen G75: the 'new' viscoelastic polymer model with adiabatic heating effects was compared to previous polymer model (a); the Guth reinforcement equation was used to reinforce the 'new' viscoelastic polymer model (b); the same damage parameters ε_a and k was used (c), to compare the 'new' model outputs with empirical data (d). The modelling of the composite behaviour performed at 0.01 s^{-1} and 20 °C. The parameters, R_{Guth}, ε_a, k were as follows: G75: 16.8, 0.042, 0.99.

3.7 Strain recovery of SPU-based composites

The SPU matrix used in these composites has been shown to partially recover its geometry after deformation[1]; an investigation into strain recovery, and behaviour on reloading, of the filled composites was also performed. The test specimens were prepared in the same way as above, loaded in quasi-static compression at a constant true strain rate of 0.01 s^{-1}. The temperature was controlled at 25 °C during compression, and at 37 °C in the recovery periods after each test. Specimens of SPU, G25, G50, C50, I50 and G75 were investigated, raw data of strain recovery against time are given in Fig. SI-28, stress-strain data produced when re-testing the specimens after recovery can be reviewed in Fig. SI-29. Fig. 5-20 shows logarithmic strain recovery against time. It is observed that this shows a linear dependence with a gradient that depends on the composition of the material. These gradients are then linked to the volume fraction or filler diameter.

In terms of the strength after recovery, the composites have capability of recovery in both strength and modulus when volume fraction is below 50%, demonstrated at Fig. SI-29 (d) and （f) with almost same responses to the initial loading behaviour without recovery treatments. In Fig. SI-29 (l), specimen G75 exhibited the second-loading behaviour at strength was higher than that when composite undergoing first post-yielding deformation, although such phenomenon is not significant at specimens C50 and I50 (see in Figures SI-29 (h) and (j)). This implied the recoverable capacity has both relevance to the volume fraction and filler size.

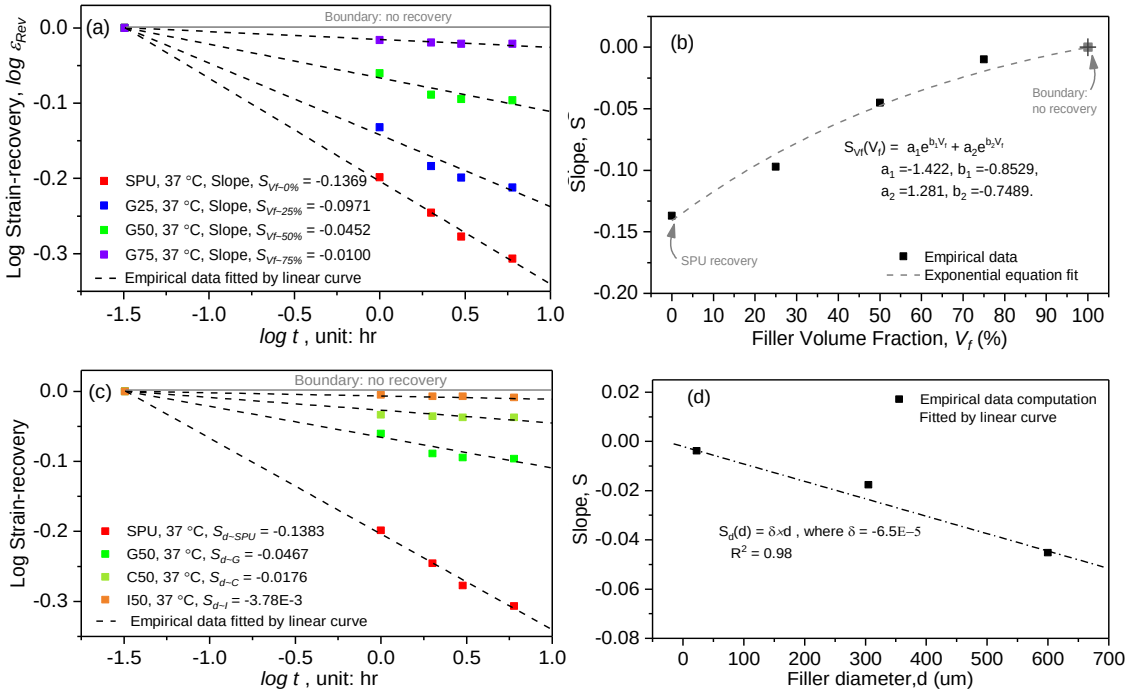


Fig. 5-20: Strain recovery in specimens (a) SPU, G25, G50, G75 (c) SPU, G50, C50, I50 at 37 °C. The gradient of the logarithmic recovery is plotted against volume fraction (b) and filler size (d).

4 Discussion and conclusions

The research presented here characterised low- and high-rate mechanical behaviour of sugar-filled SPU composites. Specimens were manufactured consisting of an SPU matrix with fillers of granulated, caster or icing sugar particles with different filler loadings. A practical multipurpose modelling method was proposed, which generalized the fundamental viscoelastic polymer model for the unfilled polymer to model the behaviour of sugar-filled SPU composites *via* progressive reinforcement and damage equations. Several reinforcement and damage models were introduced, and the optimal equation combination was adopted. Assigning appropriate parameters into the equations, the model was able to represent the properties of composites tested in quasi-static compression. The same modelling procedure and parameters from quasi-static experiments were then used to model high rate experiments, in order to validate the use of both the viscoelastic model and the damage equation. For composites which had not yet tested in low-rate experiments, the determination of their parameters for modelling were obtained from a set of phenomenological 3D surface plots which associated the parameters with filler size and volume fraction. The effect of adiabatic heating to reduce the stress in the high rate experiments was taken into account in order to optimize the agreement of the model with empirical data.

The modelling procedure began with a constitutive viscoelastic polymer model from the literature[65]. Several filler reinforcement models were introduced: Guth's equation, Kerner's equation and Hursch's equation. Guth's equation was chosen as the best of these equations, even though it was not fully able to describe the experimental results.

Three damage equations, based on the formulation of the Weibull distribution were proposed. Full simulation results were computed, and the damage equation lead to the best fit to empirical data was chosen. The chosen equation uses two parameters, an activation energy to describe damage, assumed to be caused by debonding of the particles from the matrix, ε_a, and a second parameter k, representing the residual strength of the material. Unlike previous

models in the literature, the underlying rate and temperature dependent polymer behaviour was retained by degrading the secant modulus of the filled polymer (which is equivalent to multiplying the stress-strain curve for the polymer by the damage factor).

For materials already tested in low-rate experiments, parameters can be determined, then used to predict mechanical behaviour at different rates. For materials without pre-assigned parameters, a mapping of parameters, ε_a and k to filler size and volume fraction provided a good prediction. Further, the model was capable of modelling rate dependence in the material, albeit with less accuracy at very high strain rates. Errors and discrepancies might be seen as a result of specimen preparation, errors in the reinforcement factor or the parameter estimation. Further errors from the viscoelastic polymer model might be expected at higher rates, where the rate dependence is larger and the model is therefore more sensitive. The model parameters could also be fit to the high rate data, providing an improvement here at the expense of predictive capability.

The potential effect of adabatic heating on the model output was also considered, this provides a small improvement in the model output compared to the experimental results. However, the new model stress outputs are still slightly over-estimated compared to the empirical values at very large strain. This is possibly because the damage scenarios were different between quasi-static experiments and high-rate impact experiments. From the literature, it is know that when stress or strain is small, the debonding mechanism is predominant, while at large stresses, fracture might appear in both the filler and the matrix rich area. This may occur preferentially at high strain rates, because the stresses are higher, and would accelerate the damage process and reduce the empirical strain-stress behaviour compared to the model. There may also be non-uniform deformation (e.g. shear bands) in high rate experiments, and the filler-matrix interface may be sensitive to polymer properties in a manner that affect the high rate behaviour.

The recoveries of strain and stress during cyclic loadings were briefly investigated. A logarithmic recovery of strain with time was evolved, with the rate of recovery depending on the particle size and volume fraction. The recovery of strength was minimal in these specimens; however, it is likely that this would be improved if they were allowed to recover in more confined conditions, or for longer.

In conclusion, this study on sugar-filled SPU polymers characterised their properties at quasi-static and high strain rates for different filler types and loading proportions. The modelling procedure built up a clear concept of using a predictive unfilled polymer model combined with a reinforcement equation and damage model to produce a practicable modelling procedure for the overall material using the viscoelastic polymer model and composition information from the composites.

5 Acknowledgements and compliance with ethical standards

The authors would like to thank Air Force Office of Scientific Research, Air Force Material Command, USAF under Award Nr. FA9550-15-1-0448. We are also grateful to the University of Reading for access to materials instrumentation. We also would like to thank Igor Dyson for technical support at Oxford University.

Funding: This material is based upon work supported by the Air Force Office of Scientific Research, Air Force Material Command, USAF under Award No. FA9550-15-1-0448.

Conflict of Interest: The authors declare that they have no conflict of interest.

6 References

1. Feula A, Tang X, Giannakopoulos I, et al. An adhesive elastomeric supramolecular polyurethane healable at body temperature. *Chem Sci*. 2016;7(7):4291-4300. doi:10.1039/C5SC04864H
2. Huang WM, Yang B, Zhao Y, Ding Z. Thermo-moisture responsive polyurethane shape-memory polymer and composites: a review. *J Mater Chem*. 2010;20(17):3367-3381.
3. Rivero G, Nguyen L-TT, Hillewaere XKD, Du Prez FE. One-pot thermo-remendable shape memory polyurethanes. *Macromolecules*. 2014;47(6):2010-2018.
4. Feula A, Pethybridge A, Giannakopoulos I, et al. A Thermoreversible Supramolecular Polyurethane with Excellent Healing Ability at 45 °c. *Macromolecules*. 2015;48(17):6132-6141. doi:10.1021/acs.macromol.5b01162
5. Petrović ZS, Ferguson J. Polyurethane elastomers. *Prog Polym Sci*. 1991;16(5):695-836.
6. Koberstein JT, Galambos AF, Leung LM. Compression-molded polyurethane block copolymers. 1. Microdomain morphology and thermomechanical properties. *Macromolecules*. 1992;25(23):6195-6204.
7. Ramakrishna S, Mayer J, Wintermantel E, Leong KW. Biomedical applications of polymer-composite materials: a review. *Compos Sci Technol*. 2001;61(9):1189-1224.
8. Rothon R. *Particulate-Filled Polymer Composites*. iSmithers Rapra Publishing; 2003.
9. Swetha M, Sahithi K, Moorthi A, Srinivasan N, Ramasamy K, Selvamurugan N. Biocomposites containing natural polymers and hydroxyapatite for bone tissue engineering. *Int J Biol Macromol*. 2010;47(1):1-4.
10. Lee G-W, Park M, Kim J, Lee JI, Yoon HG. Enhanced thermal conductivity of polymer composites filled with hybrid filler. *Compos Part A Appl Sci Manuf*. 2006;37(5):727-734.
11. Huang X, Jiang P, Tanaka T. A review of dielectric polymer composites with high thermal conductivity. *IEEE Electr Insul Mag*. 2011;27(4):8-16.
12. Bhadra S, Rahaman M, Khanam PN. Electrical and electronic application of polymer--carbon composites. In: *Carbon-Containing Polymer Composites*. Springer; 2019:397-455.
13. Xu C, Lin M, Wang X, et al. Fabrication of high-performance magnetic elastomers by using natural polymer as auxiliary dispersant of Fe3O4 nanoparticles. *Compos Part A Appl Sci Manuf*. 2021;140:106158.
14. Rao Y, Pochan JM. Mechanics of polymer- clay nanocomposites. *Macromolecules*. 2007;40(2):290-296.
15. Ojha S, Acharya SK, Raghavendra G. Mechanical properties of natural carbon black reinforced polymer composites. *J Appl Polym Sci*. 2015;132(1).
16. Mora-Barrantes I, Rodr\'\iguez A, Ibarra L, González L, Valent\'\in JL. Overcoming the disadvantages of fumed silica as filler in elastomer composites. *J Mater Chem*. 2011;21(20):7381-7392.
17. Saba N, Tahir PM, Jawaid M. A review on potentiality of nano filler/natural fiber filled polymer hybrid composites. *Polymers (Basel)*. 2014;6(8):2247-2273.
18. Vollenberg PHT, Heikens D. Particle size dependence of the Young's modulus of

filled polymers: 1. Preliminary experiments. *Polymer (Guildf)*. 1989;30(9):1656-1662.

19. Fu S-Y, Feng X-Q, Lauke B, Mai Y-W. Effects of particle size, particle/matrix interface adhesion and particle loading on mechanical properties of particulate--polymer composites. *Compos Part B Eng*. 2008;39(6):933-961.
20. Samal S. Effect of shape and size of filler particle on the aggregation and sedimentation behavior of the polymer composite. *Powder Technol*. 2020;366:43-51.
21. Singh SS, Parameswaran V, Kitey R. Dynamic compression behavior of glass filled epoxy composites: Influence of filler shape and exposure to high temperature. *Compos Part B Eng*. 2019;164:103-115.
22. Cooper CA, Ravich D, Lips D, Mayer J, Wagner HD. Distribution and alignment of carbon nanotubes and nanofibrils in a polymer matrix. *Compos Sci Technol*. 2002;62(7-8):1105-1112.
23. Chen W, Tao X. Self-organizing alignment of carbon nanotubes in thermoplastic polyurethane. *Macromol Rapid Commun*. 2005;26(22):1763-1767.
24. Xie X-L, Mai Y-W, Zhou X-P. Dispersion and alignment of carbon nanotubes in polymer matrix: a review. *Mater Sci Eng R Reports*. 2005;49(4):89-112.
25. Verbeek CJR. The influence of interfacial adhesion, particle size and size distribution on the predicted mechanical properties of particulate thermoplastic composites. *Mater Lett*. 2003;57(13-14):1919-1924.
26. Jin L, Wang H, Yang Y. Polyurethane composites in situ molecularly reinforced by supramolecular nanofibrillar aggregates of sorbitol derivatives. *Compos Sci Technol*. 2013;79:58-63.
27. Habibpour S, Um JG, Jun Y, Bhargava P, Park CB, Yu A. Structural impact of graphene nanoribbon on mechanical properties and anti-corrosion performance of polyurethane nanocomposites. *Chem Eng J*. 2021;405:126858.
28. Olonisakin K, Fan M, Xin-Xiang Z, et al. Key Improvements in Interfacial Adhesion and Dispersion of Fibers/Fillers in Polymer Matrix Composites; Focus on PLA Matrix Composites. *Compos Interfaces*. 2021:1-50.
29. Li T, Meng Z, Keten S. Interfacial mechanics and viscoelastic properties of patchy graphene oxide reinforced nanocomposites. *Carbon N Y*. 2020;158:303-313.
30. Daniel MA. *Polyurethane Binder Systems for Polymer Bonded Explosives*.; 2006.
31. Lee S, Choi JH, Hong I-K, Lee JW. Curing behavior of polyurethane as a binder for polymer-bonded explosives. *J Ind Eng Chem*. 2015;21:980-985.
32. Ahmed T late AE-SI, Ali AA, El-Masry AM, Tawfik SM. Development of Polyurethane-Based Solid Propellants Using Nanocomposite Materials. *Propellants, Explos Pyrotech*. 2016;41(2):286-294.
33. Siviour CR, Laity PR, Proud WG, et al. High strain rate properties of a polymer-bonded sugar: their dependence on applied and internal constraints. *Proc R Soc A Math Phys Eng Sci*. 2008;464(2093):1229-1255.
34. Kendall MJ, Siviour CR. Experimentally simulating high rate composite deformation in tension and compression: polymer bonded explosive simulant. *J Dyn Behav Mater*. 2015;1(2):114-123.
35. Huang X, Huang Z, Lai J-C, Li L, Yang G-C, Li C-H. Self-healing improves the stability and safety of polymer bonded explosives. *Compos Sci Technol*.

2018;167:346-354.

36. Sadasivuni KK, Ponnamma D, Kumar B, et al. Dielectric properties of modified graphene oxide filled polyurethane nanocomposites and its correlation with rheology. *Compos Sci Technol*. 2014;104:18-25.

37. Du W, Liu J, Wang Y, Li Y, Li Z. Polyurethane encapsulated carbon black particles and enhanced properties of water polyurethane composite films. *Prog Org Coatings*. 2016;97:146-152.

38. Maganty S, Roma MPC, Meschter SJ, et al. Enhanced mechanical properties of polyurethane composite coatings through nanosilica addition. *Prog Org Coatings*. 2016;90:243-251.

39. Jenczyk J, Woźniak-Budych M, Jancelewicz M, Jarek M, Jurga S. Structural and dynamic study of block copolymer--Nanoparticles nanocomposites. *Polymer (Guildf)*. 2019;167:130-137.

40. Roy M, Nelson JK, MacCrone RK, Schadler LS, Reed CW, Keefe R. Polymer nanocomposite dielectrics-the role of the interface. *IEEE Trans Dielectr Electr Insul*. 2005;12(4):629-643.

41. Pukanszky B. Influence of interface interaction on the ultimate tensile properties of polymer composites. *Composites*. 1990;21(3):255-262.

42. Sadeghpour E, Guo Y, Chua D, Shim VPW. A modified Mori--Tanaka approach incorporating filler-matrix interface failure to model graphene/polymer nanocomposites. *Int J Mech Sci*. 2020;180:105699.

43. Zhuk A V, Knunyants NN, Oshmyan VG, Topolkaraev VA, Berlin AA. Debonding microprocesses and interfacial strength in particle-filled polymer materials. *J Mater Sci*. 1993;28(17):4595-4606.

44. Arora H, Tarleton E, Li-Mayer J, Charalambides MN, Lewis D. Modelling the damage and deformation process in a plastic bonded explosive microstructure under tension using the finite element method. *Comput Mater Sci*. 2015;110:91-101.

45. Ferdous SF, Sarker MF, Adnan A. Role of nanoparticle dispersion and filler-matrix interface on the matrix dominated failure of rigid C60-PE nanocomposites: A molecular dynamics simulation study. *Polymer (Guildf)*. 2013;54(10):2565-2576.

46. Gao Z, Tsou AH. Mechanical properties of polymers containing fillers. *J Polym Sci Part B Polym Phys*. 1999;37(2):155-172.

47. Bréchet Y, Cavaillé J-Y, Chabert E, et al. Polymer Based Nanocomposites: Effect of Filler-Filler and Filler-Matrix Interactions. *Adv Eng Mater*. 2001;3(8):571-577.

48. Ravindran S, Tessema A, Kidane A. Multiscale damage evolution in polymer bonded sugar under dynamic loading. *Mech Mater*. 2017;114:97-106.

49. Ravindran S, Gupta V, Tessema A, Kidane A. Effect of particle mass fraction on the multiscale dynamic failure behavior of particulate polymer composites. *Exp Mech*. 2019;59(5):599-609.

50. Lee BL, Song JW, Ward JE. Failure of Spectra®polyethylene fiber-reinforced composites under ballistic impact loading. *J Compos Mater*. 1994;28(13):1202-1226.

51. Lee J-H, Veysset D, Singer JP, et al. High strain rate deformation of layered nanocomposites. *Nat Commun*. 2012;3(1):1-9.

52. Silva R V, Spinelli D, Bose Filho WW, Neto SC, Chierice GO, Tarpani JR. Fracture

toughness of natural fibers/castor oil polyurethane composites. *Compos Sci Technol*. 2006;66(10):1328-1335.

53. Wong KJ, Yousif BF, Low KO, Ng Y, Tan SL. Effects of fillers on the fracture behaviour of particulate polyester composites. *J Strain Anal Eng Des*. 2010;45(1):67-78.

54. Gray III GT, Blumenthal WR. Split-Hopkinson pressure bar testing of soft materials. *ASM Handb*. 2000;8:488-496.

55. Hu Z, Luo H, Bardenhagen SG, Siviour CR, Armstrong RW, Lu H. Internal deformation measurement of polymer bonded sugar in compression by digital volume correlation of in-situ tomography. *Exp Mech*. 2015;55(1):289-300.

56. Drodge DR, Williamson DM. Understanding damage in polymer-bonded explosive composites. *J Mater Sci*. 2016;51(2):668-679.

57. Siviour CR, Jordan JL. High strain rate mechanics of polymers: a review. *J Dyn Behav Mater*. 2016;2(1):15-32.

58. Song B, Chen W. Split Hopkinson pressure bar techniques for characterizing soft materials. *www.lajss.org Lat Am J Solids Struct*. 2005;2(January 2005):113-152.

59. Chen WW. Experimental methods for characterizing dynamic response of soft materials. *J Dyn Behav Mater*. 2016;2(1):2-14.

60. Chen W, Lu F, Frew DJ, Forrestal MJ. Dynamic Compression Testing of Soft Materials. *J Appl Mech*. 2002;69(3):214. doi:10.1115/1.1464871

61. Ravindran S, Tessema A, Kidane A. Local deformation and failure mechanisms of polymer bonded energetic materials subjected to high strain rate loading. *J Dyn Behav Mater*. 2016;2(1):146-156.

62. Catalanotti G, Kuhn P, Xavier J, Koerber H. High strain rate characterisation of intralaminar fracture toughness of GFRPs for longitudinal tension and compression failure. *Compos Struct*. 2020;240:112068.

63. Sassi S, Tarfaoui M, Yahia H Ben. An investigation of in-plane dynamic behavior of adhesively-bonded composite joints under dynamic compression at high strain rate. *Compos Struct*. 2018;191:168-179.

64. Koerber H, Xavier J, Camanho PP, Essa YE, De La Escalera FM. High strain rate behaviour of 5-harness-satin weave fabric carbon--epoxy composite under compression and combined compression--shear loading. *Int J Solids Struct*. 2015;54:172-182.

65. Chen H, Hart LR, Hayes W, Siviour CR. Mechanical characterisation and modelling of a thermoreversible superamolecular polyurethane over a wide range of rates. *Polymer (Guildf)*. 2021:123607.

66. Jerabek M, Major Z, Renner K, Móczó J, Pukánszky B, Lang RW. Filler/matrix-debonding and micro-mechanisms of deformation in particulate filled polypropylene composites under tension. *Polymer (Guildf)*. 2010;51(9):2040-2048.

67. ASR Group. ASR Group Tate & Lyle Speciality Ingredients. Tate & Lyle, UK, Ltd. www.sugarandsyrup.com. Published 2019. Accessed May 2, 2020.

68. ILO and WHO. SUCROSE ICSC: 1507. ICSC: 1507. www.ilo.org/dyn/icsc. Published 2003. Accessed May 5, 2020.

69. Siviour CR. High strain rate characterization of polymers. *AIP Conf Proc*. 2017;1793.

doi:10.1063/1.4971585

70. Cady CM, Blumenthal WR, Gray III GT, Idar DJ. Mechanical properties of plastic-bonded explosive binder materials as a function of strain-rate and temperature. *Polym Eng Sci*. 2006;46(6):812-819.
71. Ahmed S, Jones FR. A review of particulate reinforcement theories for polymer composites. *J Mater Sci*. 1990;25(12):4933-4942.
72. Einstein A. *Investigations on the Theory of the Brownian Movement*. Courier Corporation; 1956.
73. Guth E. Theory of filler reinforcement. *Rubber Chem Technol*. 1945;18(3):596-604.
74. Lewis TB, Nielsen LE. Dynamic mechanical properties of particulate-filled composites. *J Appl Polym Sci*. 1970;14(6):1449-1471.
75. Broutman LJ, Krock RH. *Modern Composite Materials: Editors: LJ Broutman and RH Krock*. Addison-Wesley Publishing Company; 1967.
76. Hirsch TJ. Modulus of elasticity iof concrete affected by elastic moduli of cement paste matrix and aggregate. In: *Journal Proceedings*. Vol 59. ; 1962:427-452.
77. Anthoulis GI, Kontou E. Micromechanical behaviour of particulate polymer nanocomposites. *Polymer (Guildf)*. 2008;49(7):1934-1942.
78. Rae PJ, Goldrein HT, Palmer SJP, Field JE, Lewis AL. Quasi--static studies of the deformation and failure of $β$--HMX based polymer bonded explosives. *Proc R Soc London Ser A Math Phys Eng Sci*. 2002;458(2019):743-762.
79. Jun-Ling LI, Hua FU, Duo-Wang TAN, Fang-Yun LU, Rong C. Fracture behaviour investigation into a polymer-bonded explosive. *Strain*. 2012;48(6):463-473.
80. Yan-Qing W, Feng-Lei H. A micromechanical model for predicting combined damage of particles and interface debonding in PBX explosives. *Mech Mater*. 2009;41(1):27-47.
81. Wang X, Wu Y, Huang F. Numerical mesoscopic investigations of dynamic damage and failure mechanisms of polymer bonded explosives. *Int J Solids Struct*. 2017;129:28-39.
82. Lv L, Yang M, Long Y, Chen J. Molecular dynamics simulation of structural and mechanical features of a Polymer-bonded explosive interface under tensile deformation. *Appl Surf Sci*. 2021;557:149823.
83. Weibull W, others. A statistical distribution function of wide applicability. *J Appl Mech*. 1951;18(3):293-297.
84. Weibull W. A survey of statistical effects in the field of material failure. *Appl Mech Rev*. 1952;5(11):449-451.
85. Weibull W. A statistical theory of strength of materials. *IVB-Handl*. 1939.
86. Weibull W. The phenomenon of rupture in solids. *IVA Handl*. 1939;153.
87. Kendall MJ, Siviour CR. Experimentally simulating adiabatic conditions: Approximating high rate polymer behavior using low rate experiments with temperature profiles. *Polym (United Kingdom)*. 2013;54(18):5058-5063. doi:10.1016/j.polymer.2013.06.049

CHAPTER 6 DISCUSSION & LIMITATION

6.1 Introduction

The research presented in this thesis concerns two primary polymers: carbon black-filled polyurethane (CB-TPU) and a synthetic, healable, supramolecular polyurethane (SPU). The former polymer has elastic modulus of about 60 MPa at ambient temperature, and is representative of polymers in commercial use; the latter has much smaller modulus of about 7 MPa, and potentially can be used in biomedical applications. The SPU was also mixed with sugar particles to fabricate sugar-filled polymer composites, for exploring the future application and polymer-bonded products.

The study on CB-TPU included the characterisation of thermo-mechanical behaviour, using low-to-high rate monotonic tests and cyclic experiments. A predictive model based on the theory of viscoelasticity and continuous damage was implemented to reproduce the results observed in these mechanical experiments. This research was introduced in Chapter 3. The same methodology and a similar modelling framework were used in the study on the SPU polymer: thermo-mechanical experiments were executed; the mechanical behaviour from low-to-high strain rates was characterised; additionally, rheometry was performed to demonstrate the effect of thermal history. A phenomenological model was proposed in which rate-dependent behaviour was characterised from quasi-static and rheometry experiments, and able to reproduce mechanical behaviour at high rates. This research was introduced in Chapter 4. The further development of using viscoelastic theory was to model the sugar-filled SPU composites, introduced in Chapter 5. The study characterised the mechanical properties from low- to high- strain rates of composites that varied by sugar type and volume fraction. A phenomenological model was proposed, following the framework of strain-induced damage and continuous damage mechanism. The fitting parameters with different values were assigned for several composites, and then mapped to their own filler size and filler loadings. The model

also is capable of reproducing the mechanical behaviour at high strain rates by using parameters determined from low rates experiments. This research built on the viscoelastic model from Chapter 4, modelling mechanical properties of filled polymer composites using the unfilled polymer model. Comparisons between empirical results and the models have been discussed in each chapter respectively. Here the significance of the study, the principle of the methodology, experimental correlations, and limitations of the research are discussed.

6.2 Material

Polyurethane has a very wide range of applications in both industrial use and scientific research. The work in this thesis presented the application of viscoelastic theory to both soft and stiff polyurethane material, for their mechanical behaviour from small to large deformation, low to high strain rates. The CB-TPU is representative of stiffer TPUs, with Shore-A90 degree of hardness, commercially used as load-bearing cushion, tires and wheels products. The characterisation of stiff polyurethane in dynamic behaviour is the supplementary data and supports for industrial manufacture and future product design. On the other hand, the soft SPU was studied. One of the novel applications is to use as biomaterials, such as artificial skin, therefore the dynamic behaviour for this particular polymer is more significant and attractive. In ambient temperature, SPU only has an initial modulus about 7 MPa, at a deformation of strain rate of 0.01 s^{-1}. Increasing rates to 0.1 s^{-1}, the initial modulus becomes stiffer, about 80 MPa, which is 10 times stiffer than low rate behaviour. The characterisation of sensitivity in rate dependent on this TPU is significant and helpful in further study. Another application of SPU was then studied. It takes advantage of the features of flexible-resilience and healibility from SPU, to explore the possibility of making polymer-bonded explosive (PBX) composites. Therefore, the in-situ sugar-filled SPU was fabricated. Again, the thermo-mechanical properties and high rate behaviour were examined. The empirical work provided a lot useful supplementary data for this particular composite at different compositions. It also exhibited

recovery capability (after deformation) in this composite, hinted a possibility and advantage of using SPU into PBX with good functionality. However, the study also pointed out SPU composites had different degrees of damage (i.e. strain softening) if filler size and filler loadings were different. In high-rate loadings (e.g. impact), the damage procedure and its structural failure might become worse and more likely to happen at an early stage.

6.3 Time-temperature equivalence

All three projects used a fundamental principle, i.e. time-temperature superposition, to interpret the measured thermo-mechanical properties. DMA experiments were performed over a wide range of temperatures using a strain amplitude of 0.1% and frequency sweeps from 1 to 100 Hz. The storage modulus can be compared to data from monotonic experiments performed from low- to high-strain rates, presented in Chapter 3 for the CB-TPU. Whilst it is difficult to establish accurate moduli from the monotonic experiments, especially at high strain rates, the stress at a strain of ~0.05 can be used to give an understanding of when the polymer response is affected by internal transitions. An example is given in Fig. 6-1, where the conversion between strain rate frequency is made using

$$4 f \varepsilon_{DMA} = \dot{\varepsilon}\,, \tag{6-1}$$

where f is the DMA frequency and ε_{DMA} is the strain amplitude.

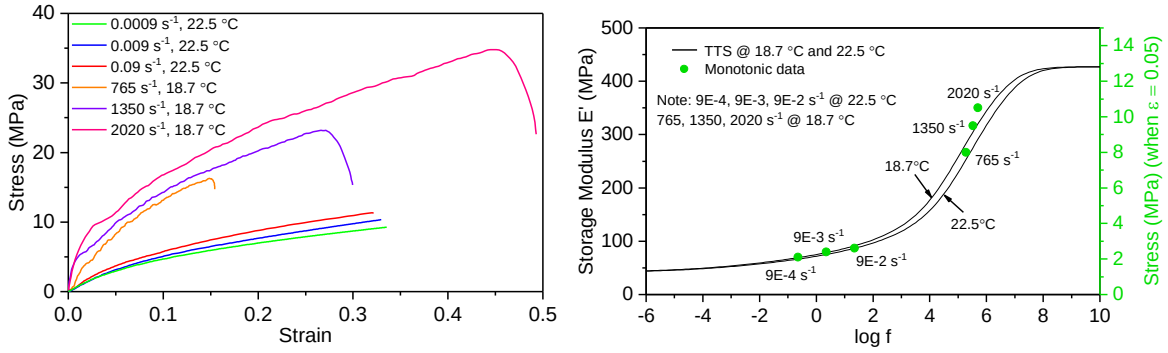


Fig. 6-1. CB-TPU rate dependence (a). Mastercurves of storage modulus, calculated from DMA experiments compared to characteristic stress (~0.05 ε) from monotonic loading (b). This demonstrates the effect of the glass transition on the high strain rate response.

For temperature-induced effects, the behaviour of CB-TPU at a temperature from 15-25 °C was introduced in Chapter 3, additional experiments were later performed down to -40 °C, Fig. 6-2. The stress at ~0.05 ε is again plotted against temperature, showing again the transition from rubbery to glassy as the temperature is reduced. The glass transition temperature is consistent with the value observed in Chapter 3.

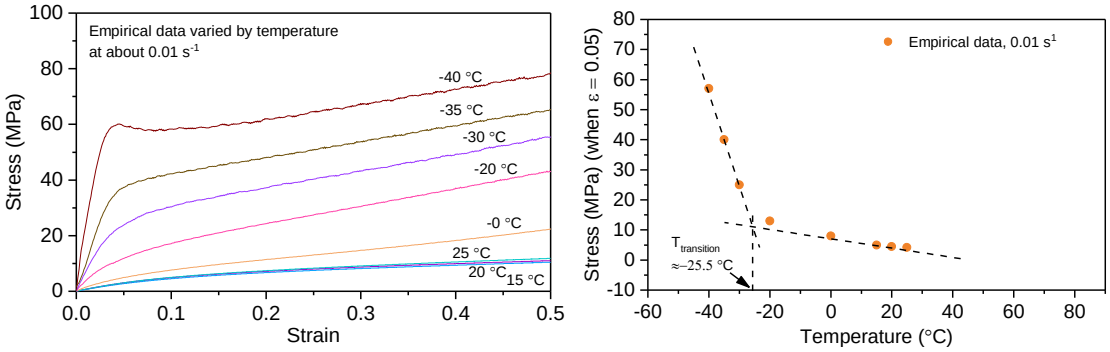


Fig. 6-2. CB-TPU temperature dependence (a). Stress at ~0.05 ε against temperature, showing the transition from rubbery to glassy as the temperature is reduced (b).

The conversion between log f and $\dot{\varepsilon}$ gives an approximate indication of whether the material behaves in a rubbery or glassy manner at high strain rate. In Chapter 3, the highest strain rate of 2020 s^{-1}, is equivalent to log f of about 5.7. At room temperature, this is in the intermediate region of the glass transition, and CB-TPU might exhibit a certain degree of glassy-like behaviour, although this is not obvious from the empirical data. For the SPU in Chapter 4, the highest rate of 1200 s^{-1} corresponded to a frequency of log f =5.5, at room temperature this is just at initiation of the glass transition range. Therefore, the empirical results did not show glassy behaviour at all. In both cases, the inability to produce data at very high rates reduces the opportunity to correlate high rate tests and DMA experiments in the glassy state. This is one of the limitations of this study.

6.4 Experimental apparatus considerations

The characterisation of thermo-mechanical properties underpins the methods adopted in this paper, where moduli are linked between cyclic DMA / rheometry tests and large-deformation experiments. In Chapter 3, the DMA data were able to provide adequate understanding of the rate dependence in polymer. The damage model is following, to fit large deformation but essentially took advantages of empirical DMA data. A similar principle of modelling was employed in Chapter 4, where the softening model was utilised empirical data from DMA-rheometry. Although the modelling results gave good compliance to empirical data, it has to notice that potential risks existed if thermo-dynamic experiments were not accurate. The FE model in Chapter 3 indicated the clamp compliance and fixing method might introduce more significant effects.

The observation in DMA and rheometry device in Chapter 4 revealed faults might from experimental errors due to machine limitations and specimen geometry. In the tension DMA experiment it is suggested to monitor the deflection (position) of the clamps to help validate the data. If the specimen yields at a specific temperature, there is a distinct elongation between the two clamps, so the measured deflection becomes larger. Another potential uncertainty comes from the alignment of the specimen between clamps. In experiments, we often observed the specimen yielded and necked at the clamp position or nearby. This can give a force (e.g. bending or twisting) to the specimen due to the poor alignment, further affecting measurements.

A weakness when assembling plots of modulus from DMA and rheometry is the need to have a good value of Poisson's ratio. DMA gives a calculation of Young's modulus (i.e. E' and E''), and the rheometer gives shear modulus (i.e. G' and G''). In this study, the values were converted by assuming a Poisson's ratio of 0.5, but this may not be correct.

In the rheometry data, the mechanical properties were observed to be somewhat dependent on the thermal histories; however no distinct evidence verifying conformation changes (from SAXS data), molecularity changes (from NMR data), phase changes (from GPC data). At this moment, small deviations were found from DSC data and compression tests for polymer specimens undergoing different cooling rates, but this is not direct evidence to support the phenomenon in rheometry, and also not the demonstration for any change in molecular conformation. This indicates that the small changes in rheological properties might be associated with recoverable features in the supramolecular conformation, i.e. the structural changes leading to the observed cooling rate dependence quickly reach equilibrium and cannot be observed in post-test characterisation. Another reason might be because any changes in local structure due to the thermal history changes introduced are not strong enough to display signals in the scattering technique used, e.g. SAXS. The processed specimen has to be dissolved within the solvents prior to NMR and GPC experiments, the change in the physical state might offset the imperceptible changes on molecular conformation which lead by the previous thermal process.

6.5 Type of 'damage' model and their capabilities

Phenomenological models were used to reproduce the strain-stress behaviour of the polymers. In Chapter 3, a phenomenological damage model was used: the decline of local moduli resulted from strain-stress behaviour that matched the empirical data well. The degree of damage increased with increasing modulus in monotonic loadings, whilst in cyclic loadings, each loading or unloading was considered separately to perform strain-induced damage. Therefore, for the material tested, the model calibrated using monotonic experiments could also be used to model cyclic tests. It was also observed that the model calibrated using low rate data could be used to predict high rate behaviour.

In Chapter 4, a viscoelastic softening model was proposed, this combined a Maxwell SLS model with an additional damper in series, thus reducing the strain and strain rate in the SLS element and hence the overall stress at large strains. This is another phenomenon of 'strain softening' behaviour that inhibited stress output without modifying input of strain or strain rates to the entire system. This model was again successful in capturing the rate dependence and predicting the high strain rate behaviour.

In Chapter 5, the third phenomenological damage model was developed: it acted on the secant moduli and again followed the continuous damage concept. A reinforcement equation was first used. Then, several damage equations were attempted to reproduce empirical behaviour and finally a modified Weibull distribution equation with the best fitting was adopted. The damage equation literally reduced the local stress to a smaller value by assigning appropriate damage parameters into the equation. Although the realistic debonding damage phenomenon in micro-scale was not characterised, the relations among fitting parameters, filler size and filler loading contents were correlated. Since the specimen did not change its composition at both quasi-static and high rate experiments, it was observed that using all parameters from low rate experiments could be used to predict high rate behaviour. It supported assumptions in the strain-induced damage and continuous damage theory, and also verified of using de-bonding mechanism to describe stress degradation in both low and high rate behaviour. The over-estimated stress was observed at large deformation in high rate experiments, this might be because the filler sensitivity towards rate dependence is not considered into the damage model. Additionally, the debonding mechanism might not the only one failure mechanism taking place during the high rate experiments, therefore the resultant softening was insufficient to reproduce the same empirical stress.

All three phenomenological models indicated a method of using viscoelastic theory as the principle to model polymers at large strains and high rates. The degree to soften the stress

from the linear viscoelastic model has a direct association with the strain in the polymer system. However, all three models have limitations for glassy polymers or the polymer exhibiting glassy-like properties, because they often exhibit yield and plastic flow; hence it is important to be aware, for example, that CB-TPU begins to exhibit yielding at -40°C. Another limitation is that these models do not really consider the complicated damage mechanisms that really occur in these materials. In terms of the filled polymer, when strain is small, de-bonding might dominate the stress degradation; when the strain becomes intermediate, the voids and micro-cracks might be important; when the strain goes larger, the fracture, macro-tearing, cracks and delamination might occur. Therefore, it is difficult and impossible to using one damage mechanism or one simplified damage hypothesis to describe polymer from small deformations to very large. The damage mechanism between low strain rate (quasi-static tests) and high strain rate (impact test) also might be different, as pulse propagation, inertial stresses, and respective rate-sensitivity of matrix and filler must be considered.

CHAPTER 7 CONCLUSION

7.1 Conclusion

This research has investigated three types of polyurethane: commercial carbon black-filled polyurethane (CB-TPU); healable supramolecular polyurethane (SPU); SPU composite with sugar filler. The thermal/thermo-mechanical properties of viscoelasticity, and low-to-high strain rate response have been measured, and three practicable, predictive, phenomenological models calibrated to reproduce the mechanical behaviour in high strain rates.

The study on CB-TPU used continuum damage theory combined with a viscoelastic constitutive model. The model was calibrated using the low-rate experiments in compression, and was able to predict behaviour at different temperatures and loading rates up to 2000 s^{-1}. The study incorporated DMA data using the time-temperature superposition principle. For the SPU polymer, the thermo-mechanical behaviour was again characterised, and the effect of cooling rate on rheological behaviour was investigated and a simple model produced. A viscoelastic model was proposed to reproduce the response in monotonic loading at strain rates up to 1200 s^{-1}. This model is also capable of modelling the strain recovery. Finally, this model was extended to encompass sugar-filled SPU composites. A reinforcement equation and a continuous damage equation were calibrated and combined with the viscoelastic model for the matrix The specific parameters used in the damage equation were associated to the filler size and volume fraction. The ultimate model also predicted the response of several representative composite specimens in high strain rates up to 1800 s^{-1}.

The whole project focused on the thermo-mechanical behaviour of different polyurethanes and the application of viscoelastic theory from small to large deformation. The work aimed to explore efficient, simplified and accessible phenomenological models to describe the polymer and polymer-based composites at high strain rate by using empirical data from low rates. This research broadens the experimental characterisation and the scope of

thermo-mechanical behaviour in polyurethane polymer and its composites; it also made contributions in constitutive models and modelling methodology to the family of polyurethane polymers, for both industrial and scientific applications.

7.2 Future plan

For CB-TPU, experiments from low-to-high strain rates were performed and modelled taking advantage of time-temperature equivalence. However, from the empirical results, the glassy-like behaviour has not yet been triggered in the high rate experiments presented here. It is now necessary to validate the principle of time-temperature equivalence between high strain rates and low temperatures. The full map of the transition from the rubbery to the glassy state, and the correlations between a wider range of temperature and loading rates need to be explored. This should also be accompanied by measurements to larger strains, the current project focussed on strains less than 0.5. Further experiments in tension would also be valuable, as this mode of loading is particularly difficult to achieve at high strain rates. A study like this would also generate useful additional data for industrial use of these materials.

For SPU, there is very little literature on such healable polyurethane, especially the characterisation and modelling of mechanical properties. Again, work to investigate properties in the glassy state and at larger strains, as well as the capacity of strain/stress recovery after impact or damage would be valuable. One potential, significant application of this polymer is artificial skin or bio-implants. Further dynamic characterisations, e.g. shear, bending, torsion might be needed to fully understand material properties in different loading scenarios. The experiments or model simulations at body temperature or higher temperatures might also be necessary, as well as to explore whether the thermal degradation, modulus degradation, or even chemical degradation might be experienced in use.

For sugar-filled SPU, experiments on a broader range of compositions would give a better understanding of the interaction between volume fraction and particle size dependence. The full mapping diagram among strain-stress behaviour, filler size and filler loadings is helpful to associate with the distinction of damage mechanism at different composites. Further observation, and simulation of how matrix properties affect overall behaviour would be useful, and can be achieved simply by performing experiments over a range of temperatures. Another important step will be to better understand the detailed configuration, evolutions and movements of the filler component using SEM, X-ray topography, micro-CT, etc. The collaboration of SEM with DIC technique might help identify the shear band, debonding or re-bonding phenomenon of greatest importance, however, is a systematic survey of whether the healable SPU can be translated into a healable composite, and whether in turn this can give more longevity and resilience in relevant applications. Measurements of the re-bonding behaviour, supported by structural analysis, would be an interesting topic to understand the recovery of filled SPU, and to further to relate micro-mechanisms to macroscopic phenomena. Most of these experiments cannot be performed at high strain rates, underpinning the need to continue exploring the use of time-temperature superposition to interpret the high rate and impact response of these materials.

APPENDIX

Supplementary Information for Chapter 3 - Paper A

The discrete patterns of E′ and log f was first obtained from DMA test. The approach to produce a Prony Series data is fitting this discrete patterns into Generalized Maxwell Model, which enable an optimal curve can be constructed to fit the experimental data and further calibrate numerical stress-strain curves. There is a relation between plots for the variations of moduli E′ and relaxation time spectrum, as a function of frequency. Relaxation and retardation time spectra can be calculated exactly from stress relaxation by using simple Alfrey Approximations in which the exponential term for a single Maxwell unit is replaced by a step function. The exponential term is expressed as

$$E(t) = [E_r] + \int_{-\infty}^{\infty} H(\tau) \exp(\frac{-t}{\tau}) d(\ln \tau) \quad \text{(A1)}$$

If we assume that $e^{-t/\tau}=0$ up to the time $\tau=t$, and $e^{-t/\tau}=1$ for $\tau>t$. We can write

$$E(t) = [E_r] + \int_{\ln \tau}^{\infty} H(\tau) d(\ln \tau) \quad \text{(A2)}$$

The relaxation time spectrum is expressed to an approximation in terms of the real and imaginary parts of the complex modulus:

$$H(\tau) = [\frac{dE'(\omega)}{d \log \omega}]_{\frac{1}{\omega}=\tau} = \frac{2}{\pi}[E''(\omega)]_{\frac{1}{\omega}=\tau} \quad \text{(A3)}$$

The relationship between storage modulus and relaxation time spectrum are illustrated diagrammatically for the case of a single relaxation transition in Fig.A1. The distribution of time spectrum for the model is the derivative results from a continuous distribution of storage modulus. The element of area at $log\ \omega$: $H(\tau) \cdot log\omega$ represents the local strength of the relaxation at $log\omega$. The integrated area represents a single Maxwell elements, and equals strength contribution to entire set of Maxwell elements.

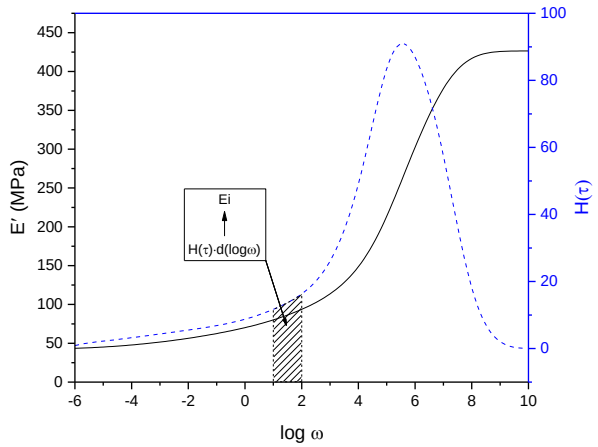


Figure A1-Alfrey Approximations

Prony Series is governed by the integration of all individual integral area from time spectrum patterns in figure above. The individual time spectrum ω and τ can be replaced by symbol of time *t* and frequency *f*. The distribution of relaxation time *H(t)* is derivative by fitting the discrete data in the plot of storage modulus against logarithm frequency term, further the shape of the *H(t)* function are reproduced into 60 individual Maxwell elements (listed below). The left endpoint in primary plot is picking as the value of first elastic element to form an eventual Generalized Maxwell Model.

The Table A1-A4, listing the Prony Series produced at from temperature 25 °C to 16.8 °C. The optimal curve fitting was restructured by substituting all 61 sets of parameters into Generalized Maxwell Model. The experimental data and Prony fits are shown in Fig. 3-5 and Fig. 3-6. in the body text.

Table A1- Prony Series at Temperature 25 °C			
Maxwell Element Number	Young's Moduli E' (MPa)	Relaxation Time τ (s)	Viscosity η (MPa·s)
0	43.3317	∞	∞
1	0.3603	7.4989E+05	2.7022E+05
2	0.4074	4.2170E+05	1.7180E+05
3	0.4581	2.3714E+05	1.0864E+05
4	0.5124	1.3335E+05	6.8329E+04
5	0.5700	7.4989E+04	4.2746E+04
6	0.6308	4.2170E+04	2.6600E+04
7	0.6943	2.3714E+04	1.6465E+04
8	0.7602	1.3335E+04	1.0138E+04
9	0.8281	7.4989E+03	6.2100E+03
10	0.8975	4.2170E+03	3.7848E+03
11	0.9679	2.3714E+03	2.2954E+03
12	1.0390	1.3335E+03	1.3856E+03
13	1.1104	7.4989E+02	8.3268E+02
14	1.1819	4.2170E+02	4.9839E+02
15	1.2535	2.3714E+02	2.9725E+02
16	1.3255	1.3335E+02	1.7676E+02
17	1.3986	7.4989E+01	1.0488E+02
18	1.4738	4.2170E+01	6.2148E+01
19	1.5523	2.3714E+01	3.6811E+01
20	1.6361	1.3335E+01	2.1818E+01
21	1.7272	7.4989E+00	1.2952E+01
22	1.8281	4.2170E+00	7.7090E+00
23	1.9411	2.3714E+00	4.6030E+00
24	2.0684	1.3335E+00	2.7583E+00
25	2.2119	7.4989E-01	1.6587E+00
26	2.3729	4.2170E-01	1.0006E+00
27	2.5518	2.3714E-01	6.0514E-01
28	2.7489	1.3335E-01	3.6657E-01
29	2.9641	7.4989E-02	2.2227E-01
30	3.1988	4.2170E-02	1.3489E-01
31	3.4573	2.3714E-02	8.1985E-02
32	3.7487	1.3335E-02	4.9990E-02
33	4.0894	7.4989E-03	3.0666E-02
34	4.5040	4.2170E-03	1.8993E-02
35	5.0250	2.3714E-03	1.1916E-02
36	5.6898	1.3335E-03	7.5874E-03
37	6.5359	7.4989E-04	4.9012E-03
38	7.5992	4.2170E-04	3.2046E-03
39	8.9170	2.3714E-04	2.1146E-03
40	10.5377	1.3335E-04	1.4052E-03
41	12.5177	7.4989E-05	9.3869E-04
42	14.8798	4.2170E-05	6.2748E-04
43	17.5237	2.3714E-05	4.1555E-04
44	20.1479	1.3335E-05	2.6868E-04
45	22.2312	7.4989E-06	1.6671E-04
46	23.5258	4.2170E-06	9.9208E-05
47	23.7118	2.3714E-06	5.6230E-05
48	23.0457	1.3335E-06	3.0732E-05
49	21.8782	7.4989E-07	1.6406E-05
50	20.4407	4.2170E-07	8.6198E-06
51	18.7011	2.3714E-07	4.4347E-06
52	16.5351	1.3335E-07	2.2050E-06
53	13.8907	7.4989E-08	1.0417E-06
54	10.9321	4.2170E-08	4.6100E-07
55	7.9844	2.3714E-08	1.8934E-07
56	5.3842	1.3335E-08	7.1800E-08
57	3.3472	7.4989E-09	2.5101E-08
58	1.9221	4.2170E-09	8.1054E-09
59	1.0261	2.3714E-09	2.4332E-09
60	0.5162	1.3335E-09	6.8831E-10

Table A2- Prony Series at Temperature 22.5 °C			
Maxwell Element Number	Young's Moduli E' (MPa)	Relaxation Time τ (s)	Viscosity η (MPa·s)
0	43.6797	∞	∞
1	0.3929	7.4989E+05	2.9463E+05
2	0.4425	4.2170E+05	1.8661E+05
3	0.4957	2.3714E+05	1.1756E+05
4	0.5524	1.3335E+05	7.3664E+04
5	0.6122	7.4989E+04	4.5912E+04
6	0.6750	4.2170E+04	2.8464E+04
7	0.7402	2.3714E+04	1.7554E+04
8	0.8076	1.3335E+04	1.0769E+04
9	0.8766	7.4989E+03	6.5733E+03
10	0.9467	4.2170E+03	3.9923E+03
11	1.0177	2.3714E+03	2.4132E+03
12	1.0890	1.3335E+03	1.4522E+03
13	1.1604	7.4989E+02	8.7020E+02
14	1.2320	4.2170E+02	5.1953E+02
15	1.3039	2.3714E+02	3.0919E+02
16	1.3765	1.3335E+02	1.8357E+02
17	1.4509	7.4989E+01	1.0880E+02
18	1.5283	4.2170E+01	6.4447E+01
19	1.6103	2.3714E+01	3.8186E+01
20	1.6990	1.3335E+01	2.2656E+01
21	1.7967	7.4989E+00	1.3473E+01
22	1.9058	4.2170E+00	8.0366E+00
23	2.0286	2.3714E+00	4.8105E+00
24	2.1671	1.3335E+00	2.8899E+00
25	2.3227	7.4989E-01	1.7418E+00
26	2.4963	4.2170E-01	1.0527E+00
27	2.6879	2.3714E-01	6.3739E-01
28	2.8975	1.3335E-01	3.8639E-01
29	3.1262	7.4989E-02	2.3443E-01
30	3.3768	4.2170E-02	1.4240E-01
31	3.6570	2.3714E-02	8.6722E-02
32	3.9807	1.3335E-02	5.3084E-02
33	4.3701	7.4989E-03	3.2771E-02
34	4.8554	4.2170E-03	2.0475E-02
35	5.4730	2.3714E-03	1.2978E-02
36	6.2609	1.3335E-03	8.3490E-03
37	7.2553	7.4989E-04	5.4407E-03
38	8.4924	4.2170E-04	3.5812E-03
39	10.0163	2.3714E-04	2.3752E-03
40	11.8831	1.3335E-04	1.5846E-03
41	14.1336	7.4989E-05	1.0599E-03
42	16.7147	4.2170E-05	7.0485E-04
43	19.3887	2.3714E-05	4.5978E-04
44	21.6681	1.3335E-05	2.8895E-04
45	23.2658	7.4989E-06	1.7447E-04
46	23.7600	4.2170E-06	1.0020E-04
47	23.3139	2.3714E-06	5.5286E-05
48	22.2630	1.3335E-06	2.9688E-05
49	20.8991	7.4989E-07	1.5672E-05
50	19.2604	4.2170E-07	8.1220E-06
51	17.2367	2.3714E-07	4.0875E-06
52	14.7287	1.3335E-07	1.9641E-06
53	11.8350	7.4989E-08	8.8750E-07
54	8.8461	4.2170E-08	3.7304E-07
55	6.1118	2.3714E-08	1.4493E-07
56	3.8932	1.3335E-08	5.1917E-08
57	2.2885	7.4989E-09	1.7161E-08
58	1.2474	4.2170E-09	5.2603E-09
59	0.6375	2.3714E-09	1.5117E-09
60	0.3120	1.3335E-09	4.1612E-10

Table A3- Prony Series at Temperature 18.7 °C			
Maxwell Element Number	Young's Moduli E' (MPa)	Relaxation Time τ (s)	Viscosity η (MPa·s)
0	44.3730	∞	∞
1	0.4131	7.4989E+05	3.0981E+05
2	0.4651	4.2170E+05	1.9614E+05
3	0.5213	2.3714E+05	1.2362E+05
4	0.5816	1.3335E+05	7.7560E+04
5	0.6460	7.4989E+04	4.8444E+04
6	0.7143	4.2170E+04	3.0122E+04
7	0.7863	2.3714E+04	1.8646E+04
8	0.8616	1.3335E+04	1.1490E+04
9	0.9400	7.4989E+03	7.0487E+03
10	1.0208	4.2170E+03	4.3049E+03
11	1.1038	2.3714E+03	2.6175E+03
12	1.1882	1.3335E+03	1.5845E+03
13	1.2737	7.4989E+02	9.5512E+02
14	1.3596	4.2170E+02	5.7332E+02
15	1.4454	2.3714E+02	3.4277E+02
16	1.5311	1.3335E+02	2.0417E+02
17	1.6165	7.4989E+01	1.2122E+02
18	1.7020	4.2170E+01	7.1774E+01
19	1.7886	2.3714E+01	4.2415E+01
20	1.8779	1.3335E+01	2.5042E+01
21	1.9723	7.4989E+00	1.4790E+01
22	2.0751	4.2170E+00	8.7504E+00
23	2.1904	2.3714E+00	5.1944E+00
24	2.3235	1.3335E+00	3.0984E+00
25	2.4797	7.4989E-01	1.8595E+00
26	2.6647	4.2170E-01	1.1237E+00
27	2.8837	2.3714E-01	6.8383E-01
28	3.1409	1.3335E-01	4.1885E-01
29	3.4395	7.4989E-02	2.5793E-01
30	3.7817	4.2170E-02	1.5947E-01
31	4.1709	2.3714E-02	9.8908E-02
32	4.6148	1.3335E-02	6.1539E-02
33	5.1302	7.4989E-03	3.8471E-02
34	5.7492	4.2170E-03	2.4244E-02
35	6.5235	2.3714E-03	1.5470E-02
36	7.5240	1.3335E-03	1.0033E-02
37	8.8310	7.4989E-04	6.6224E-03
38	10.5134	4.2170E-04	4.4335E-03
39	12.5958	2.3714E-04	2.9869E-03
40	15.0233	1.3335E-04	2.0034E-03
41	17.6364	7.4989E-05	1.3225E-03
42	20.1681	4.2170E-05	8.5048E-04
43	22.2650	2.3714E-05	5.2799E-04
44	23.5363	1.3335E-05	3.1386E-04
45	23.7280	7.4989E-06	1.7793E-04
46	23.0109	4.2170E-06	9.7036E-05
47	21.8484	2.3714E-06	5.1811E-05
48	20.4263	1.3335E-06	2.7239E-05
49	18.6373	7.4989E-07	1.3976E-05
50	16.4315	4.2170E-07	6.9291E-06
51	13.8315	2.3714E-07	3.2800E-06
52	10.9260	1.3335E-07	1.4570E-06
53	7.9660	7.4989E-08	5.9737E-07
54	5.3143	4.2170E-08	2.2410E-07
55	3.2570	2.3714E-08	7.7235E-08
56	1.8727	1.3335E-08	2.4973E-08
57	1.0529	7.4989E-09	7.8953E-09
58	0.6128	4.2170E-09	2.5840E-09
59	0.3881	2.3714E-09	9.2044E-10
60	0.2717	1.3335E-09	3.6231E-10

Table A4- Prony Series at Temperature 16.8 °C			
Maxwell Element Number	Young's Moduli E' (MPa)	Relaxation Time τ (s)	Viscosity η (MPa·s)
0	44.7505	∞	∞
1	0.4272	7.4989E+05	3.2038E+05
2	0.4828	4.2170E+05	2.0358E+05
3	0.5428	2.3714E+05	1.2871E+05
4	0.6072	1.3335E+05	8.0973E+04
5	0.6759	7.4989E+04	5.0685E+04
6	0.7486	4.2170E+04	3.1568E+04
7	0.8250	2.3714E+04	1.9563E+04
8	0.9046	1.3335E+04	1.2063E+04
9	0.9870	7.4989E+03	7.4017E+03
10	1.0717	4.2170E+03	4.5192E+03
11	1.1579	2.3714E+03	2.7458E+03
12	1.2451	1.3335E+03	1.6603E+03
13	1.3326	7.4989E+02	9.9928E+02
14	1.4199	4.2170E+02	5.9875E+02
15	1.5066	2.3714E+02	3.5727E+02
16	1.5926	1.3335E+02	2.1237E+02
17	1.6782	7.4989E+01	1.2584E+02
18	1.7641	4.2170E+01	7.4390E+01
19	1.8518	2.3714E+01	4.3913E+01
20	1.9436	1.3335E+01	2.5918E+01
21	2.0426	7.4989E+00	1.5317E+01
22	2.1529	4.2170E+00	9.0785E+00
23	2.2793	2.3714E+00	5.4051E+00
24	2.4275	1.3335E+00	3.2371E+00
25	2.6030	7.4989E-01	1.9520E+00
26	2.8113	4.2170E-01	1.1855E+00
27	3.0568	2.3714E-01	7.2488E-01
28	3.3429	1.3335E-01	4.4578E-01
29	3.6718	7.4989E-02	2.7535E-01
30	4.0459	4.2170E-02	1.7062E-01
31	4.4707	2.3714E-02	1.0602E-01
32	4.9590	1.3335E-02	6.6130E-02
33	5.5372	7.4989E-03	4.1523E-02
34	6.2507	4.2170E-03	2.6359E-02
35	7.1661	2.3714E-03	1.6994E-02
36	8.3648	1.3335E-03	1.1155E-02
37	9.9245	7.4989E-04	7.4423E-03
38	11.8889	4.2170E-04	5.0135E-03
39	14.2295	2.3714E-04	3.3743E-03
40	16.8137	1.3335E-04	2.2421E-03
41	19.3952	7.4989E-05	1.4544E-03
42	21.6402	4.2170E-05	9.1256E-04
43	23.1924	2.3714E-05	5.4998E-04
44	23.7783	1.3335E-05	3.1709E-04
45	23.3592	7.4989E-06	1.7517E-04
46	22.2521	4.2170E-06	9.3836E-05
47	20.8859	2.3714E-06	4.9528E-05
48	19.2779	1.3335E-06	2.5708E-05
49	17.2086	7.4989E-07	1.2905E-05
50	14.7039	4.2170E-07	6.2006E-06
51	11.8516	2.3714E-07	2.8105E-06
52	8.8625	1.3335E-07	1.1818E-06
53	6.1548	7.4989E-08	4.6155E-07
54	3.9403	4.2170E-08	1.6616E-07
55	2.2479	2.3714E-08	5.3305E-08
56	1.1435	1.3335E-08	1.5249E-08
57	0.5725	7.4989E-09	4.2930E-09
58	0.3230	4.2170E-09	1.3622E-09
59	0.2111	2.3714E-09	5.0054E-10
60	0.1511	1.3335E-09	2.0153E-10

The goal of beam theory is to simplify the mechanical analysis to beams. Timoshenko beam theory includes the effect of shear deformation which is ignored in Euler-Bernoulli beam theory. All loads on a beam act parallel to an axis that is transverse to its longitudinal axis. Euler-Bernoulli beam theory is extensively applied to the structural analysis and beam design if the length of a beam is much larger than its width and depth. However, the problem with Euler-Bernoulli beam theory is that it is inaccurate for deep beams. The effect from the deep depth is not negligible compared to the length. Shear deformation, which are absent in Euler-Bernoulli beam theory, are included in Timoshenko beam theory. The basic assumptions for Timoshenko beam theory are: The longitudinal axis of the unloaded beam is straight; All applied loads act transverse to the longitudinal axis; All deformations and strains are small. Hooke's law can be used to relate stresses and strains; Plane cross sections, which are initially normal to the longitudinal axis, will remain plane after deformation.

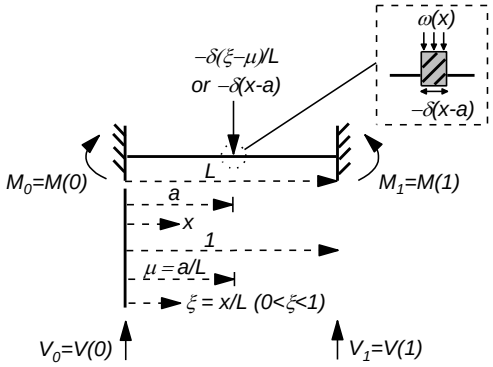


Figure B.1: The simplified bending mechanism of Timoshenko beam in DMA

To analyse the DMA test, energy principles, the stiffness matrix, and Green's functions are formulated to solve a typical Timoshenko beam problem in which the beam has a downward unit point load acting at location $x=a$, $\delta=\mu$. The point load is represented as a delta function: $\omega(x) = -\delta(x-a)$. In terms of the dimensionless variable ξ, we set $\mu = a/L$. The delta function obeys the scaling property:

$$\delta(x-a)=\delta(\frac{1}{L}(\zeta-\mu))=\frac{1}{L}\delta(\zeta-\mu) \tag{B1}$$

Thus we write: $\omega(\xi)= -\delta(\xi-\mu)/L$. We also require the fact that the integral of the delta function is the Heavside function:

$$\int_0^{\xi}\delta(\tau-\mu)d\mu=H(\zeta-\mu)=\begin{cases}1 & if\ \xi\geq\mu\\ 0 & f\ \xi<\mu\end{cases} \tag{B2}$$

Successive integrals of the Heavisible function are given by the formula:

$$\int_0^{\xi}(\tau-\mu)^n H(\tau-\mu)d\tau=\frac{(\xi-\mu)^{n+1}}{n+1}H(\zeta-\mu),\quad n\geq 0 \tag{B3}$$

These properties allow explicit integration of the solutions below to apply Green's function.

The shear force is computed to be:

$$V(\xi)=L\int_0^{\xi}\omega(\tau)d\tau+V_0 \tag{B4}$$

$$V(\xi)=L\int_0^{\xi}-\frac{1}{L}\delta(\tau-\mu)d\tau+V_0 \tag{B5}$$

$$V(\xi)=-H(\xi-\mu)+V_0 \tag{B6}$$

The bending moment is given as:

$$M(\xi)=L\int_0^{\xi}V(\tau)d\tau+M_0 \tag{B7}$$

$$M(\xi)=L\int_0^{\xi}[-H(\tau-\mu)]d\tau+M_0 \tag{B8}$$

$$M(\xi)=L[-(\xi-\mu)H(\xi-\mu)+V_0\xi]+M_0 \tag{B9}$$

The angle of deflection can be simplified:

$$\theta(\xi)=L\int_0^{\xi}\frac{M(\tau)}{EI}d\tau+\theta_0 \tag{B10}$$

$$\theta(\xi)=\frac{L^2}{EI}\int_0^{\xi}[-(\tau-\mu)H(\tau-\mu)+V_0\tau+\frac{1}{L}M_0\xi]d\tau+\theta_0 \tag{B11}$$

$$\theta(\xi)=\frac{L^2}{EI}[-\frac{1}{2}(\xi-\mu)^2H(\xi-\mu)+\frac{1}{2}V_0\xi^2+\frac{1}{L}M_0\xi]+\theta_0 \tag{B12}$$

$$\theta(\xi)=\frac{L^2}{2EI}[-(\xi-\mu)^2H(\xi-\mu)+V_0\xi^2+\frac{2}{L}M_0\xi]+\theta_0 \tag{B13}$$

Finally, the deflection is calculated in the form:

$$u(\xi)=L\int_0^{\xi}\theta(\tau)d\tau-\frac{1}{GA_S}\int_0^{\xi}V(\tau)d\tau+\mu_0 \tag{B14}$$

$$u(\xi)=\frac{L^3}{2EI}\int_0^{\xi}[-(\tau-\mu)^2H(\tau-\mu)+V_0\tau^2+\frac{2}{L}M_0\tau+\frac{2EI}{L^2}\theta_0]d\tau-\frac{1}{GA_S}\int_0^{\xi}[-H(\xi-\mu)+V_0]d\tau+\mu_0 \tag{B15}$$

$$u(\xi)=\frac{L^3}{2EI}[-\frac{1}{3}(\xi-\mu)^3H(\xi-\mu)+\frac{1}{3}V_0\xi^2+\frac{1}{L}M_0\xi^2+\frac{2EI}{L^2}\theta_0\xi]+\frac{1}{GA_S}[(\xi-\mu)H(\xi-\mu)-V_0\xi]+\mu_0$$

(B16)

$$u(\xi)=\left[\frac{L^3}{2EI}[-(\xi-\mu)^3H(\xi-\mu)+V_0\xi^2+\frac{3}{L}M_0\xi^2]\right]+\left[\frac{1}{GA_S}[(\xi-\mu)H(\xi-\mu)-V_0\xi]+L\theta_0\xi+\mu_0\right]$$

(B17)

where G is shear modulus of material property and A_s is cross-section shear area along longitudinal axis. In terms of the deflection expression Eq.(B17), the first part is the deflection functions for the Euler-Bernoulli beam. The second part is the shear deformation upon Green's function compensating the bending effects, which results in a softer bending response and application of the eventual deflection in DMA calibration shown in Figure B.2.

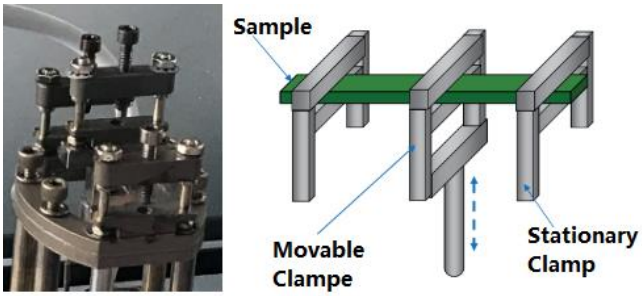


Figure B.2: The bending mechanism in DMA

The properties of TPU were determined by DMA (TA Q800). This is a technique in which a beam (35×10×5 mm) is placed in dual-cantilever clamps and subjected to a cyclic deformation (Figure B.2). The machine outputs modulus (*E'* and *E''*), loss tangent (tan δ), stress, temperature and frequency which are calculated from the amplitude and phase of the force and displacement. Isothermal frequency sweeps were performed at 2 °C intervals between -50 °C to 80 °C, and frequencies 0.5, 2, 5, 10 Hz. The displacement amplitude was 30 μm. An example of phase retardation between force and deflection in DMA experiment is shown in Figure B.2.

The clamp device in Figure B.2 can be simplified as a beam and under the centering loading. Substituting V_0 = 1/2, M_0 = −L/8, θ_0 = 0, μ_0 = 0 as the boundary conditions; ξ= 1/2, μ = 1/2 as the loading conditions, into Green's functions, the deflection expression is calculated as:

$$u(\frac{1}{2}) = \left[\frac{L^3}{192EI}\right] + \left[\frac{L}{4GA_S}\right], \text{ where } G = \frac{E}{2(1+\upsilon)} \text{ and } A_S = \frac{bd}{2} \quad \text{(B18)}$$

Substituting the loading into this equation, and further substituting shear modulus G and shear area A_S , giving the full deflection expression:

$$u = \left(\frac{L^3}{192IE} + \frac{3L}{2bdE}\right)W \quad \text{(B19)}$$

where u is the bending deflection, W is the force, E is Young's modulus, G is shear modulus, v is Poisson's ratio, I is second moment of area, and A_S is cross-section shear area along longitudinal axis. The first term $PL^3/192EI$ is the derivative from Euler–Bernoulli theory, representing force-bending-curvature, while the second term $PL/4GA_s$ relates to the shear effect along the neutral axis in length, representing shear-bending-curvature. Re-writing the equation gives the force response in bending test:

$$W = \frac{u}{\left(\frac{L^3}{192I} + \frac{3L}{2bd}\right)}E^* \quad \text{(B20)}$$

where E^* is the complex modulus value when viscoelastic material undergoes stress relaxation situation.

For a viscoelastic material undergoing cyclic deformation, the stress is found to lag behind the strain, with a phase shift δ which depends on the related properties and frequency of applied loading, shown in Figure B.3.

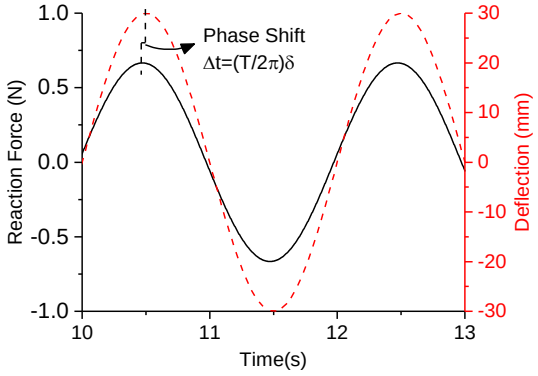


Figure B.3: The DMA experimental phase retardation between force and deflection in 1 Hz frequency

To express the dynamic stress and strain responses, we write the strain and stress as:

$$\varepsilon = \varepsilon_0^* e^{i\omega_0 t} \tag{B21}$$

$$\sigma = \sigma_0^* e^{i\omega_0 t} \tag{B22}$$

The individual element of generalized Maxwell model, is generally recognised as Standard Linear Solid Model. The standard model have been developed to allow both stress relaxation and creep situation upon stress-strain relation by expressing its complex modulus (including storage modulus, loss modulus and phase shift) in time spectrum:

$$E^* = \frac{\sigma_0^*}{\varepsilon_0^*} = \left[E_0 + E_1 \frac{\tau^2 \omega_0^{\,2}}{1+\tau^2 \omega_0^{\,2}} \right] + i \left[E_1 \frac{\tau \omega_0}{1+\tau^2 \omega_0^{\,2}} \right] \tag{B23}$$

$$E^{'} = E_0 + E_1 \frac{\tau^2 \omega_0^{\,2}}{1+\tau^2 \omega_0^{\,2}} \tag{B24}$$

$$E^{''} = E_1 \frac{\tau \omega_0}{1+\tau^2 \omega_0^{\,2}} \tag{B25}$$

$$\tan \delta = \frac{E^{''}}{E^{'}} \tag{B26}$$

where the E_0 represents the elastic element, while E_1 and τ_1 belongs to the Maxwell elements. The equivalent functions of complex modulus for the Generalized Maxwell Model are expressed as:

$$E^{'}(\omega) = E_0 + \sum_{i=1}^{m} E_i \frac{\tau_i^{\,2} \omega^2}{1+\tau_i^{\,2} \omega^2} \tag{B27}$$

$$E^{''}(\omega) = \sum_{i=1}^{m} E_i \frac{\tau_i \omega}{1+\tau_i^{\,2} \omega^2} \tag{B28}$$

where ω is the angular velocity of the applied deformation, E_0, E_i and τ_i indicate the properties of elements from the Generalized Maxwell Model. We then define the storage and loss moduli as the real and imaginary parts of the complex modulus during the dynamic harmonic cyclic loading. The phase shift factor $tan\ \delta = E'/E''$ is the ratio of imaginary modulus to real modulus and represents the lag between strain-stress responses.

A FE model in compression (Figure B.4) was meshed using C3D8I elements, with 5 elements through the thickness of the specimen. The model has fixed bottom plate (ENCASTRE), while the top plate was driven under velocity control to achieve uniaxial

compression at strain rates 0.09, 0.009, 0.0009, 0.08, 0.008 and 0.0008 s^{-1}. The simulation was compared to the results from analytical implementation of the Generalized Maxwell Model using 61 legs of Prony series at reference temperature of 25 °C. Figure B.5 exhibits the same strain-stress response in both FE model and analytical Models.

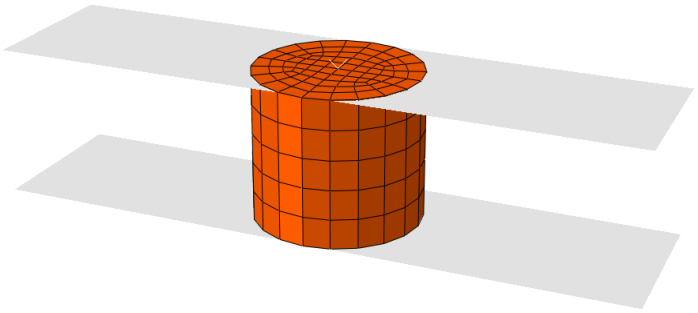


Figure B.4: FE model in compression to validate the implementation of the Generalized Maxwell Model.

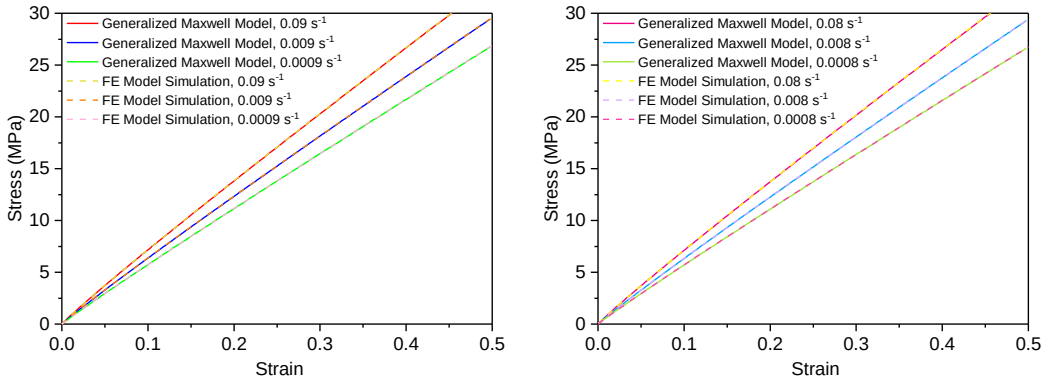


Figure B.5: FE and analytical implementations of the Generalised Maxwell Model at different strain rates

TPU is a relatively soft elastomer which has mechanical properties that are is easily affected by experimental technique. In addition, certain systematic and experimental errors are inevitable, such as ambient temperature changes, contact problems, as well as the inherent property variations from its manufacture. In compression experiments, the test sample - rubber cylinder has an aspect ratio of 1 (height: diameter = 1:1) to reduce any possible buckling or barrelling during the loading. However, the asymmetrical barrelling generally happened when true strain was above 0.4. In quasi-static tests, the imperfection of alignment in load cell and clamps could affect the loading results. Particularly in tensile tests, tearing may occur in the

clamp which would seriously affect the strain rate control. To eliminate these errors, an extra extensometer (Figure C.1) travelling along the compression or tensile axis was implemented into the INSTRON in order to valid the accuracy of strain data obtained from DIC analysis. Additionally, the laboratory temperature and experiments were performed 3-5 times for each compression and tensile conditions was recorded before use in further calculation and analysis.

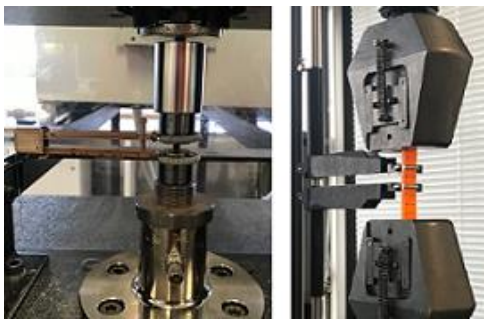


Figure C.1: The extensometer used in quasi-static tests

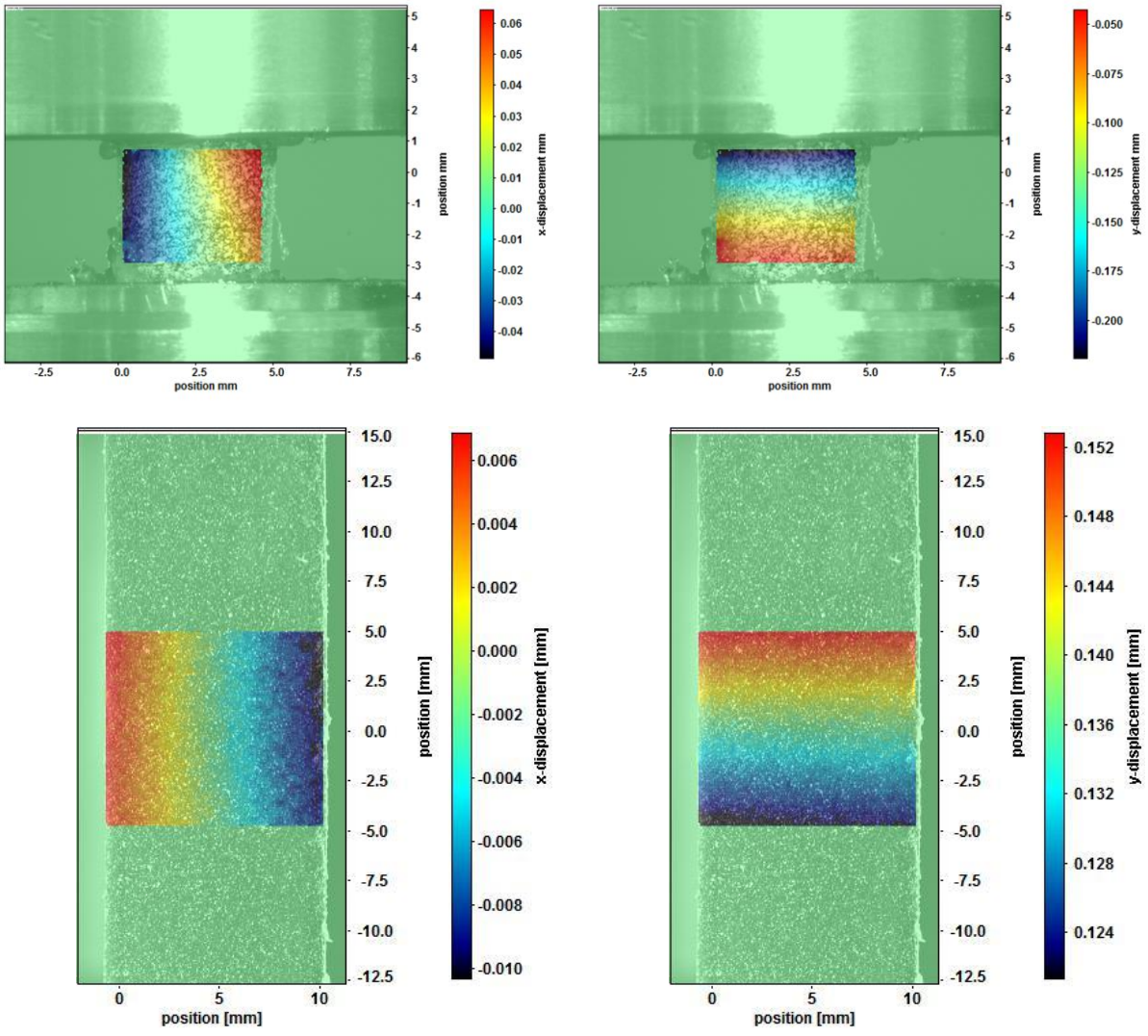


Figure C.2: Use of DIC to confirm strains in quasi-static tests

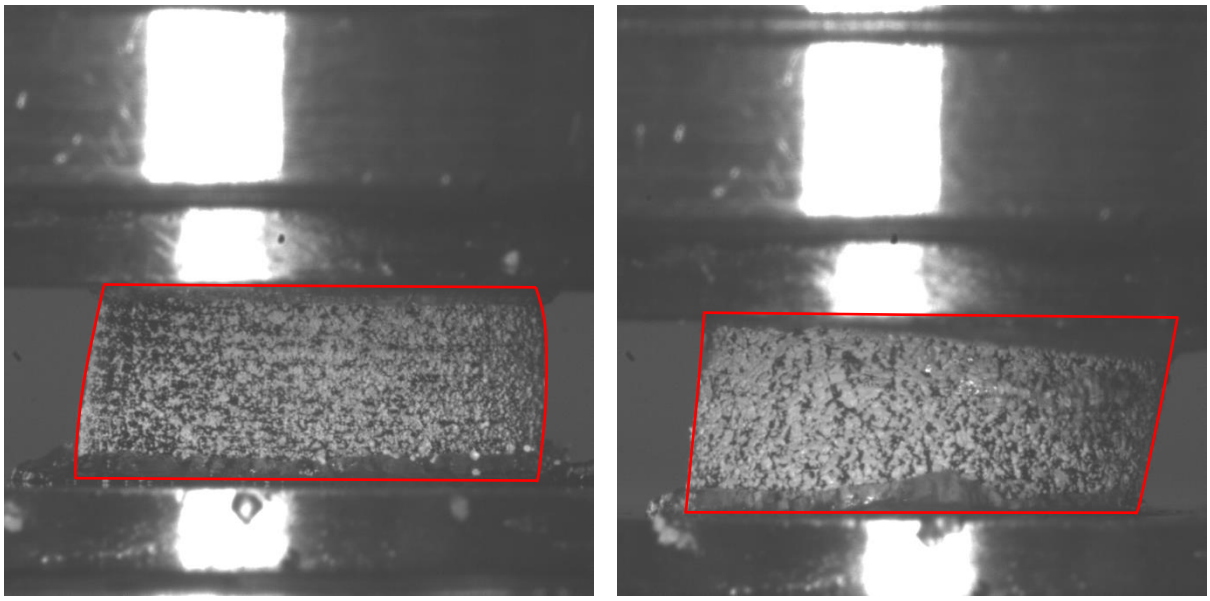


Figure C.3: Asymmetrical barrelling deformation occurred in compression experiments state the strain here

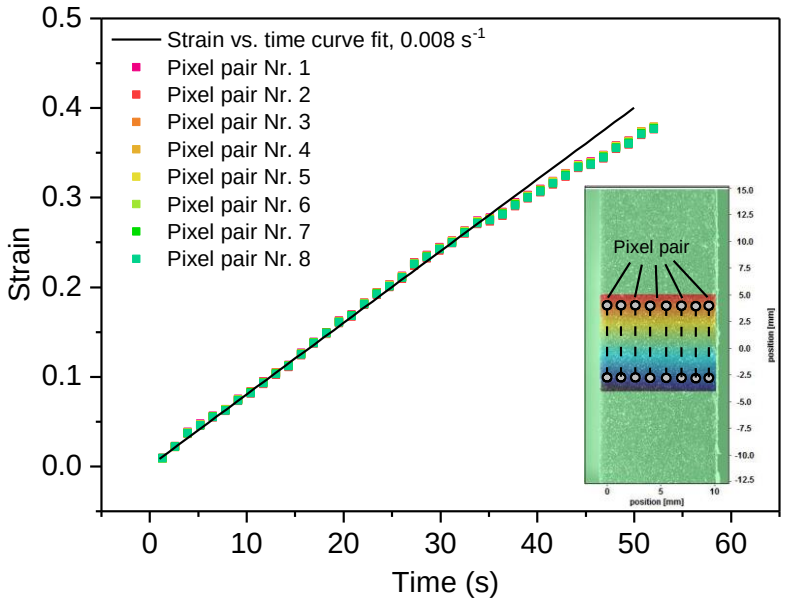


Figure C.4: DIC implemented into strain rate calculation: the mean of 50 pixel-to-pixel extensions against time indicates that the strain rate can only be maintained up to 0.35 strain in tensile experiments. Here, pixel-to-pixel extensions of 8 pairs of pixels are shown for schema.

Full data in quasi-static tensile and compression tests are shown in Figure C.5, Figure C.6 and Figure C.7. The test data closest to the mean value were used in main text. The simulation plots are analysed, plotted and compared to other experimental results to examine

the validation of the viscoelastic damage model.

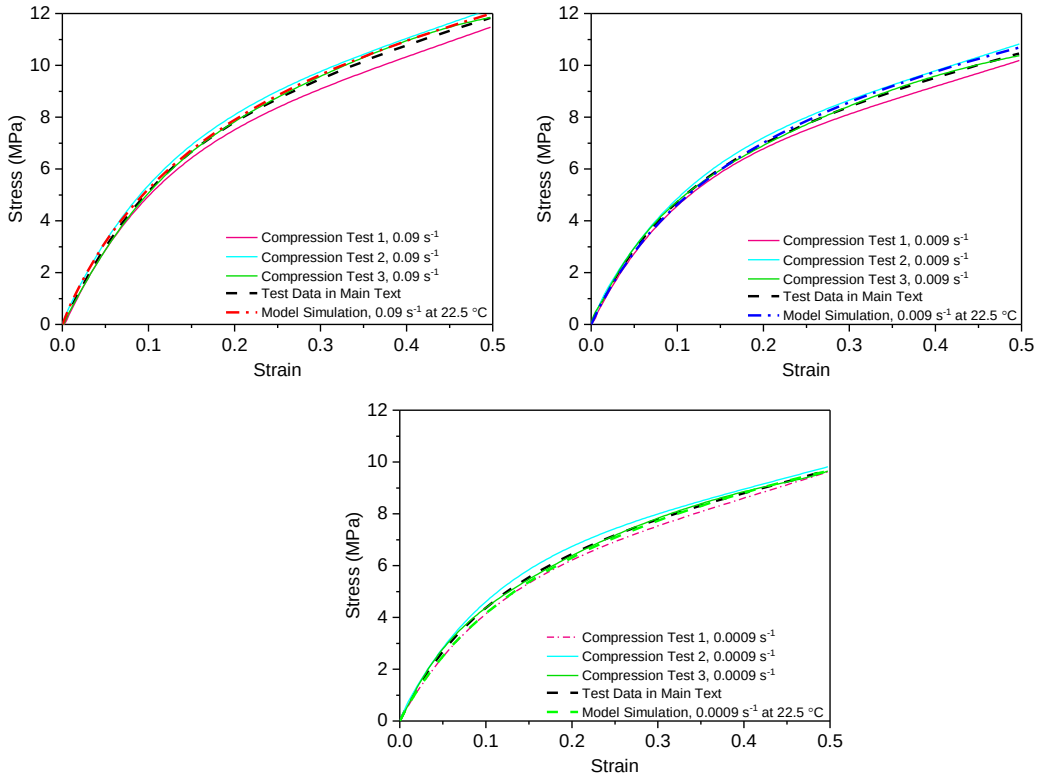


Figure C.5: The quasi-static compression tests data and calibration results for Fig. 3-9 in main text

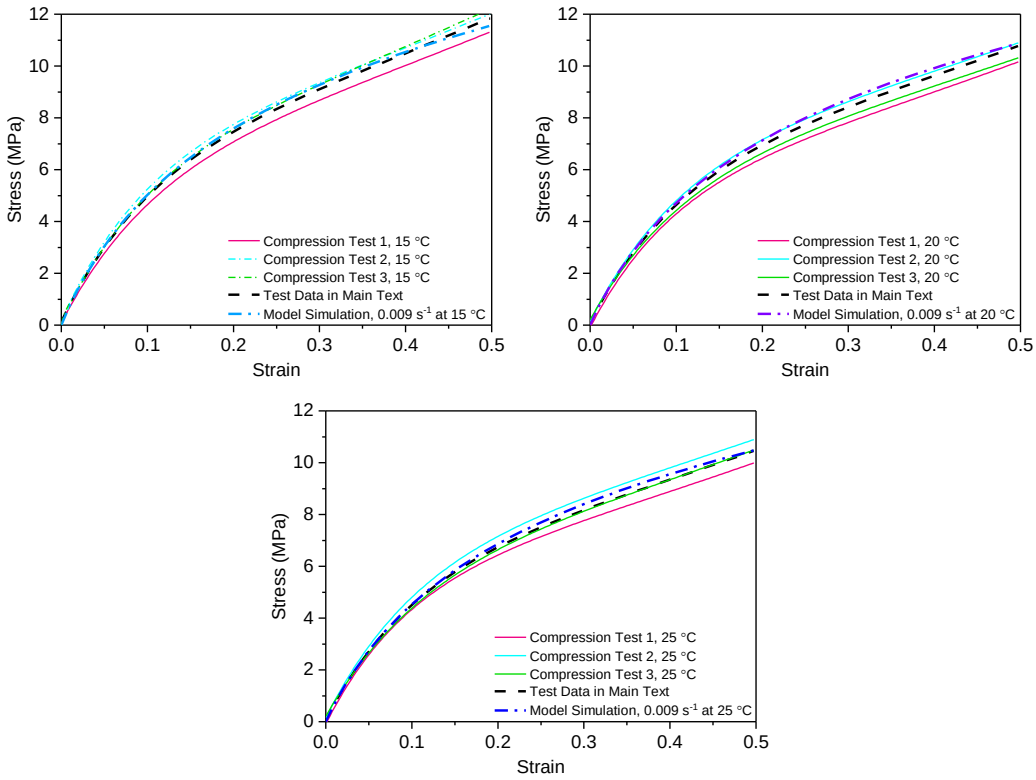


Figure C.6: The quasi-static compression tests data and calibration results for Fig. 3-10 in main text

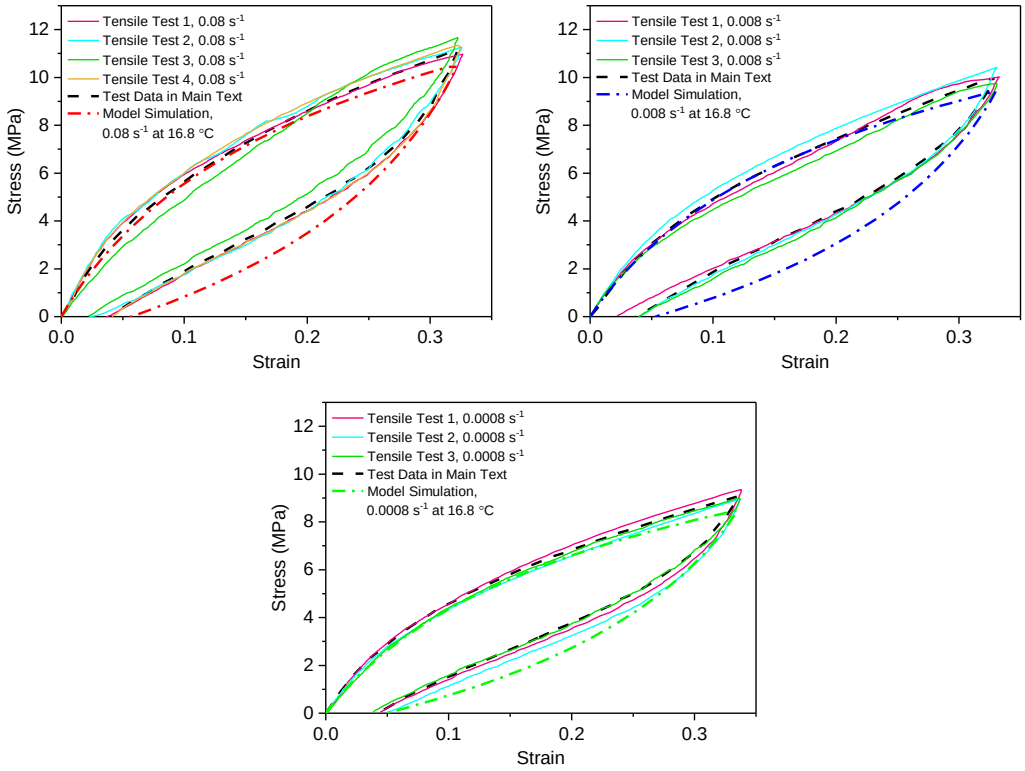


Figure C.7: The quasi-static tensile tests data and calibration results for Fig. 3-11 in main text

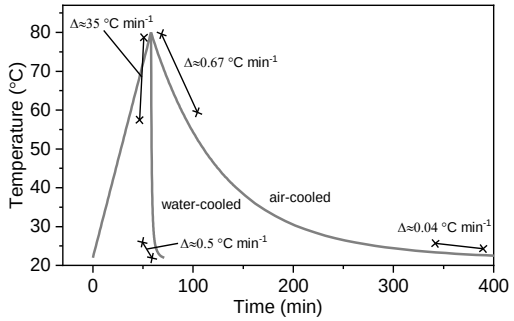


Fig. SI 1: Temperature profiles for air- and water-cooled specimens

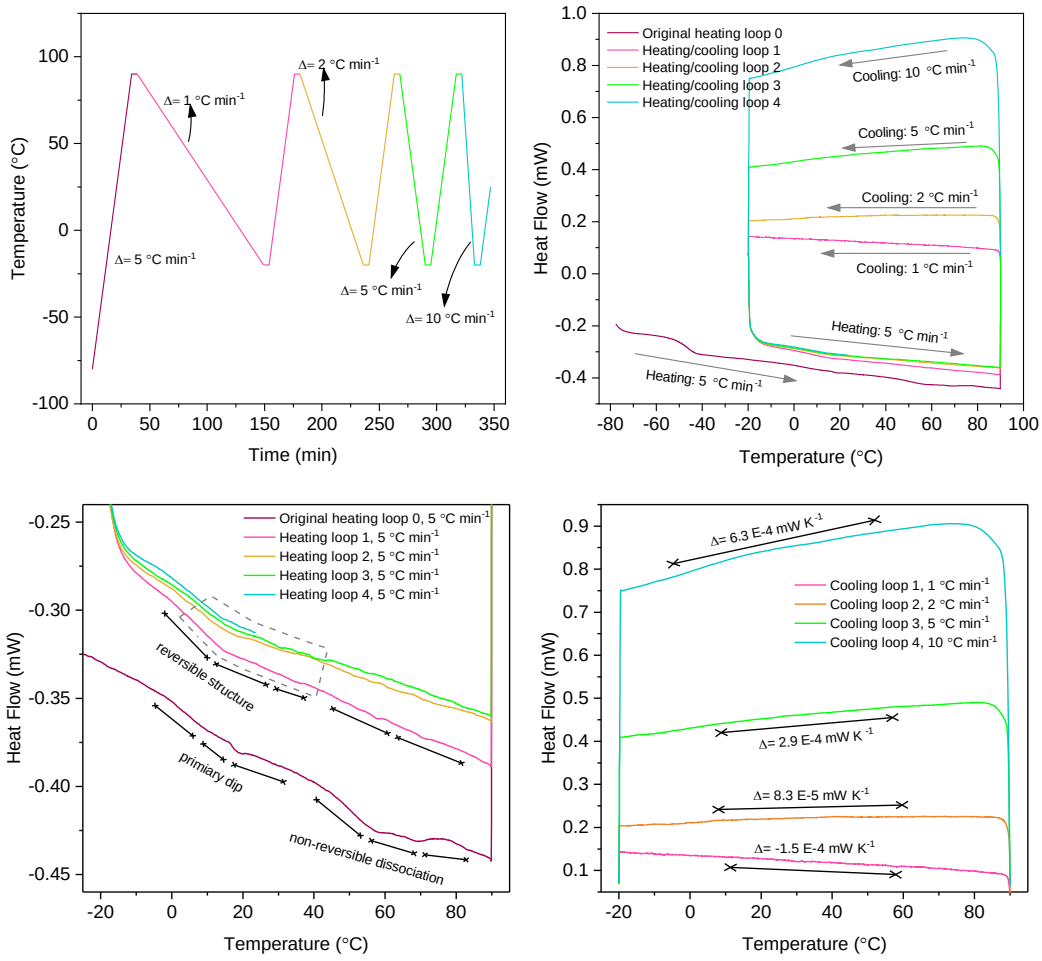


Fig. SI 2: DSC experiments for 'Sample DSC1' with different cooling rates performed on a cast (raw) specimen: (a) temperature profile used; (b) measured heat flow for the different heating and cooling loops; (c) detail of heating loops; (d) detail of cooling loops.

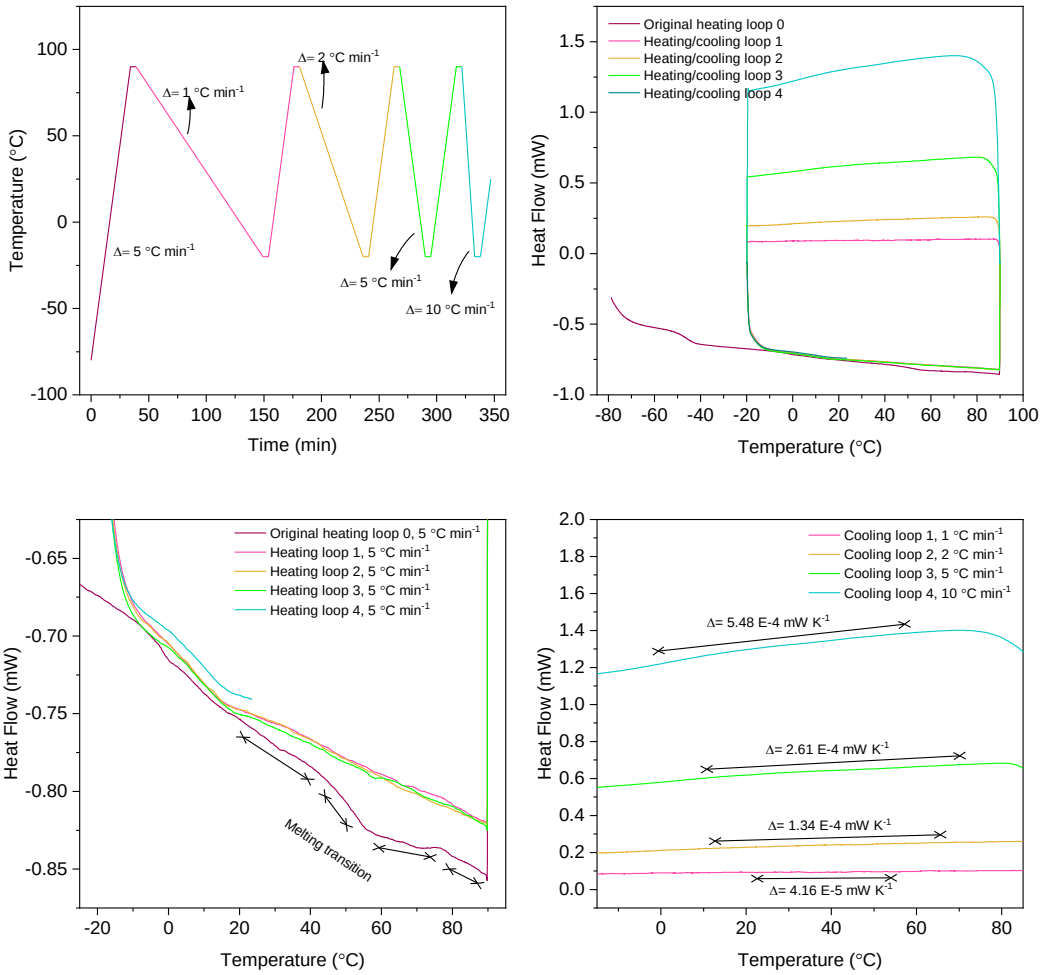
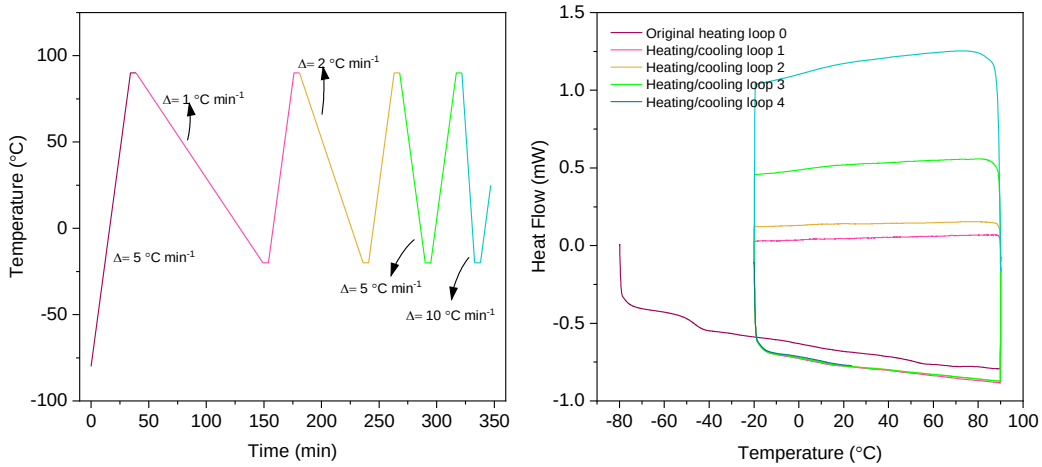


Fig. SI 3: DSC experiments for 'Sample DSC2' with different cooling rates performed on a cast (raw) specimen: (a) temperature profile used; (b) measured heat flow for the different heating and cooling loops; (c) detail of heating loops; (d) detail of cooling loops.



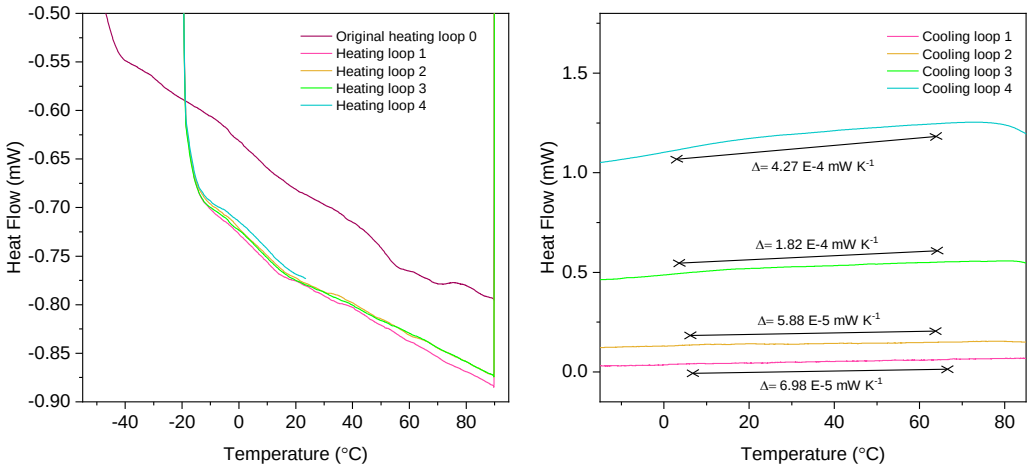


Fig. SI 4: DSC experiments for 'Sample DSC3' with different cooling rates performed on a cast (raw) specimen: (a) temperature profile used; (b) measured heat flow for the different heating and cooling loops; (c) detail of heating loops; (d) detail of cooling loops.

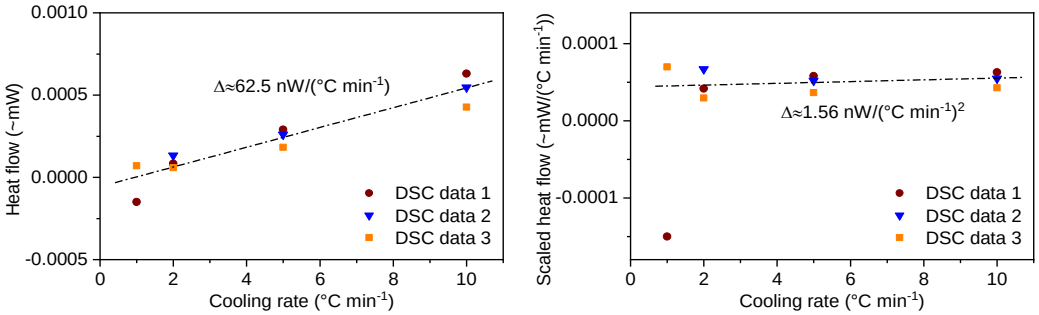


Fig. SI 5: (a) Heat flow against cooling rate in each DSC loop; (b) Heat flow normalized by the cooling rate to give a scaled unit value, which is almost consistent for each rate, indicating that the underlying thermodynamic process is not affected by cooling rate.

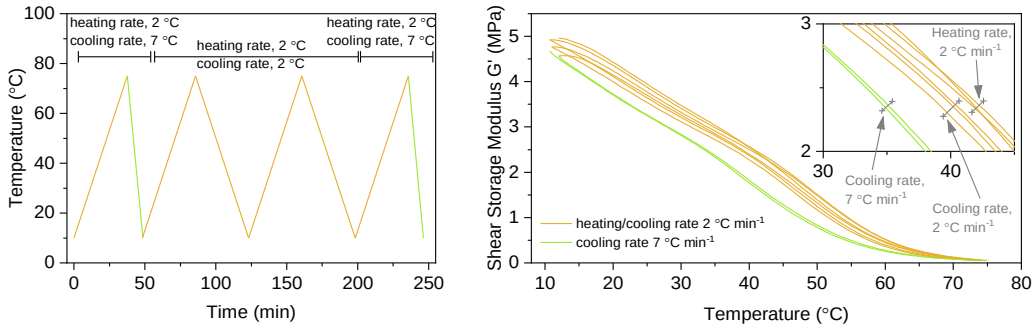


Fig. SI 6: The reproducibility of the rheological data was confirmed by conducting repeated dynamic rheological analysis at two rates, to see whether the temperature history was fully erased in each new thermal cycle. A single specimen was heated at 2 °C min^{-1} and cooled at 7 °C min^{-1}, followed by 2 °C min^{-1} twice, and then 7 °C min^{-1} again.

In the ‘shift method’, the modulus-temperature curves produced by different heating or cooling rates in main paper are shifted horizontally to overlap at a ‘reference’ rate, here 2 °C min^{-1}. The shifted curves are shown in Fig. SI 7 along with the required shift factors, which were modelled using an equation, similar to the formation of the WLF equation (introduced in Section 4), given by

$$SF = -\frac{\alpha(\dot{T} - \dot{T}_{ref})}{\beta + (\dot{T} - \dot{T}_{ref})} \qquad Eq.\ (1)$$

where α and β are fitting parameters, $\dot{T}$ is the cooling or heating rate and, $\dot{T}_{ref}$ is the reference rate. The parameters were obtained by fitting to the empirical data, after which it was observed that the parameters fit the same relation in both heating and cooling experiments.

This relationship was then validated, again using a reference curve at 2 °C min^{-1}, at cooling rates of 3, 8, 12 °C min^{-1}, Fig. SI 8. These experiments were performed at temperatures from 0 to 90 °C; a comparison of these data to the earlier rheometry results, Fig. SI 9, shows good agreement. Here the limitations of the Peltier temperature control system in the rheometer should be noted; in particular, that the cooling rate decreases towards the end of each cooling ramp. This causes discrepancies in the data around room temperature in the first set of experiments and around 0 °C in the second set. Details of the temperature-time profiles are shown in Fig. SI 10-11.

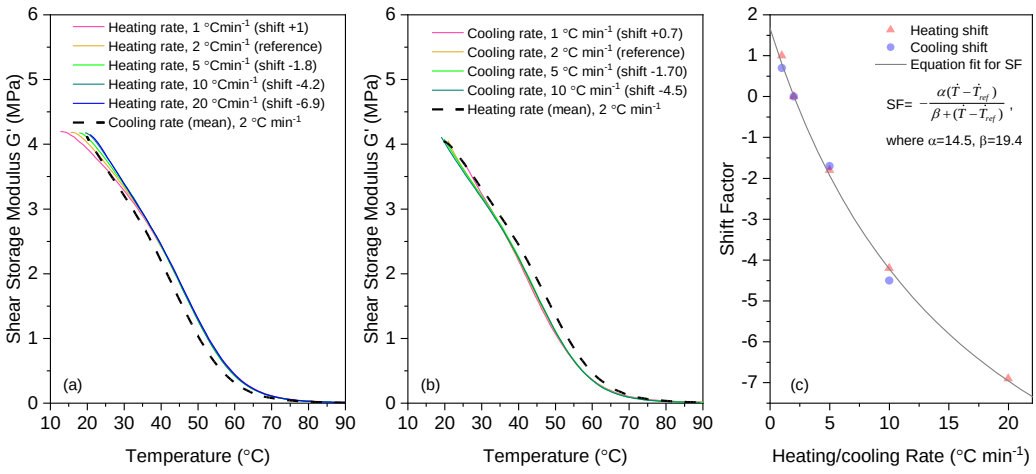


Fig. SI 7: (a) and (b) The modulus-temperature curves obtained at different temperatures can

be horizontally shifted to overlap; this produces a rate dependent shift factor shown in (c). Oscillation frequency 1 Hz and amplitude 0.1%.

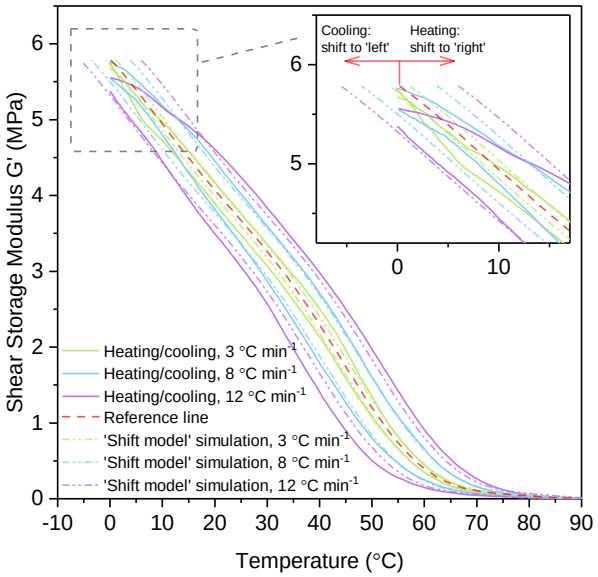


Fig. SI 8: Application of the 'shift method' using previously obtained shift factors to describe the rheological data at 3, 8, 12 °C min^{-1}. The reference curve was extrapolated from the average of the data obtained at 2 °C min^{-1}. Oscillation frequency 1 Hz and amplitude 0.1%.

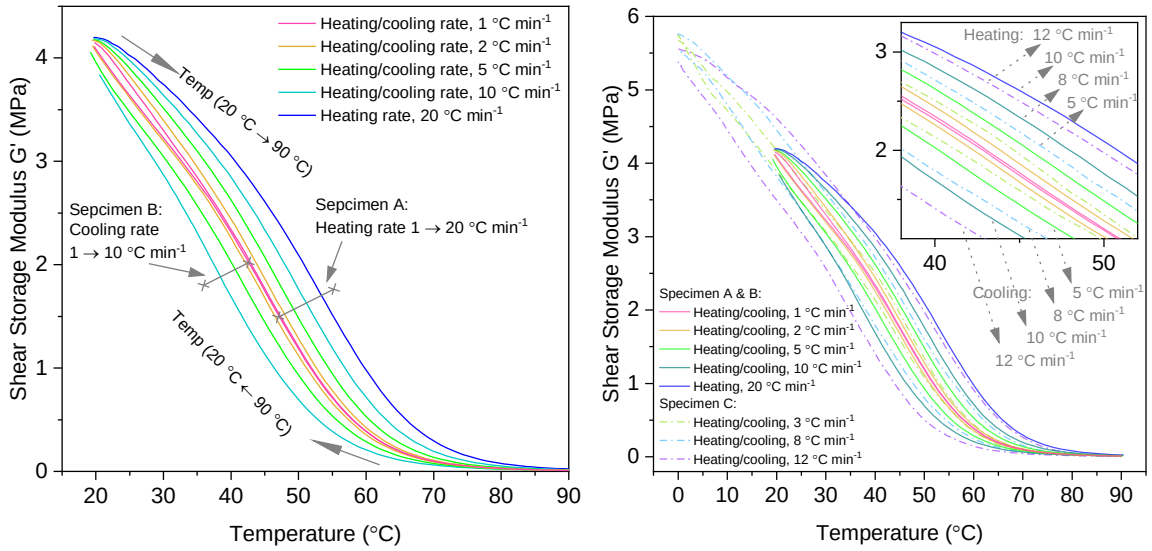


Fig. SI 9: Comparison of rheological data from three different samples: (a) assembled data from specimens A & B which underwent heating/cooling rates of 1, 2, 5, 10, 20 °C min^{-1}, also shown in the main text, Fig. 4-7. (b) comparison of the combination of data A & B to the specimen C, the latter was tested at rates of 3, 8, 12 °C min^{-1} over a wider temperature range. Oscillation frequency 1 Hz and amplitude 0.1%.

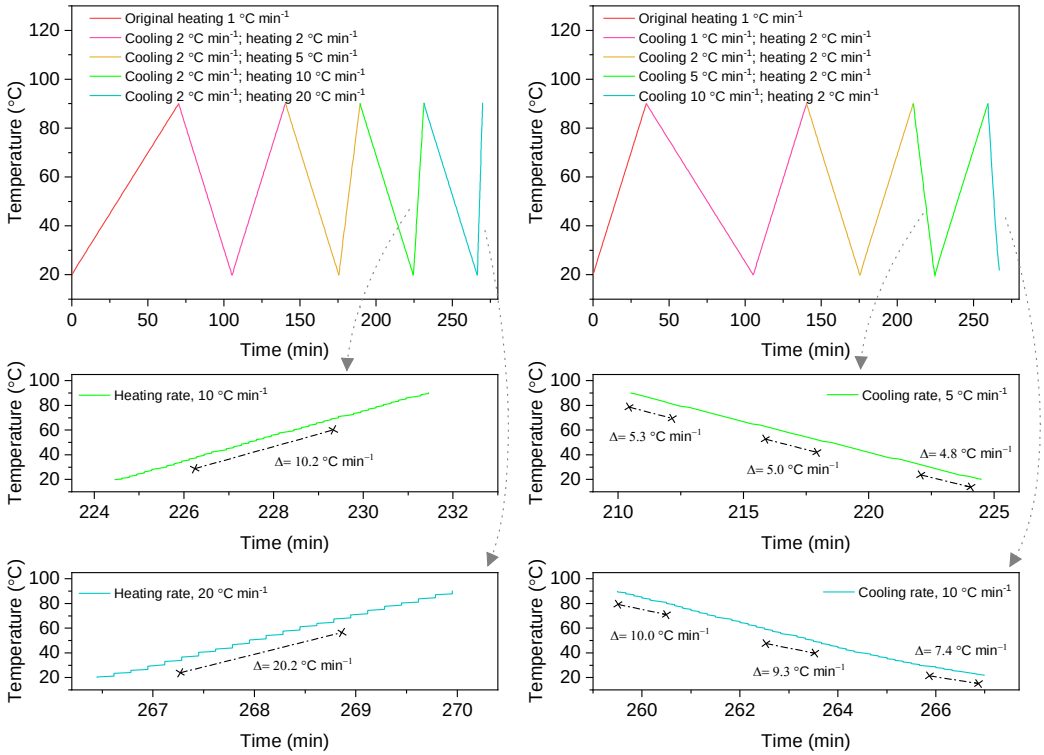


Fig. SI 10: The temperature profile for rheological analysis at heating and cooling rates of 1, 2, 5, 10 and 20 °C min^{-1}. The Peltier temperature control system has good consistency in slow cooling and fast heating, but for fast cooling the rate decreased towards the end of the cycle.

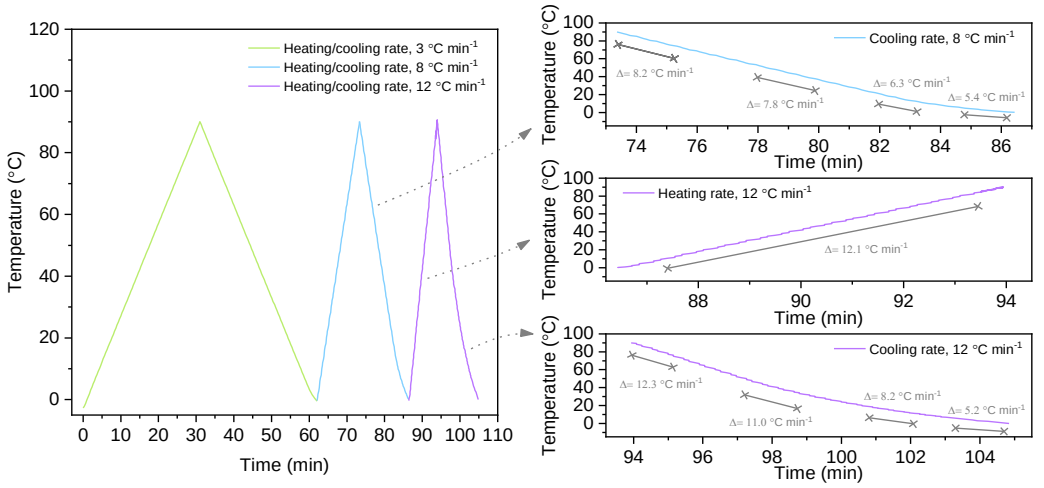


Fig. SI 11: The temperature profile for rheological analysis at heating and cooling rates of 3, 8 and 12 °C min^{-1}

The parameters derived in the main text (r_0 = 2 s^{-1} and U/k = 1312 K) were used to model the experiments with nominal temperature profiles of 3, 8, 12 °C min^{-1} (Fig. SI 11), results are shown in Fig. SI 12. The advantage of this model over the shifting method is that,

in principle, it can be applied to arbitrary temperature profiles, and the parameters have a better physical interpretation, as rate of evolution and thermal activation. It was also noted that this model has better continuity than the 'shift method' for thermal cycles because it can use the experimental temperature profiles. To demonstrate the importance this, model outputs at different constant heating/cooling rates are shown in Fig. SI 13 whilst a comparison of results from constant and empirical rates is shown in Fig. SI 14.

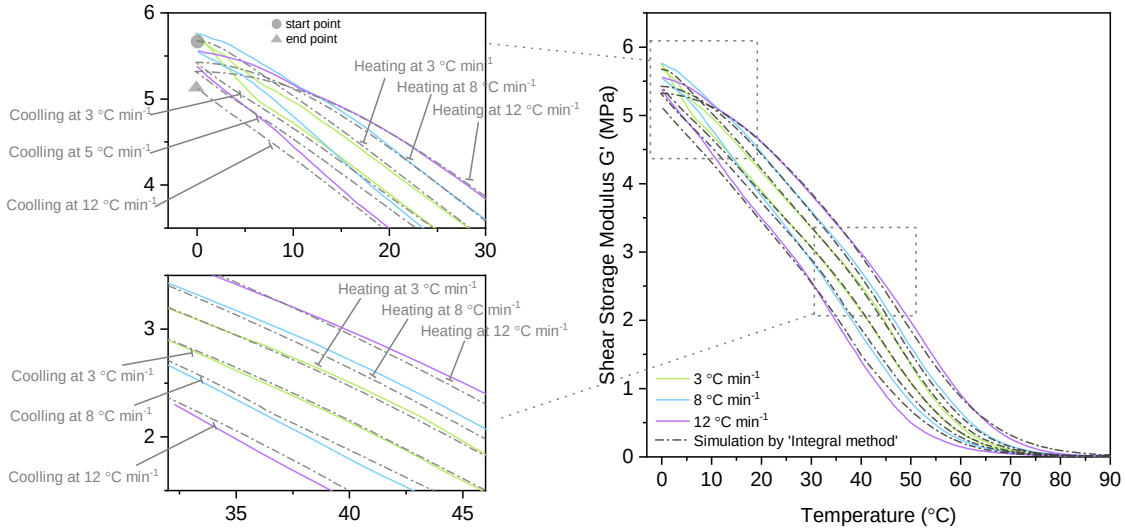


Fig. SI 12: Application of the Arrhenius equation based model to heating and cooling processes at 3, 8, 12 °C min^{-1}. The reference curve was produced by extrapolation of the previous reference curve. The same parameters as in Fig. 4-11 and the experimental temperature profiles were applied. Oscillation frequency 1 Hz and amplitude 0.1%.

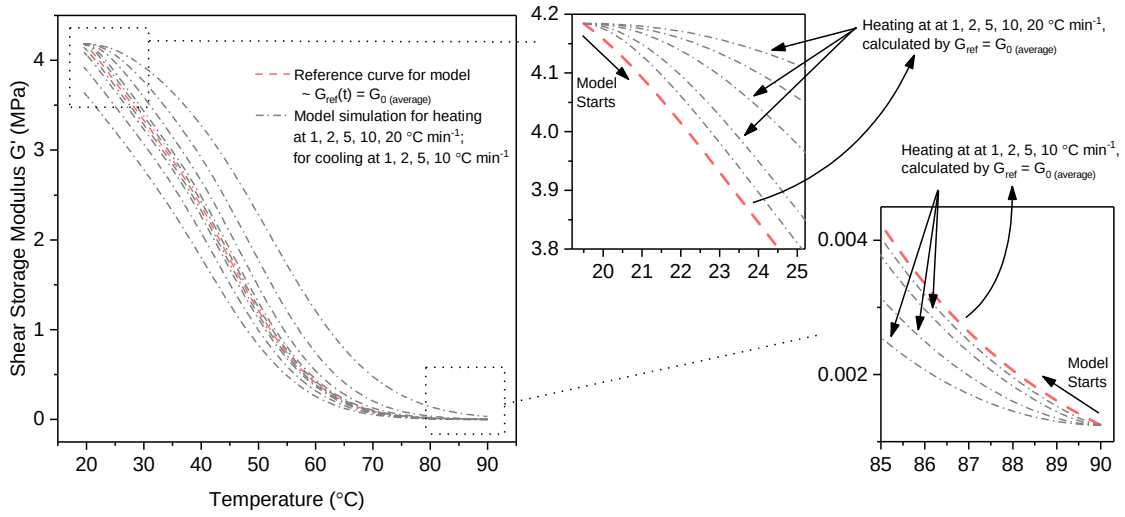


Fig. SI 13: An example of applying the Arrhenius equation based model to heating/cooling processes from 1 to 20 °C min^{-1}. Here, a constant heating or cooling rate is assumed. Oscillation frequency 1 Hz and amplitude 0.1%.

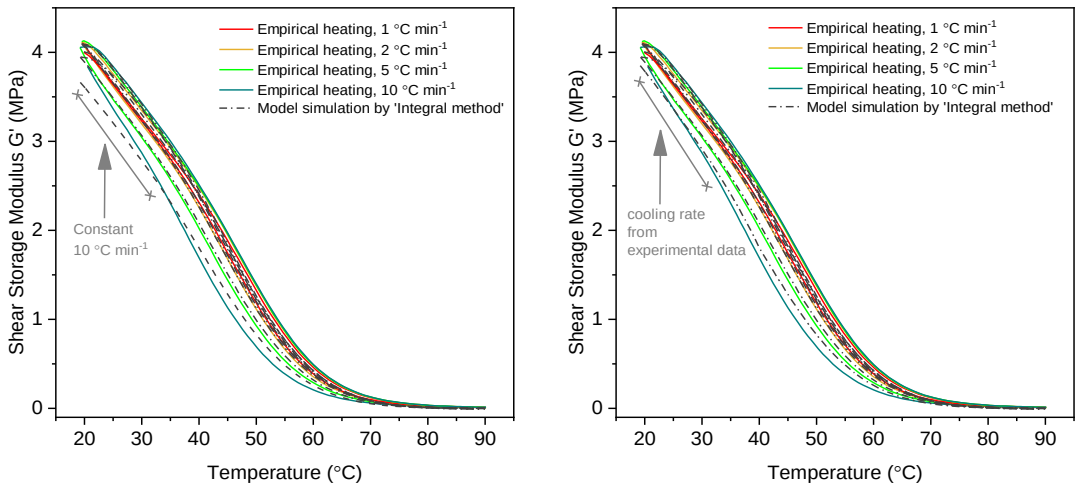


Fig. SI 14: Comparison of data obtained using (a) constant cooling rate of 10 °C and (b) the empirical cooling rate, in Arrhenius equation based model. Oscillation frequency 1 Hz and amplitude 0.1%.

A final rheological experiment was performed to investigate the evolution of mechanical response when held at 80 °C; here all the heating and cooling cycles were performed at 2 °C min^{-1}, whilst during the hold the specimen was maintained at a strain of 0.1 % with no oscillation. The data obtained are shown in Fig. SI 15. Here, Fig. SI 15a, shows the temperature profiles used whilst Fig. SI 15b shows that the storage modulus profiles are consistent between cycles. Finally, Fig. SI 15c shows the relaxation of the modulus with time at 80 °C. In particular, it is interesting to re-derive the Arrhenius parameters to fit these data. An estimate of the long-term modulus was taken as the reference, G_{ref}; whilst r_0 and U/k were fit to the relaxation data: the resulting value of r_0 was the same as obtained from the previous fit, whilst U/k was different. In order to confirm that these differences are significant, a comparison of model outputs for heating and cooling cycles using three values of U/k is shown in Fig. SI 16. The changes in value indicate that there may be more than one process involved in the polymer response, with different activation energies.

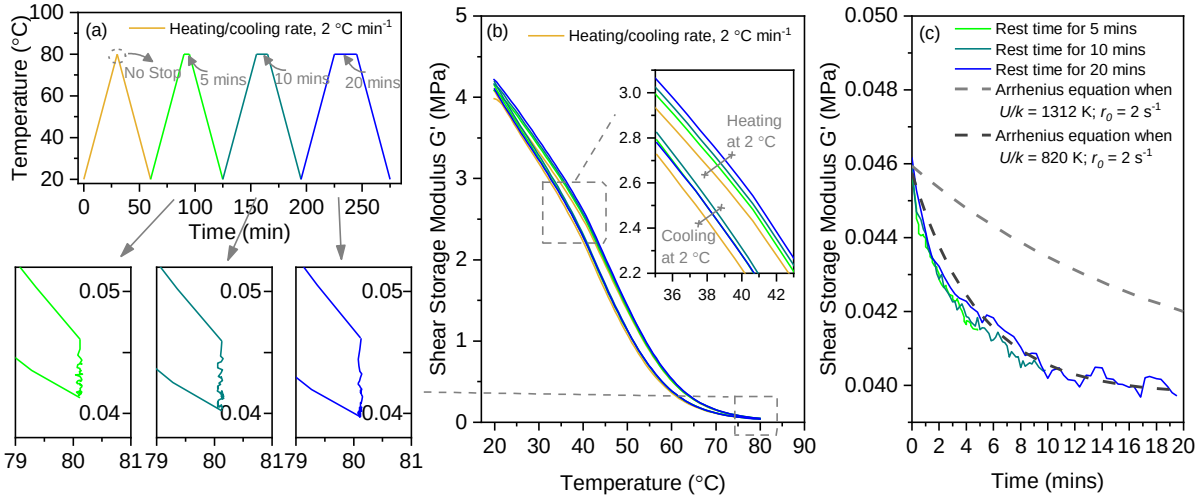


Fig. SI 15: One single specimen subjected to rheological analysis at 2 °C min^{-1} on both heating and cooling but held for different times between 0 and 20 minutes at 80 °C. (a) heating profiles (b) The mechanical behavior during heating and cooling is consistent, also shown is a magnification of the detail at 80 °C. (c) The Arrhenius equation based model was applied again to model the high temperature relaxation. Here, G_{ref} was set equal to 0.0397 MPa, estimated from the long-term stress response from the experiments. Unit r_0 is s^{-1}, U/k is K. Changing the activation energy term U/k from 1312 K to 820 K gives a better fit to the experimental data.

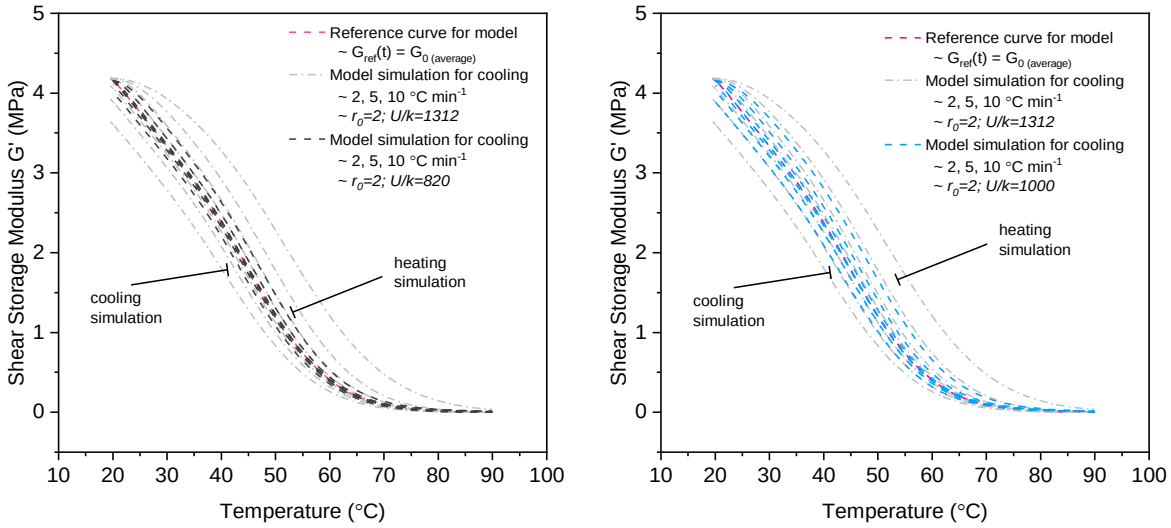


Fig. SI 16: Comparisons of the Arrhenius based Integral model using three different values of U/k: 1312, 820 and 1000 K for heating and cooling simulation.

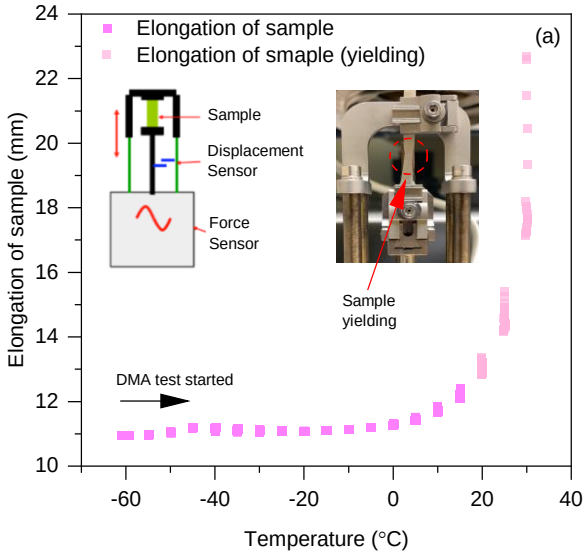


Fig. SI 17: Specimen elongation and necking were observed in DMA experiments at temperatures over 15 °C.

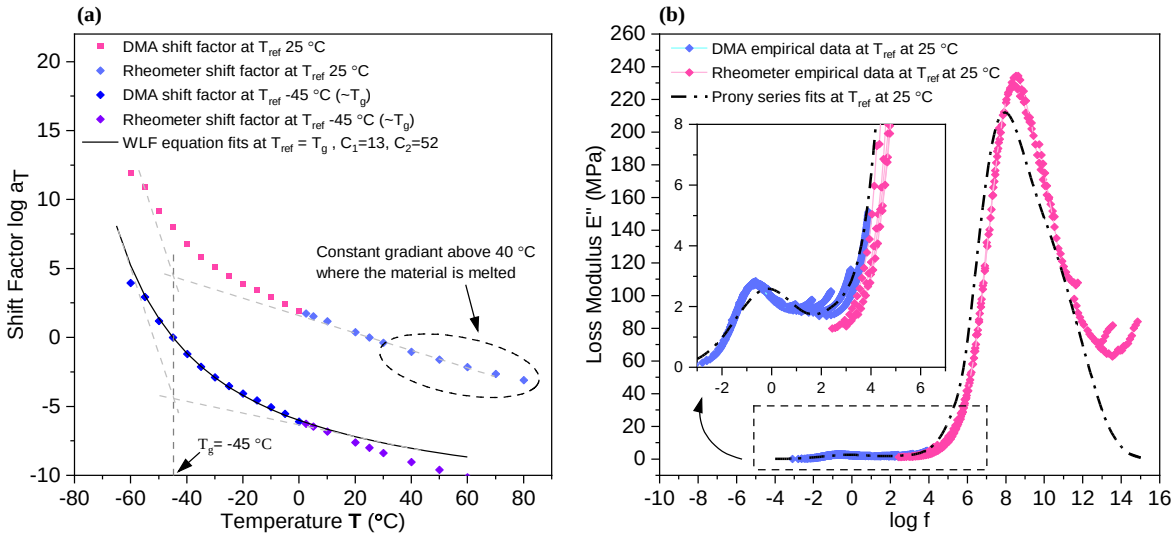


Fig. SI 18: (a) Plot of shift factor vs temperature for master curves produced at 25 and -45 °C. The WLF equation with parameters C_1=13, C_2=52 °C fits the shift factors. (b) The Prony series fit to the storage data can be used to derive loss modulus as a function of frequency; here it is compared to empirical data.

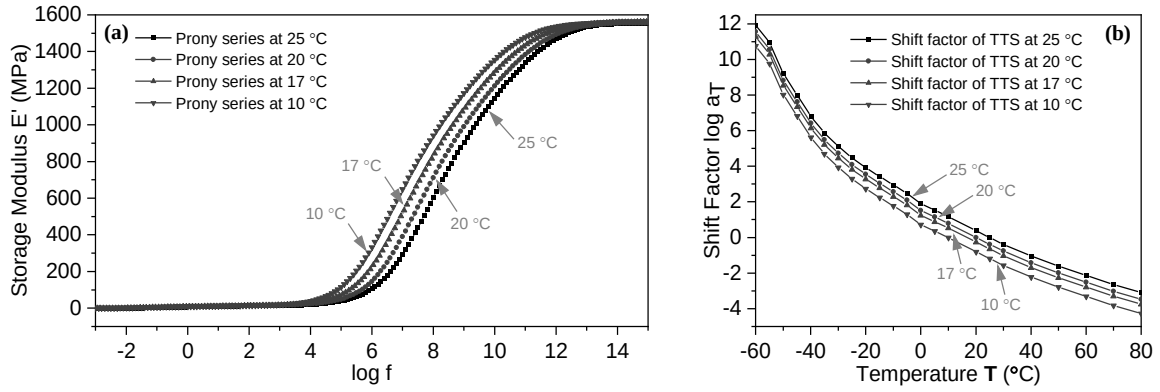


Fig. SI 19: The Prony series and TTS shift factors for reference temperatures of 25, 20, 17, 10 °C.

Table SI 1- Prony Series at Temperature 25 °C			
Maxwell Element Number	Young's Moduli E' (MPa)	Relaxation Time τ (s)	Viscosity η (MPa·s)
0	0	∞	∞
1	0.268	1.778E+02	4.769E+01
2	0.741	5.623E+01	4.164E+01
3	1.758	1.778E+01	3.126E+01
4	2.340	5.623E+00	1.315E+01
5	2.097	1.778E+00	3.728E+00
6	1.587	5.623E-01	8.923E-01
7	1.378	1.778E-01	2.449E-01
8	1.420	5.623E-02	7.986E-02
9	1.420	1.778E-02	2.524E-02
10	1.344	5.623E-03	7.557E-03
11	1.334	1.778E-03	2.371E-03
12	1.515	5.623E-04	8.519E-04
13	2.469	1.778E-04	4.390E-04
14	5.710	5.623E-05	3.210E-04
15	12.667	1.778E-05	2.252E-04
16	22.184	5.623E-06	1.247E-04
17	33.113	1.778E-06	5.888E-05
18	70.830	5.623E-07	3.983E-05
19	117.73	1.778E-07	2.093E-05
20	154.84	5.623E-08	8.707E-06
21	169.45	1.778E-08	3.013E-06
22	162.30	5.623E-09	9.126E-07
23	144.05	1.778E-09	2.561E-07
24	125.96	5.623E-10	7.083E-08
25	112.75	1.778E-10	2.005E-08
26	102.31	5.623E-11	5.753E-09
27	90.52	1.778E-11	1.609E-09
28	75.64	5.623E-12	4.253E-10
29	58.88	1.778E-12	1.047E-10
30	42.09	5.623E-13	2.366E-11
31	26.27	1.778E-13	4.671E-12
32	12.86	5.623E-14	7.236E-13
33	5.506	1.778E-14	9.791E-14

Table SI 2- Prony Series at Temperature 20 °C			
Maxwell Element Number	Young's Moduli E' (MPa)	Relaxation Time τ (s)	Viscosity η (MPa·s)
0	0	∞	∞
1	0.838	1.778E+02	1.490E+02
2	1.842	5.623E+01	1.035E+02
3	2.316	1.778E+01	4.118E+01
4	2.072	5.623E+00	1.165E+01
5	1.594	1.778E+00	2.834E+00
6	1.362	5.623E-01	7.659E-01
7	1.389	1.778E-01	2.470E-01
8	1.396	5.623E-02	7.847E-02
9	1.269	1.778E-02	2.256E-02
10	1.220	5.623E-03	6.859E-03
11	1.520	1.778E-03	2.703E-03
12	2.325	5.623E-04	1.307E-03
13	4.102	1.778E-04	7.294E-04
14	8.469	5.623E-05	4.762E-04
15	18.406	1.778E-05	3.273E-04
16	36.848	5.623E-06	2.072E-04
17	73.496	1.778E-06	1.307E-04
18	120.34	5.623E-07	6.767E-05
19	156.36	1.778E-07	2.780E-05
20	169.53	5.623E-08	9.533E-06
21	161.37	1.778E-08	2.869E-06
22	142.88	5.623E-09	8.034E-07
23	125.04	1.778E-09	2.223E-07
24	112.11	5.623E-10	6.304E-08
25	101.70	1.778E-10	1.808E-08
26	89.74	5.623E-11	5.046E-09
27	74.69	1.778E-11	1.328E-09
28	57.87	5.623E-12	3.254E-10
29	41.11	1.778E-12	7.311E-11
30	25.38	5.623E-13	1.427E-11
31	12.21	1.778E-13	2.172E-12
32	5.35	5.623E-14	3.012E-13
33	8.99	1.778E-14	1.599E-13

Table SI 3- Prony Series at Temperature 17 °C			
Maxwell Element Number	Young's Moduli E' (MPa)	Relaxation Time τ (s)	Viscosity η (MPa·s)
0	0	∞	∞
1	1.352	1.778E+02	2.404E+02
2	2.171	5.623E+01	1.220E+02
3	2.257	1.778E+01	4.013E+01
4	1.821	5.623E+00	1.024E+01
5	1.435	1.778E+00	2.552E+00
6	1.363	5.623E-01	7.662E-01
7	1.416	1.778E-01	2.518E-01
8	1.349	5.623E-02	7.587E-02
9	1.224	1.778E-02	2.175E-02
10	1.324	5.623E-03	7.445E-03
11	1.855	1.778E-03	3.298E-03
12	3.032	5.623E-04	1.705E-03
13	5.805	1.778E-04	1.032E-03
14	12.53	5.623E-05	7.048E-04
15	26.46	1.778E-05	4.706E-04
16	52.05	5.623E-06	2.927E-04
17	97.12	1.778E-06	1.727E-04
18	140.76	5.623E-07	7.916E-05
19	166.04	1.778E-07	2.952E-05
20	167.57	5.623E-08	9.423E-06
21	152.64	1.778E-08	2.714E-06
22	133.43	5.623E-09	7.503E-07
23	118.00	1.778E-09	2.098E-07
24	106.86	5.623E-10	6.009E-08
25	96.090	1.778E-10	1.708E-08
26	82.563	5.623E-11	4.642E-09
27	66.384	1.778E-11	1.180E-09
28	49.423	5.623E-12	2.779E-10
29	33.067	1.778E-12	5.880E-11
30	18.293	5.623E-13	1.028E-11
31	7.680	1.778E-13	1.365E-12
32	5.722	5.623E-14	3.217E-13
33	5.113	1.778E-14	8.891E-14

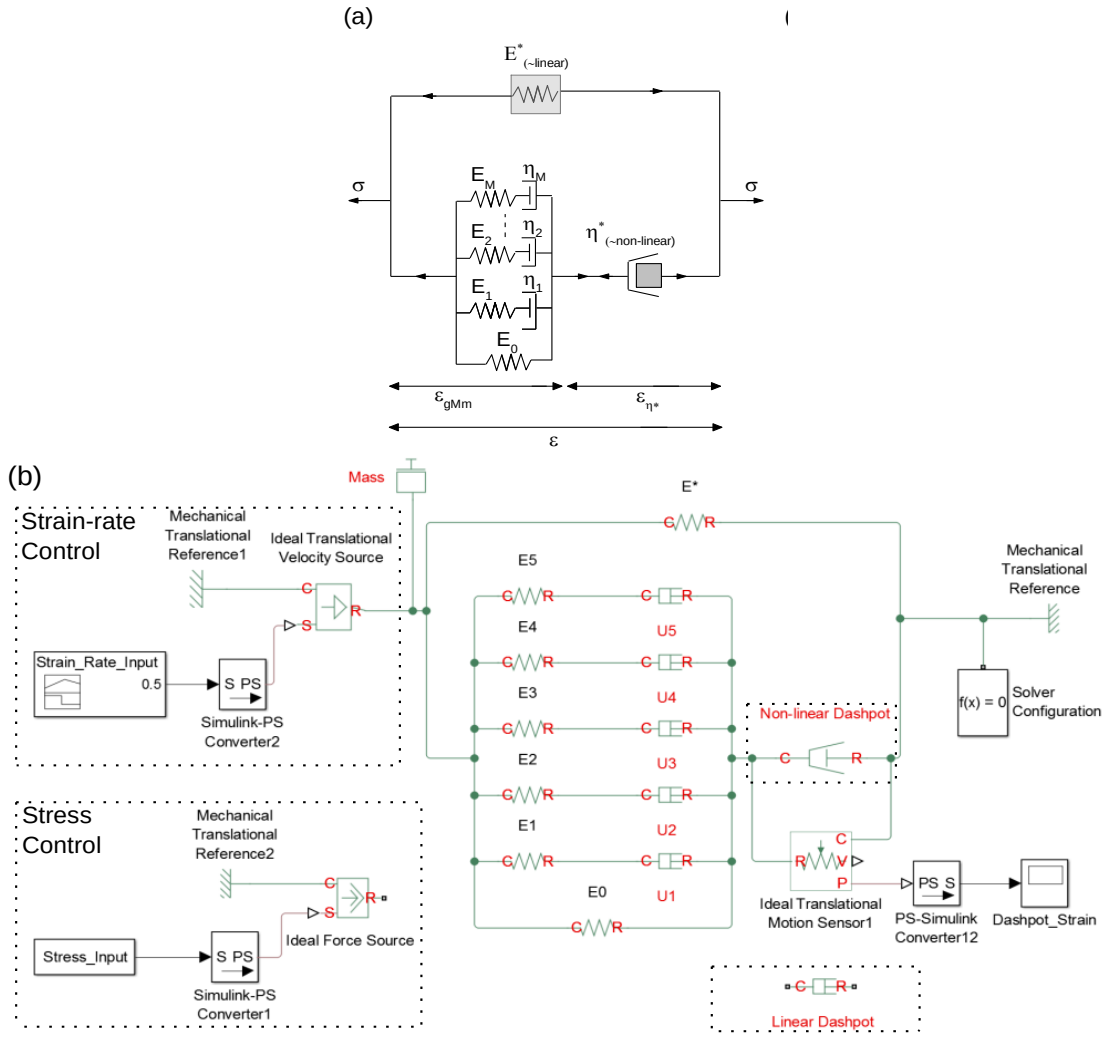


Fig. SI 20: The viscoelastic softening model implemented in Simscape and used to describe the mechanical responses including loading, unloading and recovery. (a) The model combines springs and dashpots described by the Prony series, an additional dashpot η^* and a recovery spring E^*. (b) The model implemented in Simulink, the deformation was applied by either a velocity source control or a force control, allowing either strain or stress profiles. A motion sensor measures the strain behaviour in each element but can be replaced by force sensor if stress values are required.

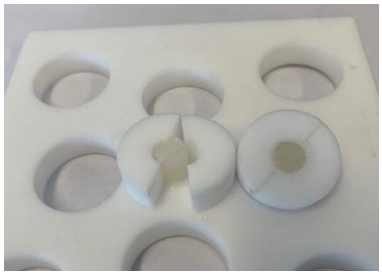


Fig. SI 21: (Left) Specimen preparation and can be compressed as a cylinder or disk with desired dimension for experiments by using PTFE mould.

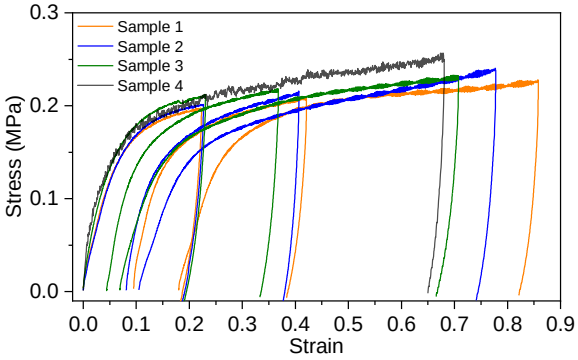


Fig. SI 22: (Right) Empirical strain-stress curves for three samples for recovery tests: key strain values are given in Table SI4.

Table SI 4: Strain data for Fig. SI 22

ε	**After Loadin**	**After 3hrs Recove**	**After 6hrs Recove**	**After 12hrs Recove**
Sample 1				
	0.185	0.112	0.09	N/A
1st Loading				
$\varepsilon_0/\varepsilon_f$ (%)	100	60.15	48.65	N/A
2nd Loading	0.386	0.248	0.181	N/A
$\varepsilon_0/\varepsilon_f$ (%)	100	64.25	46.89	N/A
Sample 2				
1st Loading	0.190	0.118	0.081	N/A
$\varepsilon_0/\varepsilon_f$ (%)	100	62.25	42.63	N/A
2nd Loading	0.38	N/A	0.145	0.105
$\varepsilon_0/\varepsilon_f$ (%)	100	N/A	38.16	27.63
Sample 3				
1st Loading	0.194	N/A	N/A	0.044
$\varepsilon_0/\varepsilon_f$ (%)	100	N/A	N/A	22.68
2nd Loading	0.335	N/A	N/A	0.0688
$\varepsilon_0/\varepsilon_f$ (%)	100	N/A	N/A	20.54

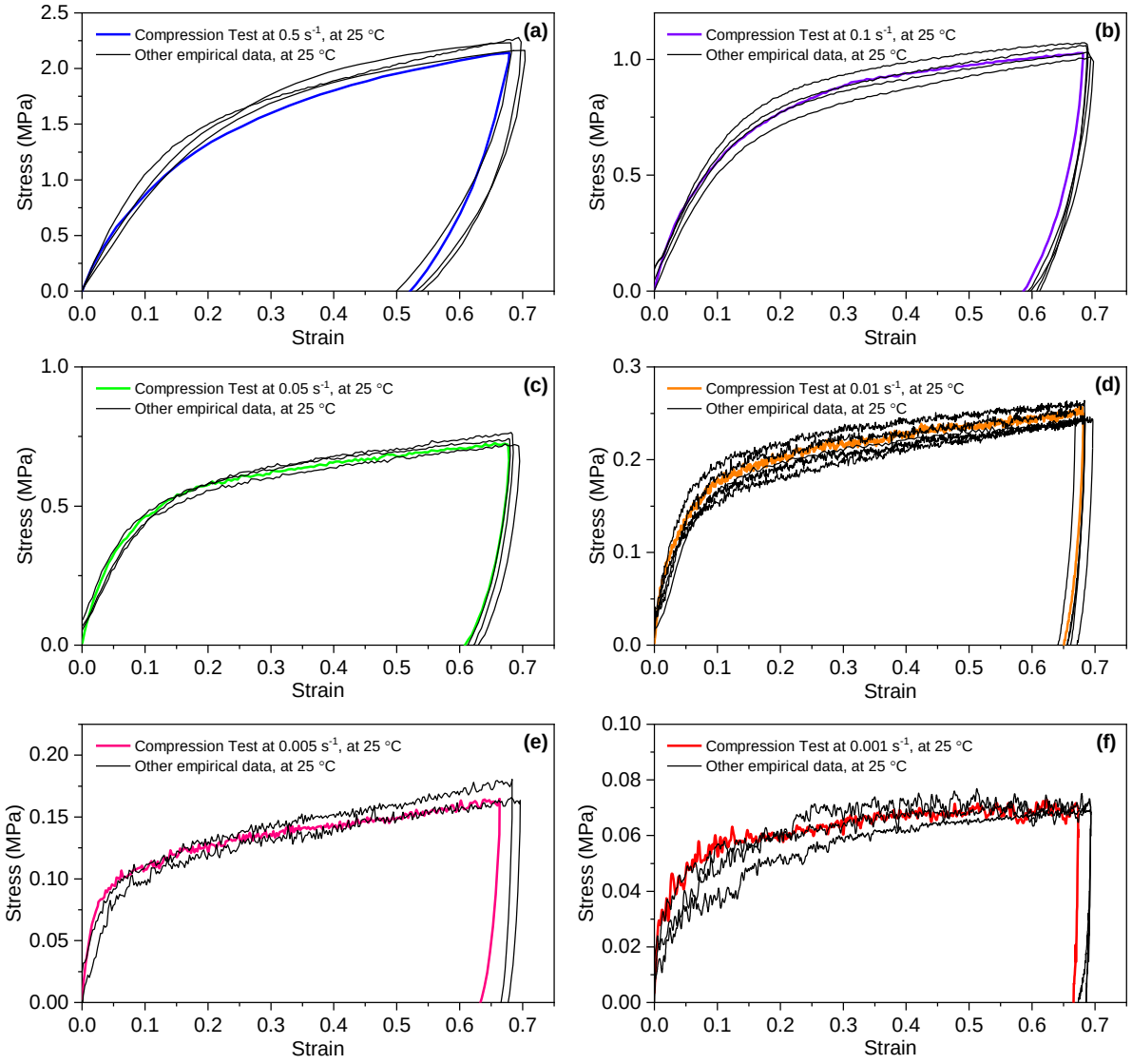
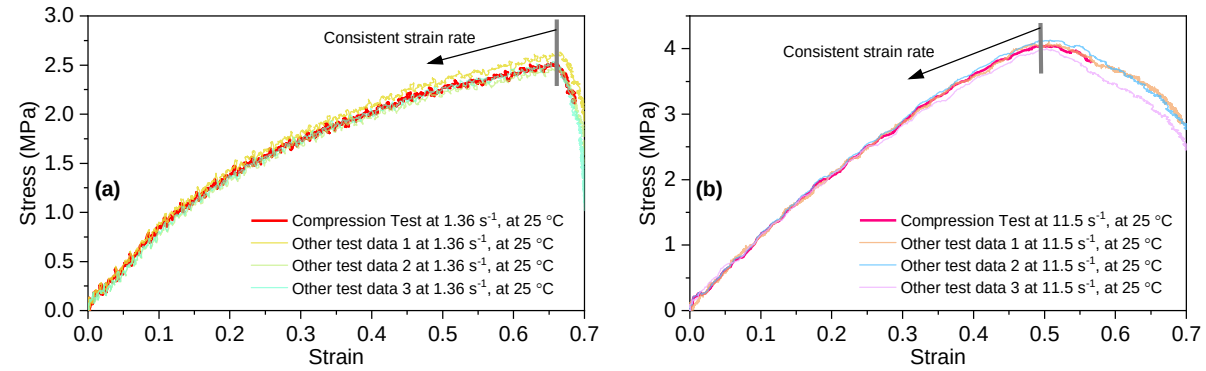


Fig. SI 23: Full data of low-rate compression experiments at 25 °C but varying strain rates: 0.001, 0.005, 0.01, 0.05, 0.1, 0.5 s^{-1}. The result used in the main paper is indicated by a coloured line, the other results are presented with black lines.



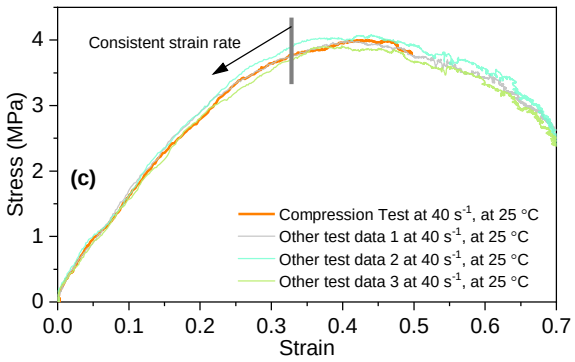


Fig. SI 24: Full data of medium-rate compression experiments at 25 °C but varying strain rates: 1.36, 11.5, 40 s^{-1}; regions of constant strain rate are indicated, as are the test data used in the main paper.

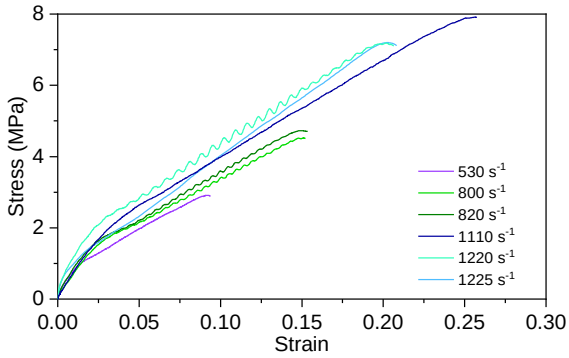


Fig. SI 25: Full data from high-rate compression experiments at 17 °C but varying strain rates.

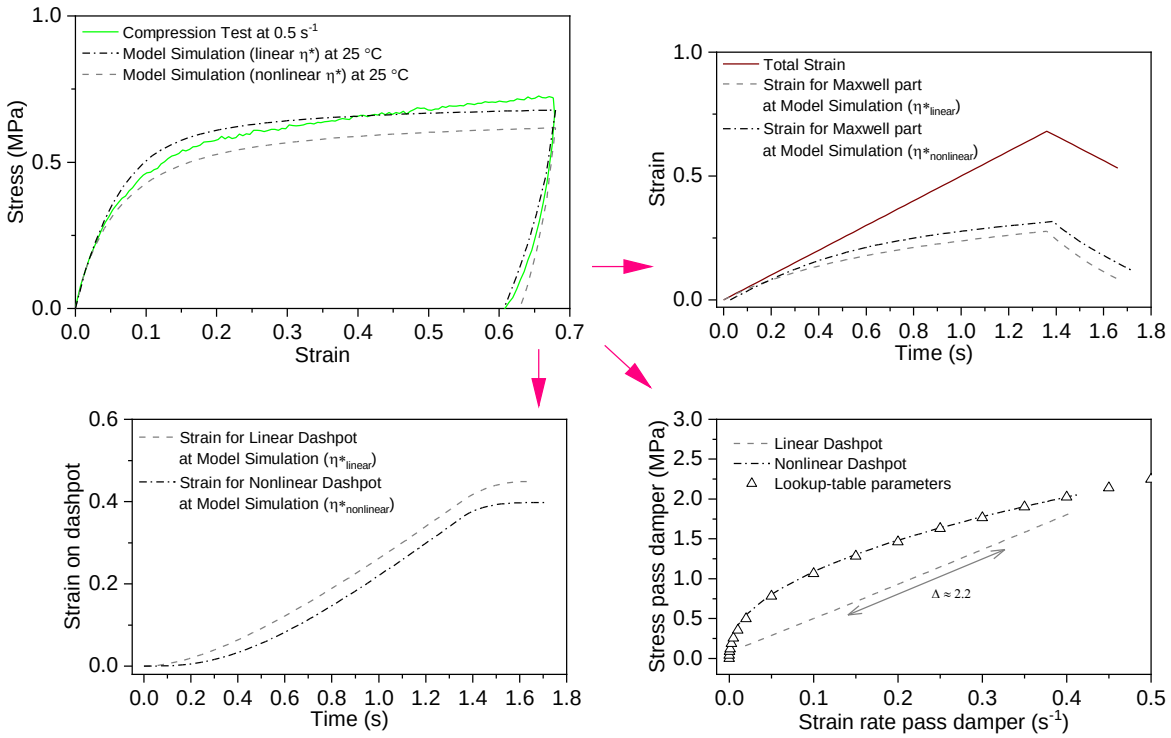


Fig. SI 26: The strain history for each element of the model at a strain rate 0.5 s^{-1} at 25 °C and the stress and strain rate in the damper.

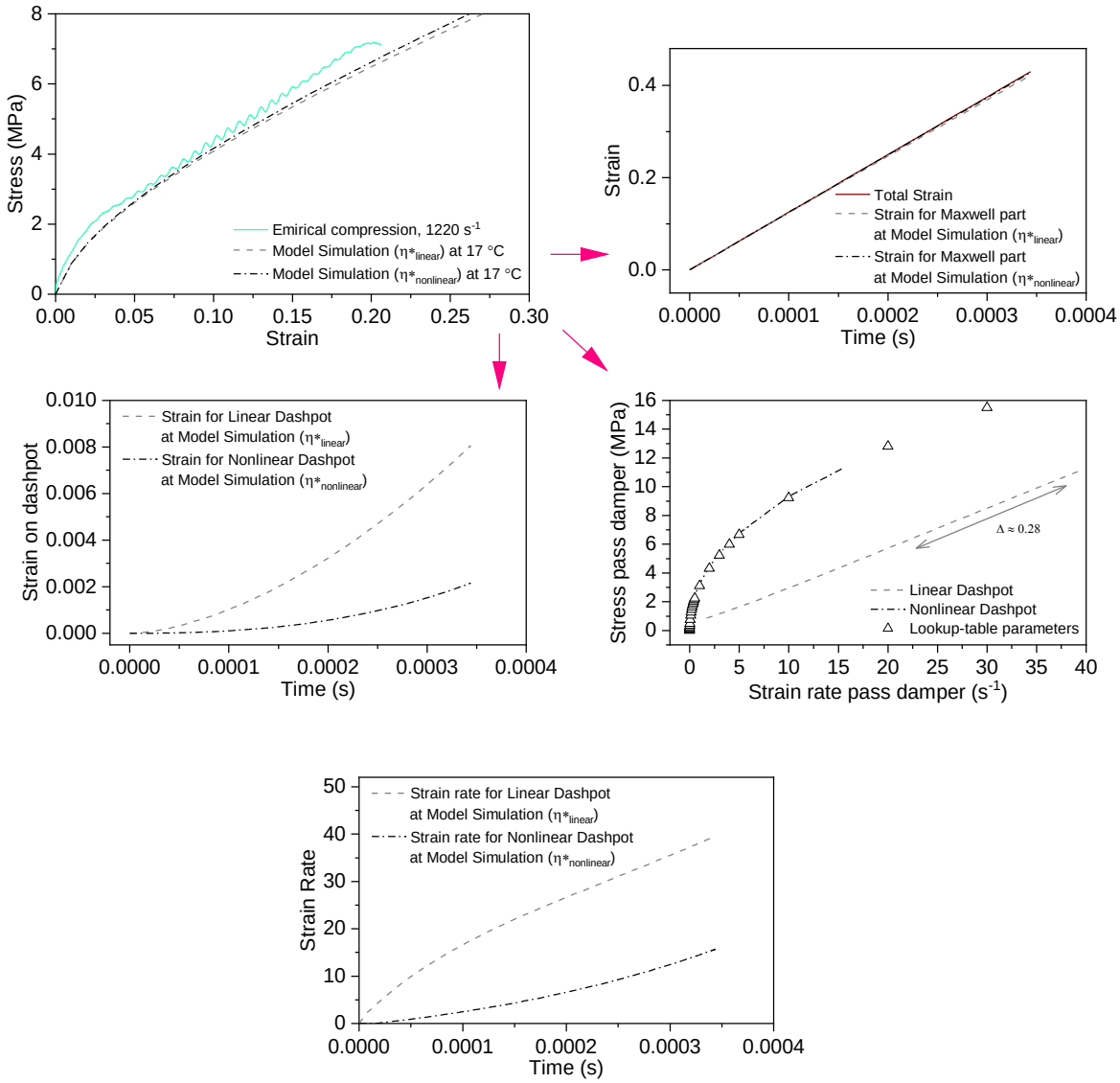


Fig. SI 27: The strain history for each element from the model at a strain rate 1220 s^{-1} at 17 °C and the stress and strain rate in dashpot η^*.

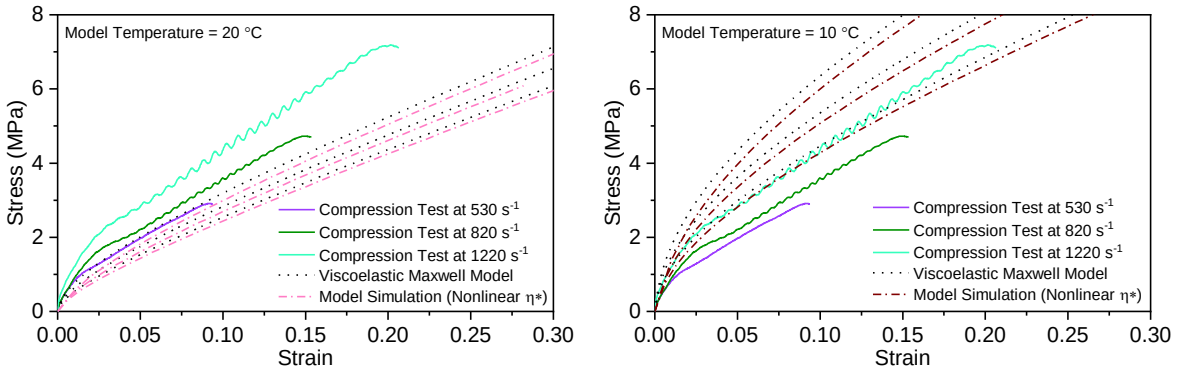


Fig. SI 28: Comparison of data obtained using the Prony series to predict the viscoelastic response at high strain rates at 20 and 10 °C. Note the strong temperature sensitivity.

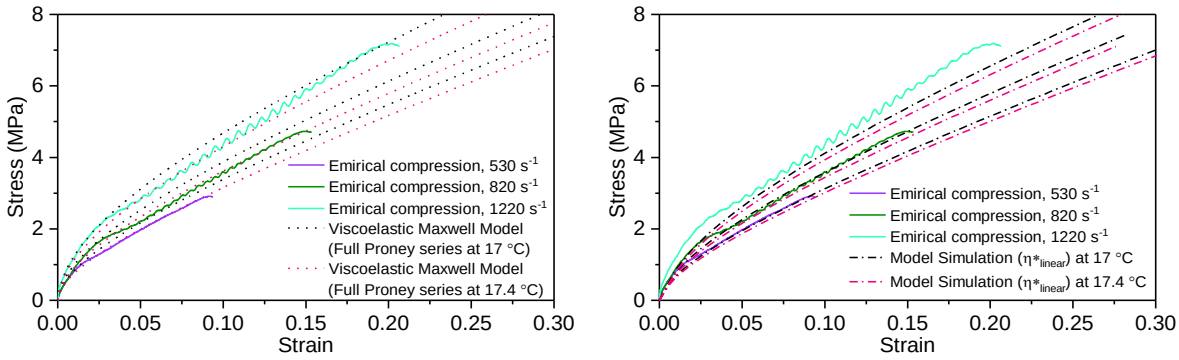


Fig. SI 29: Comparison of model outputs using Prony series calibrated at 17 and 17.4 °C, indicating the effect that adiabatic heating could have on the response.

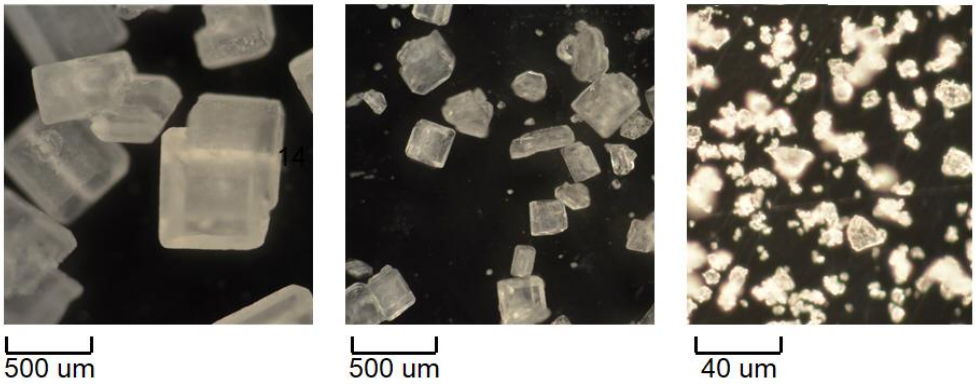


Fig. SI-1: Micrographs of Granulated, Caster and Icing Sugars

Table SI-1: Product standards obtained from Tate & Lyle Sugars, Ltd, UK.

Fairtrade

Product Name	Colour	Description
Granulated Sugar	White	Crystals: 0.53 - 0.67 size
Extra Fine Granulated Sugar	White	Crystals: 0.34 - 0.42 mm size
Caster Sugar	White	Crystals: 0.27 - 0.34 mm size
Icing Sugar	White	Powder: 20 - 25 micron
Demerara Cane Sugar	2200 IU	Crystal: 1.1 mm average size
Light Brown Soft Cane Sugar	5400 IU	Soft syrupy fine grained sugar
Dark Brown Soft Cane Sugar	24000 IU	Soft syrupy fine grained sugar
Golden Cane Invert Syrup 50-83	1700 IU	Invert 50 / Brix 83
White Cane Invert Syrup 76-76	White	Invert 76 / Brix 76.4
Refined Cane Molasses	Black	Invert 26 / Brix 76
Black Cane Treacle Syrup 26-83	Black	Invert 26 / Brix 83
Black Cane Treacle Syrup 34-83	Black	Invert 34 / Brix 83

Organic

Product Name	Colour	Description
Organic Evaporated Cane Juice	500 IU	Free flowing golden crystal: 0.9 mm average size
Organic Demerara	2300 IU	Free flowing brown crystal: 1.3 mm average size

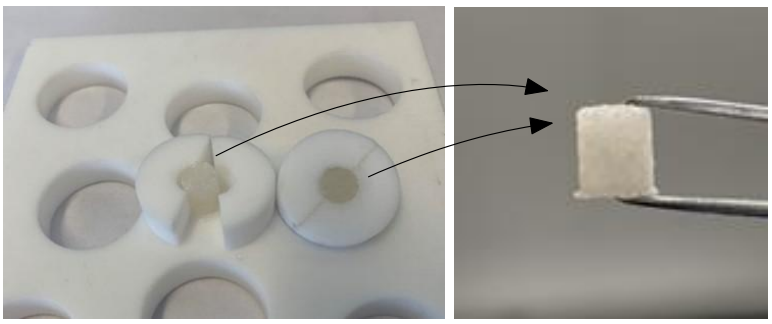


Fig. SI-2: Specimen preparation using a PTFE mould.

Table SI-2: Confirmation of specimen density for an example filled polymer				
Unfilled polymer	Diameter = 6.35 mm Height = 7.45 mm	Volume = 236 mm^{-3}	Mass = 0.2243 g	Density ≈ 0.95 g mm^{-3}
Filled polymer G50: measured	Diameter = 6.35 mm Height = 7.45 mm	Volume = 236 mm^{-3}	Mass = 0.3012 g	Density ≈1.28 g mm^{-3}
Filled polymer G50: expected		Volume polymer = 118 mm^{-3} Volume sugar = 118 mm^{-3}	Density polymer = 0.95 g mm^{-3} Density sugar = 1.6 g mm^{-3}	Expected density ≈ 1.28 g mm^{-3}

Weibull distribution 1: Equations (5-6) to (5-8)

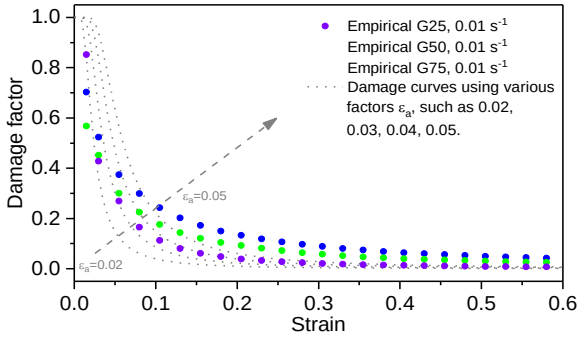


Fig. SI-3: Damage curve using damage equation $\left[1-\exp\left(-\left(\varepsilon_a/\varepsilon\right)^2\right)\right]$ with different value of ε_a compared to damage curves calculated from experimental data. The empirical damage was determined by $E_{secant,test} / E_{Young's\ modulus,test}$. $E_{Young's\ modulus,test}$ is 15, 55 and 145 MPa for G25, G50 and G75 respectively.

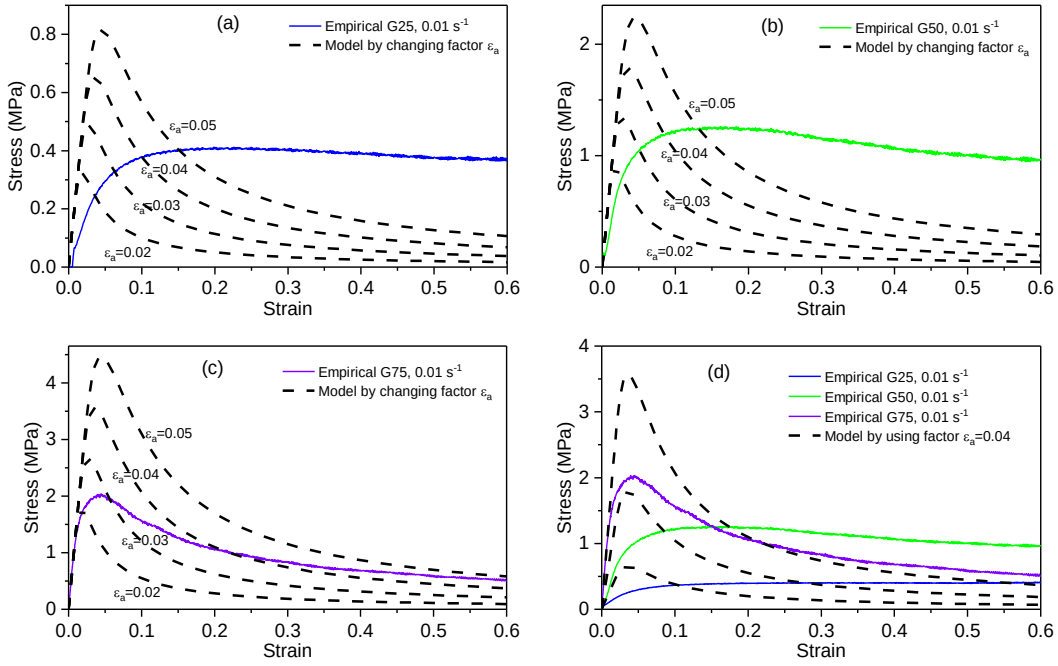


Fig. SI-4: Stress-strain simulation using damage equations (5-6) to (5-8) with different values of ε_a.

Weibull distribution 2: Equations (5-9) and (5-10)

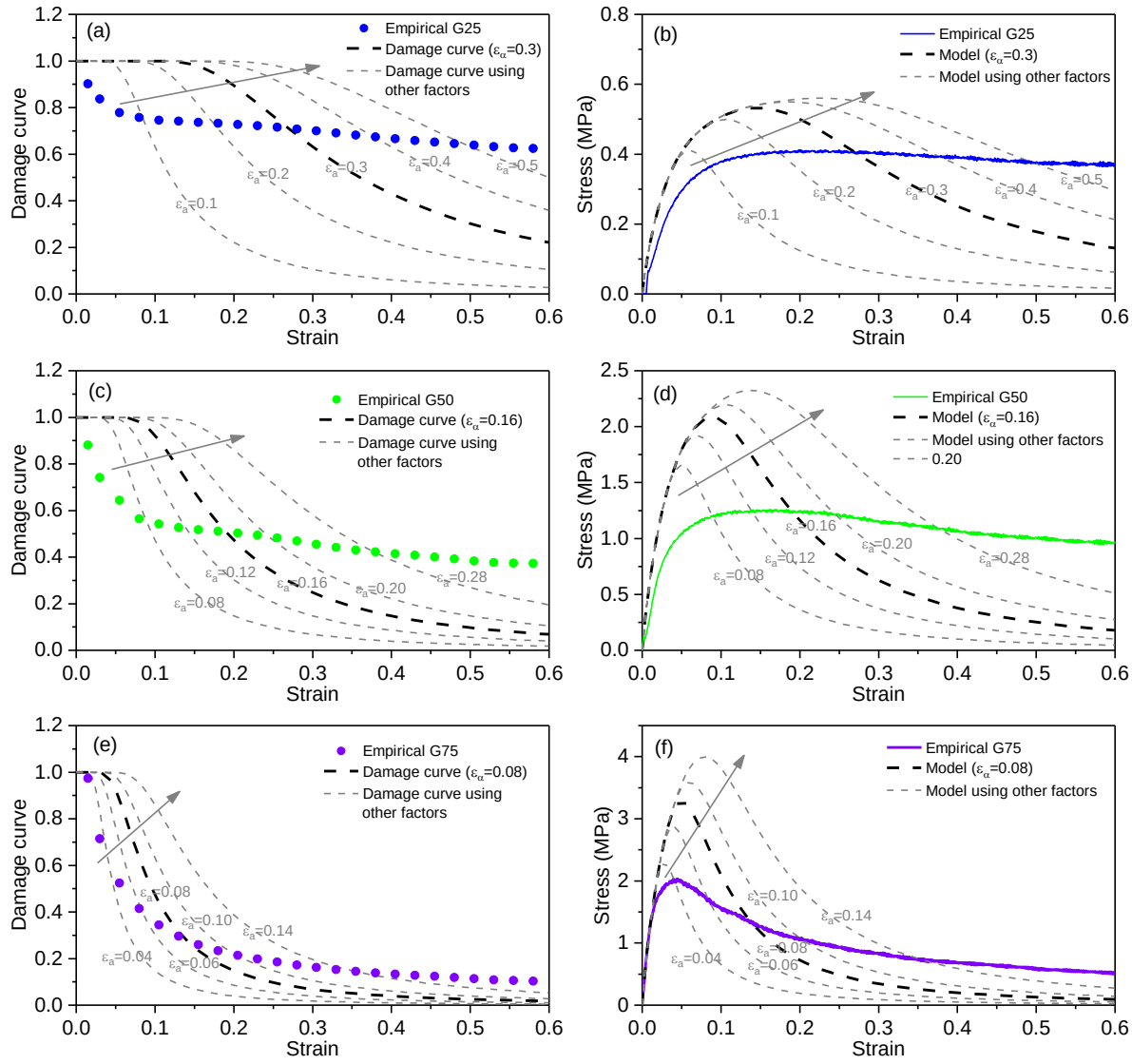


Fig. SI-5: Damage curves and strain-stress behaviour from simulations using equations (5-9) and (5-10) with different values of ε_a. The stress was determined *via* $\sigma = E \cdot \varepsilon$. The empirical damage plot was determined by $E_{secant,test}$ / ($E_m \times R_{Guth}$). E_m is the local secant modulus determined by viscoelastic polymer model (VPM).

Weibull distribution 3: Eq. (5-11):

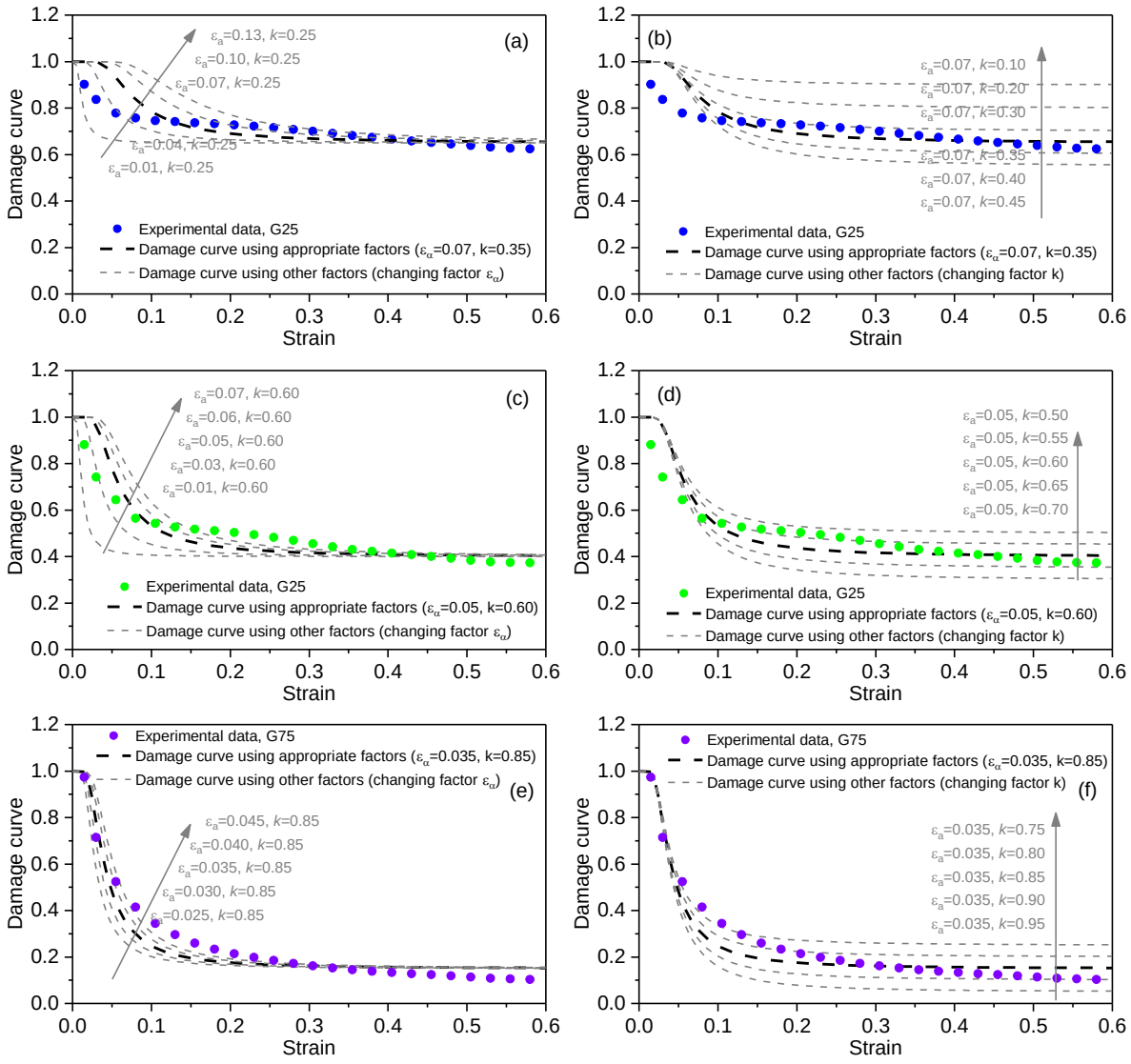


Fig. SI-6: Damage curve using damage equation (5-11) with different values of ε_a and k. The empirical damage was determined by $E_{secant,test}$ / ($E_m \times R_{Guth}$). E_m is the local secant modulus determined by the viscoelastic polymer model (VPM).

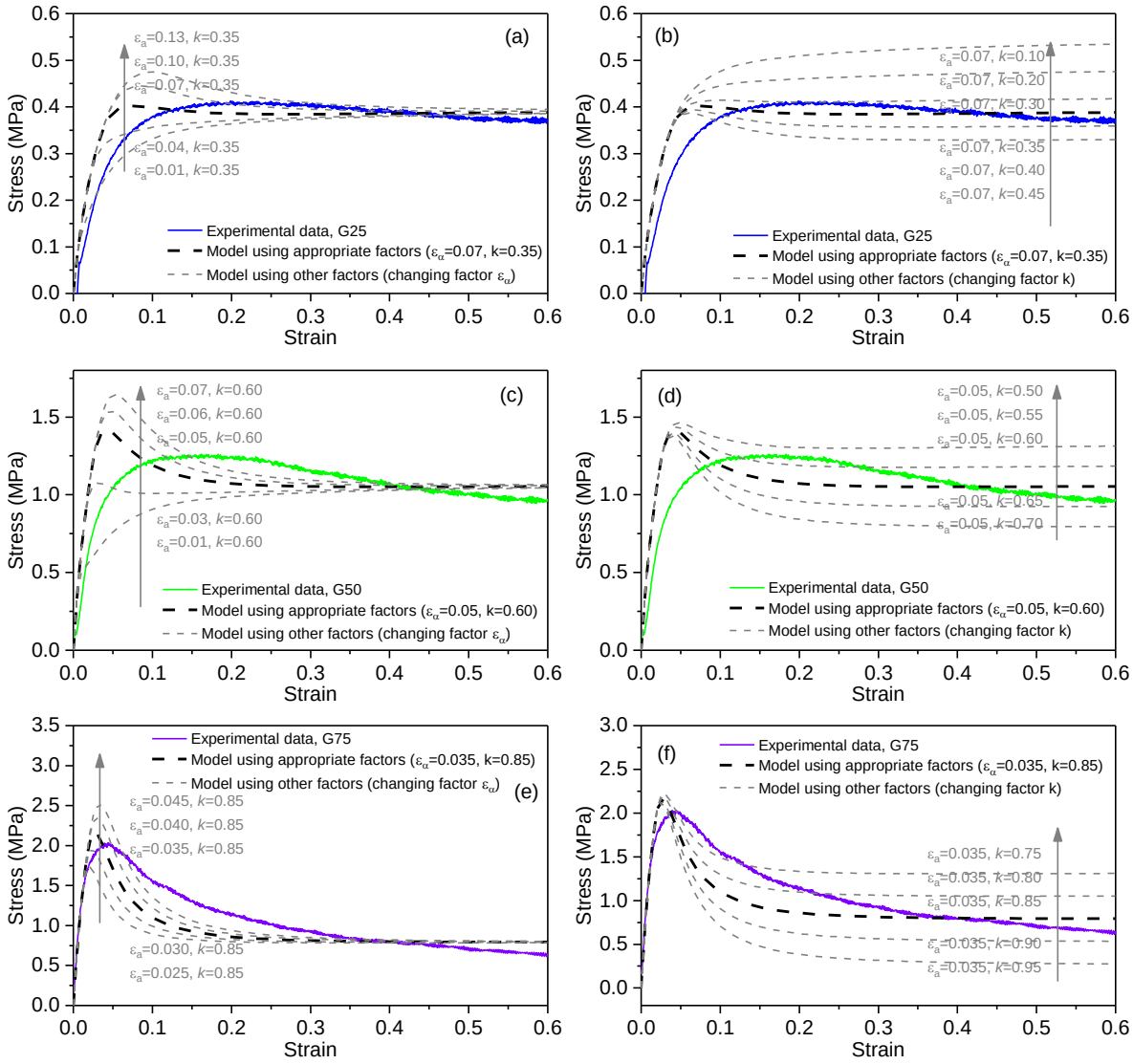


Fig. SI-7: Strain-stress behaviour modelled using damage equation (5-11) with different value of ε_a and k. The ultimate stress was determined *via* $\sigma = E \cdot \varepsilon$.

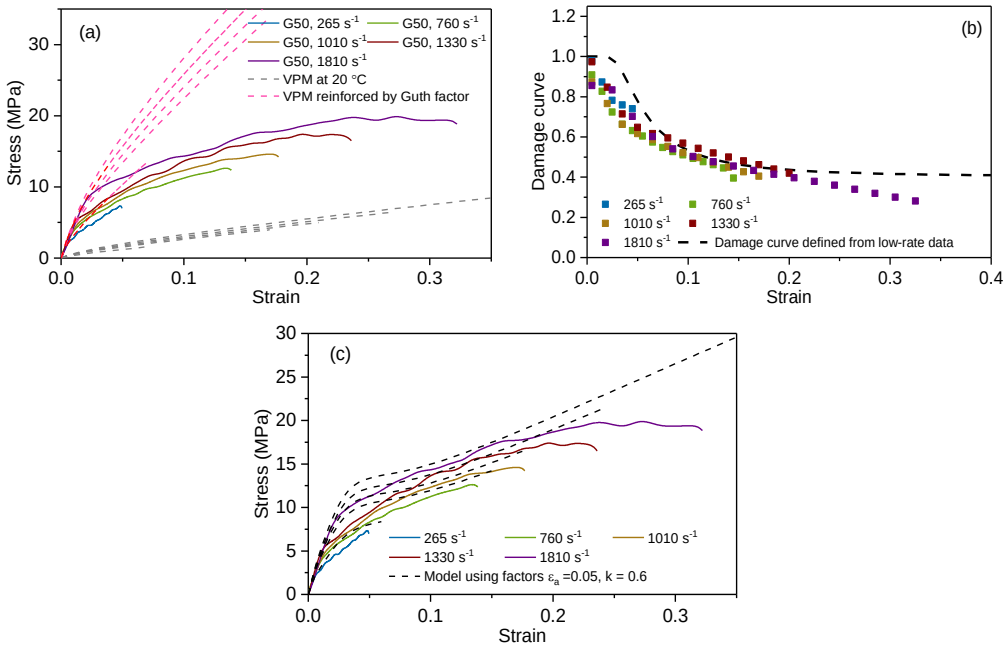


Fig. SI-8: Using the same values of parameters ε_a and k, from Fig. 5-5, to model the strain-stress behaviour of G50 composite in high rate experiments. The same parameters R_{Guth}, ε_a, k were assigned as G50: 8.5, 0.05, 0.6.

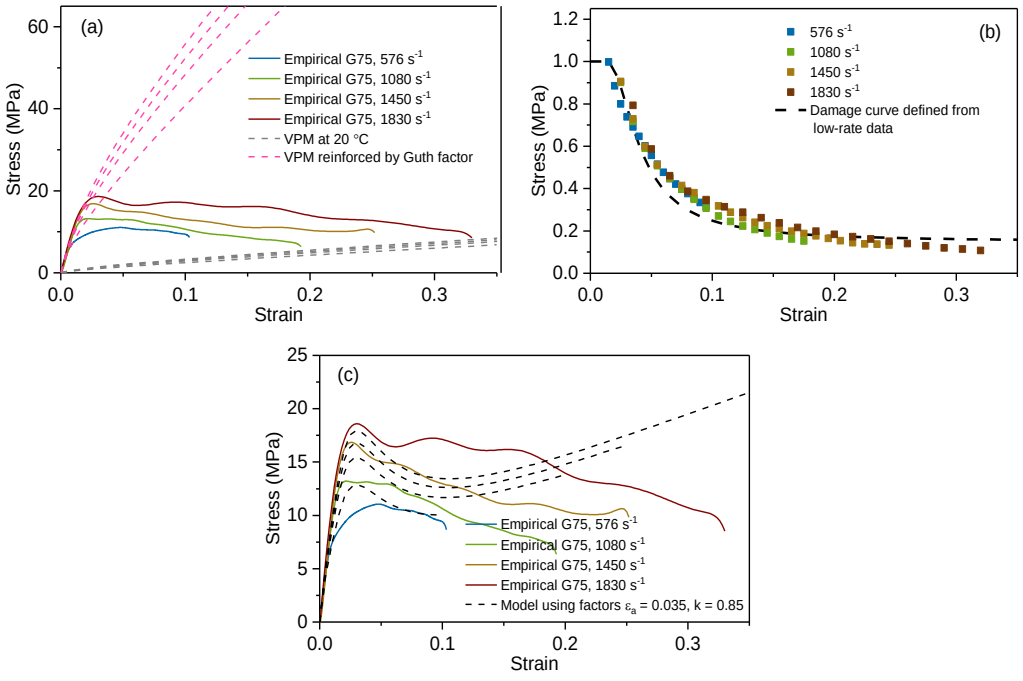


Fig. SI-9: Using the same values of parameters ε_a and k, from Fig. 5-5, to model the strain-stress behaviour of G75 composite in high rate experiments. The same parameters R_{Guth}, ε_a, k were assigned as G75: 16.8, 0.035, 0.85.

Weibull distribution 4: Eq. (5-12):

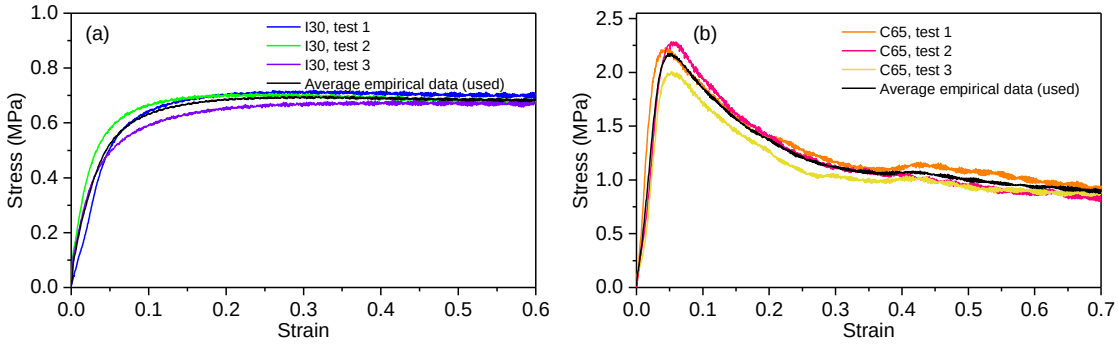


Fig. SI-10: Full experimental data for I30 and C65 in compression at 0.01 s^{-1} and 25 °C.

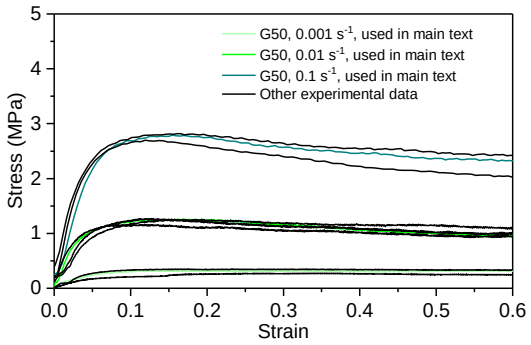


Fig. SI-11: Full experimental data for G50 undergoing compression at strain rates from 10^{-3} to $0.1s^{-1}$.

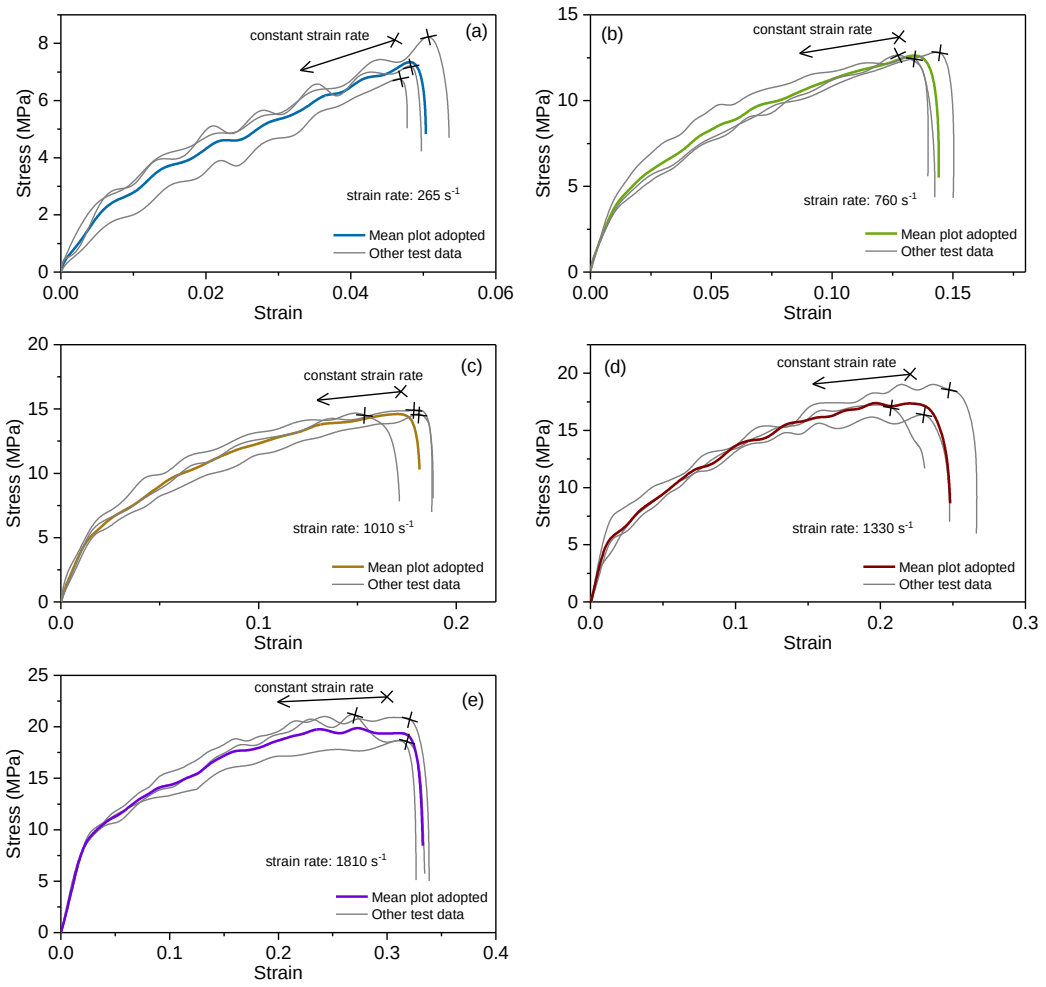


Fig. SI-12: Full experimental data for G50 in high strain rate compression at 20 °C, strain rates up to 1800 s^{-1}.

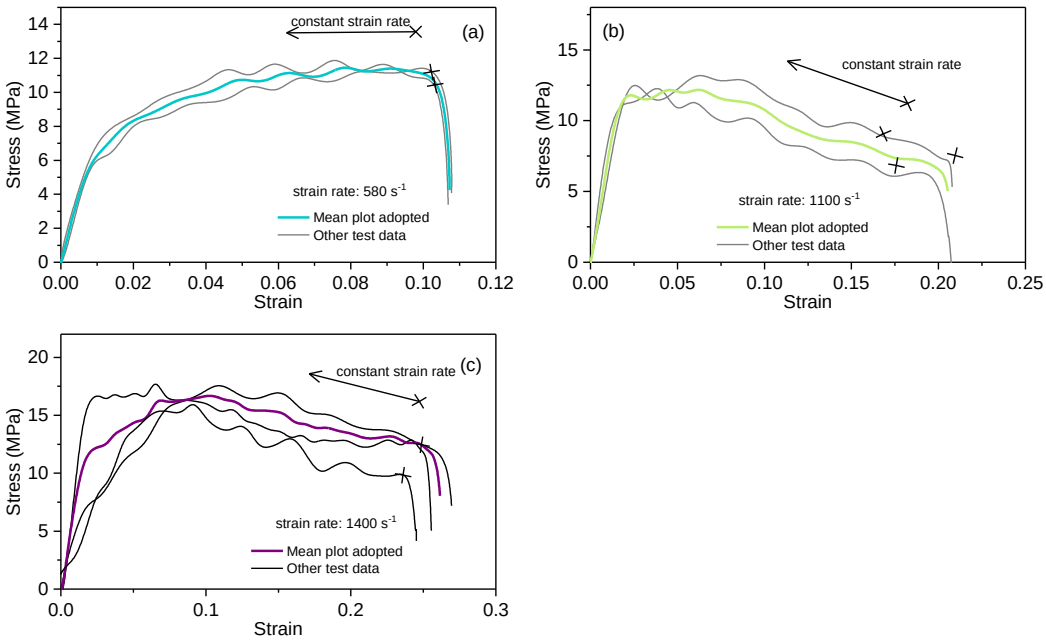


Fig. SI-13: Full experimental data for G70 in high strain rate compression at 20 °C, strain rates up to 1400 s^{-1}.

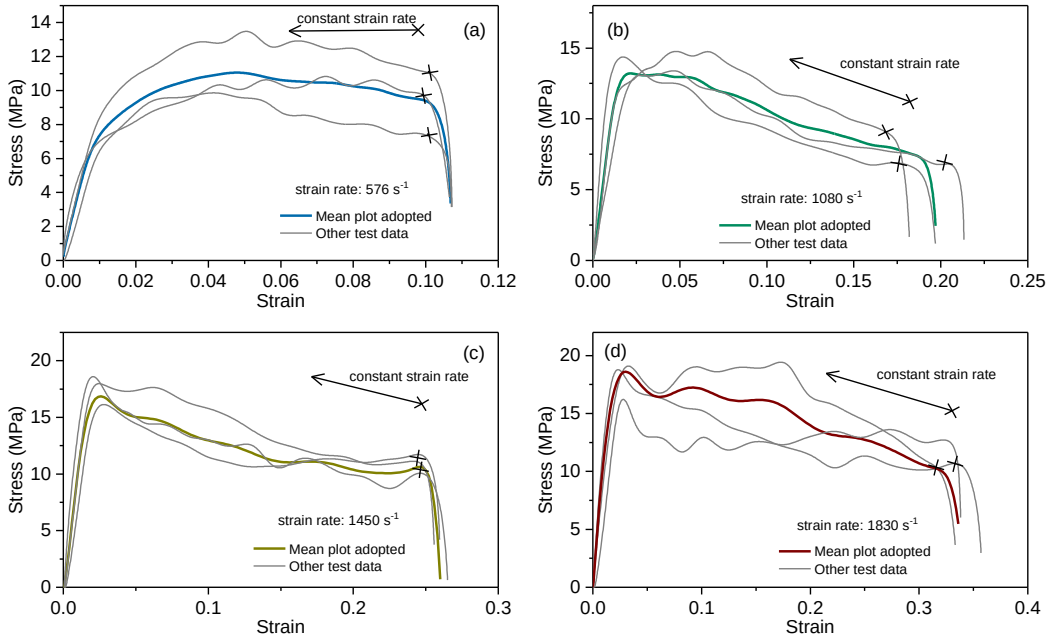


Fig. SI-14: Full experimental data for G75 in high strain rate compression at 20 °C, strain rates up to 1800 s^{-1}.

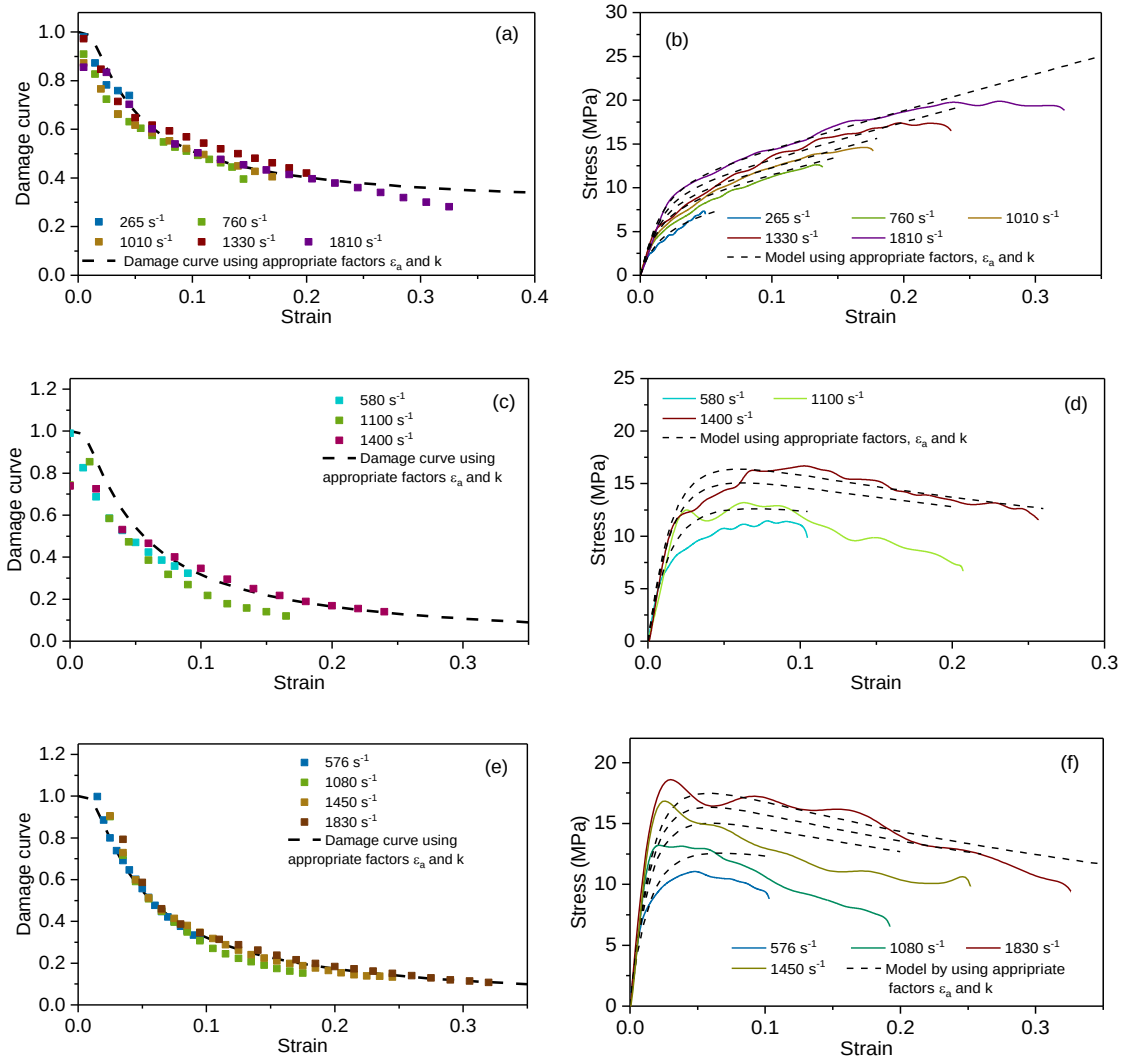


Fig. SI-15: Compression experiments performed on G50, G70 and G75 at high strain rates and the model fit using parameters optimised for these experiments. The VPM and Guth reinforcement factors were the same as used before. However, the damage parameters, ε_a and k, were optimally assigned to fit the high rate data. The parameters R_{Guth}, ε_a, k were assigned as G50: 8.5, 0.04, 0.73; G70: 14.9, 0.041, 1.01; G75: 16.8, 0.042, 1.02.

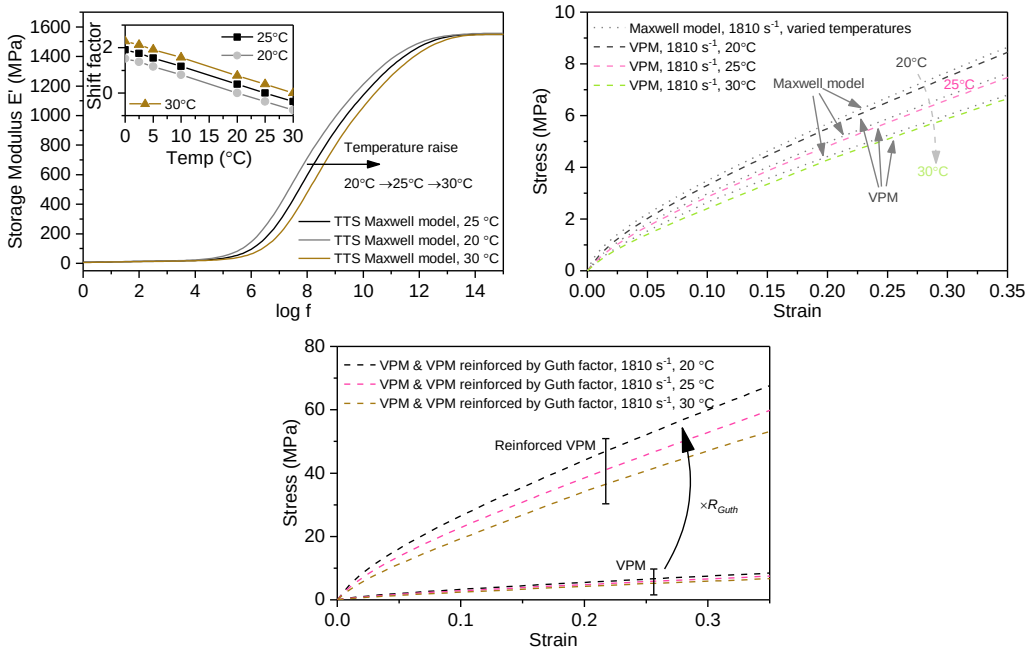


Fig. SI-16: Demonstration of TTS shift to model polymer behaviour at higher temperatures.

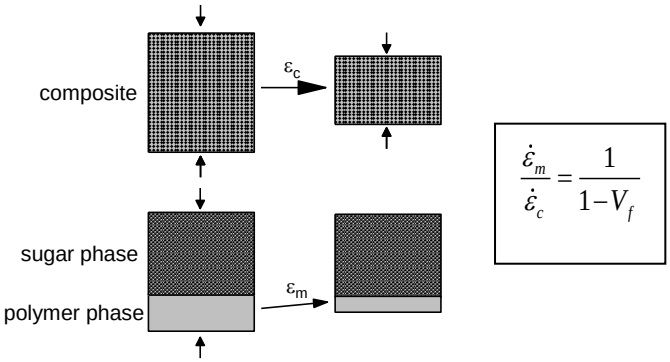


Figure SI-17: The strain and strain rate applied to a composite specimen, if all strain is sustained by the polymer component, the strain rates between $\dot{\varepsilon}_m$ and $\dot{\varepsilon}_c$ have the ratio given by the above equation. This gives the increase of strain rate in the polymer: for G25 this is equal to $1.33\,\dot{\varepsilon}_c$; in G50 $2\,\dot{\varepsilon}_c$; in G70 $3.3\,\dot{\varepsilon}_c$; in G75 $4\,\dot{\varepsilon}_c$.

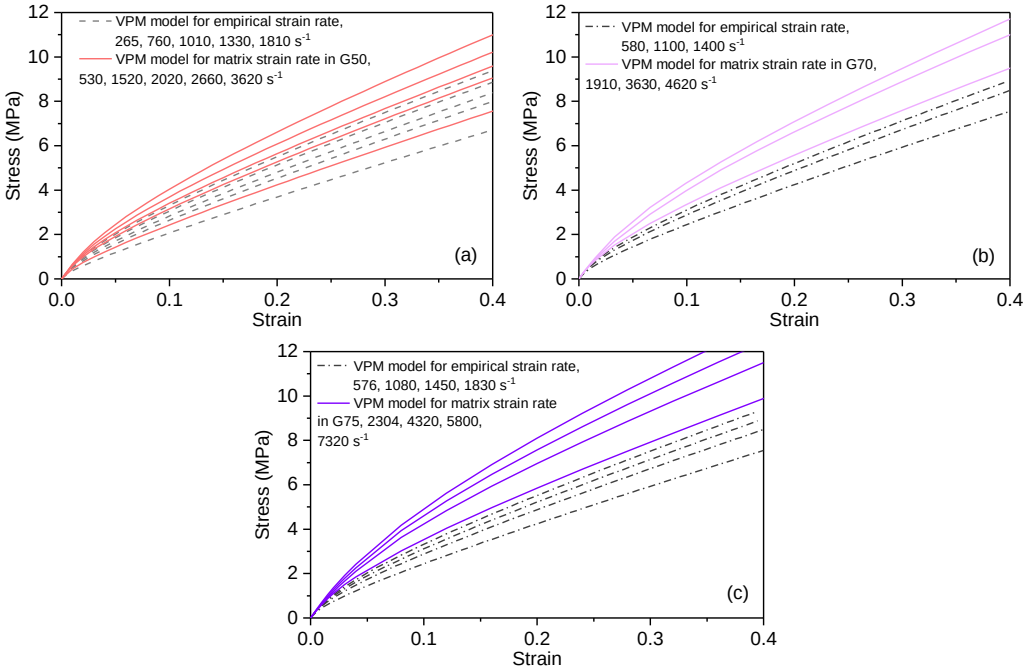


Fig. SI-181: Stress-strain curve produced by the viscoelastic polymer model at the elevated strain rates expected to be seen in the matrix materials for composites G50, G70 and G75 compared to those produced using the strain rate of the overall specimen. The higher stress-strain relationship is used to calculate the instantaneous temperature raise for adiabatic heating.

Table SI-3. Temperature rise for G50 undergoing high-rate deformation

G50	External Applied Strain	$\Delta T \rightarrow T_{Adb}$	Shift factor, log a_T, to move TTS master-curve (log *f* axis) to higher frequencies (from 20°C), for higher temperatures
	From TTS at 20 °C	+0.00 °C → 20.00 °C	log a_T: = 0.00
265 s^{-1}	Strain: 0.05	+0.08 °C → 20.08 °C	log a_T: ≈ 0.01
760 s^{-1}	Strain: 0.1 Strain: 0.15	+0.35 °C → 20.35 °C +0.70 °C → 20.70 °C	log a_T: ≈ 0.03 log a_T: ≈ 0.06
1010 s^{-1}	Strain: 0.1 Strain: 0.2	+0.37 °C → 20.37 °C +1.24 °C → 21.24 °C	log a_T: ≈ 0.03 log a_T: ≈ 0.10
1330 s^{-1}	Strain: 0.1 Strain: 0.2 Strain: 0.25	+0.42 °C → 20.42 °C +1.33 °C → 21.33 °C +1.97 °C → 21.97 °C	log a_T: ≈ 0.04 log a_T: ≈ 0.11 log a_T: ≈ 0.14
1810 s^{-1}	Strain: 0.1 Strain: 0.2 Strain: 0.3 Strain: 0.35	+0.44 °C → 20.44 °C +1.45 °C → 21.45 °C +2.92 °C → 22.92 °C +3.83 °C → 23.83 °C	log a_T: ≈ 0.04 log a_T: ≈ 0.12 log a_T: ≈ 0.24 log a_T: ≈ 0.30
	From TTS at 20 °C	20.00 °C → 25.00 °C	log a_T: ≈ 0.38

Table SI-4 Temperature rise for G70 undergoing high rate experiments

G70	External Applied Strain	$\Delta T \rightarrow T_{Adb}$	Shift factor, log a_T, to move TTS master-curve (log *f* axis) to higher frequencies (from 20°C), for higher temperatures
	From TTS at 20 °C	+0.00 °C → 20.00 °C	log a_T: = 0.00
580 s^{-1}	Strain: 0.1	+0.86 °C → 20.86 °C	log a_T: ≈ 0.08
1100 s^{-1}	Strain: 0.1	+1.03 °C → 21.03 °C	log a_T: ≈ 0.09
	Strain: 0.2	+3.45 °C → 23.45 °C	log a_T: ≈ 0.28
1400 s^{-1}	Strain: 0.1	+1.10 °C → 21.10 °C	log a_T: ≈ 0.10
	Strain: 0.2	+3.67 °C → 23.67 °C	log a_T: ≈ 0.29
	Strain: 0.25	+5.42 °C → 25.42 °C	log a_T: ≈ 0.39
	From TTS at 20 °C	20.00 °C → 25.00 °C	log a_T: ≈ 0.38

Table SI-5 Temperature rise for G75 undergoing high rate experiments

G75	External Applied Strain	$\Delta T \rightarrow T_{Adb}$	Shift factor, log a_T, to move TTS master-curve (log *f* axis) to higher frequencies (fro 20°C), for higher temperatures
	From TTS at 20 °C	+0.00 °C → 20.00 °C	log a_T: = 0.00
576 s^{-1}	Strain: 0.1	+1.28 °C → 21.28 °C	log a_T: ≈ 0.11
1080 s^{-1}	Strain: 0.1	+1.51 °C → 21.51 °C	log a_T: ≈ 0.13
	Strain: 0.2	+5.05 °C → 25.05 °C	log a_T: ≈ 0.38
1450 s^{-1}	Strain: 0.1	+1.64 °C → 21.64 °C	log a_T: ≈ 0.13
	Strain: 0.2	+5.44 °C → 25.44 °C	log a_T: ≈ 0.39
	Strain: 0.25	+8.03 °C → 28.03 °C	log a_T: ≈ 0.61
1830 s^{-1}	Strain: 0.1	+1.74 °C → 21.74 °C	log a_T: ≈ 0.14
	Strain: 0.2	+5.78 °C → 25.78 °C	log a_T: ≈ 0.40
	Strain: 0.3	+11.66 °C → 31.66 °C	log a_T: ≈ 0.83
	From TTS at 20 °C	20.00 °C → 25.00 °C	log a_T: ≈ 0.38
	From TTS at 20 °C	20.00 °C → 30.00 °C	log a_T: ≈ 0.76

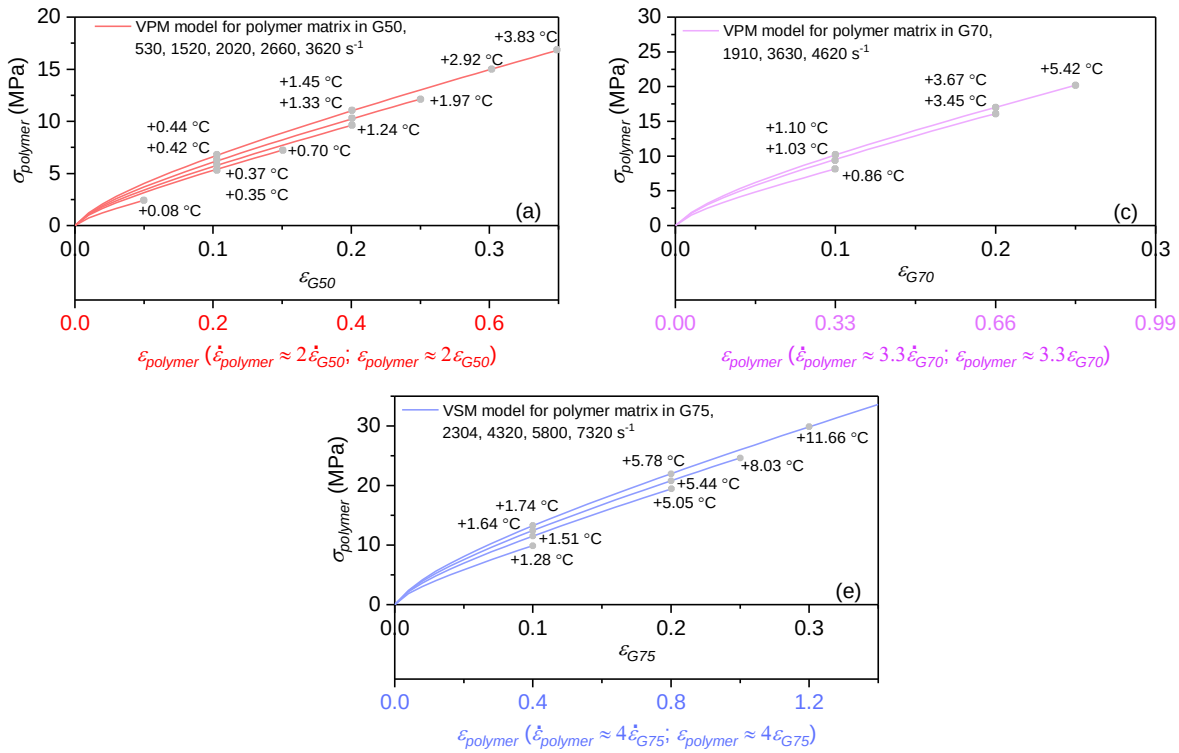
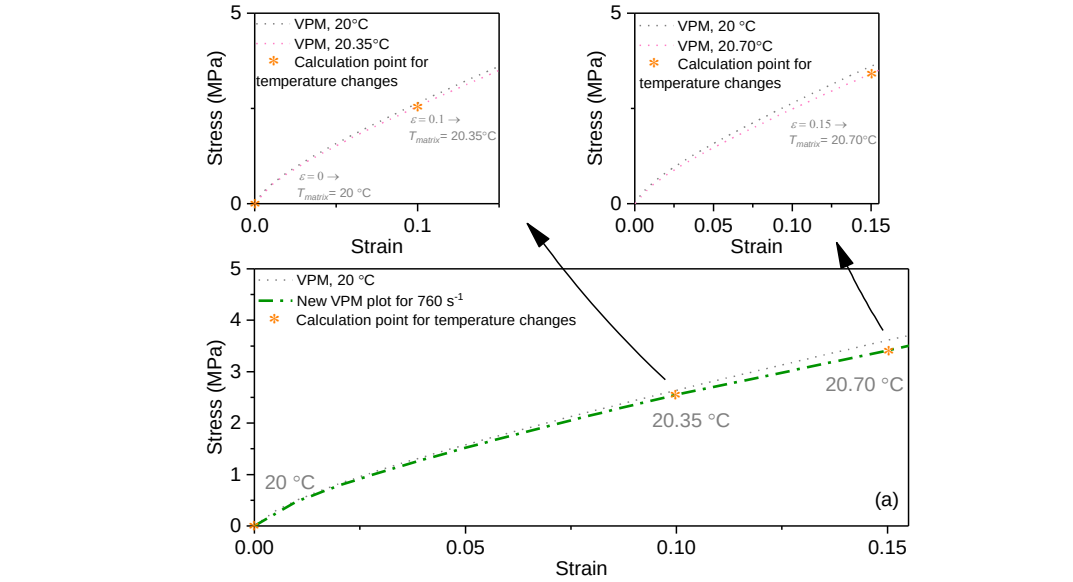
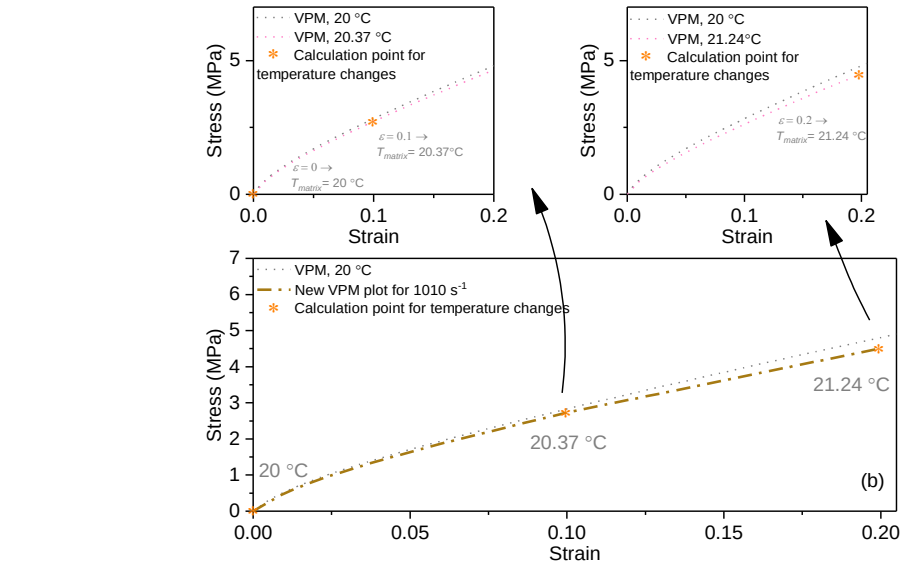
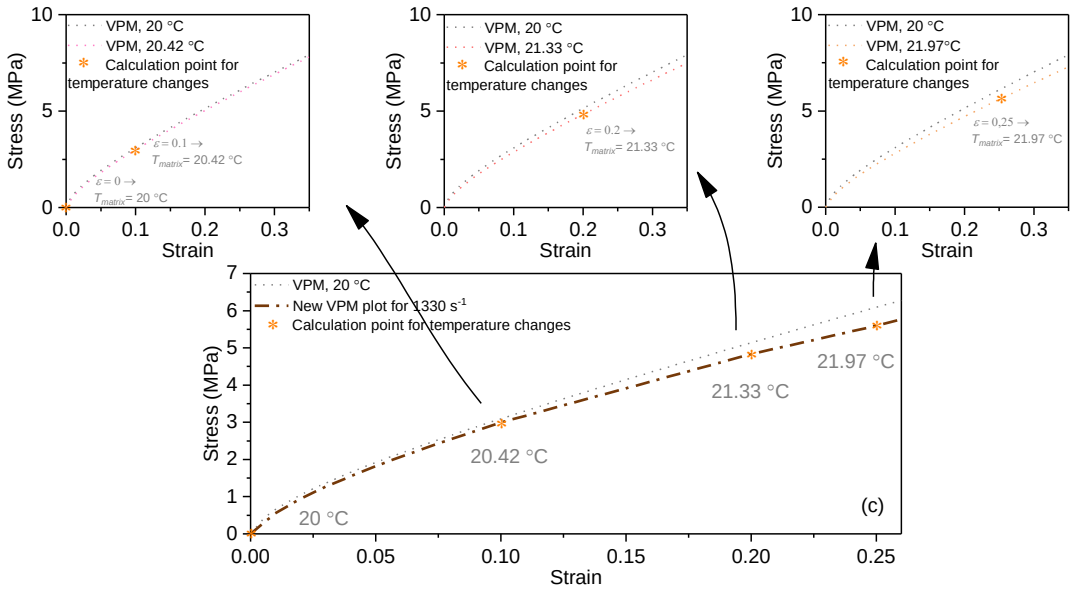


Fig. SI-19: The estimated amount of temperature rise at different strains due to adiabatic heating effects in G50, G70 and G75.


VPM, 20°C
VPM, 20.35°C
Calculation point for temperature changes
ε = 0.1 →
T_matrix = 20.35°C
ε = 0 →
T_matrix = 20 °C
Stress (MPa)
Strain
VPM, 20 °C
VPM, 20.70°C
Calculation point for temperature changes
ε = 0.15 →
T_matrix = 20.70°C
VPM, 20 °C
New VPM plot for 760 s-1
Calculation point for temperature changes
20.70 °C
20.35 °C
20 °C
(a)


VPM, 20 °C
VPM, 20.37 °C
Calculation point for temperature changes
ε = 0.1 →
T_matrix = 20.37°C
ε = 0 →
T_matrix = 20 °C
Stress (MPa)
Strain
VPM, 20 °C
VPM, 21.24°C
Calculation point for temperature changes
ε = 0.2 →
T_matrix = 21.24 °C
VPM, 20 °C
New VPM plot for 1010 s-1
Calculation point for temperature changes
21.24 °C
20.37 °C
20 °C
(b)


VPM, 20 °C
VPM, 20.42 °C
Calculation point for temperature changes
ε = 0.1 →
T_matrix = 20.42 °C
ε = 0 →
T_matrix = 20 °C
Stress (MPa)
Strain
VPM, 20 °C
VPM, 21.33 °C
Calculation point for temperature changes
ε = 0.2 →
T_matrix = 21.33 °C
VPM, 20 °C
VPM, 21.97°C
Calculation point for temperature changes
ε = 0,25 →
T_matrix = 21.97 °C
VPM, 20 °C
New VPM plot for 1330 s-1
Calculation point for temperature changes
21.97 °C
21.33 °C
20.42 °C
20 °C
(c)

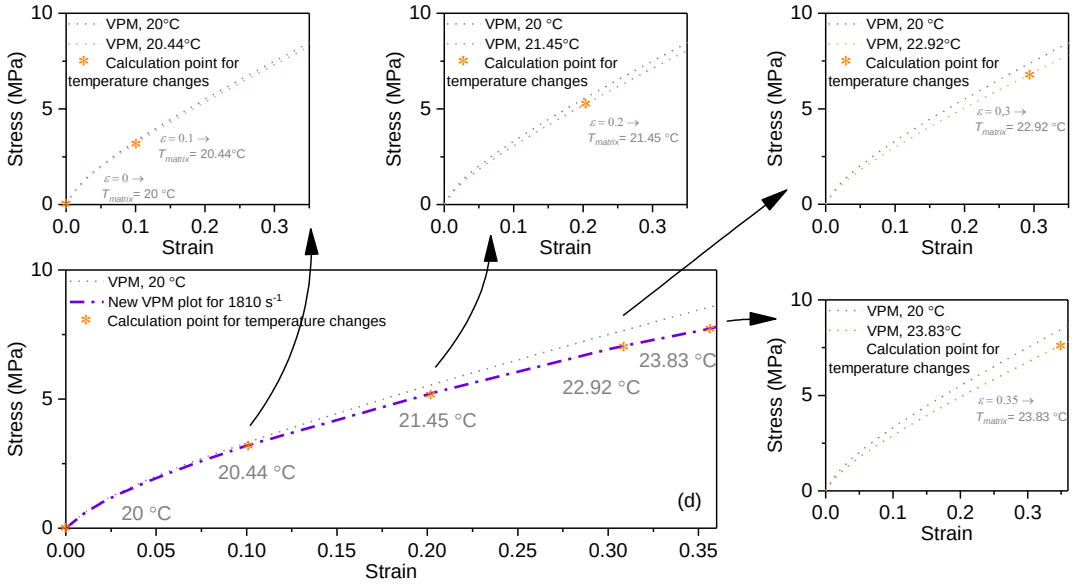
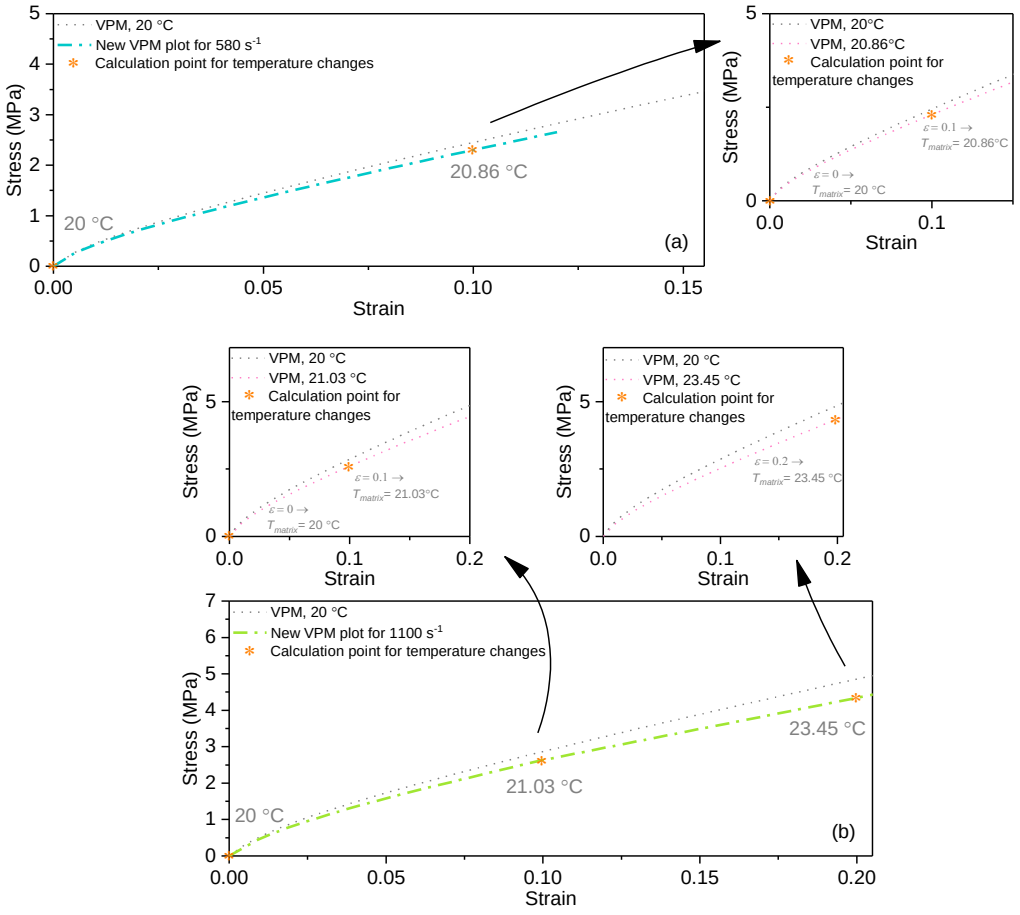


Figure SI-20: Using the temperature rises calculated at intervals of 0.1 strain, new stress-strain curves were produced from the viscoelastic softening model at each derived temperature. These were then combined to estimate a continuous representation of heating-induced softening behaviour in the SPU polymer matrix during the deformation. Here shown for a G50 specimen.



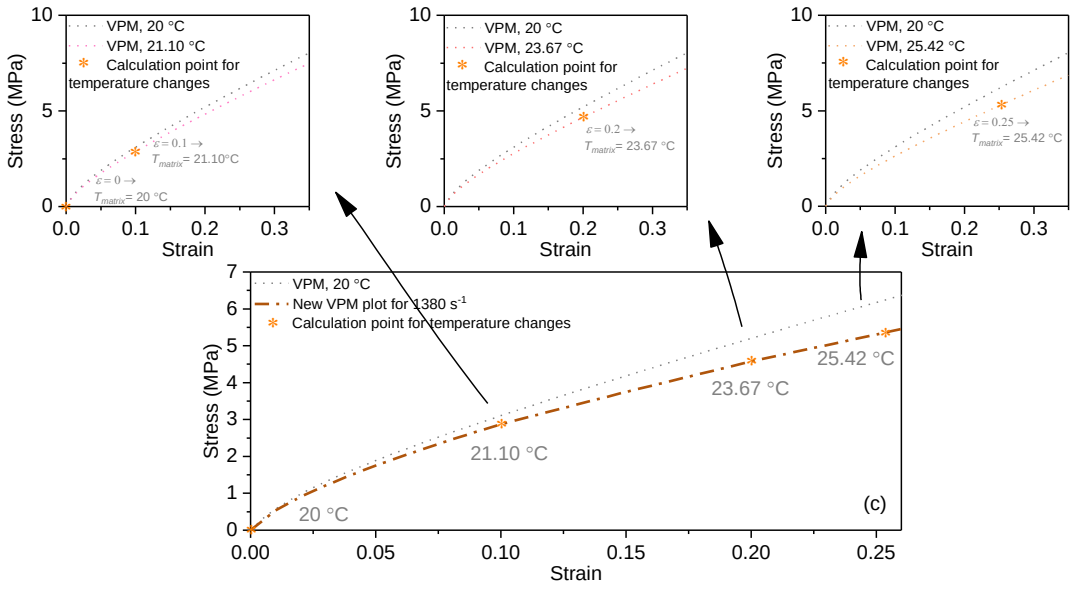
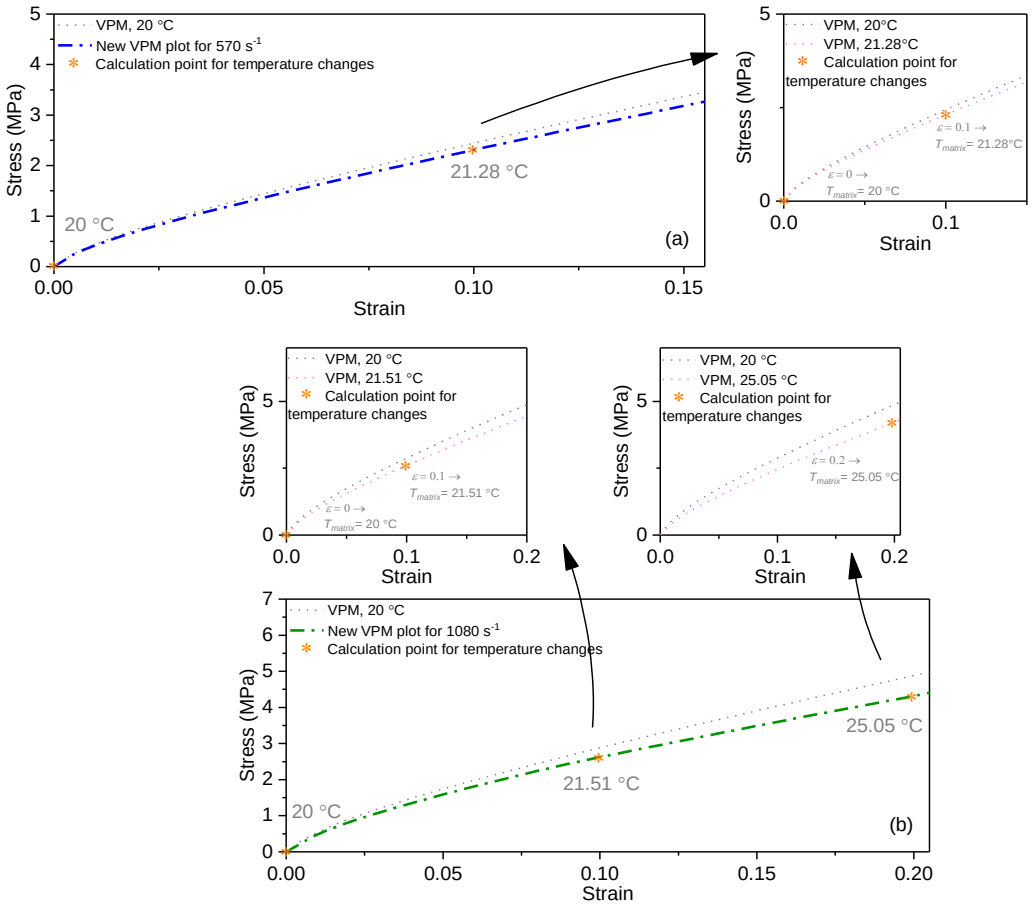


Figure SI-21: Constructed stress-strain curves for polymer matrix undergoing adiabatic heating in a G70 specimen.



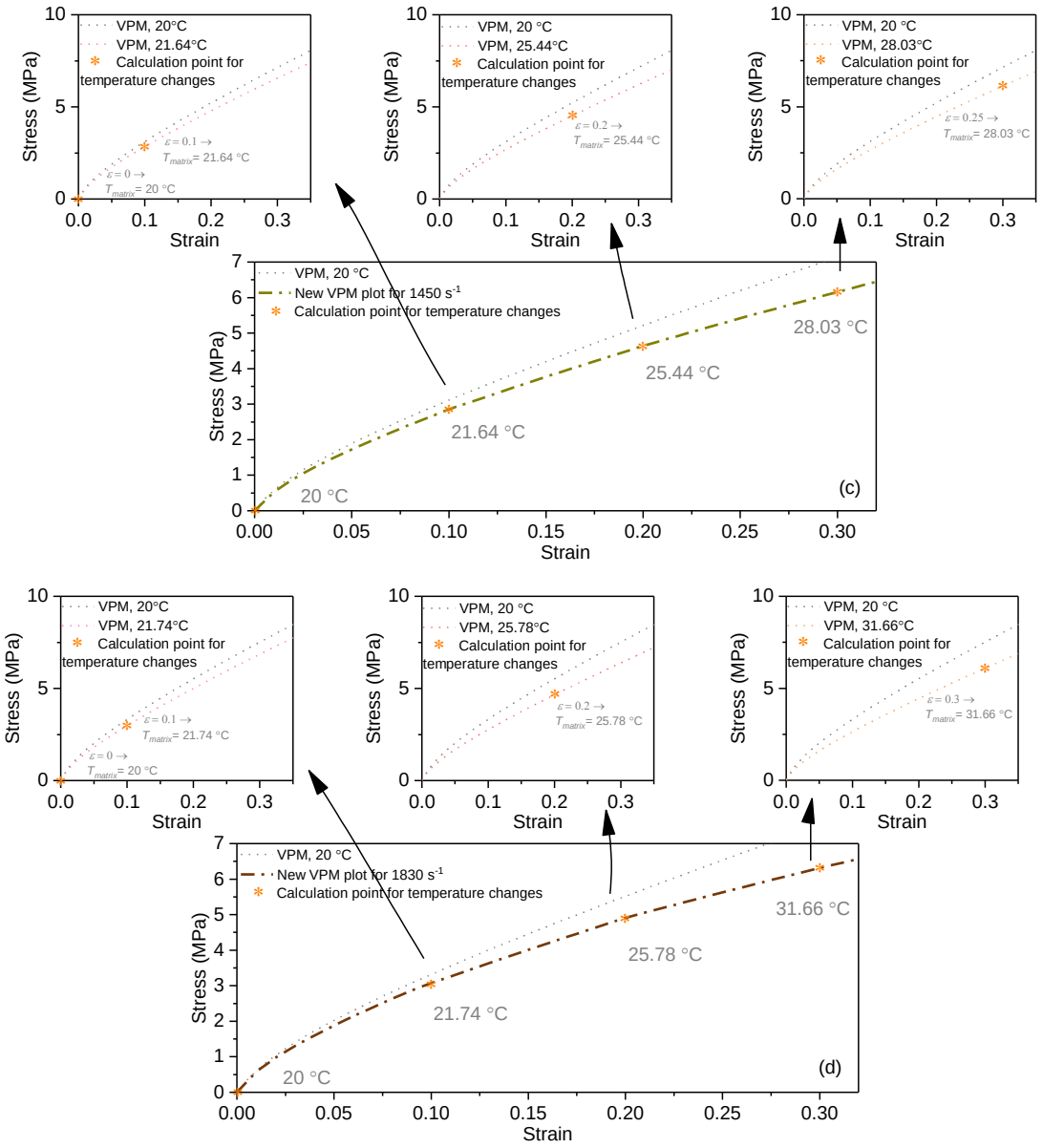


Figure SI-22: Constructed stress-strain curves for polymer matrix undergoing adiabatic heating in a G75 specimen.

Modelling using 'accelerated strain rate' in viscoelastic model

In this section, we adopted increased strain rate of polymer matrix as the foundation to re-construct the modelling procedure using the same reinforcement and damage equations as before. In composites G25, G50 and G75, the ratio of the strain rate in the polymer to the strain rate in the overall composite has been calculated as 1.33 in G25; 2 in G50; and 4 in G75. The strain in the polymer at any time increases by the same ratio.

In order to perform the re-calculation, firstly, the strain-stress behaviour of the polymer at the increased strain rates was determined from the VPM, then all plots were re-plotted with the strain axis scaled to the new strain rate in the composite, as shown in Fig. SI-23. Secondly, the 'new' VPM plots from Fig. SI-23(b) were used to re-calculate 'new' reinforced VPM curves, which were found to allow the damage factors derived above to reproduce the strain-stress behaviour at low rates. However, this process, which is shown in Figs SI-24 and SI-25 did not work at high strain rates. Further re-calculation of the strain-stress behaviour of G50 and G75 at high rates is shown in Figs SI-26 and SI-27.

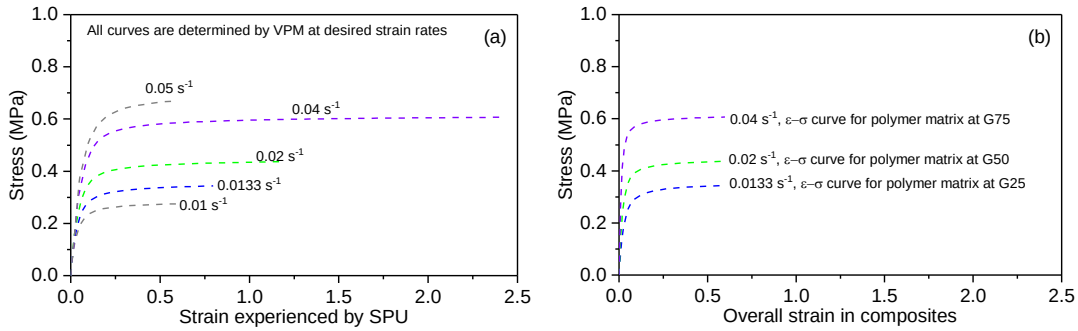


Figure SI-23: (a) The strain-stress behaviour for VPM operating at different strain rates. The strain-stress behaviour was when rescaled to the composite's applied strain value, shown for a strain rate of 0.01 s^{-1}in (b). The latter is used to calculate the reinforced VPM in the following steps.

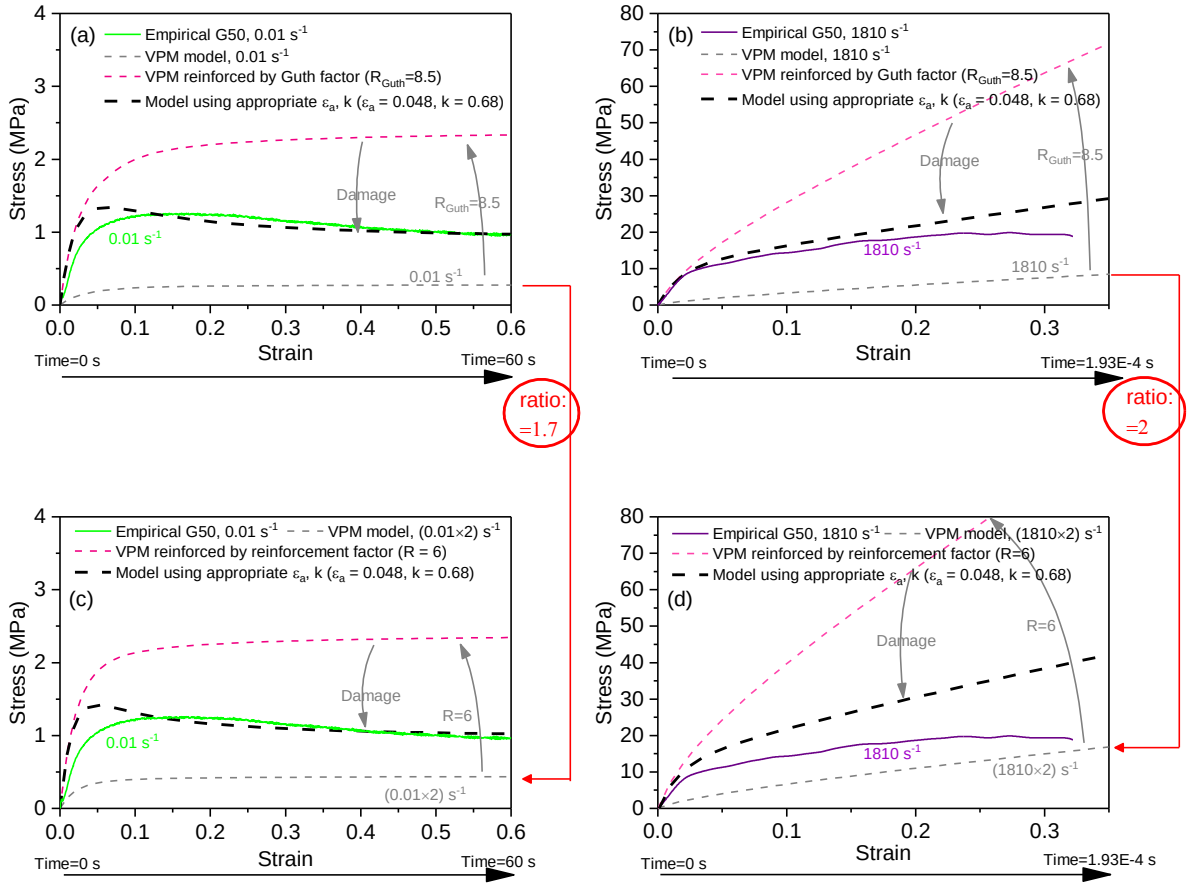


Figure SI-24: (a) and (b) The modelling process to reproduce the strain-stress behaviour for G50 composite at 0.01 and 1810 s^{-1} assuming the rate in the polymer is the same as in the composite. This model uses the same parameters as derived earlier in the paper. In (c) the strain rate in the VPM is doubled, and a new reinforcement factor, *R*, is derived which matches the reinforced stress-strain curve to the experimental data; this allows the same damage factors to be used to reproduce the strain-stress curve at low rate. However, at high rates, (d), this combination of model parameters and the increased strain rate in the polymer leads to too *high* a stress.

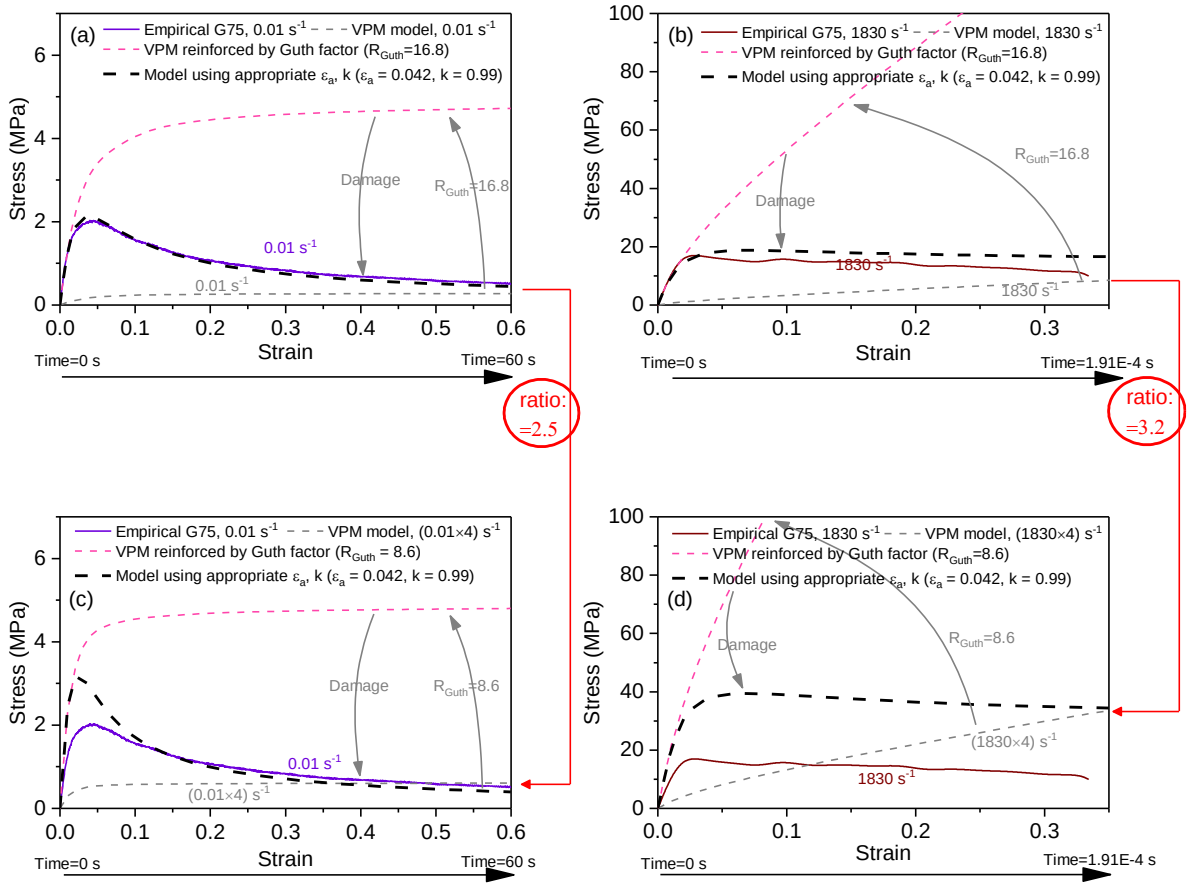


Figure SI-25: (a) and (b) The modelling process to reproduce the strain-stress behaviour for G75 composite at 0.01 and 1830 s^{-1} assuming the rate in the polymer is the same as in the composite. This model uses the same parameters as derived earlier in the paper. In (c) the strain rate in the VPM is doubled, and a new reinforcement factor, *R*, is derived which matches the reinforced stress-strain curve to the experimental data; this allows the same damage factors to be used to reproduce the strain-stress curve at low rate. However, at high rates, (d), this combination of model parameters and the increased strain rate in the polymer leads to too *high* a stress.

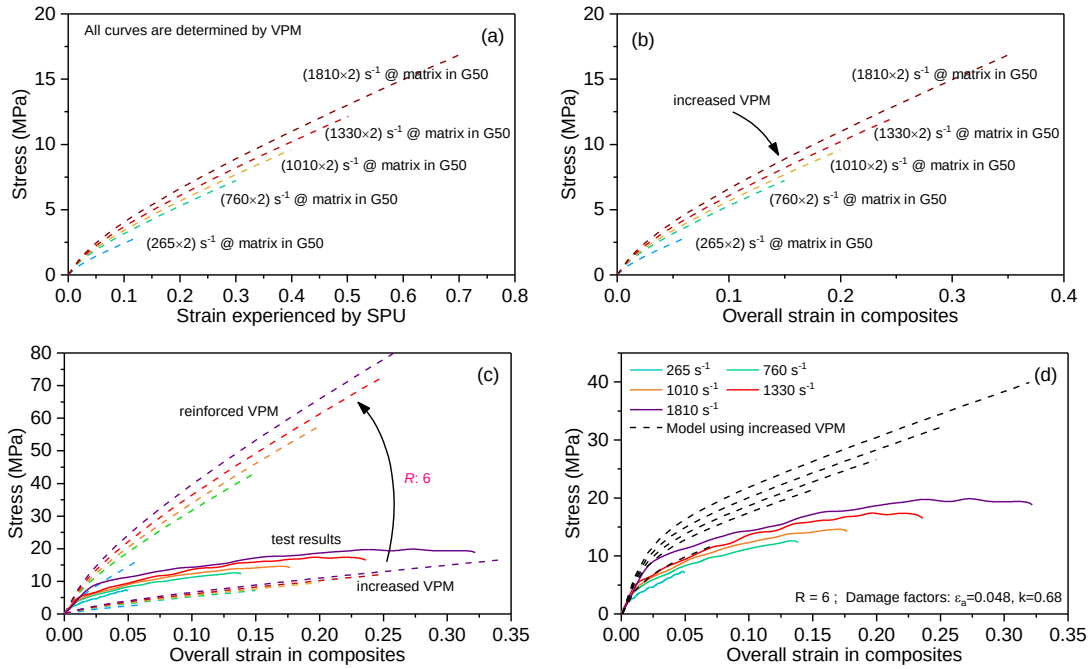


Fig. SI-26: (a) The strain-stress behaviour for VPM operating at different strain rates. These plots were converted to plots with composite's strain on the x-axis (b). The 'new' plots of increased VPM plots were reinforced by using same reinforcement factor from Fig. 5-24 (c). Using the same damage factors and determined reinforcement factor gives strain-stress behaviour for G50 specimen at high rates shown in (d).

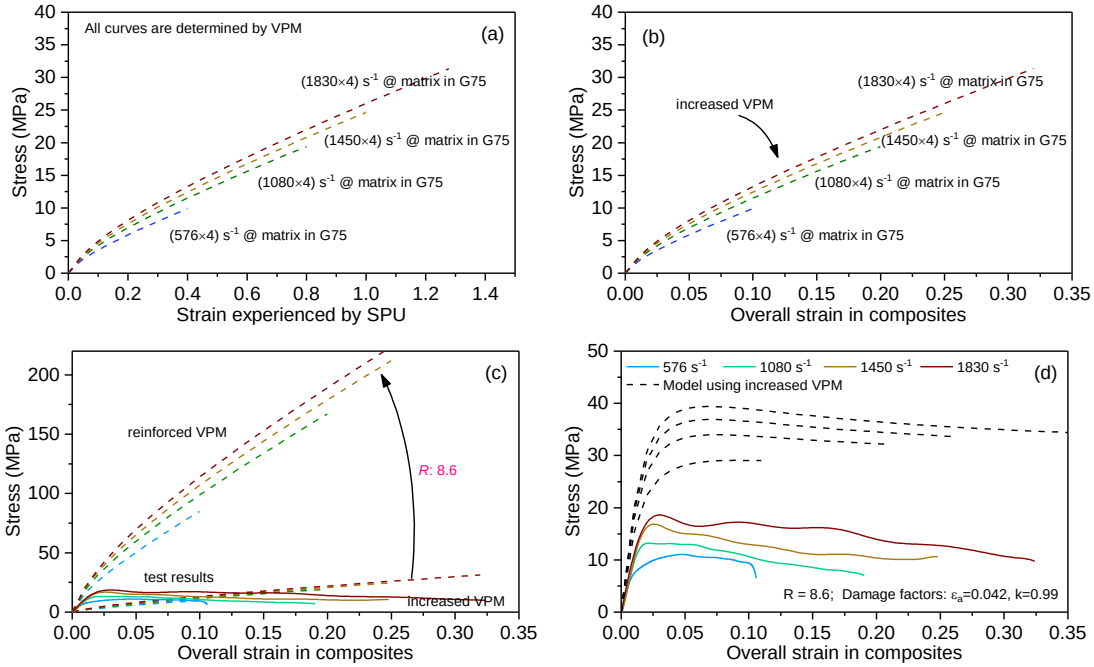


Fig. SI-27: (a) The strain-stress behaviour for VPM operating at different strain rates. These plots were converted to plots with composite's strain on the x-axis (b). The 'new' plots of increased VPM plots were reinforced by using same reinforcement factor from Fig. 5-25 (c). Using the same damage factors and determined reinforcement factor can reproduce the strain-stress behaviour for G75 specimen at high rates shown in (d).

It was observed that the model using the increased VPM is much over-estimating the stress value at high rates. In G50, the ratio index increased from 1.7 to 2 when the strain rate was doubled to (1810×2) s^{-1}; In G75, the ratio index increased from 2.5 to 3.2 when the strain rates was quadrupled to (1830×4) s^{-1}. This discrepancy resulted in the over-estimated calculations especially in composites with high filler loadings.

Strain and strength recovery data

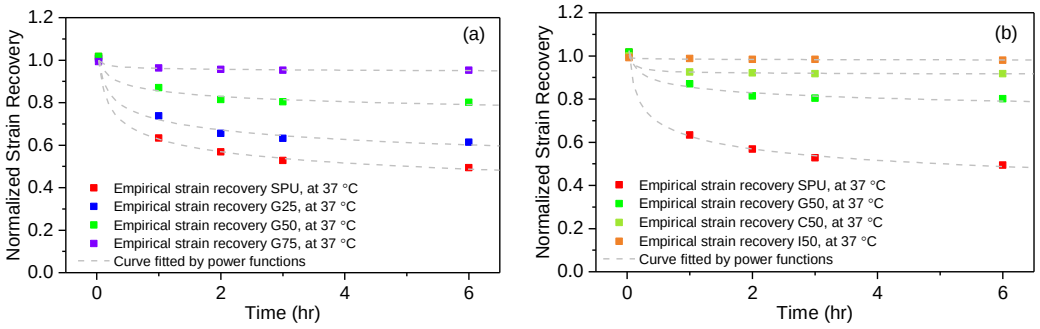
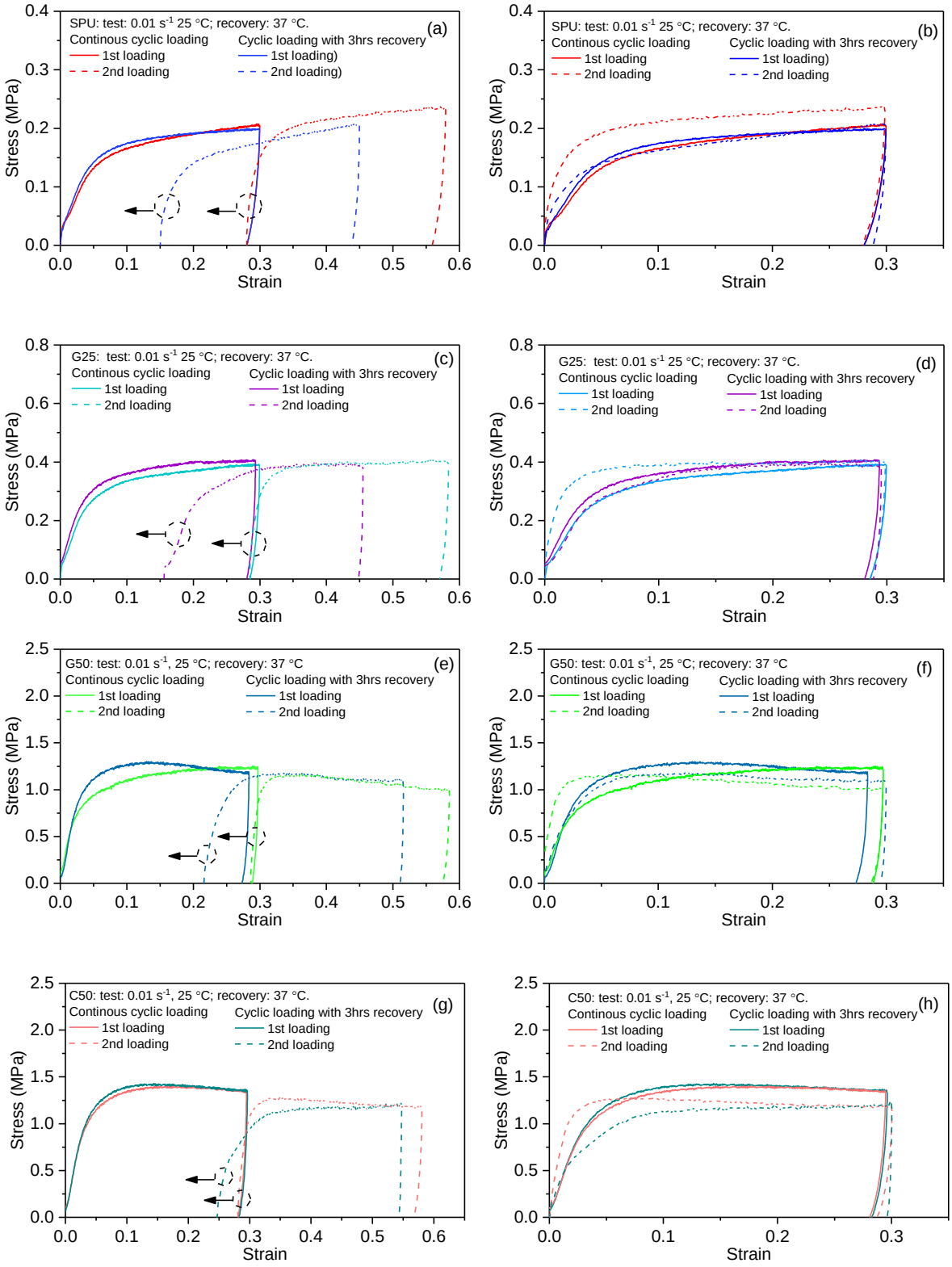


Fig. SI-28: Measured strain recovery for specimens with (a) different volume fraction and (b) different sugar particle sizes.


SPU: test: 0.01 s-1 25 °C; recovery: 37 °C.
(a)
Continous cyclic loading
1st loading
2nd loading
Cyclic loading with 3hrs recovery
1st loading)
2nd loading)
Stress (MPa)
Strain
SPU: test: 0.01 s-1 25 °C; recovery: 37 °C.
(b)
Continous cyclic loading
1st loading
2nd loading
Cyclic loading with 3hrs recovery
1st loading)
2nd loading
Stress (MPa)
Strain
G25: test: 0.01 s-1 25 °C; recovery: 37 °C.
(c)
Continous cyclic loading
1st loading
2nd loading
Cyclic loading with 3hrs recovery
1st loading
2nd loading
Stress (MPa)
Strain
G25: test: 0.01 s-1 25 °C; recovery: 37 °C.
(d)
Continous cyclic loading
1st loading
2nd loading
Cyclic loading with 3hrs recovery
1st loading
2nd loading
Stress (MPa)
Strain
G50: test: 0.01 s-1, 25 °C; recovery: 37 °C
(e)
Continous cyclic loading
1st loading
2nd loading
Cyclic loading with 3hrs recovery
1st loading
2nd loading
Stress (MPa)
Strain
G50: test: 0.01 s-1, 25 °C; recovery: 37 °C
(f)
Continous cyclic loading
1st loading
2nd loading
Cyclic loading with 3hrs recovery
1st loading
2nd loading
Stress (MPa)
Strain
C50: test: 0.01 s-1, 25 °C; recovery: 37 °C.
(g)
Continous cyclic loading
1st loading
2nd loading
Cyclic loading with 3hrs recovery
1st loading
2nd loading
Stress (MPa)
Strain
C50: test: 0.01 s-1, 25 °C; recovery: 37 °C.
(h)
Continous cyclic loading
1st loading
2nd loading
Cyclic loading with 3hrs recovery
1st loading
2nd loading
Stress (MPa)
Strain

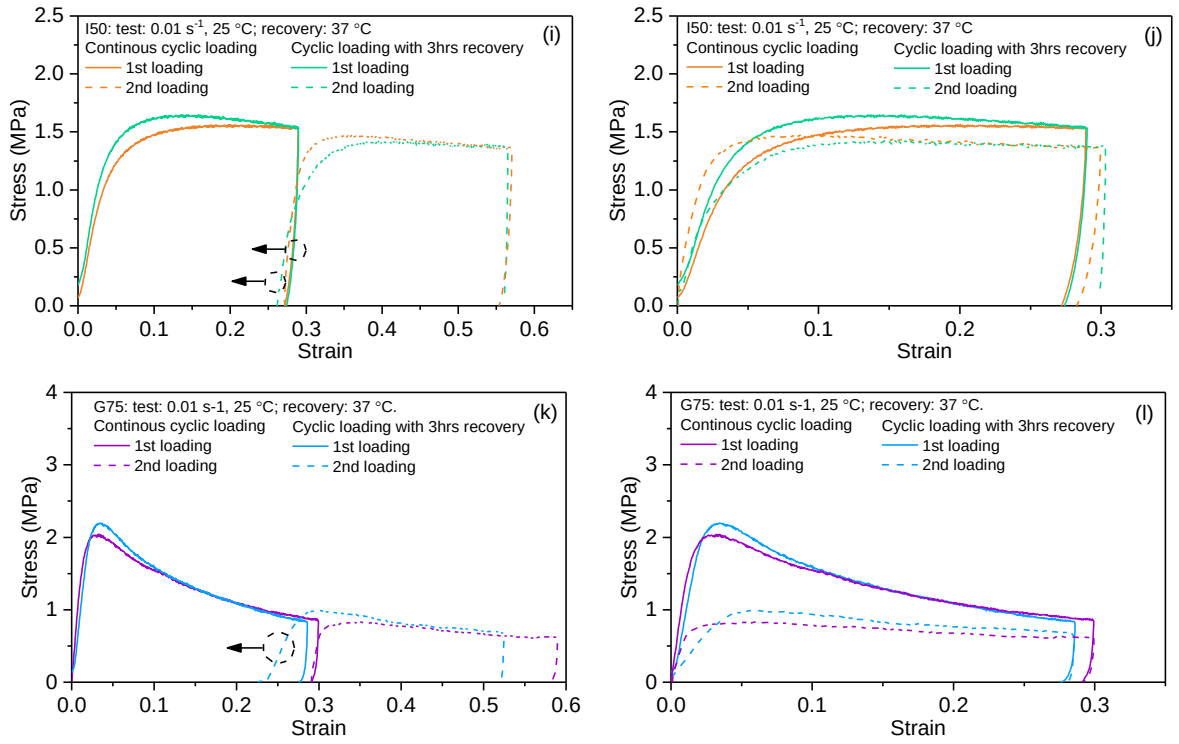


Fig. SI-29: The cyclic loading with/without a recovery period were executed for specimens SPU (a, b), G25 (c, d), G50 (e, f), C50 (g, h), I50 (I, j) and G75 (k, l). The re-loading stress-strain curves after three hours recovery for these specimens were compared to the initial strain-stress behaviour in (b), (d), (f), (h), (j) and (l). All experiments were conducted at 0.01 s^{-1}, 25 °C, and rested in a temperature chamber for recovery at 37 ° C.